



HAL
open science

Structural Aluminum alloy processed by Laser Powder Bed Fusion (L-PBF) : A fundamental understanding of cracking

Akash Arun Sonawane

► **To cite this version:**

Akash Arun Sonawane. Structural Aluminum alloy processed by Laser Powder Bed Fusion (L-PBF) : A fundamental understanding of cracking. Material chemistry. Université Grenoble Alpes [2020-..], 2021. English. NNT: 2021GRALI062 . tel-03368062

HAL Id: tel-03368062

<https://theses.hal.science/tel-03368062v1>

Submitted on 6 Oct 2021

HAL is a multi-disciplinary open access archive for the deposit and dissemination of scientific research documents, whether they are published or not. The documents may come from teaching and research institutions in France or abroad, or from public or private research centers.

L'archive ouverte pluridisciplinaire **HAL**, est destinée au dépôt et à la diffusion de documents scientifiques de niveau recherche, publiés ou non, émanant des établissements d'enseignement et de recherche français ou étrangers, des laboratoires publics ou privés.

THÈSE

Pour obtenir le grade de

DOCTEUR DE L'UNIVERSITE GRENOBLE ALPES

Spécialité : **Matériaux, Mécanique, Génie Civil, Electrochimie (2MGE)**

Arrêté ministériel : 25 mai 2016

Présentée par

Akash SONAWANE

Thèse dirigée par **Prof. Jean-Jacques BLANDIN**
préparée au sein du **CEA Grenoble** et du **laboratoire SIMaP**
dans l'**École Doctorale I-MEP2**

Mise en œuvre d'un alliage d'aluminium structural par fusion laser sur lit de poudres: étude des mécanismes de fissuration

Thèse soutenue publiquement le **6 Juillet 2021**
devant le jury composé de :

M. Alexis DESCHAMPS

Professeur à l'INP de Grenoble (Président)

M. Jean-Marie DREZET

Professeur, École Polytechnique Fédérale de Lausanne (Rapporteur)

Mme Aude SIMAR

Professeure, Université Catholique de Louvain (Rapporteuse)

M. Jean-Jacques BLANDIN

Directeur de Recherche CNRS, SIMaP, Université Grenoble Alpes
(Directeur de thèse)

M. Guilhem MARTIN

Maître de conférence, SIMaP, Université Grenoble Alpes (Co-encadrant)

M. Guilhem ROUX

Ingénieur chercheur, LITEN, CEA de Grenoble (Co-encadrant)

M. Marc THOMAS

Ingénieur chercheur, Office National d'Études et de Recherches
Aérospatiales (ONERA), Chatillon (Examineur)



Structural Aluminum alloy processed by Laser Powder Bed Fusion (L-PBF): A fundamental understanding of cracking

Ph.D. Thesis (2017-2021)

Akash SONAWANE

Akash SONAWANE

Date: July 2021

Supervisor: Dr. Guilhem ROUX (CEA Grenoble)

Supervisor: Dr. Guilhem MARTIN (Laboratory SIMAP, Grenoble INP)

Thesis Director: Prof. Jean-Jacques BLANDIN (Laboratory SIMAP, Grenoble INP)

Grenoble, France.

ॐ साईं

*“I am born with potential.
I am born with goodness and trust.
I am born with ideas and dreams.
I am born with greatness.
I am born with confidence.
I am born with wings.*

*So, I am not meant for crawling,
I have wings, I will fly
I will fly and fly”.*

- Dr. APJ Abdul Kalam



Abstract

Metal Additive Manufacturing also referred to as 3D printing has flourished rapidly into sectors such as aerospace and automotive, where high strength-to-weight ratio and defect-free parts are key requirements. Until today only a few aluminum alloys like AlSi10Mg and AlSi7Mg are manufactured by laser powder bed fusion (L-PBF) [1]. Unfortunately, structural alloys from the 6XXX-series (Al-Si-Mg) and 7XXX-series (Al-Zn) are frequently reported to be crack-sensitive under high cooling rate conditions typical of the L-PBF process [2,3]. In the literature, few technical solutions have been suggested to overcome hot cracking issues. Martin et al. [4] proposed to add nano-particles to promote grain nucleation and thus refine grain size. Others suggest modifying the alloy composition by adding elements like Si [5] or rare-earth elements like Sc in Scalmalloy®. However, there are still debates regarding the mechanism leading to hot cracks in parts made of 6061-grade built by L-PBF. This lack of in-depth understanding of the root causes of hot cracking is an impediment for designing engineering parts for safety-critical applications.

The mechanism at the origin of cracks has been identified as solidification cracking based on the observation of the fracture surface of as-built parts where a dendritic morphology gives evidence of the presence of liquid films trapped in the interdendritic space. Also besides, our experimental outcomes based on EBSD characterization, demonstrate that cracking occurs only along columnar grain boundaries of higher misorientation ($>20^\circ$). We rationalize this cracking along high misorientation grain boundaries behavior using the Rappaz model based on the critical coalescence undercooling [6]. Thus, the critical coalescence undercooling can be estimated as a function of misorientation.

The Rappaz-Drezet-Gremaud (RDG) hot cracking criterion [7] is then applied using inputs that comply with L-PBF processing conditions. First, the solidification path of the 6061-alloy is calculated relying on the Scheil-Gulliver assumption. Second, the critical coalescence undercooling is included in the RDG model by modifying the lower integration limit to account for the fact that liquid films are stable at lower temperatures along high misorientation grain boundaries. Finally, the thermal gradients (G) and solidification velocity (v) required into the RDG are estimated with the help of thermal simulations using the Rosenthal analytical model to get values typical of the L-PBF process.

Our findings for 6061 alloy show that the existence of stable liquid films is linked to grain boundary misorientation, which causes a sudden increase in pressure drop leading to cracking. We also evaluate thanks to our modeling approach:

- the effect of the processing conditions, namely the first-order melting parameters (laser power and scanning speed) on the thermal gradient and solidification velocity inferred from thermal simulations, on the hot tearing sensitivity. This led us to an understanding of the required (G , v) and therefore the required laser power and speed to decrease the cracking susceptibility and propose improvements to process the 6061 alloy using L-PBF.
 - the effect of solute content modification on the cracking sensitivity. This can be further used as guidelines to suggest chemical composition modification of the 6061 Al-alloy to improve its processability by L-PBF.
-



Résumé

Dans cette thèse, une analyse de la sensibilité à la fissuration à chaud en fonction (i) des paramètres de premier ordre (puissance, vitesse) du procédé de fusion laser sur lit de poudres (L-PBF : Laser Powder Bed Fusion) et (ii) de la variation de la teneur en soluté (Si et Mg principalement) est présentée pour l'alliage d'aluminium à durcissement structural 6061 (Al-0.8Si-1.2Mg wt%). Le mécanisme de fissuration à chaud est identifié comme une fissuration par solidification sur la base d'observations expérimentales des microstructures. En accord avec des travaux antérieurs publiés sur d'autres familles d'alliages, les fissures se propagent aux joints de grains de fortes désorientations et sont préférentiellement situées au centre des bains de fusion. En utilisant le critère de Rappaz-Drezet-Gremaud (RDG criterion) combiné à des simulations thermiques utilisant le formalisme de Rosenthal, la localisation des fissures correspond aux régions des bains de fusion ou la sollicitation mécanique intergranulaire est la plus élevée lors de la solidification. Des cartes de sensibilité à la fissuration à chaud sont ensuite développées pour prédire de manière simple les variations de sensibilité à la fissuration à chaud en fonction des paramètres du procédé de premier ordre, à savoir la puissance laser et la vitesse de balayage ainsi que des conditions de préchauffage. Les tendances prédites sont qualitativement en accord avec les observations expérimentales. Les résultats permettent de discuter de l'impact des conditions d'élaboration sur la réduction de la fissuration à chaud et également d'identifier les paramètres métallurgiques clés de ce mécanisme de fissuration.



Acknowledgments

A journey of 3.5 years but a lifetime to cherish. I have experienced all the emotions a human can feel in these past years: joy, pride, curiousness, motivation, satisfaction, hunger, sadness, helplessness, anger (sometimes!). I don't want future Ph.D. students to be demoralized but instead think differently. A Ph.D. degree is more than just a degree. It teaches you how to live life constructively, without getting affected by the difficulties, and reaching the ultimate goal. Yes, it is not a one-man show. There are several key people involved in your Ph.D. These people come into your life and they ignite your mind in such a way, that there is no turning back. So before reading my detective novel (~250 pages) about who cracked the Aluminum alloy, I would like to take the opportunity to put my personal feelings into words and give a glimpse of those important people in my PhD journey.

The year 2015 was probably a joyful year for me, as my motivation to pursue material science made me cross countries (India → France → Germany). Yes, I was fortunate to attend the Erasmus Mundus Masters (FAME- Functionalized Advanced Materials Engineering) from Grenoble INP, France, and TU Darmstadt, Germany. It is a double degree program, where you get expertise from two different institutes. I cannot thank enough to **Prof. Eirini**, who was the coordinator of our program in Grenoble. She was very helpful throughout the masters as me and my friends (**Akshya, Devang, Hardik, Juhi**) struggled a bit to understand "Franglish". Now that I am used to it, well, it was not obvious during that time since the strong accent made us sometimes skip classes. Nevertheless, I must thank all those professors (**Prof. Alexis, Prof. Blandin, Prof. Veron, Prof. Duffar, Dr. Annie**) who made a dedicated effort to teach us materials science. In Darmstadt, the story was different. **Prof. Müller, Prof. Bai-Xiang Xu, Dr. Joachim Brötz** made us so strong conceptually that we were ready to take up any materials design challenges, but all that enthusiasm was crushed during the oral exams at TU Darmstadt. Especially the exam with Prof. Müller, it was so brutal, that they tested our interdisciplinary application of the metallurgical concepts. But I think, this is the correct method to educate someone, to embed a logical thought process and problem-solving approach. No doubt why German engineers are renowned for their simplicity yet effectiveness. This was the biggest lesson from TU Darmstadt, and I want to thank Prof. Müller to teach us how to handle stress without any strain!

By the time of 2016, I had already lived in two countries, France and Germany. I already had a preference in mind to be in France because of the love for language and super welcoming mentality of the people. Concerning my subject of the master thesis, it all started in 2016, when I developed a keen interest in the process of 3D printing of metals when **Dr. Raphael Salapete** mentored my internship work in the Ariane group, Vernon. It was the first time I was introduced to the field of additive manufacturing and I immediately realized that the process has huge potential. During my time at Constellium (Voreppe) in 2017, I learned that Structural Al-alloys are quite difficult to process by 3D printing since they develop cracks. Without the mentors like Dr. Salapete and **Dr. Bechir Chehab**, this orientation in my profile towards 3D printing of metals would not be possible. All these past experiences and my interest in metallurgy made a solid foundation for me to pursue my Ph.D. thesis on this subject.

I joined the French Alternative Energies and Atomic Energy Commission (CEA) Grenoble at the end of 2017 to pursue my Ph.D., and I am fortunate to **Dr. Guilhem Roux (GR)**, **Dr. Guilhem Martin (GM)** and **Prof Jean-Jacques Blandin (Director)** for allowing me to work on this exciting field of Aluminum 3D printing. Thanks to **Institute Carnot FAMERGIE** for funding the research work by establishing the link between CEA-LITEN, Grenoble, and SIMAP laboratory of Grenoble University Alpes. I still remember my good friend **Rodrigo** from Brazil who transferred me the email of job announcement at CEA. Without this email, I probably would be somewhere else. Speaking about the acceptance process, just with a single interview, Prof. Blandin and Guilhem (R) accepted me to do the job, I suppose they found something in me or they were short of candidates, this will remain a mystery. To be honest, the first year of my Ph.D., was a big challenge, as I had to manage three supervisors and there were instances when it was difficult to get a unanimous opinion. I have had sleepless nights due to our monthly meetings, when Prof. Blandin used to get lost during my presentations. He never expressed any sort of anger to me, but instead always asked me the right questions, always gave important suggestions, always observed something unique which we three did not notice, and most importantly was always available when I asked for help.

Few words about the GEM of a person I encountered during my Ph.D., my co-supervisor **Dr. Guilhem Martin**. Very subtle in his approach and very kind to help anyone. As Prof. Blandin rightly pointed out that, it was Guilhem (M), who performed the role of my Director. I would agree with this statement since Guilhem (M) made a significant contribution to uplift my work and made a decisive contribution to orient my Ph.D. Without his thoughtfulness nature and decision-making ability, I suppose I won't be able to defend my thesis. It was him (GM) who introduced me to the Hot cracking models and this was the turning point of the thesis, where we started to shift the gears. The time he has offered me during the first lockdown of the Covid pandemic (beginning of 2020), is priceless. Say it 8h in the morning or 23h in the night, he was always there for me on skype to understand my work and suggest improvements. Under his daily guidance and constructive advice, I was able to publish my first work. Say it work issues, personal issues, mental troubles faced by Ph.D. students during the pandemic, he was ALWAYS there to help. Not just for me, for other Ph.D. students as well. This shows his amazing qualities, which I am forever thankful to him. I was fortunate to work under your solid guidance, merci beaucoup Guilhem (M)!

The second Guilhem of the trio is **Dr. Guilhem Roux (GR)**, who supervised my day-to-day activities in CEA Grenoble. We all know the work quality expectation of Guilhem (M), and in my Ph.D. thesis, we had a second Guilhem (R) to raise the bar. About GR, I must say he took care of me by following my work and handled all the CEA administration issues I had. He screened all my presentations before anyone. I learned a lot from him, managing industrial projects, working autonomously, and more importantly his "what to present attitude". As a person, I always felt he is very kind and made me feel integrated into his team. Every Monday morning meeting with him gave me a sense of enthusiasm since every week we had a new problem and its solution to discuss. Sometimes calm, sometimes direct, he is exotic and this is his style that everyone in the L3M laboratory appreciates. I am thankful to him that every month he took a tram with me to Saint Martin d'Herès for our meetings with the other supervisors.

The few minutes of awkward silence in that 30-40 min tram ride followed by motivational advice will always stay with me. Thanks for all Guilhem (R) and giving me the opportunity to work at CEA.

The experience with an incredible team from SIMAP laboratory, and CEA-LITEN, has made a huge contribution in enhancing my knowledge, competencies and shaping my research journey. I would like to thank all the colleagues at CEA L3M laboratory : **Thierry, Gilles, Pascal, Guillaume, Violaine, Michel, Luc, Vincent, Jean-Yves, Jean-Paul**, and my Ph.D. circle: **Charlotte (office mate), Claudia, Mathieu, Florian, Romain** for their welcoming attitude which made me feel integrated into the French working culture. I want to thank all the people who helped me in my experimental work: **M. Sebastien** (fabrication of 3D parts), Pascal (etching work, sandblasting), **M. Romain and Camille from PFNC** (helping me with EBSD), **M. Frederic from CMTTC**, especially to train me on the SEM machines in Saint Martin d'Herès. On the simulation side, it was my junior Ph.D. student **M. Mathieu** who always cleared my doubts in Comsol. Without the inputs of these people, any research would be incomplete, a big thanks to all of you.

Speaking about few things that many might not know, about the logistics issues I faced during the end of my Ph.D. All my work, simulations were performed on the CEA laptop and when my contract terminated, I had to, unfortunately, return the laptop leaving with me just the 3 years of data. In such conditions to finish the manuscript and run some last calculations, I had to rely on my personal laptop, which had many technical issues. Under such stress to finish the thesis, it was my neighbor **M. Morgan Brassel**, who rescued me. He not only repaired my laptop but also helped me install a few software. Similarly, my close friend **Pranav Gupta (Cornell, US)** helped me to run Origin's license and **Swapnil** solved all Matlab/LaTeX related issues. I also want to thank my very close friend **Emmanuel (Manu)** to host me for few months (April-July, 2021) in his Maison. It was at 7 Rue de la Sure, Fontaine where I made corrections to my thesis and defended it on 6th July 2021. So many thanks to Manu and all the souls in the Maison: **Danny, Veronique, David, Patrice, Mia** to make me feel at home and at peace to finish my thesis. Such people help you in the right moment to move ahead. My French connection in France will be incomplete, without mentioning the name of **Thibault De Roquefeuil**, because of whom I probably know so many things about France and their culture. Being my roommate to a very close friend, he was there for me and still is. Thanks to this Quasicrystal diffraction pattern we created, where Thibault is the center and all of us (myself, Manu, Marc, Charlotte, Florian, Antoine, Justine, Jenna, Adele, Romain,) are around Thibault.

Special thanks to all the jury members: **Prof. Jean-Marie Drezet (EPFL, Switzerland), Prof. Aude Simar (UCL, Belgium), Dr. Marc Thomas (Onera), Prof. Alexis Deschamps (Grenoble INP)** for their constructive discussions. Thanks all for taking out time and reading my manuscript to evaluate it. Especially Prof. Drezet, since he came to Grenoble to attend my Defense. This shows his love for the subject and thanks to him for having a fruitful/lively scientific discussion during the Ph.D. defense. Another person I would like to thank is **Prof. Rappaz (EPFL)** who was not involved in my Ph.D. directly but his work on developing the famous RDG hot cracking model along with Prof. Drezet, was the heart of my thesis.

Moving towards someone to who I am forever bound is **Ekaterina**. She was there for me when I came the first time in France in 2015, when I started my Ph.D. in 2017 and when I finished my Ph.D. in 2021. I cannot thank her enough for her daily support and motivation during my stay in France and especially during the tough phase of thesis writing. Miss your delicious bakery and healthy breakfast at 40 Rue Thiers ☺ We survived the pandemic together, I owe you, Спасибо Kate!

Without the constant support, contribution of my family: **Arun Sonawane (Dad), Archana Sonawane (Mother), and Juhi (sister)** and blessings of our ancestors, this is not possible. I will never forget the efforts my mom took to improve my mathematics. She used to solve the complicated problems first and once understood the technique, she made me learn the correct/efficient methodology. Right from making this bold decision to send us out of India, my dad has seen it all. Since he knew the importance of education, he never pulled my leg behind but instead motivated me to perform best in academics. Whatever we have asked, my dad through his capabilities has always fulfilled it. Due to Pandemic, my parents were not able to attend the Defense physically in France, but they saw it live and I know the emotions they must have gone through. I just want to thank them for everything they have done for Juhi and me. Love you all.

Thanks to all for bearing with my emotions. I agree this is not a traditional acknowledgment, but indeed a short story to acknowledge the key people in my career, and sincerely want to express my gratitude to all of them.

Good lecture of my so-called Detective Novel. The journey into the exciting field of additive manufacturing has just begun!

Akash SONAWANE.

Grenoble, 6th July 2021.



Table of Contents

Context	1
1. Introduction	3
1.1. Laser powder bed fusion (L-PBF)	3
1.2. Aluminum alloys in L-PBF	5
1.3. Thesis aim and methodology	7
1.4. Thesis Structure	9
2. Literature review	13
2.1. Aluminum Alloys fabricated in L-PBF	15
2.1.1. Review of Al alloys tested in L-PBF.....	15
2.1.2. 6061 Al-alloys	20
2.1.3. Metallurgy of 6061 Al-alloy.....	22
2.2. Defects encountered in Aluminum alloys during L-PBF.....	27
2.2.1. Cracks	27
2.2.2. Origin of porosities in Al-alloys.	27
2.2.3. High reflectivity of Aluminum	30
2.2.4. Oxide film formation.	31
2.3. Cracking mechanism (Review)	32
2.3.1. Solidification cracking.....	34
2.3.2. Liquation cracking	38
2.3.3. Summary	39
2.4. Cracking sensitivity criteria.....	39
2.4.1. Solidification temperature range.....	40
2.4.2. Sindu Kou criterion.....	41
2.4.3. Rappaz, Drezet and Gremaud (RDG criterion)	43
2.4.4. Summary	45
2.5. Cracking mitigation strategies in Al-alloys (L-PBF and welding literature)	46
2.5.1. Processing route.....	46
2.5.2. Grain refinement through external nucleating agents.	49
2.5.3. Solute composition modification.	51
2.5.4. Summary	54
3. Powder Characterization	55
3.1. Chemical composition	57
3.2. Powder size distribution	58
3.3. Powder morphology and flowability	59
3.3.1. Morphology	59
3.3.2. Flowability.....	61

4.	Process parameter optimization and microstructural observations	65
4.1.	Process Optimization.....	67
4.1.1.	Introduction.....	67
4.1.2.	Reflectivity of the bulk-substrate and the powder	69
4.1.3.	Elementary powder layer experiments	71
4.1.4.	Fabrication of 3D cubes by L-PBF	84
4.2.	Multi-scale characterization of the as-built microstructure (optimized parameters)	90
4.2.1.	Experimental procedures	90
4.2.2.	Macrostructure: grain structure	91
4.2.3.	Cracking pattern.....	93
4.2.4.	Cracking mechanism	96
4.2.5.	Microstructure.....	99
4.2.6.	Microstructure: Discussion	109
4.3.	Summary of Chapter 4.....	111
5.	Developing cracking sensitivity criteria (based on RDG model)	113
5.1.	Rappaz, Drezet & Gremaud (RDG criterion)	115
5.2.	Thermodynamic calculations.....	116
5.2.1.	Introduction to Scheil-Gulliver Model.....	116
5.2.2.	Solidification path of 6061 Al-alloy (f_s).....	117
5.3.	Rationalizing cracking at HAGB's	118
5.3.1.	Coalescence undercooling.....	118
5.3.2.	Estimating grain boundary energy $\gamma_{gb}(\theta)$	121
5.4.	Estimating solidification conditions typical of L-PBF (thermal gradient and solidification velocity).....	124
5.4.1.	Introduction to Rosenthal analytical solution.....	124
5.4.2.	Rosenthal simulations	126
5.4.3.	Rationalizing centerline cracking.....	132
5.5.	Predicting critical pressure drop.....	135
5.5.1.	Region with critical pressure inside the melt pool.....	143
5.6.	Summary	144
6.	Effect of processing parameters on hot cracking sensitivity	147
6.1.	Introduction.....	149
6.2.	Evaluating cracking sensitivity for L-PBF melting parameters.....	149
6.3.	Effect of preheating conditions.....	155
6.4.	Sensitivity studies for different parameters.....	159
6.4.1.	Primary dendrite arm spacing (λ)	159
6.4.2.	Strain rate (ϵ).....	164
6.4.3.	Viscosity (μ)	166
6.5.	Summary	171

7. Effect of chemical composition modification on the hot cracking sensitivity	173
7.1. Introduction.....	175
7.2. Effect of Solute content modification.....	175
7.2.1. Effect of Silicon and Magnesium additions	178
7.2.2. Summary	183
7.3. Effect of Zirconium (Zr) addition	183
7.3.1. Microstructure of Zr-modified 6061 Al-alloy	185
7.3.2. Summary	188
8. Conclusions and recommendation for future work	189
8.1. Conclusions	191
8.2. Perspectives	197
Appendix	203
Laser tracks on 6061 Al-alloy (bulk substrates)	203
List of Figures	216
List of Tables	223
References	224

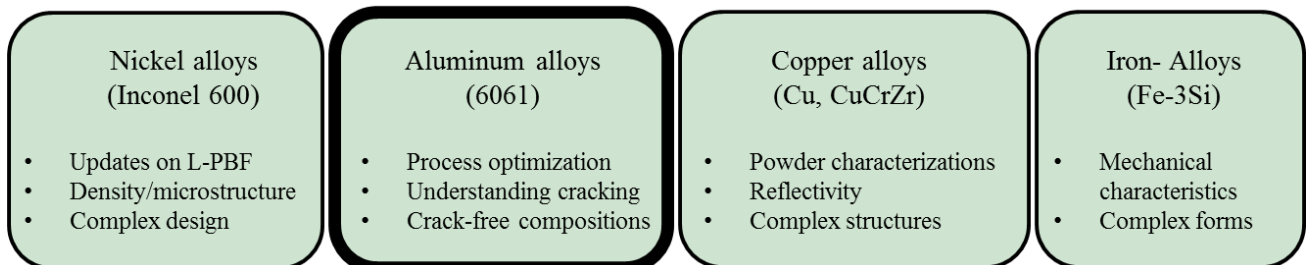
Context

The present work focuses on the research done as a part of doctoral research in the framework of the FAMERGIE project (Fabrication Additive for Energy). The work was carried out in collaboration between two labs namely, L3M (Laboratory of Materials research and materials modeling), CEA Grenoble, and SIMAP laboratory of Grenoble University Alps.

Out of the four metallic alloys studied in the Framework of FAMERGIE, the work carried out under this study focusses on Aluminum 6061 alloy (Al-0.8Si-1.2Mg). This structural alloy has applications in heat exchangers and structural aerospace. Currently, it is not considered a favorable candidate for additive manufacturing due to its high cracking sensitivity. The 6061 alloy has better mechanical properties up to temperatures 200°C in comparison to other casting Al alloys like AlSi7Mg, AlSi10Mg which are easily fabricated. The work reported in this thesis deals with 6061 alloy processed by laser powder bed fusion (L-PBF), a technique used for rapid prototyping.

The study of hot cracking at a microstructural level and its sensitivity to L-PBF processing and chemical composition modification has been discussed in this report. Finally, the work aims to understand the cause of cracking associated with the 6061 Al-alloy and ultimately propose a way to minimize or eliminate it.

Laser powder bed fusion (L-PBF)



1. Introduction

Traditional manufacturing techniques for aerospace and automotive components involve time input and are restricted in terms of design complexities. They involve post-manufacturing heat treatments to obtain the desired properties. Components that require a high level of precision need a machining step and this can induce defects that are detrimental to mechanical properties. Apart from manufacturing less complex shapes, they are also susceptible to wastage of material.

To improve the ongoing traditional manufacturing, additive manufacturing can be considered a vital option. It is a technique that involves rapid fabrication of the parts through layer by layer deposition of the material. It involves the fabrication of complex shapes designed with computer-aided software, which is then decomposed in layers for the machine to print successively. This is the reason additive manufacturing is also referred to as 3D printing.

1.1. Laser powder bed fusion (L-PBF)

Most of the metallurgical alloy developments are driven by the technological needs of industries for a specific application. Various processes for manufacturing safety-critical parts have proliferated in recent years, one of them being metal additive manufacturing (AM), also referred to as 3D printing. Amongst the AM processes listed in ASTM F2792–12a [8], laser powder bed fusion (L-PBF) deals with selective laser melting of the metal powder, layer-by-layer, to achieve the desired complex parts, as shown in **Figure 1-1a**.

L-PBF involves powder bed fusion using a laser beam, which melts the powder in a specific location. That is why previously it was also known as ‘selective laser melting (SLM)’. Once the layer of powder is melted, the build piston on which the powder was lying, lowers down for the next powder layer to be deposited. This results in a deposition of fresh unfused powder on the build chamber, which is again fused by the laser. These steps are repeated consequently until the final 3-dimensional part is created (which is designed using the CAD software’s, as shown in **Figure 1-1b**). This process of layer-wise deposition of powder and its simultaneous fusion using the laser is thus termed as laser powder bed fusion (L-PBF).

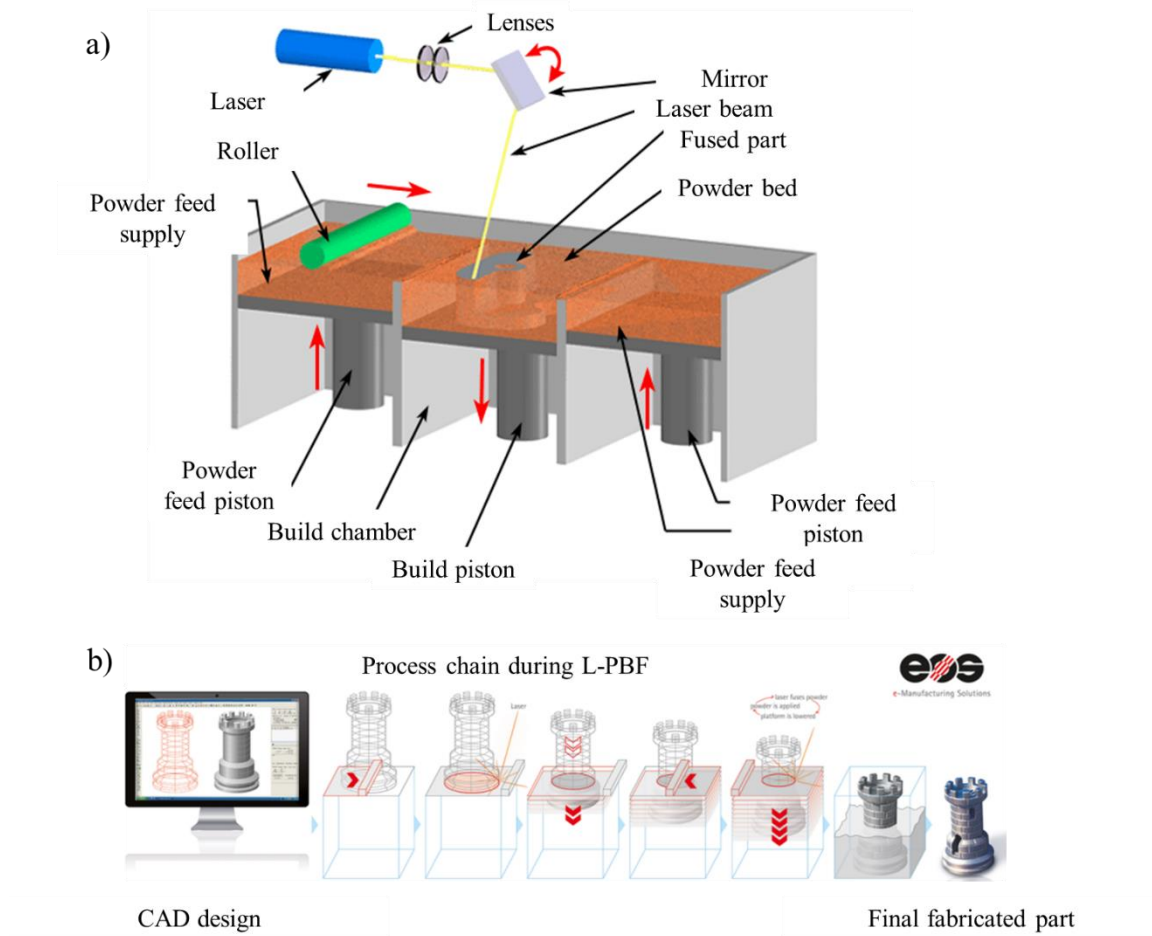


Figure 1-1 a) Principle of laser powder bed fusion (L-PBF), adapted from [9] b) Steps involved in L-PBF fabrication, adapted from [10].

L-PBF fabrication process mainly consists of the parameters shown in **Figure 1-2a**). Depending on the L-PBF machine, laser parameters are controlled by its laser power and the spot size (area of exposition). Similarly during the scanning, the speed with which the laser melts the layer (i.e. the laser scan speed) can also be controlled. Out of the ones listed in **Figure 1-2a**), laser power (P), laser speed (v_{laser}), hatch spacing between two successive scans (as shown in **Figure 1-2b**) and the layer thickness are the most important process parameters for the L-PBF. Depending on these parameters the solidification can be affected. There are also parameters related to the powder feedstock used in the L-PBF. Usually, the size distribution, the morphology, and the flowability of the powder play a key role. In general two types of powder size distribution are used in L-PBF, 10-45 μm , and 20-63 μm [1]. Similarly, a good flowability of the powder along with a better aspect ratio of the powder particles is needed to achieve a dense final part.

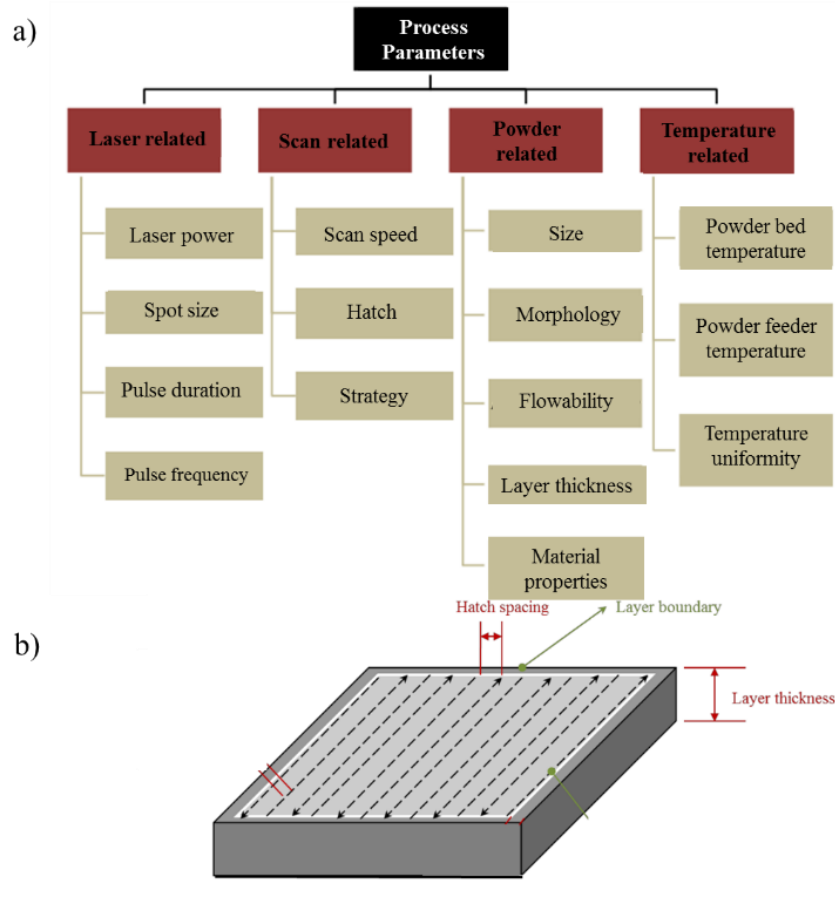


Figure 1-2 a) Process parameters for L-PBF process and b) schematic of a scan strategy depicting the hatch spacing, adapted from [1]

1.2. Aluminum alloys in L-PBF

L-PBF has emerged rapidly into sectors such as aerospace, where a high strength-to-weight ratio and defect-free parts are key requirements. Therefore, for lightweight applications, the use of structural Aluminum (Al) alloys has the potential to be exploited using L-PBF.

Aluminum (Al) exists in FCC (face-centered cubic) crystal structure, having a lattice parameter of $\sim 0.4\text{nm}$ [11]. Compared to other metals like steel, nickel-based alloys, Aluminum has a lower density. It also possesses higher corrosion resistance with good thermal and electrical conductivity. With such properties, Aluminum is frequently used in industries dedicated to automobiles, aerospace, naval-based industries, etc. However, pure Aluminum lacks mechanical strength. Several alloying elements are frequently added to the pure Al to form precipitates and phases which give strengthening to the material. Depending on the solute elements added to the Al, several alloys are classified into two major categories (casting and wrought), as shown in **Figure 1-3**. The typical numbering system consists of four digits. The first digit in the alloy

numbering system denotes the alloy series (ranging from 1-8), the second digit refers to the purity or version number of the modifications to the original composition, the third and fourth digits are to identify specific alloys. Moreover, the classification into different series relies on the addition of specific solute elements (Si, Cu, Fe, Mg, Zn, Mn), and based on their heat treatability as shown in **Figure 1-3**.

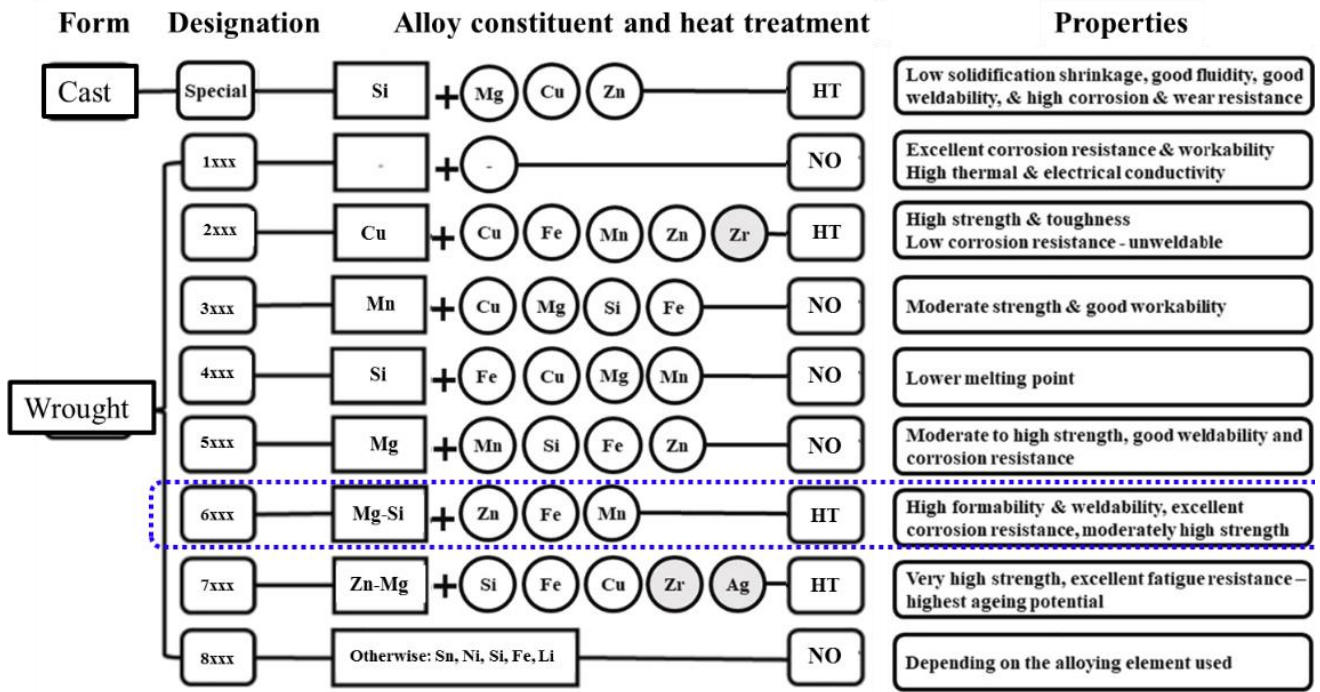


Figure 1-3 Classification of Al-alloys based on the alloying elements, adapted from [12][1].

Of the different series listed in **Figure 1-3**, the 6XXX and 7XXX series have better mechanical properties compared to casting alloys (AlSi10Mg and AlSi12). During the casting process, to refine the microstructures, chemical modifiers are usually added. On the other hand, due to the high cooling rate ($\sim 10^6\text{K/s}$) associated with the L-PBF process, refined microstructures can be directly obtained. Thus, with L-PBF processing of Al alloys, it is possible to achieve complex parts having fine microstructures, which can complement the high strength to weight ratio of the Al-alloys. The most easily manufactured aluminum alloys using L-PBF are the AlSi10Mg and AlSi7Mg alloys [1,2,13–15]. These alloys were originally developed for casting applications due to their near eutectic silicon composition. However, as already mentioned, their mechanical properties are inferior to the structural alloys from the 6XXX and 7XXX series [1,11,14,16]. One of the wrought alloys from the 6XXX series is the heat treatable 6061 Al-alloy composed mainly of Si and Mg as their main alloying elements. The 6061 grade can be used in various sectors such as the automotive or aeronautic industries using conventional manufacturing techniques, due to its high thermal conductivity [17], good corrosion resistance, and high yield strength after a T6-heat treatment [16]. However, welding of the 6061-grade still remains a challenge due to its cracking susceptibility during rapid solidification [18–20].

Similarly, under typical high cooling rate conditions of the L-PBF process, the 6061 Al-alloy is frequently reported to be crack-sensitive [2–4,21]. As mentioned previously, the refinement of microstructure under L-PBF conditions compared to casting is due to its solidification with high cooling rates occurring in a small region. From a macro scale of the L-PBF process as shown in **Figure 1-4a)**, the molten region or the melt pools (where the solid gets melted) are formed on a micro-scale (see the red region of **Figure 1-4b)**). **Owing to the dendritic morphology (Figure 1-4b)), the resultant as-built columnar microstructure of the structural Al-alloy (6XXX and 7XXX series), is frequently reported to be cracking, as shown in Figure 1-4c) [2–4,21].**

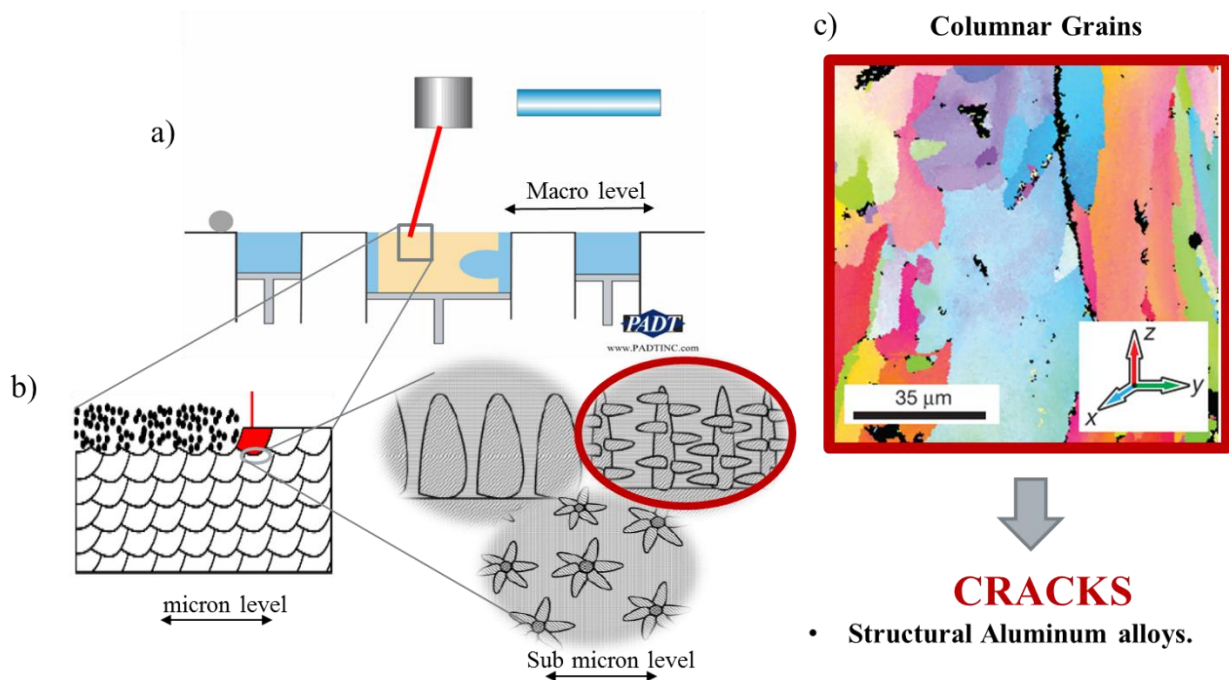


Figure 1-4 a) Schematic of L-PBF process. b) Typical length scale in which solidification happens and different modes of solid-liquid modes. c) Typical as-built microstructure of an alloy from 6XXX fabricated by L-PBF, adapted from [4].

1.3. Thesis aim and methodology

The cracking mechanism affecting structural aluminum alloys is well documented for casting and welding but not as much for additive manufacturing. According to the literature [22,23], hot cracks develop from a mechanism of either solidification cracking (occurring at the last stages of solidification) or liquation cracking (during remelting). While the hot cracking mechanism in welding literature of 6061 grade has been identified as liquation cracking [18,24,25], it is not obvious that this must be the case for laser powder bed fusion.

Moreover, Mauduit *et al.* [26] also reported the evaporation of Mg and Zn to cause a change in composition and thus increasing the cracking sensitivity. For example, hot cracking in laser powder bed fusion applied to other kinds of alloys such as nickel-based superalloys [27] is identified as solidification cracking. Thus, the mechanism of cracking in 6061 Al-alloy when fabricated by L-PBF is still unknown. A possible route to guide the alloy design strategy of Al-alloys dedicated to AM is to improve our understanding of the mechanism causing cracks.

Here, the objective of this thesis is to provide new insights into the hot cracking mechanism affecting the 6061 Al-alloy processed by L-PBF with experiments and modeling, as illustrated in **Figure 1-5**. One of the objectives is to resolve the ambiguity about the governing mechanism occurring in the 6061 Al-alloy. This allowed us to investigate the effect of (i) the processing conditions typically encountered in L-PBF, and, (ii) of alloying additions of major elements such as Si and Mg, on the cracking sensitivity. These results should enhance our knowledge about the cracking mechanism affecting the 6061 grade manufactured by L-PBF and help us to suggest guidelines regarding processing conditions and possible chemical composition modifications to improve its manufacturability.

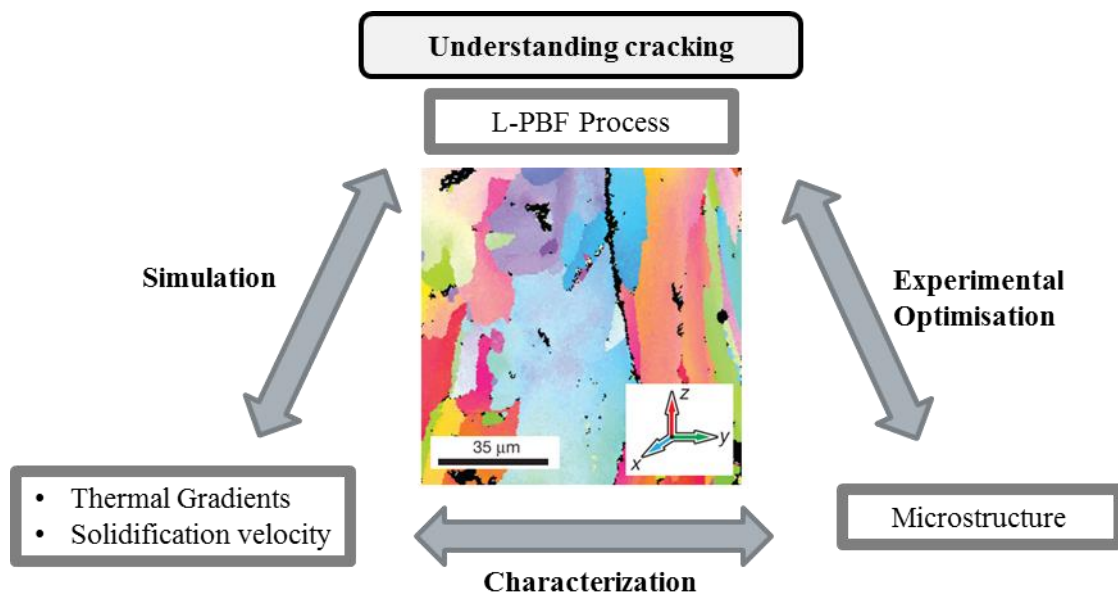


Figure 1-5 Schematic of the thesis methodology in understanding the cracking in 6061 Al-alloy fabricated during L-PBF.

Methodology:

In this thesis, we investigate by experiments and modeling the hot cracking mechanism of 6061 Al-alloy fabricated by L-PBF and its sensitivity to the processing and compositional changes. First, we optimize the processing parameters based on the stable melting parameters. Second, we characterize experimentally the cracking mechanism and the location of cracks relative to the melt pool geometry. The experimental observations are then rationalized with the help of modeling. Using the melt pool temperature field predicted by Rosenthal simulations [28], hot cracking sensitivity maps are generated using the hot cracking model of Rappaz, Drezet, and Gremaud [7]. The results allow the hot cracking sensitivity to be mapped as a function of the processing parameters. A qualitative comparison is made between experimental observations and predictions. Finally, the potential role of metallurgical parameters on the hot cracking sensitivity is discussed. The detailed microstructural study of cracking, the as-built microstructure along with the modeling approach, allowed us to identify:

- The cracking mechanism operating under L-PBF conditions.
- The cracking pattern and its sensitivity to L-PBF processing conditions.
- Role of solute elements present in the 6061 Al-alloy.
- A cracking sensitive criterion for 6061 Al-alloy during L-PBF, based on the Rappaz, Drezet, and Gremaud [7] model.
- The effect of chemical composition modification on the cracking sensitivity.
- Metallurgical parameters playing a major role in depicting cracking.

Studying the cracking mechanism and its sensitivity in detail, allowed us to provide guidelines in reducing cracking in 6061 Al-alloy fabricated by L-PBF.

1.4. Thesis Structure

To give an overview of the thesis structure, a schematic of the thesis is presented in **Figure 1-6**. The thesis chapter's mutual link and the basic feedback loop is highlighted.

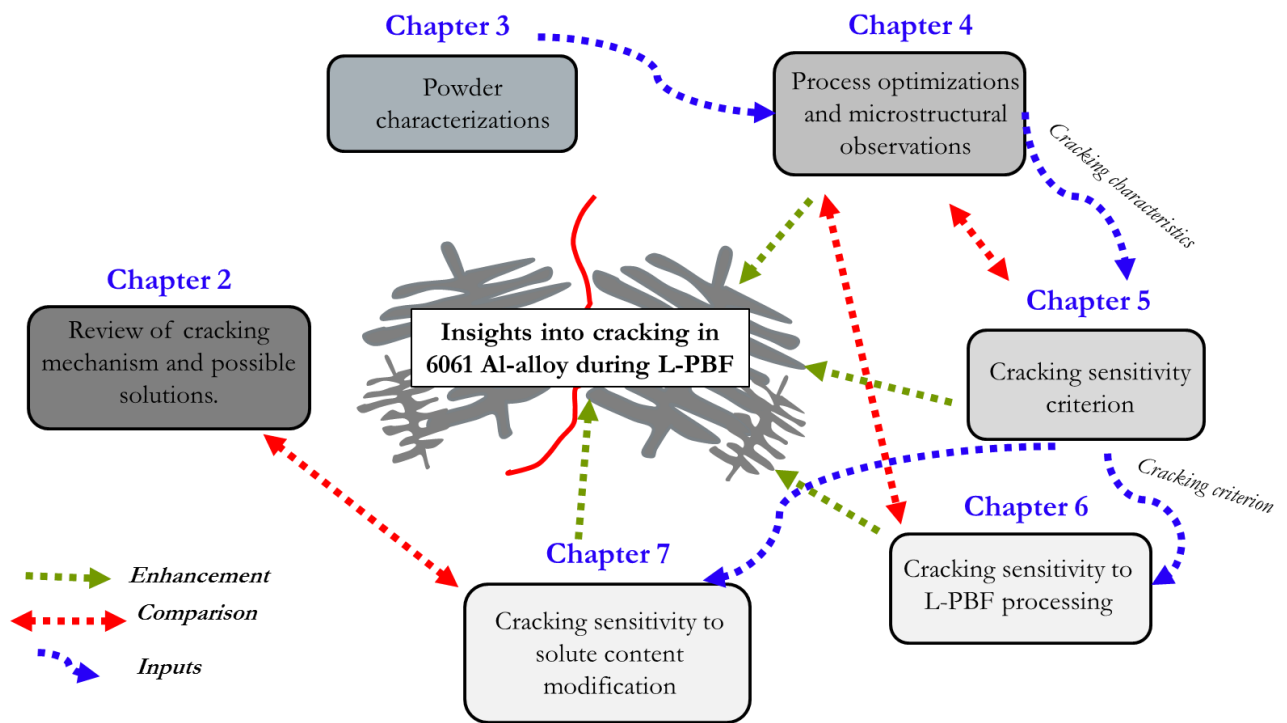


Figure 1-6 Overview of the thesis chapters and their mutual link.

1. To give a comprehensive understanding of the thesis, the introduction i.e. the present chapter briefly describes the problem, the objective, and the methodology used in the present study. The introduction also gives an overview of the thesis's upcoming chapters and their inter-connections.
2. The second chapter, host the literature review of the Al-alloys tested in L-PBF and their frequent defects encountered. The chapter provides a systematic review of the identified cracking mechanism in the 6061 Al-alloy. Basic alloy metallurgy including the microstructure and the phases reported in the literature are also highlighted. Various cracking mitigation strategies employed in welding and L-PBF literature are presented to get an understanding of the existing solutions. Moreover, different hot cracking criteria existing in the literature are also described.
3. The third chapter details the 6061 Al-alloy powders used in the present study. Powder characteristics like chemical composition, size distribution, morpho-granulometry, flowability, etc. are presented.
4. Chapter 4 reports the results obtained through the course of experimental studies. Results comprising of the processing parameter optimization and observation of cracking with respect to the microstructure are reported. Experimental evidence of the cracking mechanism and its pattern with respect to the processing conditions is analyzed. Detailed microstructural studies of the as-built 6061 Al-alloy samples are done.

5. Chapter 5 is established on the cracking mechanism and cracking pattern identified in chapter 4. With the experimental inputs from chapter 4 and its combination with the hot cracking criterion (Rappaz, Drezet, and Gremaud [7]), a cracking parameter is established. Similarly, cracking location with respect to microstructure is also rationalized, with the results obtained through the modeling approach reported in this chapter.
6. Chapter 6 uses the cracking criterion established in chapter 5, as feedback to analyze the sensitivity to L-PBF processing conditions. Hot cracking sensitivity (HCS) maps are developed for the 6061 Al-alloy under L-PBF conditions. Processing conditions less sensitive to cracking are predicted and qualitatively compared with the experimental results reported in chapter 4. Various metallurgical parameters, which can be detrimental to cracking are identified and their sensitivity analysis is presented in this chapter.
7. Chapter 7 hosts the last aspect of the thesis, which is predicting the effect of solute content modification on the cracking sensitivity, based on the criterion developed in chapter 5. Solute elements comprising the standard 6061 alloy composition are analyzed for their beneficial or detrimental effect on the cracking sensitivity. Using the cracking sensitive criterion of chapter 5, compositions less sensitive to cracking under L-PBF conditions are identified. Similarly, the beneficial role of nucleating agents in suppressing cracking in 6061 Al-alloy is also discussed. The chapter can be considered as a crude methodology for designing alloys less prone to cracking during L-PBF.
8. Finally, the last chapter concludes the thesis and identifies the new advancement brought to the field. It includes perspectives for future research efforts and identifies the aspects which need to be considered to fabricate crack-free structural Al-alloys during L-PBF.

2. Literature review

In this chapter, a review of Al-alloys tested in L-PBF is presented. Different types of defects and their causes are discussed. The fundamental reasoning for the cracking issues identified in Al-alloys is reported and various remedies existing in literature are consolidated. A review of different hot cracking criteria is also presented to give the reader an overview of the existing techniques to assess the cracking sensitivity.

2.1. Aluminum Alloys fabricated in L-PBF

This section will cover the different Al-alloys tested in L-PBF. The typical microstructures encountered during the fabrication process and ease of processing are discussed.

2.1.1. Review of Al alloys tested in L-PBF

- Al-Si alloys

Al-Si alloys are used in the casting industry due to their ease of processing. This is the family of alloys that was the first to attract attention in the additive manufacturing industry. Depending on the silicon content, the alloy family can be divided into three categories. As shown in the Al-Si phase diagram in **Figure 2-1a)**, there is an eutectic point at 12.2 wt% Si. Thus, hypoeutectic, eutectic, and hypereutectic compositions can be present [29]. Among the hypoeutectic alloys, the AlSi10Mg alloy is by far the most studied in L-PBF [13,14,30–32]. According to several reports [13,14,30–32], these alloys are easy to fabricate and there is no evidence of cracking reported, as shown in **Figure 2-1b)-f)**.

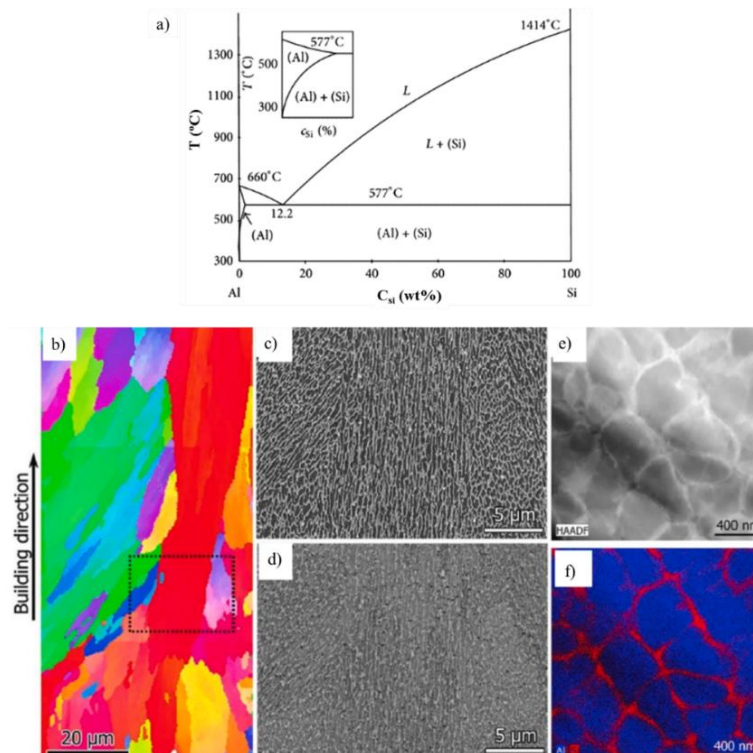


Figure 2-1 a) Al-Si binary phase diagram. b) Building direction EBSD map of the as-built AlSi10Mg alloy. c), d)&f) High magnification microstructure images and e) EDX mapping with Al in blue and Si in red, adapted from [1].

As shown in **Figure 2-1c)-d)**, due to the fine cellular dendritic microstructure the mechanical properties in as-built samples can be elevated compared to the fabrication by casting process [13]. The EBSD image of **Figure 2-1b)** indicates the fine columnar grains with $\sim 20\mu\text{m}$ width. Moreover, due to the absence of cracks and the fine microstructure, dense parts of $\sim 99\%$ relative density can be obtained. A typical feature of the Al-Si alloys fabricated by L-PBF is the ability of Si to distribute itself in the cellular dendritic region. This is also observed for the AlSi12 alloys fabricated by L-PBF since Si is readily rejected into the liquid. According to the phase diagram of **Figure 2-1a)**, the solubility of Si in Al decreases as the solidification progresses, however during rapid solidification of the L-PBF process, supersaturation of Si content in as-built L-PBF samples is usually observed.

- **2XXX alloys**

It is known in welding literature that 2xxx Al-alloys (2219, 2014, 2024) are crack sensitive alloys [33]. Zhang *et al.* [34] investigated the L-PBF fabrication of 2024 alloy (Al-Cu-Mg). $10\times 10\times 10\text{ mm}^3$ cubes of 2024 alloy were fabricated using L-PBF and reported evidence of cracking in line with the welding literature. The relative density obtained was around 99.8% post-fabrication. They also showed that the post-fabrication relative density of $>99.5\%$ can be obtained by increasing the laser energy input during the fabrication.

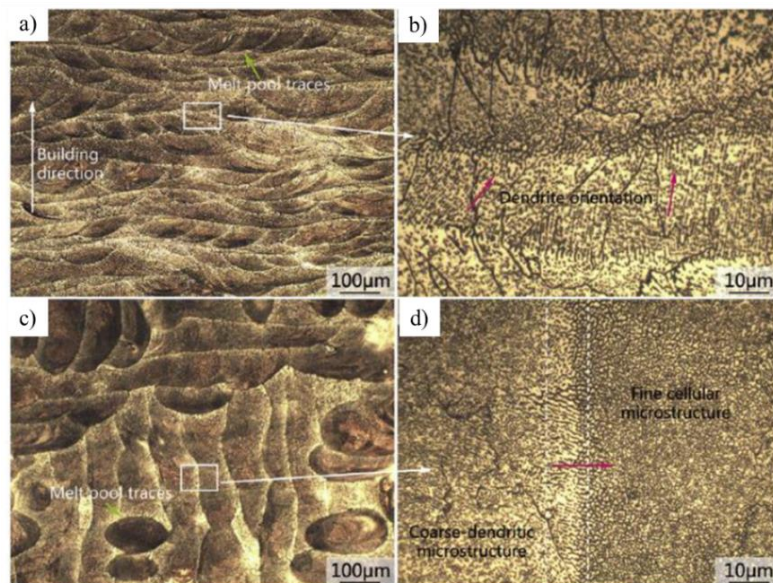


Figure 2-2 Optical microstructure of 2024 Al-alloy fabricated via L-PBF a) vertical section/building direction, b) zoomed image of a, c) horizontal section, d) magnified image of figure c) [34]

Figure 2-2 shows the typical L-PBF microstructure for the as-built 2024Al-alloy. **Figure 2-2a)** shows the vertical section microstructure showing the build direction and the traces of the melt pool. **Figure 2-2b)** shows a high magnification image demonstrating the epitaxial growth along the build direction. **Figure 2-2c)**

shows the horizontal section microstructure revealing the alternative laser scans in x and y-directions. **Figure 2-2d)** shows the cellular microstructure, which is very fine, separated by a columnar region in the boundary. Similarly, Karg *et al.* [35] fabricated 2xxx series Al-alloys in L-PBF. Following are few highlights from their work:

- A relative density >99.5% can be achieved.
- A small processing parameter window for 2xxx alloys compared to Al-Si alloys.
- Mechanical anisotropy from the anisotropic microstructure (along the building direction and the transverse direction) was mainly observed.

- **7XXX series**

Reschetnik *et al.* [36] made a study on 7075 alloy (5.1Zn-2.1Mg-1.2Cu) wt% when fabricated via L-PBF. The 7075 Al-alloy consists of Zn, Cu and Mg as its principal alloying elements. Similar anisotropy of mechanical properties was observed in 7075 alloy as in the case of 2xxx alloys. The fracture toughness tests yielded poor results due to the presence of microcracks in the building direction as shown in **Figure 2-3**. Higher relative densities (>98%) were obtained for this alloy but microcracks were still degrading the mechanical properties [36]. Similar to the 6061 Al-alloy, the 7075 Al-alloy also demonstrated severe cracking in the as-built samples.

According to Reschetnik *et al.* [36], the observed cracks in 7075 Al-alloy and attributed it to cracking due to liquid films. A similar conclusion was made by Stopyra *et al.* [37], in which they reported the cause of cracking due to the liquid films being able to persist down to lower temperatures. They reported the presence of elements like Zn/Cu/Mg to cause the formation of non-equilibrium eutectics at the grain boundaries, which play a major role in causing cracking in 7075 Al-alloys. Moreover, they also pointed out to lower the silicon content in the alloy, since silicon is known to stabilize the liquid films by lowering the solid-liquid interface energy [37].

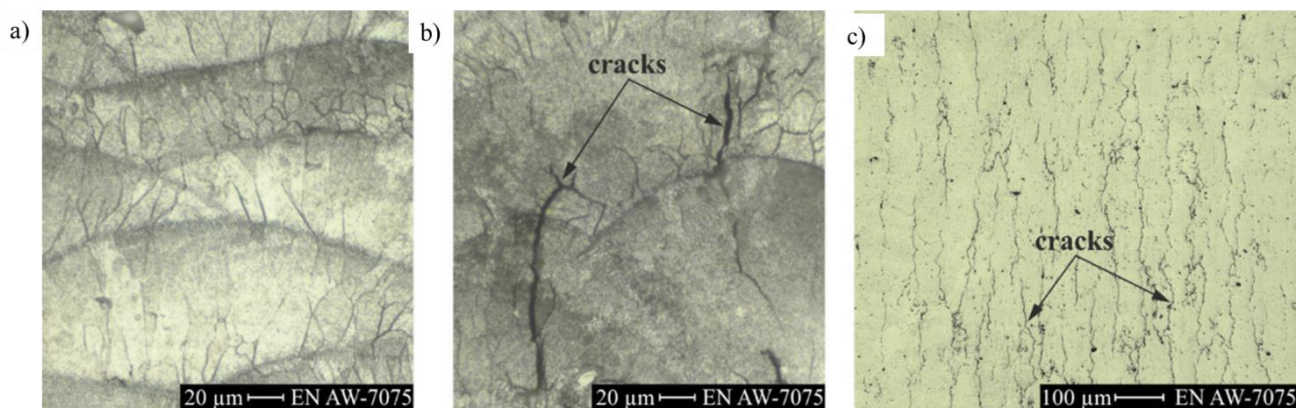


Figure 2-3 Cracking observed in the as-built 7075 samples along the building direction, adapted from [36].

- **Al-alloys (comparison)**

Table 2-1 shows the list of Al-alloys tested in L-PBF and their cracking tendency. Alloys are classified based on highly sensitive (HS), moderately sensitive (MS), and not sensitive (NS) to cracking. Similarly, the obtained build relative density is also classified in a similar manner, where obtained densities >99% are marked as (+) in **Table 2-1**. According to this classification, it turns out that alloys from the 2XXX series (2219, 2024, 2022), 6061, and 7075 alloys are highly sensitive to cracking. Whereas, alloys from 1XXX, 4XXX, and 8XXX series are easily fabricated in L-PBF as a result of the absence of cracking.

Table 2-1 Review of Al-alloys tested in L-PBF for hot cracking sensitivity/build density [38].

Series	Alloy	Hot cracking sensitivity NS: not sensitive MS: moderately HS: highly sensitive	Relative Density +: >99% 0: 97%-99% -: <97% NR: not reported	References
1xxx	Al	NS	NR	[39][35,40]
2xxx	AlCu2	MS	NR	
	AlCu5	MS	NR	
	AlCu6.8	NS	NR	
	AlCu11.8	NS	NR	
	AlCu5Mg (2022)	HS	+	
	AlCu4Mg1 (2024)	HS	+	
	AlCu6Mn (2219)	HS	+	
	AlCuMg	MS	+	
	AlCu2Mg1.5Ni	NS	NR	

	(2618)			
4xxx	AlSi7Mg0.3 (A356)	NS	+	[41–46][11,47–50]
	AlSi7Mg0.6 (A357)	NS	+	
	AlSi20Fe5Cu3Mg1	NS		
	AlSi20	NS	+	
	AlSi12	NS	+	
	AlSi50	NS	NR	
	AlSi10Mg	NS	+	
	AlSi12Mg	NS	+	
	AlSiNi	NS	+	
5xxx	AlMg5.7	NS	NR	[39,51–54]
	AlMg6	NS	NR	
	AlMgScZr (Scalmalloy®)	NS	+	
6xxx	6061	HS	–	[2–4,55,56]
7xxx	AlZn5	MS	NR	[5,40,57]
	AlZn2	MS	NR	
	AlZn10	MS	NR	
	AlZnMgCu		NR	
	AlZn5.5MgCu (7075)	HS	0	
8xxx	AlFe8.5V1.3Si1.7 (8009)	NS	+	[58–60]

Compared to the Al-Si alloys, the 2XXX series and the 7XXX series, the 6061 Al-alloys have better mechanical properties. As shown in **Table 2-2**, mechanical properties (YS: yield strength, UTS: ultimate tensile strength, Vickers hardness and elongation %) of some of the alloys tested in L-PBF conditions are mentioned. The 6061 Al-alloy (Al-0.8Si-1.2Mg) has a high yield strength of 290 MPa after the T6 heat treatment [3]. On the contrary, the casting alloys (AlSi10Mg) and other alloys from the 2XXX series show comparatively lower mechanical properties. Despite the good mechanical properties of 6xxx alloy, their processing through L-PBF is quite difficult, due to the cracking issues as reported by refs. [2–4,21].

Table 2-2 Comparison of mechanical properties of some of the Al-alloys tested in L-PBF.

Alloys	UTS (MPa)	YS (MPa)	Average hardness (HV)	Elongation (%)
Wrought-6061-T6[3]	310	276	95	12
6061 (as-built)[61]	290-396	196-246	54-84	11-15
6061 (L-PBF + T6) [3]	318	290	119	3.5-5.4
AlSi10Mg (as-built)	333	268	110	1.4
AlSi10Mg (T6) [61][35]	280	220	116	3.9
2219 (as-built L-PBF)	240	120	94	-
2219 (L-PBF + T6) [62]	275	150	147	
7075 (as-built) [1,36]	42-203	-	160	0.5
7075 (T6) [1,36]	45-206	-	170	0.2-0.5

2.1.2. 6061 Al-alloys

Fulcher *et al.* [2] and Maamoun *et al.* [61] reviewed the feasibility of 6xxx family alloys and mainly the 6061 (Al-0.8Si-1.2Mg) by L-PBF fabrication. The as-fabricated optical images shown in **Figure 2-4** indicate that the base alloy 6061 consists of porosity defects and cracks that are detrimental to mechanical properties. The 6061 Al-alloy show similar behavior of cracking as observed in welding literature. According to Maamoun *et al.* [61], the cracks were oriented along the building direction and the microstructure had a lot of porosities. Moreover, the microstructure did not possess any Si enriched interdendritic regions, as seen in the Al-Si alloys. On the contrary, nano-sized Si particles were found to be precipitated on the Al-matrix

grain boundaries [61]. In general, the 6XXX family of alloys has problems due to poor fabrication microstructures. The major reason for this according to Fulcher *et al.* [2] is probably due to the presence of an oxide layer between the layers that generate these cracks. This leads to a relatively low density of only 96% for as-fabricated samples.

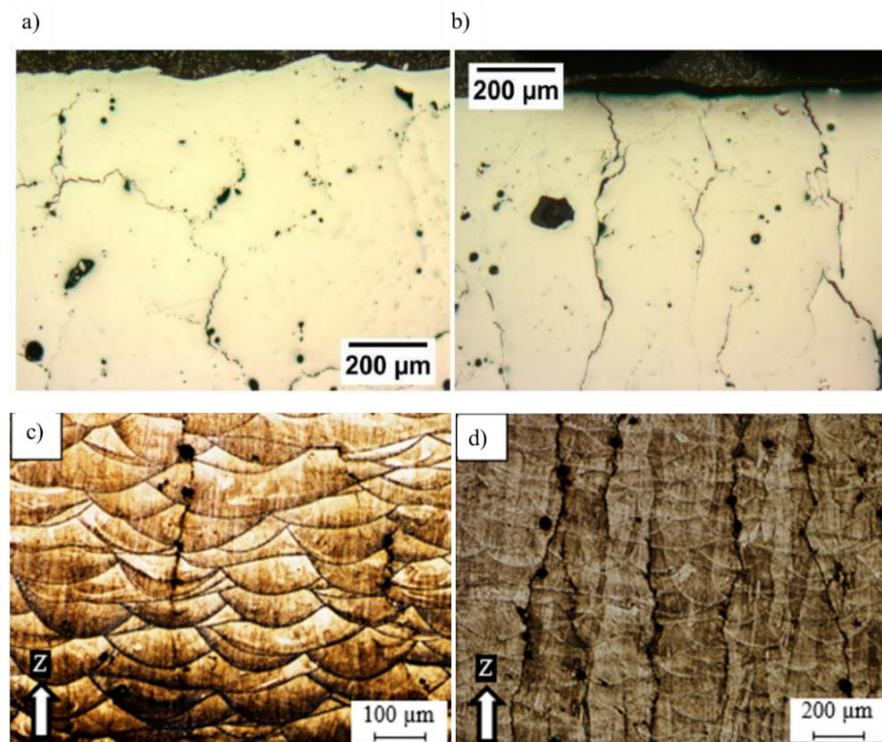


Figure 2-4 a)-b) Showing the as-built microstructure of 6061 Al-alloy along the building direction (non-etched). c)-d) Etched microstructure showing the location of cracks and porosities with respect to the melt pool boundaries [2][61].

According to Maamoun *et al.* [61], the occurrence of cracks in the as-built 6061 samples was due to the high solidification shrinkage (density of solid is significantly greater than the liquid) and high thermal contraction in the partially melted regions of the melt pools. For Aluminum, the solidification shrinkage is $\sim 6.6\%$ [63].

Table 2-3 shows the studied alloys in L-PBF from the 6XXX series. In all the reviewed articles, the as-built sample showed cracks throughout the sample and possessed porosities. Few reported presence of oxides film, this was mainly due to the presence of oxygen in the fabrication chamber. Some even reported the evaporation of Mg, since it is a volatile element. In the reviewed literature on the 6xxx series, the maximum relative density obtained for the as-built samples was always $<98\%$.

Table 2-3 Review on as-built 6061 Al-alloy (L-PBF fabricated)

Alloy tested	L-PBF sample	Observation/Conclusion	References
6061	–	No information on fabrication quality, only thermal study.	[64]
6061	Cubes 10 mm ³	Oxide film formation, problems concerning Mg evaporation, and low relative density	[29]
6061 6061 + 6%Cu 6061 + 30%Cu	14x14x10 mm ³	The maximum density obtained on L-PBF samples was around 96% and compared to 6061 alloy, the hardness increased from 50 HV to 200 HV by the addition of 30%Cu.	[65]
6061	Cubes 10 mm ³	Cracks throughout the sample. Maximum relative density: 98%	[2][61][3]

2.1.3. Metallurgy of 6061 Al-alloy

The major alloying elements present in the 6xxx series of Al alloys are Mg and Si. This family is from the class of wrought Al alloys that are typically extruded and rolled to get the desired properties. Since it is a precipitation-hardened alloy, the strength comes mainly from the Mg₂Si phase (β'' and β'). However, these Mg₂Si phases occur only after the conventional heat treatments, like T6 (solution heat treatment and artificial ageing) for the case of 6061 Al-alloy [66]. The ratio of Mg to Si should be around 1.7-2 for the formation of the Mg₂Si phase [66]. **Table 2-4** shows the alloying elements content in 6061 alloy as per norms mentioned in ASTM B308.

Table 2-4 Standard composition of 6061 Al-alloy [67].

	Al	Si	Mg	Fe	Cu	Cr	Ti	Mn	Zn
Standard [67]	Bal.	0.4- 0.8	0.8- 1.2	<0.2	0.15- 0.4	0.04- 0.35	<0.15	<0.15	<0.25

Al alloys are ductile but alloying elements are often added to them to increase their strength, corrosion resistance, conductivity, etc. In terms of the effect of Si on Al alloys, it enhances strength and formability but might be detrimental for intergranular corrosion. Whereas Mg increases corrosion resistance but decreases the formability properties of the alloy. Trace element like Fe (Iron) forms coarser phases with Al in the form of $FeAl_3$, $FeAl_6$ which are detrimental to the ductility and the toughness of the alloy. Similarly, in combination with Si, the frequently reported intermetallics in casting literature are α - Al_8Fe_2Si , α - $Al_{15}(Fe, Mn)_3Si_2$, and β - $Al_9Fe_2Si_2$ [68]. To counteract the Fe effect, Cr and Mn are added as a corrector of size and shape for the Fe containing phases with Al. **Table 2-5**, summarizes the role of solute elements in 6xxx Al-alloys.

Table 2-5 Summary of the role of solute elements in 6xxx Al-alloys [66][12]

Trace elements	Concentrations (wt%)	Role of solute elements
Cu/Mg/Si	0.4-1.2	Strengthening solutes.
Fe	0.1-1	Formation of Al_3Fe and $AlFeSi$ second phase compounds, leading to a decrease in fracture toughness properties.
Ti, V, Cr	0.001-0.05	Leads to grain refinement and delay in initiation of recrystallization during deformation.
Mn	-	For corrosion resistance and as a shape corrector for Fe bearing phases.
Co/Fe	-	Improvement of machinability

The most important aspect during the solidification of an alloy system is to check the byproducts i.e. the precipitation of which phases occur. 6061 alloy is an age-hardening alloy with the most common heat treatment used as T6 (solution heat-treated at 528°C and then artificially aged-160°C) to improve its overall mechanical properties. When the alloy is quenched to room temperature after solutionizing, SSS

(supersaturated solid solution) is formed and further room temperature aging results in the formation of metastable coherent phases known as Guiner Preston (GP) zones. It is this phase along with β'' and β' (Mg_2Si), which result in overall precipitation hardening of the alloy since they create a coherency strain field around itself which interacts with the dislocations. Below is the precipitation formation sequence in the 6061 alloy [66]:



- **Typical precipitates in 6061 Al-alloy (Casting)**

The 6061-alloy is a precipitation hardened alloy, due to the formation of Mg_2Si phases after the ageing process. The Mg_2Si phase gives the alloy better workability and mechanical properties. However, during the solidification of the alloy, several intermetallic/dispersoid phases can occur. According to ref [68], during the casting process of 6061 Al-alloy, various intermetallic phases also co-exist in the microstructure. To start with the typical microstructures observed in literature for the 6061 Al alloy during casting, consider **Figure 2-5**. For example, the microstructure as shown in **Figure 2-5a)-c)** shows several intergranular intermetallic phases which are present in the microstructure. These phases decorate the equiaxed grain boundaries of the microstructure, indicating their occurrence during the last stage of solidification.

As described in the literature, typically with Fe and Si content in the 6061 Al-alloy, the frequently reported intermetallics in casting literature are: $\alpha\text{-Al}_8\text{Fe}_2\text{Si}$, $\alpha\text{-Al}_{15}(\text{Fe},\text{Mn})_3\text{Si}_2$, and $\beta\text{-Al}_9\text{Fe}_2\text{Si}_2$ [68]. Depending on the composition of the alloy, the $\alpha\text{-Fe}$ containing phases can be formed primary from the liquid with a polyhedral morphology (see **Figure 2-5c)**) [69]. When Fe content is <0.7 wt% in the alloy (case of 6061 Al-alloy), these intermetallic phases are formed at the end of solidification, as a result of eutectic solidification, giving rise to the Chinese script morphology (see **Figure 2-5c)**). At the end of solidification, the temperature is low enough for the phases to grow along the Al-dendrites in a eutectic manner, causing the Chinese script morphology.

The $\alpha\text{-Al}_8\text{Fe}_2\text{Si}$ has a hexagonal crystalline structure, the $\alpha\text{-Al}_{15}(\text{Fe},\text{Mn})_3\text{Si}_2$ is cubic and the $\beta\text{-Al}_9\text{Fe}_2\text{Si}_2$ has a monoclinic crystalline structure. All of these phases are reported to decrease the ductility of the alloy, however, the $\beta\text{-Al}_9\text{Fe}_2\text{Si}_2$ phase is considered to be more detrimental due to its needle shaped morphology. In general, during high cooling rates, this $\beta\text{-Al}_9\text{Fe}_2\text{Si}_2$ phase formation is not obtained. The other Fe containing α -phases depict a typical Chinese script morphology (if formed during last stage of solidification) as reported frequently in literature [70,71], also as shown **Figure 2-5b)-d)**. The TEM BF image of **Figure 2-5d)** shows the Chinese script morphology of the intermetallic phases. The phase mapping as shown in **Figure 2-5e)** confirms the formation of $\alpha\text{-Al}_{15}(\text{Fe},\text{Mn})_3\text{Si}_2$ phase during the last stage of solidification (see the green region). Thus to summarize, depending on the composition of the alloy and the cooling rate, various Fe containing impurity phases can co-exist in the 6061 casting microstructure.

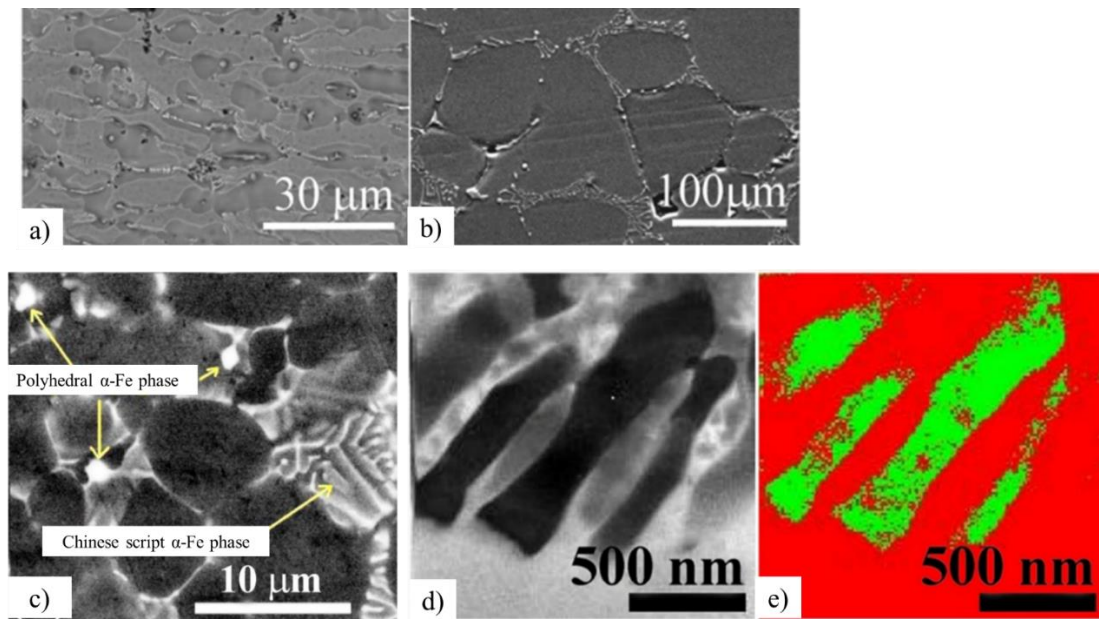


Figure 2-5 a)-c) A typical microstructure of the 6061 Al-alloy during casting using spray forming, adapted from ref. [68]. d)-e) High resolution TEM bright-field image and its corresponding phase map, showing red zone as Aluminum and green zone as the cubic α - $\text{Al}_{15}(\text{Fe},\text{Mn})_3\text{Si}_2$ phase, adapted from ref [68].

- **Typical precipitates in 6061 Al-alloy (Laser beam welding)**

During laser beam welding, the 6061 Al-alloy microstructures show some similarities with the intergranular precipitation observed during the casting. As seen in **Figure 2-6a)**, the typical weld microstructure is shown. The microstructure reported by Qiaoling *et al.* [72], was not reported to be cracked due to the use of filler wire (4xxx series Al) containing high Silicon. Three zones can be identified in the weld microstructure: the base metal (which is not welded), the fusion zone (intersection of base metal and the fusion zone) and the weld center. In general, the columnar grains tend to grow in an epitaxial manner on the base metal grains perpendicular to the fusion line, oriented towards the weld center, as seen in **Figure 2-6a)**.

Speaking in terms of precipitation, as reported by Qiaoling *et al.* [72], due to higher cooling rates with laser beam welding, there is the formation of α - $\text{Al}_8\text{Fe}_2\text{Si}$ phase at the expense of β - $\text{Al}_9\text{Fe}_2\text{Si}_2$ phase. A Chinese script morphology of the Fe containing α - $\text{Al}_8\text{Fe}_2\text{Si}$ is observed, as shown in **Figure 2-6b)**. Thus, the precipitates observed in laser beam welding consist only of Si, Mg_2Si and α - $\text{Al}_8\text{Fe}_2\text{Si}$ phases [72]. These are the precipitates, which are also observed in the constrained solidification studies done by Giraud *et al.* [73] on the 6061 Al-alloy.

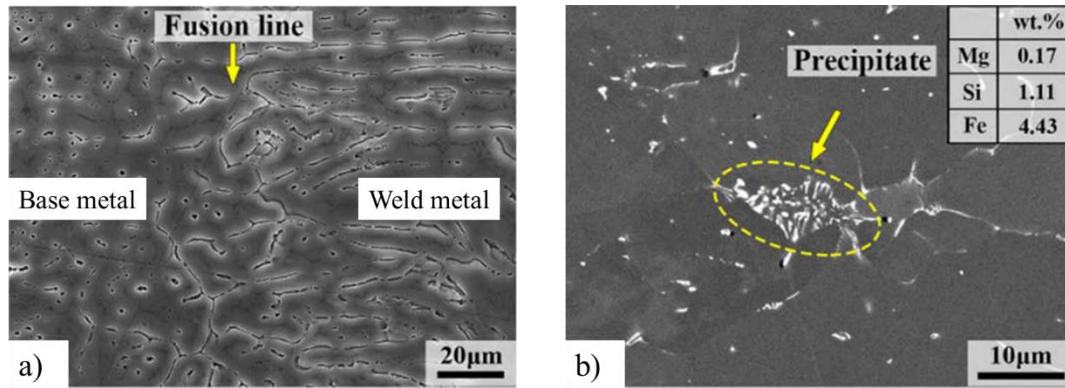


Figure 2-6 Typical microstructure of 6061 Al-alloy during laser beam welding, adapted from ref [72].

- Typical precipitates in 6061 Al-alloy (L-PBF)

According to Uddin *et al.* [3], the as-built microstructure of the 6061 Al-alloy possess many fine homogeneously distributed non-coherent dispersoids (see **Figure 2-7**) without the presence of Chinese-script morphology. The size range of these dispersoids ranged from $\sim 200\text{nm}$ to $5\mu\text{m}$ with an average spacing between them $\sim 1\text{-}3\mu\text{m}$. Based on the Energy dispersive X-ray analysis performed in SEM, Uddin *et al.* [3] concluded that those dispersoids were majorly rich in Al-Si-O, since many of them were found to contain oxygen around it. These dispersoids of Al-Si-O as claimed by Uddin *et al.* [3], are not the strengthening precipitates that are usually observed in the tempered 6061 Al-alloy, since the measured Vickers hardness of the as-built samples was low $\sim 54\text{HV}$, compared to the 119HV hardness obtained after T6 heat treatment. This low hardness of the as-built 6061 Al-alloy suggests that the dispersoids observed by Uddin *et al.* [3] did not contribute to the strengthening in the as-built 6061 Al-alloy.

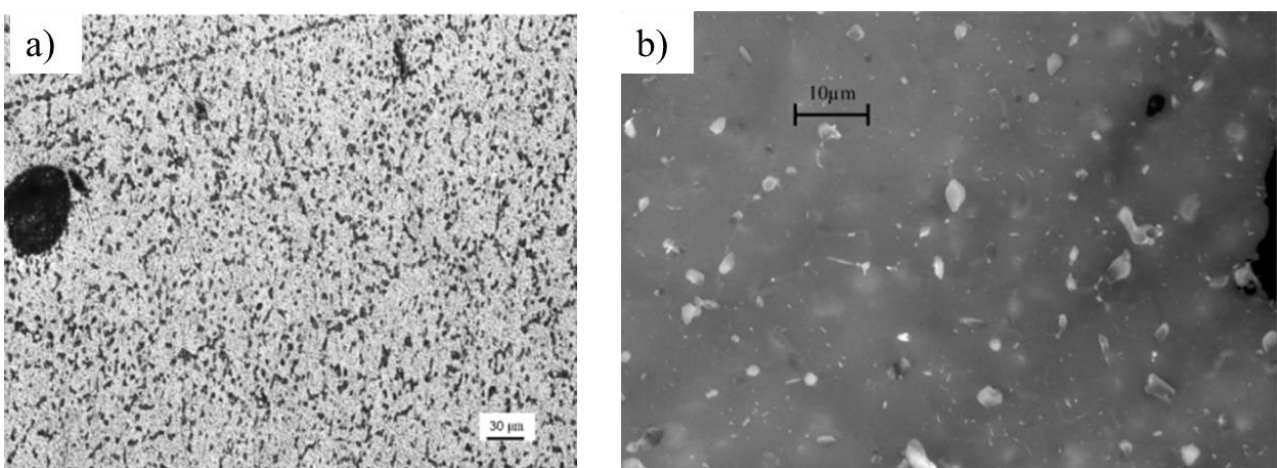


Figure 2-7 a) Optical microstructure of the as-built 6061 Al-alloy along the building direction and b) Magnified SEM image of the dispersoids.

The following section will provide insights into the defects occurring in the Al-alloys during L-PBF and their causes will be reviewed.

2.2. Defects encountered in Aluminum alloys during L-PBF.

This section describes the defects that can occur due to the fabrication of Aluminum-based alloys in different process parameter conditions of L-PBF. The key issues identified while fabricating Al-based alloys in L-PBF are as follows:

1. Cracks
2. Porosities
3. High reflectivity of Aluminum
4. Evaporation of high volatile elements like Mg, Zn
5. Oxide film formation on the surface of powders

2.2.1. Cracks

Cracking is the most important defect observed in the as-built parts of Al-alloys. Although the origins of cracking is well documented in welding literature, that is not the case for L-PBF of Al-alloys. Most of the literature for the cracking in Al-alloys during L-PBF was oriented towards mitigating cracking [4,74] and it is very rare to find reports elucidating the mechanism of cracking occurring during L-PBF. Thus, details about the origins of cracking in Al-alloys observed in the welding literature are consolidated in **section 2.3**.

2.2.2. Origin of porosities in Al-alloys.

In the process of part qualification, a lot of emphasis is placed on reducing the porosities in the as-built samples. The objective is to achieve the final build part with the highest relative density. However, according to Weingarten *et al.* [75], one of the causes of porosities in Al-alloys is due to their lower absorptivity of the incident laser (wavelength corresponding to L-PBF process, ~1064nm).

Another perspective on the occurrence of porosities in the as-built Al-samples was laid by Aboulkhair *et al.* [30]. In their work, they identified two types of porosities. The first, as shown in **Figure 2-8a**), the small circular pores (few microns in size) were identified as metallurgical pores. Their formation was due to the moisture content on the precursor Al-powders, according to Weingarten *et al.* [75]. Moreover, these metallurgical pores can also form due to the entrapped hydrogen in the Al-alloys, and thus can be also termed as 'gas pores'. In addition, gas entrapping can also occur during the atomization of powders. This is especially due to the ability of Al-alloy to entrap the hydrogen, according to Weingarten *et al.* [75]. As

shown in **Figure 2-8e**), during laser scanning, the energy from the laser is transferred to the powder for its melting. During this process, two solid-liquid interfaces are generated due to the solidification front and melting front. In front of the melting pool, the new unmelted powder can be a source of Hydrogen. When the solubility of H₂ reaches its peak value in the melted liquid, H₂ pores can occur inside the melt pool, as shown in **Figure 2-8e**). However, it must be also kept in mind that H₂ solubility can vary significantly in solid and liquid- Aluminum.

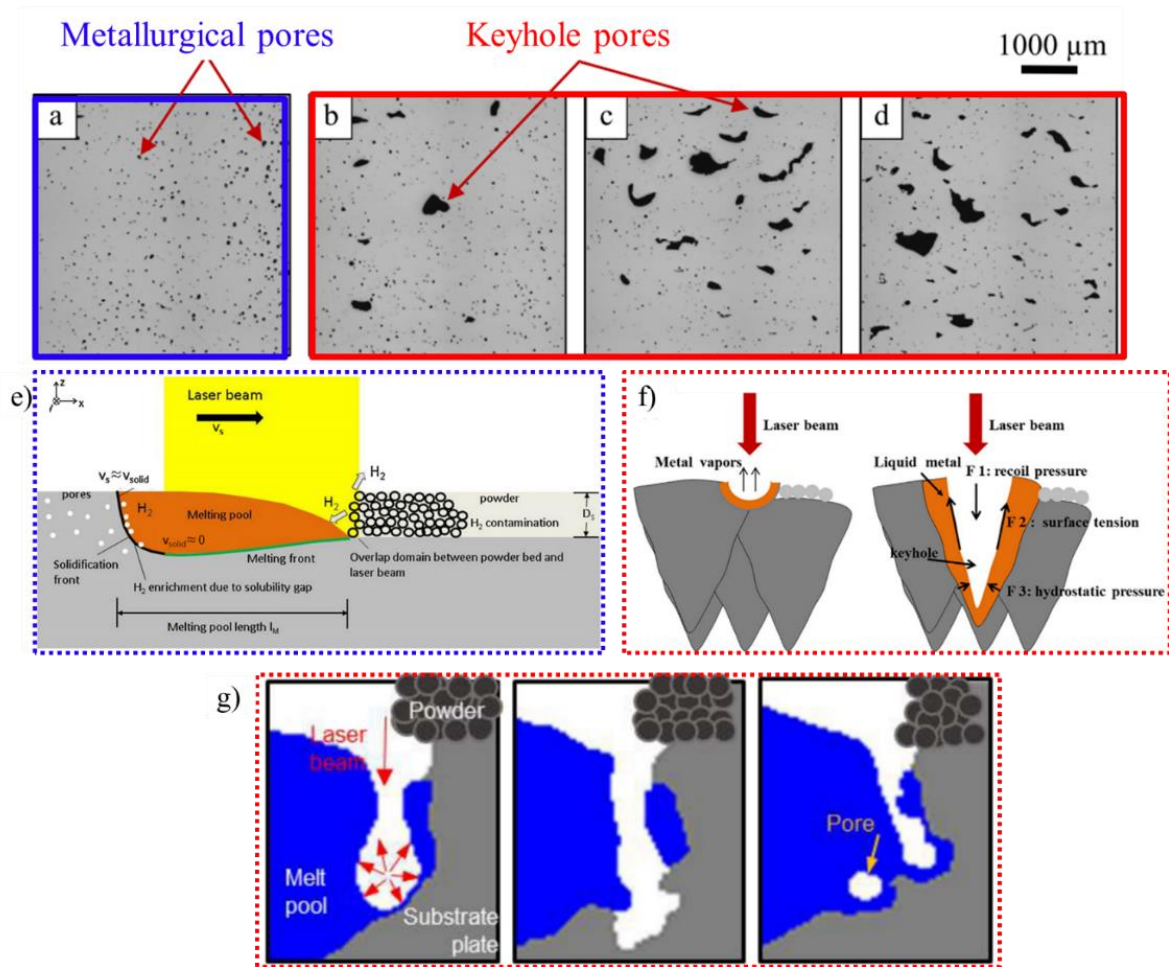


Figure 2-8 a) Metallurgical pores and b)-d) keyhole pores in as-built AlSi10Mg samples [1]. e) Schematic of the occurrence of metallurgical pores due to Hydrogen entrapment [75]. f) Schematic mechanism of keyhole melt pool formation, adapted from [76]. g) Schematic mechanism of keyhole porosity formation, adapted from [77].

The second type of pores, as shown in **Figure 2-8b)-d)**, are a bit elongated in shape and their size ranges in a few hundreds of microns [30]. These elongated pores were observed throughout the sample surface, for each layer. They were termed as ‘keyhole pores’ due to the specific keyhole mode of melting. According to Qi *et al.* [76], two kinds of melting modes (keyhole and conduction) were observed during the L-PBF of Al-alloys. These different types of melting modes occur due to differences in laser energy input and have very specific melt pool shapes. For example, keyhole mode has a goblet shape of the melt pool

(depth/width ratio of melt pool >1), whereas, for conduction mode, a hemispherical melt shape (depth/width ratio of melt pool <1) is usually observed.

The mechanism of formation of keyhole melt pools as reported by Qi *et al.* [76], is majorly due to high laser energy input. As shown in **Figure 2-8f**), due to high energy input there is vaporization of metal. This causes the recoil pressure of metal vapors to be higher than the surface tension and the hydrostatic pressure of the liquid metal, causing deep melt pools, or goblet-shaped keyhole melt pools as shown in **Figure 2-8f**). Due to this sufficient amount of laser energy, the metal vapor might get trapped inside the deep melt pools, as observed by Chen *et al.* [77] in their *in-situ* keyhole porosity studies.

On the contrary, the conduction melt pools (semi-spherical shape) are formed due to purely thermal conduction, since there is not sufficient laser energy to cause the metal vaporization. Thus in conduction mode, the thermal gradients cause the initiation of liquid flow due to Marangoni forces [76].

Thus to summarize, keyhole pores were formed specifically for higher laser intensities, according to refs. [76][77]. This is confirmed by the experimental studies of melting mode transition in L-PBF of 7050 Al-alloys done by Qi *et al.* [76]. They reported that keyhole melt pools are formed for lower scan speeds (<200 mm/s), whereas, for laser speeds >800 mm/s, a conduction mode of melting was observed, as shown in **Figure 2-9a)-h)**. Qi *et al.* [76], also reported a significant grain refinement and reduction in crack density by the formation of keyhole melt pools, as shown in **Figure 2-9i)-l)**. However, keyhole pores were always present in the microstructure, despite the reduction in cracking density.

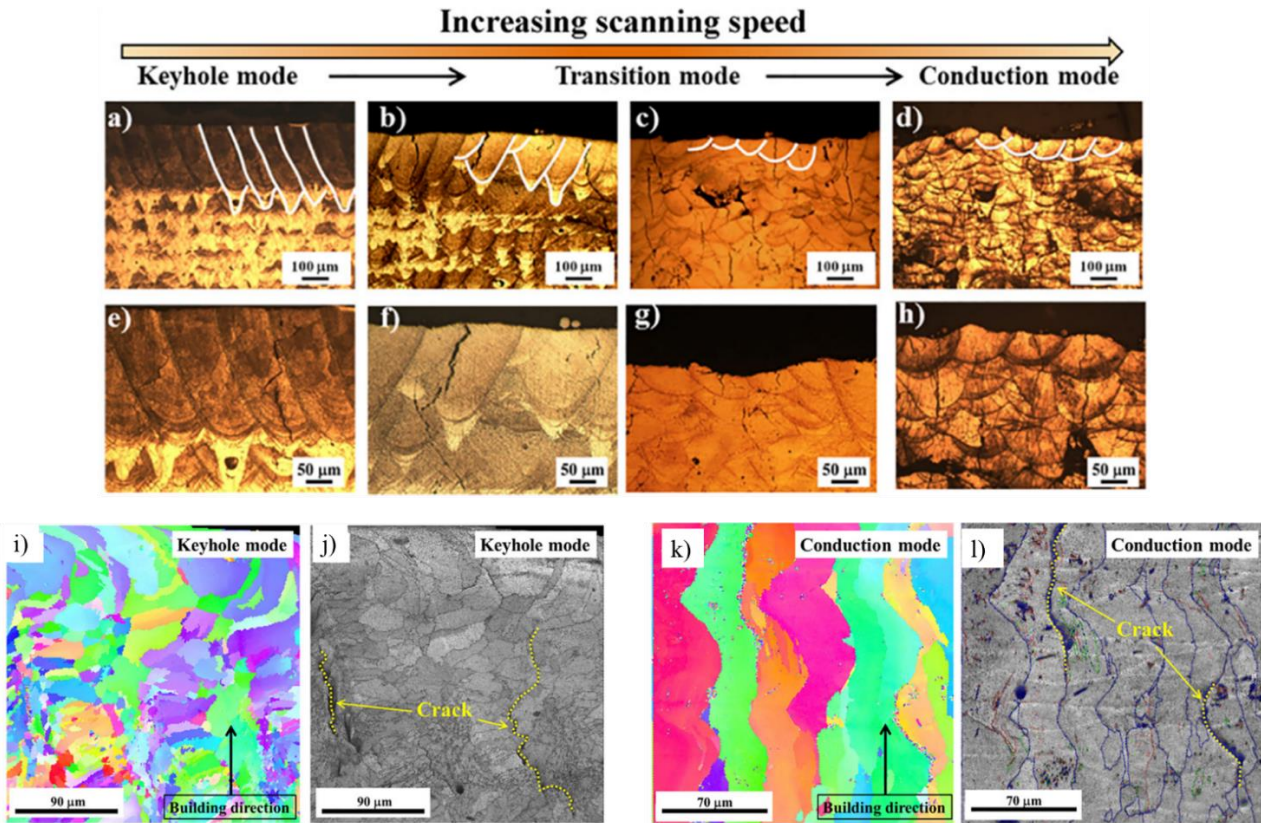


Figure 2-9 a)-f) Effect of laser scanning speed on melting mode transition in 7050 Al-alloy during L-PBF. i)-j) Typical microstructure in keyhole melting mode. k)-l) Microstructure in conduction melting mode, adapted from [76].

2.2.3. High reflectivity of Aluminum

The reflectivity of Al-alloys can reach up to $\sim 91\%$ to the incident laser. Similarly, they have high thermal conductivity ($167\text{W/m}\cdot\text{K}$). This causes issues related to poor laser absorptivity resulting in improper melting. As shown in **Figure 2-10**, the absorptivity curve as a function of laser wavelength for various metals is shown. It is evident to point out that pure Al absorptivity is low compared to other metals like Ni. Another issue with Al-alloys is their requirement for high amount of energy for melting (the latent heat of fusion 378 kJ/kg), compared to 272 kJ/kg (Fe) and 297 kJ/kg (Ni) [78]. The high reflectivity, high thermal conductivity and the high latent heat of fusion of Al-alloys make it difficult to be processed during L-PBF.

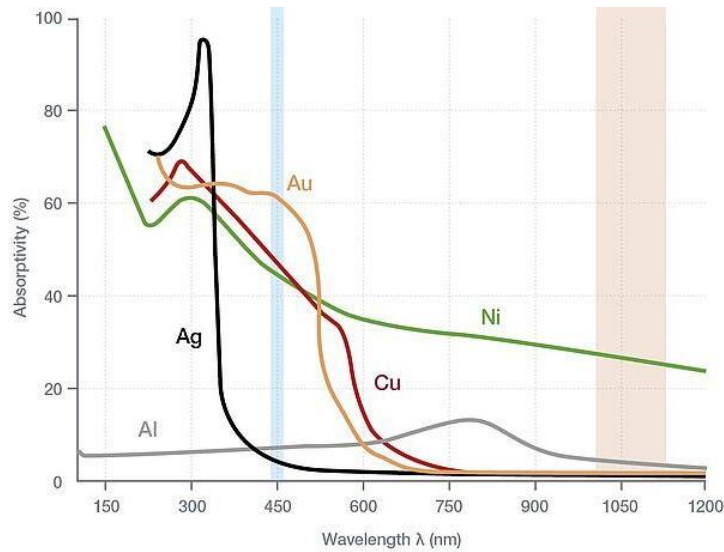


Figure 2-10 Absorptivity of metals as a function of laser wavelength [79].

Thus to reach the melting of the Al-alloys, a high amount of energy is required. But once this melting temperature is reached, the melting process proceeds quite rapidly [80]. With the high incident energy density, many times the volatile elements like Mg/Zn present in the alloy tend to evaporate. This evaporation of Mg/Zn is majorly due to their lower boiling points and higher equilibrium vapor pressures compared to Al [37]. This evaporation can often lead to change in solute composition post fabrication, which is often not desirable.

2.2.4. Oxide film formation.

Louvis *et al.* [55] examined the densification behavior of AlSi10 alloy using low power laser 50-100W in L-PBF. The maximum density achieved post-fabrication was around 89%. According to [55], the key reason for this low density is due to the oxide layer in the fabricated samples due to the presence of oxygen in the fabrication chamber. As shown in **Figure 2-11** schematic, these oxide layers were observed on the top of the solidified layers and the melt liquid surface. This oxide layer on the melt liquid surface resulted in the creation of oxygen fumes during fabrication. Also, the oxide film formed on top of the solidified surface from (n-1)th scan resulted in less interaction with the new layer from the nth scan. Such trapped oxide results in decrease density and is a possible cause of delamination for the fabricated part [55].

Louvis *et al.* [55] suggested that, since oxide film formation cannot be avoided, the research must aim at processes that can control its formation. Also breaking of these films can be a possible solution but it should be controlled by varying the process parameters and the composition of the alloy used [55].

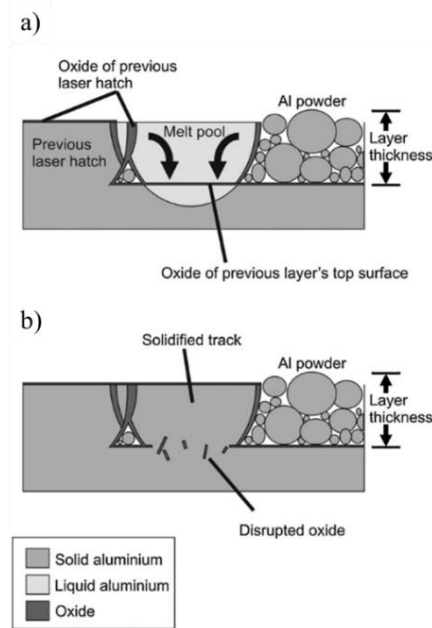


Figure 2-11 Schematic of the mechanism of oxide film formation between layers of Al-alloys fabricated by L-PBF, adapted from [55].

Apart from porosities and oxide film formation, the most important defect encountered in Al-alloys during L-PBF is cracking. The upcoming section will be dedicated to the review of cracking mechanisms occurring in 6061 Al-alloy.

2.3. Cracking mechanism (Review)

The section contains a review of the cracking mechanism reported for the 6061 Al-alloy. Various metallurgical and mechanical factors affecting cracking in the alloy are discussed in this section. Thus this section will cover the cracking mechanism reported for the 6061 Al-alloy in the well documented welding literature.

However, to start with reviewing the cracking mechanism, basic solidification understanding is needed. According to the literature [81], depending on the solidification parameters, namely the thermal gradients (G) and the solidification velocity (v), different growth morphologies of the solid/liquid (s/l) interface are possible. For example, by changing the processing conditions, from casting to welding/L-PBF, the solidification parameters will change and so does the growth morphology (see **Figure 2-12**). **Table 2-6** shows the change in solidification parameters based on the processing conditions. It is evident to notice that, L-PBF process creates solidification conditions that have the highest cooling rates ($G \times v$), compared to welding and casting. According to Kou *et al.* [81], both the parameters (G and v) are responsible to depict the microstructural features of the material. For example, the product, i.e. the cooling rate ($G \times v$) depicts the size of the microstructure and the fraction (G/v) affects the morphology of the solidifying

microstructure. Thus, the higher the cooling rate, the finer will be the microstructure, as in the case of L-PBF process. And as shown in **Figure 2-12**, the morphologies of the s/l interfaces can be affected by varying the G/v ratio. For example, a high G/v ratio will lead to a planar solidification front, whereas a low G/v will result in equiaxed morphology. In the transition between these two extremities, cellular and cellular dendritic morphologies are also possible, which is typically the case when columnar grains are present in the microstructure.

Table 2-6 Solidification parameters for different processes.

	Casting [82]		Welding [83]		L-PBF[12]	
$v(m/s)$	0.001	0.001	0.001	0.1	0.1	10
$G(K/m)$	10	10^4	10^5	10^5	10^6	10^8
$G \times v (K/s)$	0.01	10	100	10^4	10^5	10^9
$G/v (K.s/m^2)$	10^4	10^7	10^8	10^6	10^7	10^7

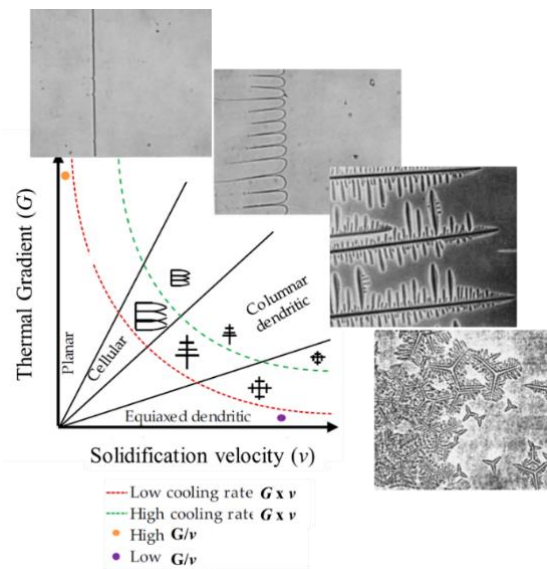


Figure 2-12 Different growth morphologies possible depending on the solidification parameters, adapted from [81].

In the welding literature, cracking mechanisms are usually classified into two categories: (i) hot cracks and (ii) solid-state cracks. Hot cracks form during solidification due to the presence of liquid films trapped between dendrites associated with shrinkage and tensile strain in the mushy zone (a region where solid

and liquid both co-exist). The typical fracture surface of hot cracks shows a dendritic morphology, demonstrating the evidence of trapped liquid films. Solid-state cracking occurs without the presence of liquid films, contrary to the previous mechanism. Several solid-state cracking mechanisms have been reported in welding literature: strain-age cracking (often reported for Ni-based superalloys) and ductility dip cracking. Out of the two, only ductility-dip cracking has been reported in aluminum alloys, caused due to the formation of brittle intermetallics along the grain boundaries, which result in loss of ductility and eventually cracking under high-stress conditions, see e.g. [84]. However, ductility dip cracking is quite rarely reported in Al-alloy compared to hot cracking.

In the literature, hot cracking can further be classified as solidification cracking and liquation cracking. Solidification cracking usually occurs in fusion zones of melt pools, whereas liquation cracking originates in partially melted zones (PMZ) [18]. Thus, the upcoming sections will solely focus on understanding these two mechanisms and their occurrence in the 6061 Al-alloy.

2.3.1. Solidification cracking

As the name suggests, solidification cracking occurs during the solidification process and is localized inside the fusion zones. Solidification cracking occurs along the grain boundaries during the terminal stage of solidification, i.e. when f_s (solid fraction) tend to 1 [81]. During the last stage of solidification, the tensile stresses in the nearby grains increases, and as a result solidification cracks develop. The origin of these tensile stresses is due to the thermal contraction and the solidification shrinkage. For example, the solidifying metal tends to contract due to the solidification shrinkage. The surrounding metal that is already solidified also tends to contract but comparatively less than the solidifying metal. This causes hindrance in the contraction of the solidifying metal, which generates stresses. These stresses act on the weak zone of the mushy region where a continuous liquid film exists. Thus, whenever a solidification crack occurs, the fracture morphology usually reveals a dendritic morphology, since cracking occurs along the grain boundary which hosts the continuous liquid films between the primary dendrites. **Figure 2-13**, shows the evidence of cracking occurring in 6061 Al-alloy inside the fusion zone during welding.

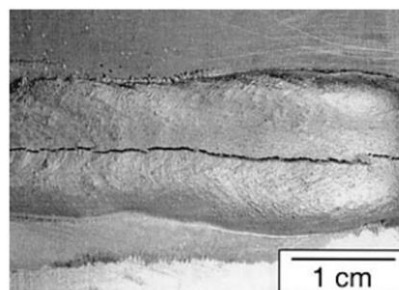


Figure 2-13 Solidification cracking in gas metal arc weld of 6061 Al-alloy, adapted from [81]

To understand the physics behind solidification cracking, Rappaz *et al.* [85] introduced his understanding of the hot cracking behavior. According to Rappaz *et al.* [85] in his coalescence theory, the solidification happens in a sequence of events happening at the dendrite scale. For example, consider the dendrites growing during the solidification, as shown in **Figure 2-14**. When the solid fraction is low enough (region 1), the morphology dendrites cause high permeability (the ability of the liquid to flow). Thus the solidification shrinkage and the deformation can be easily compensated by the liquid flow since in this region the neighboring dendrites are no longer in contact with each other. Further, the solid fraction increases and reaches a coherency point (T_{coh}), i.e. the dendrites start to be in contact with each other. From the coherency point, the liquid film between the dendrites exists in the form of the continuous thin liquid film. The thin liquid films continue to maintain their form until the dendrites start to coalesce.

The point at which dendrites start to coalesce, i.e. coalescence temperature (T_{gc}), is indicating that the dendrites will be able to transmit the tensile strain and stresses. The region between the T_{coh} to T_{gc} (region 2 in **Figure 2-14**), contains fragile continuous liquid film, which cannot bear the tensile strain/stresses and thus behaves as a brittle phase [85]. Thus any small opening in this region 2 will not be fed by liquid due to low its permeability, and thus hot cracking is most possible in this region. Once the coalescence of dendrites has occurred, the continuous liquid remains in the form of droplets and the remaining solid is more resistant to the deformations (region 3 in **Figure 2-14**).

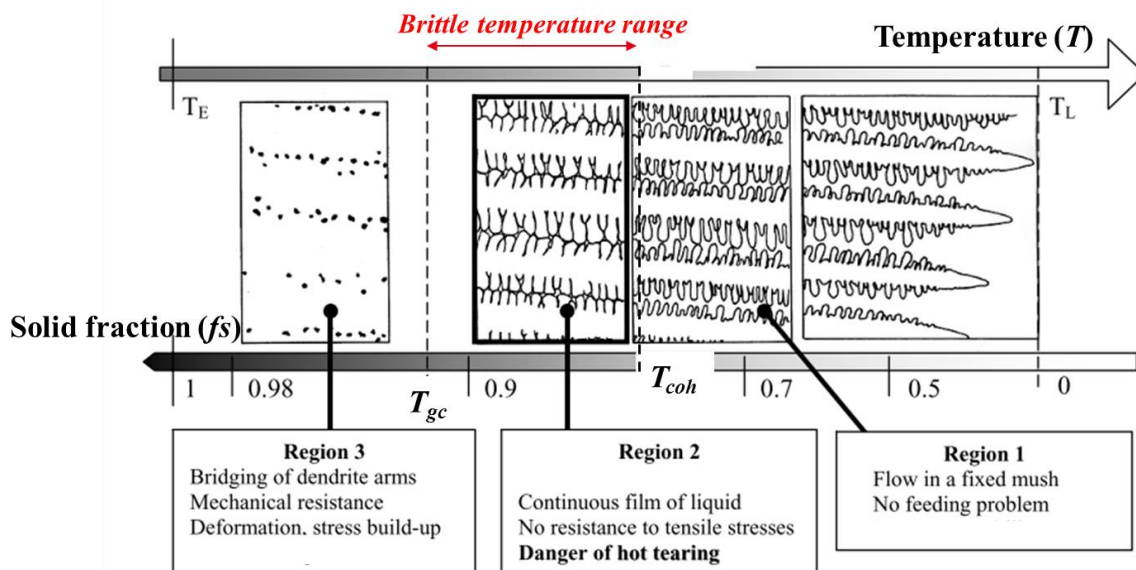


Figure 2-14 Schematic of events happening in the mushy zone during dendritic solidification of Al-alloys, adapted from [85].

Giraud *et al.* [71] did constrain solidification studies (80 K/s) on the 6061 Al-alloy to identify the solid fraction at which the alloy is sensitive to cracking. As shown in **Figure 2-15a**), the stress vs displacement studies, allowed Giraud *et al.* [71] to quantify the ductility after peak (DaP) of the 6061 Al-alloy. This allowed Giraud to estimate the ductility for various temperatures and link it to solid fraction of the alloy.

As shown in **Figure 2-15b**), the DaP of the alloy is plotted as a function of solid fraction. A U-shaped curve was identified, i.e. a ductile-brittle-ductile transition. The ductility of the alloy was found to reach a minimum value for the solid fraction range of $0.94 < f_s < 0.97$. This indicates that, during the solidification in that solid fraction range, the alloy possessed brittle behavior ($0.94 < f_s < 0.97$). According to Giraud *et al.* [71], outside this interval, the alloy is systematically ductile. For solid fractions greater than 0.97, the grains are coalesced: the numerous solid-solid contacts oppose the formation and propagation of cracks. For solid fractions less than 0.94, the liquid is present in large quantity for the cracks to be filled by flow of the liquid. For the intermediate solid fractions ($0.94 < f_s < 0.97$), the microstructure is weakened by the presence of thin liquid films, and discontinuous to allow the liquid to flow, and an insufficient number of solid-solid contacts.

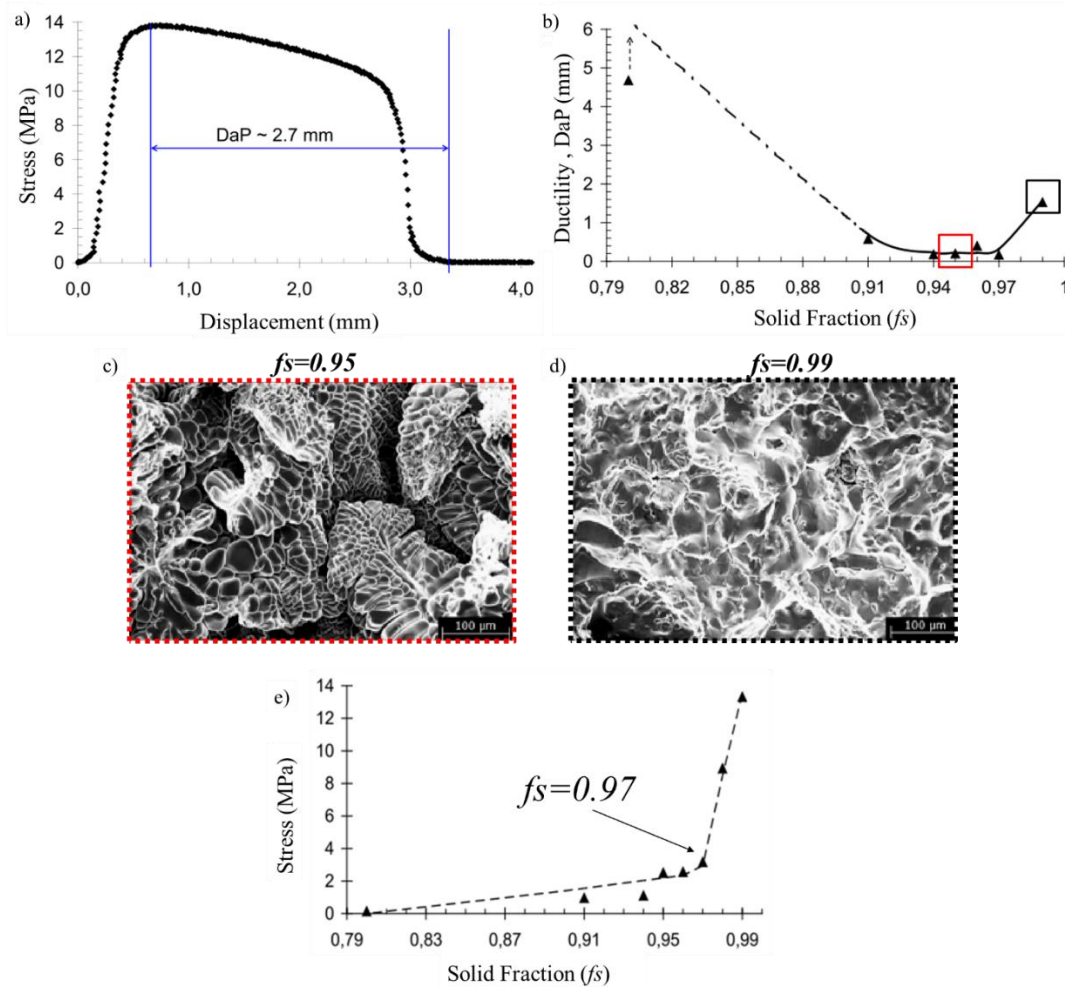


Figure 2-15 Constrained solidification studies on 6061 Al-alloy, adapted from [71]. a) Stress vs displacement curve. b) Measured ductility (mm) as a function of solid fraction. c) & d) Reveal the fracture morphology for $f_s=0.95$ and $f_s=0.99$, respectively. e) Variation of stress vs solid fraction for the 6061 Al-alloy.

This difference in the ductility behavior was examined by Giraud *et al.* [71] using the fracture surface examination at two different solid fractions (see **Figure 2-15c-d**), namely $f_s=0.95$ (within the brittle

region) and $f_s=0.99$ (within the ductile region), respectively. The fracture surface at $f_s=0.95$ revealed dendritic morphology, indicating evidence of trapped liquid films, whereas at $f_s=0.99$ showed a ductile fracture. Thus in the range of solid fraction from 0.94 to 0.97, the 6061 alloy is most sensitive to cracking, according to Giraud *et al.* [71].

Moreover, the solid fraction value of 0.97 was experimentally identified to be the coalescence solid-fraction of the 6061 Al-alloy by Giraud *et al.* [71]. As shown in **Figure 2-15e)**, the stress vs solid fraction curve shows a rapid increase after $f_s=0.97$. For $f_s>0.97$, the increase in stress is related to coalesced grains, and for $f_s<0.97$ the thin liquid films majorly govern the low stress levels. In addition, the stress increase is not rapid for increasing solid fractions (below 0.97), since the dendrites are not yet coalescence, despite the diminishing liquid film thickness. This value of coalescence solid fraction of 0.97 for the 6061 Al-alloy was similar to the typical values reported for Al-alloys [86,87].

Thus depending on the understanding of the solidification cracking occurring in the last stage of solidification due to the presence of intergranular continuous liquid films, several metallurgical factors (few of many) affecting solidification cracking can be listed:

1. **Solidification temperature range:** Generally if the solidification temperature range (T_{solidus} to T_{liquidus}) is large, larger will be the fragile region of the mushy zone. By varying the alloy composition, this freezing temperature range can be varied.
2. **Composition and the quantity of liquid film in the terminal stage of solidification:** Since solute elements present in the alloy can modify liquid film properties like net viscosity, the effective permeability can be modified [81]. It is frequently reported in the literature that peak cracking sensitivity occurs for a moderate amount of solute content [19,71][88]. For a higher amount of solute, there is a sufficient amount of liquid to backfill the cracks, whereas a very low solute content tends to not form grain boundary liquid films, and cracking will not occur [81]. In fact, depending on the solute partition in the last stage of solidification, the behavior of liquid films will be affected.
3. **The surface tension of the grain boundary liquid films:** According to Kou *et al.* [81], the surface tension of liquid plays a major role in depicting solidification cracking. Generally the higher the surface tension, the larger will be the dihedral angle between the liquid and the grain boundary, as shown in **Figure 2-16**. Thus lower surface tensions will result in better wetting of the continuous liquid films on the grain boundaries, resulting in a highly cracking sensitive region.
4. **Grain structure:** Depending on the grain structure, whether columnar grains or equiaxed, cracking sensitivity to solidification cracking is affected. Generally, columnar grains are more sensitive to solidification cracking because they cannot sustain the tensile strains occurring during solidification.
5. **Grain boundary misorientation:** Higher cracking sensitivity is usually observed for high angle grain boundaries (HAGBs, typically $>15^\circ$) [6,88,89]. The sensitivity of HAGBs to cracking can be explained by the coalescence undercooling model of Rappaz *et al.* [6]. According to Rappaz *et al.*

[6], the HAGBs will coalesce at a lower temperature compared to the low angle grain boundaries (LAGBs, typically $<15^\circ$), and thus strains are higher.

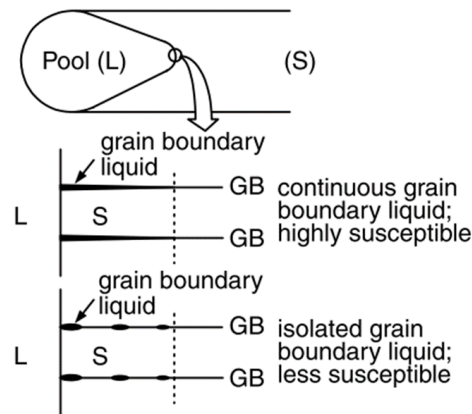


Figure 2-16 Schematic showing the effect of grain boundary liquid surface tension on solidification cracking, adapted from [81].

2.3.2. Liquation cracking

Another type of cracking that also occurs in the presence of liquid films but in the partially melted zones (PMZ) is called Liquation cracking. PMZ is the region near the fusion zones, as shown in **Figure 2-17a)**. Similar regions can exist in L-PBF, which are mostly the regions from previous layers that are remelted to a certain extent. Liquation cracking occurs due to grain boundary liquation in the PMZ, as shown in **Figure 2-17b)** for the case of 6061 Al-alloys. This means grain boundaries in the PMZ can be cracking sensitive. Several researchers in the welding literature have reported such an observation of liquation cracking for the 6061 Al-alloys [18,24,25].

Since liquation cracking does not occur in the fusion zone or during the solidification process, the concept of coalescence of dendrites will not explain its occurrence. The basic reason for liquation cracking in the PMZ as explained by Kou *et al.* [81], is due to the pulling force created by the solidifying fusion zone, as shown in the schematic of **Figure 2-17c)**. When the solidifying metal contracts, it exerts a pulling force, creating a tensile environment in the PMZ zone. The tensile atmosphere in the PMZ can be detrimental if some grain boundaries contain liquid films. Most Al-alloy from the 6XXX series (including 6061 Al-alloy) are susceptible to liquation cracking due to their wide PMZ caused by the large solidification temperature range, high thermal conductivity, large solidification shrinkage (solid density higher than the liquid), and large thermal contraction (high thermal expansion coefficient) [81].

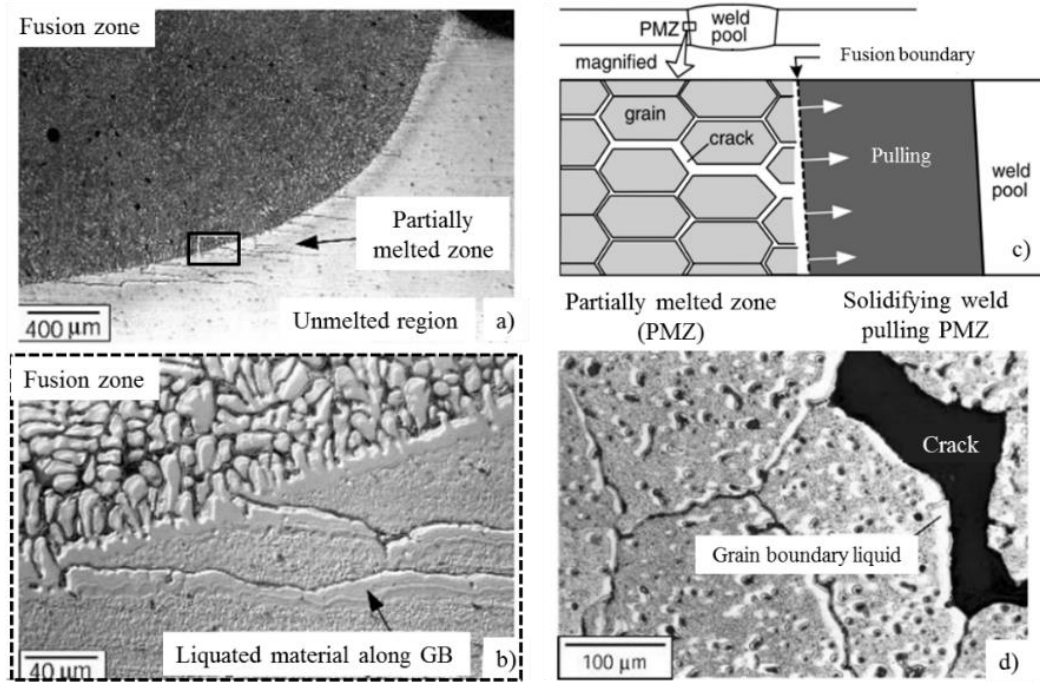


Figure 2-17 a) Gas-metal arc weld region of 6061 Al-alloy and b) shows the magnified regions. c) Schematic of the liquation cracking mechanism in the PMZ. d) adapted from [81]

2.3.3. Summary

Based on the reviewed welding literature, the cracking mechanism reported for the 6061 Al-alloy is mostly due to the presence of liquid films, i.e. classified as hot cracking. However, the reviewed welding literature does not unanimously agree on any one cracking mechanism. There is still a debate for the cracking mechanism encountered in 6061; whether it is liquation or solidification cracking. Without experimental evidence, both may, a priori, operate in L-PBF according to the welding literature. There is still ambiguity. Moreover, in the L-PBF literature, the actual mechanism that drives cracking in 6061 Al-alloy is also not well reported. The mechanism describes a strong link to solidification and alloy metallurgical parameters, namely: the solidification temperature range, role of solutes, etc. The following section will review different cracking sensitivity criteria focused on solidification and liquation cracking.

2.4. Cracking sensitivity criteria

As seen in **section 2.3**, cracking occurs through various mechanisms. Depending on the location of cracks, i.e in the fusion zone or partially melted zones, hot cracking can be distinguished. The section will review different cracking sensitivity criteria reported in the literature during the solidification process of the alloy

(focusing only on solidification and liquation cracking). Different cracking sensitivity models are reported in the literature that predicts the sensitivity of an alloy to hot cracking. The most basic criterion relies on the solidification temperature range or also commonly known as the freezing temperature range. Moreover, other advanced criteria are also reviewed, which considers metallurgical and process parameters. The idea is to review different numerical hot cracking criteria and select one of them to be applied in the framework of AM.

Eskin *et al.* [86] reviewed different cracking models and classified them based on the key parameters used. For example, some criteria include stress-based models, strain-based models, and strain-rate based models. Stress-based models rely on the fact that, if the stress in the mushy zone exceeds the strength of the semi-solid, cracking will occur. Similarly, according to strain-based criteria, cracking will occur if the tensile strains are enough to break the liquid in the grain boundaries. More recently, it was found that strain rate is more important factor to cracking than strain. Coniglio & Cross [90], confirmed experimentally the effect of critical strain rate on cracking to occur in the Al-alloy.

A thermomechanical criterion was proposed by Prokhorov [91], which was based on the rate of strain localization by the decreasing temperature, i.e. $d\varepsilon/dT$. Later, Feurer [92] proposed his cracking criterion, which was only based on liquid feeding in the mushy zone. Feurer [92] asserted that cracking will occur if the volumetric shrinkage exceeds the volumetric liquid feeding. However, the model of Feurer [92] did not consider the tensile deformation happening during the solidification.

In a more advanced form of Feurer's empirical formula, Rappaz, Drezet & Gremaud (RDG) criterion [7] considered both aspects of tensile deformation and liquid feeding, by taking into account the entire mushy zone. In similar footsteps of RDG criterion, Kou [93] also proposed his hot cracking criterion recently. However, the approach of Kou is a bit different, he concentrated on the events happening at the grain boundary rather than considering the entire mushy zone, as in the case of RDG. Both of these criteria will be detailed in the following sub-sections, including the basic criterion of the solidification temperature range.

2.4.1. Solidification temperature range

Considering the alloy during the solidification, various information can be obtained from the liquid to solid transformation. For example, the solidification path ($f_s(T)$) and the freezing temperature range can be studied. **Figure 2-18** illustrates the solidification path of 6061 alloy with temperature as a function of solid fraction, estimated by Martin *et al.* [4]. The solidification temperature range for the 6061 Al-alloy is $\sim 132^\circ\text{C}$, compared to 30°C for the AlSi₁₀Mg alloy. This indicates that 6061 Al-alloy will have wider partially melted zone (PMZ) compared to the AlSi₁₀Mg, and thus has higher sensitivity to cracking. Similarly, the solidification temperature range of 7075 Al-alloy is high $\sim 175^\circ\text{C}$. According to the literature [19], the actual cracking sensitivity cannot be accurately estimated based on the solidification temperature

range. Thus, just with the comparison of the freezing temperature range, determining the cracking sensitivity of alloys can be misleading. There are various cracking sensitive criteria, which take into account alloy metallurgical parameters, solidification process parameters, etc. This will be reviewed in the upcoming section.

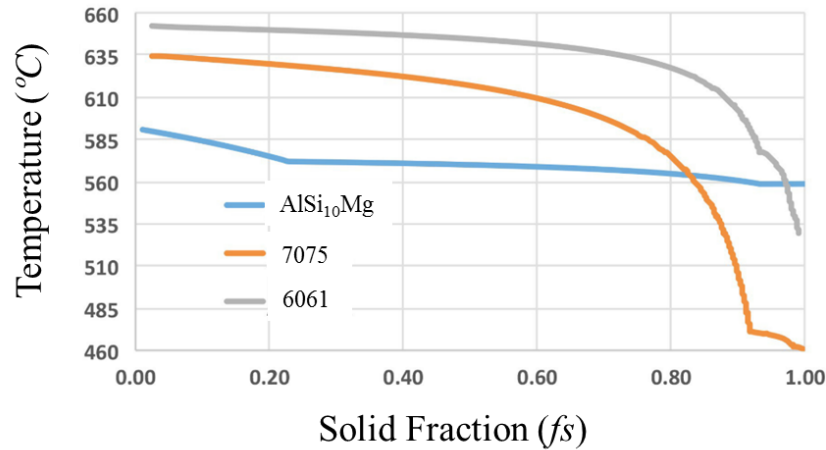


Figure 2-18 Solidification path of 6061 Al-alloy in comparison with 7075 Al-alloy and AlSi₁₀Mg [4].

2.4.2. Sindu Kou criterion

Kou in his cracking sensitivity criterion [93] assumed the growth of dendrites in one direction, tensile deformation happening in the direction perpendicular to the growth, and liquid feeding happening in the direction opposite to the dendrite growth. The criterion focusses on the grain boundary liquid region, where all the important events occur during solidification, namely:

- the separation of grains from each other due to the tensile deformation.
- the growth of grains towards each other.
- liquid feeding in the grain boundary region due to shrinkage and deformation.

The physical idea behind the Kou criterion is that cracking will occur if the net expansion of the intergranular region exceeds the net volumetric flow of liquid into that region. Thus, based on these events Kou [93] came up with his cracking index to predict the cracking sensitivity of an alloy based on the absolute value of $dT/d(f_s^{1/2})$ near $f_s=1$, where T is temperature and f_s is the fraction of solid. The index is directly linked to the lateral growth of grains towards each other by restricting the intergranular cracking. It also provides an understanding of the length of grain boundary liquid needed to be fed to avoid cracking. Thus, the higher the $dT/d(f_s^{1/2})$ near $f_s=1$, the higher will be the length of grain boundary liquid and so will be the cracking sensitivity.

As shown in **Figure 2-19**, the temperature vs $f_s^{1/2}$ curves are plotted for two example alloys (one having high steepness- $dT/d(f_s^{1/2})$ compared to the other). The Kou criterion says that the higher the steepness ($dT/d(f_s^{1/2})$) of the T vs $f_s^{1/2}$ curve near $f_s=1$, the higher will be the cracking sensitivity. Thus according to the Kou criterion, the T vs $f_s^{1/2}$ curve in **Figure 2-19a)** has lower steepness compared to the T vs $f_s^{1/2}$ curve in **Figure 2-19b)**. Another implication of the criterion is that the T vs $f_s^{1/2}$ curves near $f_s=1$ can represent the shape of the columnar dendrites region in the grain boundary, as shown in **Figure 2-19**. Thus with such an interpretation, the alloy curve in **Figure 2-19b)** will have a higher length of liquid feeding region compared to the alloy in **Figure 2-19a)**. This makes the alloy from **Figure 2-19b)** have higher cracking sensitivity.

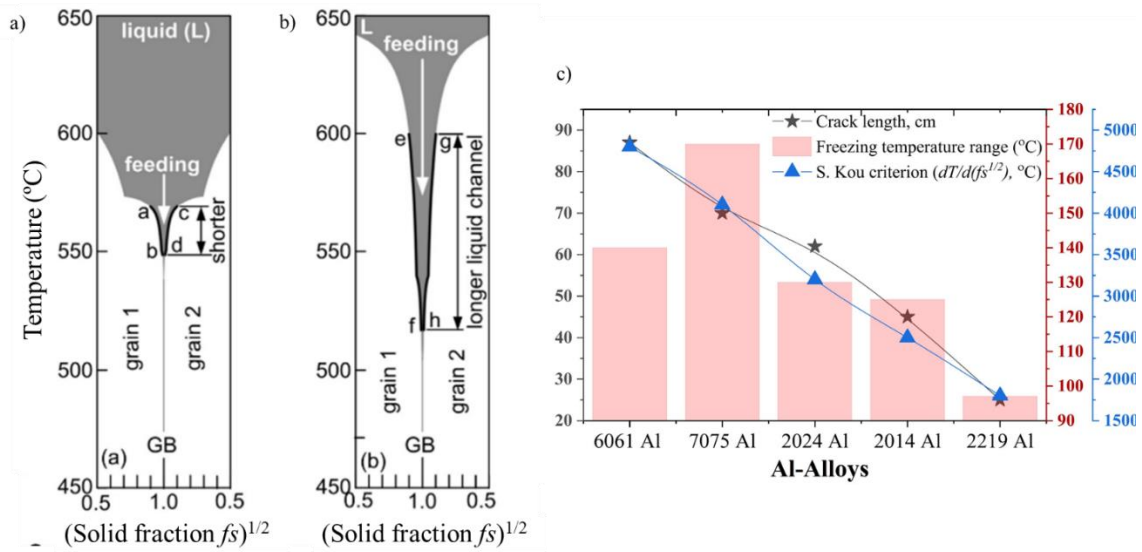


Figure 2-19 a)-b) Schematic of temperature vs $f_s^{1/2}$ curves for the example alloys, adapted from [19]. c) Comparison of actual cracking sensitivity observed for different Al-alloys with the freezing temperature range and with S. Kou cracking index (data adapted from [19]).

The region in which this steepness $dT/d(f_s^{1/2})$ is usually estimated is in the range of $0.87 < f_s < 0.94$ ($0.94 < f_s^{1/2} < 0.97$) according to Kou [93]. However, the choice of this range in which the steepness is estimated is not clear and may vary depending on the Al-alloy system [93]. Despite the fact of this uncertainty in this range, the Kou index can predict the relative cracking sensitivity of Al-alloys in casting and welding. For example, in **Figure 2-19c)**, various Al-alloys are compared for their actual cracking susceptibility (total crack length in cm) with the Kou index, and their respective freezing temperature ranges are also mentioned for reference. According to **Figure 2-19c)**, the Kou index ($dT/d(f_s^{1/2})$) can predict the cracking trend observed during the welding. It must be also reminded that, based on the freezing temperature range shown in **Figure 2-19c)**, the 7075 Al-alloy is the most cracking sensitive. However in reality the 6061 Al-alloy is the most cracking sensitive, and thus the freezing temperature range should be used with care or rather the Kou index must be preferred.

Thus to summarize, in welding literature the Kou index can predict the alloys that are cracking sensitive and the criterion also provides a simple basis to choose filler alloys during the Al-alloy welding [94,95].

2.4.3. Rappaz, Drezet and Gremaud (RDG criterion)

Based on mass balance performed over liquid and solid phases inside the mushy zone, the Rappaz, Drezet, and Gremaud criterion (RDG) [7] takes into account the tensile deformation perpendicular to the direction of thermal gradients and the interdendritic liquid feeding. RDG criterion simply states that a void will nucleate and give rise to a crack when the liquid pressure in the mushy zone falls below a certain cavitation pressure (P_c). The RDG model is the first of its type to link the microporosity to the hot cracking.

Using the metallurgical parameters like the viscosity of the liquid (μ), shrinkage factor (β), the characteristic length of the microstructure (typically the secondary or primary dendrite arm spacing) (λ), effective strain rate ($\dot{\epsilon}$) perpendicular to the direction of dendrite growth, liquidus temperature (T_l), the temperature of coalescence (T_{gc}), solid fraction $f_s(T)$ of the material and solidification parameters (thermal gradients G and solidification velocity v), Rappaz *et al.* [7] came up with a famous relation for the pressure drop, as shown in **Equation 1.1**. The total pressure drop (ΔP_{total}) is composed of the shrinkage ($\Delta P_{shrinkage}$) and the deformation ($\Delta P_{deformation}$) contributions. The drop in pressure computed using the RDG criterion is the decrease in metalostatic pressure (P_m). So ideally when $P_m - (\Delta P_{total})$ falls below P_c , a void is nucleated, as shown in **Figure 2-20**. According to Rappaz *et al.* [7], the higher the pressure drop, the higher will be the cracking sensitivity, since after reaching a critical value of pressure, the liquid feeding will not occur and the void will nucleate due to the localization of strains.

$$\begin{aligned} \Delta P_{total} &= \Delta P_{deformation} + \Delta P_{shrinkage} \\ &= \frac{180 (1 + \beta) \mu}{\lambda^2 G} \int_{T_{gc}}^{T_l} \frac{E(T) f_s(T)^2}{(1 - f_s(T))^3} dT \\ &+ \frac{180 v \beta \mu}{\lambda^2 G} \int_{T_{gc}}^{T_l} \frac{f_s(T)^2}{(1 - f_s(T))^2} dT \quad . \end{aligned} \quad (\text{equation 1.1})$$

$$\text{with } E(T) = \frac{1}{G} \int_{T_{gc}}^T f_s(T) \dot{\epsilon}(T) dT$$

Since the RDG criterion considers the dendrite microstructural parameters as well as solidification parameters with a physically sound basis, the model can be used for:

- Ranking the alloys with their relative cracking sensitivity.
- Studying the risk of hot cracking in different processes (since G and v are included in the criterion). Thus the RDG criterion is not only restricted to welding/casting processes. It can be applied to other processes like L-PBF as well if the solidification parameters (G , v) are known.

- Understanding the behavior of the mushy zone during the solidification and assessing its effect on hot cracking (since the model takes into account the coalescence temperature). For example, different alloys will have different dendrite coalescence temperatures and thus the RDG model can take precise alloy properties into account to predict their cracking sensitivity.

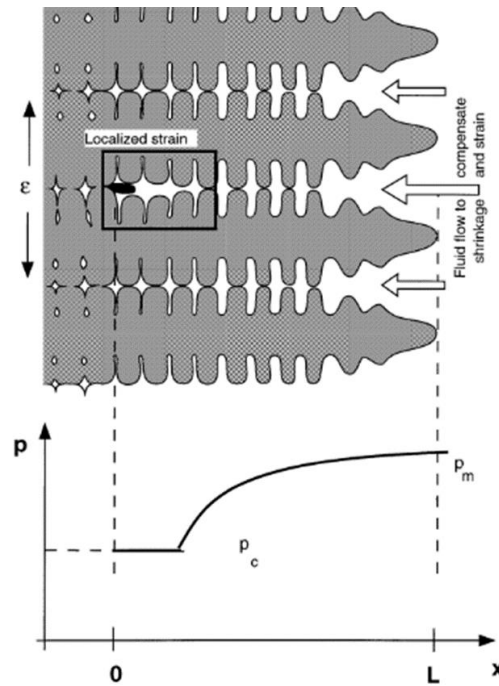


Figure 2-20 Schematic of hot crack formation due to localized strains and decrease in metallostatic pressure along the mushy zone, adapted from RDG criterion [7].

Although the RDG criterion is widely accepted and used in the hot cracking community (see refs. [56,96,97]), there are several limitations related to the model:

1. The model does not take into account the grain size of the alloy microstructure. The model only considers the secondary dendrite arm spacing as an input to estimate the pressure drop for the growing dendrites. Thus, grain refinement is not considered in the formulation of the model.
2. One of the difficulties in the RDG model is the estimation of dendrite coalescence temperature (T_{gc}). To better estimate the coalescence temperature, mechanical behavior studies in the mushy zones are needed to get an accurate estimate.
3. RDG criterion relies on the fact that strains act on the growing dendrites in the direction perpendicular to its growth, however, the longitudinal strains are not considered in the formulation of the RDG model. The longitudinal strains can also affect the expulsion of liquid feeding.

4. RDG model by itself is not able to explain the strain localization and liquid feeding at the grain boundaries since it is formulated for the growing dendrites. To isolate the dendrites at the grain boundary and the dendrites belonging to a particular grain, Rappaz *et al.* [6] came up with a coalescence model, which essentially says that, coalescence for the dendrites belonging to the same grain happens earlier compared to the ones at the grain boundaries.

To understand the liquid feeding and strain localization at the grain boundaries, several granular models are also reported in the literature [98–100]. The work done by Vernede *et al.* [98–100] uses a simplistic approach to identify the grain coalescence. At first, random nucleation centers of the grains with random orientation were generated and solidification within each grain was considered to occur with back-diffusion/microsegregation aspects. Finally, the grain boundaries correspond to the Voronoï tessellation of the nucleation centers [98–100], and the liquid flow around the grain boundaries could be analyzed. However, due to the complexity of the computation and limited mechanical inputs in the model, very few applications of the granular models are reported in the literature.

2.4.4. Summary

The major differences between the reviewed cracking criteria (Kou index [93] and the RDG model [7]) are summarized below:

- The physical idea behind the Kou index is that a crack will form if the net expansion of the intergranular space exceeds the net volumetric liquid feeding. Whereas, in the RDG criterion, the void is assumed to nucleate and form a crack when the liquid pressure falls below a certain cavitation pressure.
- In comparison to the Kou index which is only restricted to the grain boundary liquid region, the RDG criterion considers the entire mushy zone. Hence RDG criterion focuses on the processes happening on a micro-level of dendrites compared to the macro approach of the Kou index.
- The Kou index is only restricted to the steepness $dT/d(f_s^{1/2})$ near $f_s=1$. Whereas, RDG criterion can consider the metallurgical parameters ($f_s(T)$, viscosity, shrinkage, dendrite arm spacing) and solidification parameters (G, v) of the process. Thus, in addition to ranking alloys for their cracking sensitivity, the RDG criterion can also assess their sensitivity in different processing conditions.

2.5. Cracking mitigation strategies in Al-alloys (L-PBF and welding literature)

The section details different remedial solutions existing in the literature to avoid cracking in Al-alloys in general. Whether it is welding or L-PBF literature, solutions reported in both processes are summarized. Most of the solutions reported in the literature follow two paths:

1. Controlling the solidification parameters to alter the solidification condition (by processing route)
2. Compositional variation:
 - Adding nucleating agents to refine the microstructure.
 - Varying the solute content to control the liquid composition and alter the effective solidification path.

2.5.1. Processing route

- **Effect of Pre-heating the powder bed (L-PBF).**

Using the processing route, Uddin *et al.* [3] were able to produce crack-free 6061 Al-alloy in L-PBF. Uddin *et al.* [3] used the powder bed heating at 500°C (induction heating system), to get rid of the cracking. As shown in **Figure 2-21a**), the as-built sample possesses cracks that are visibly crossing several melt pools, along the building direction. The microstructure contained large columnar grains and cracking was assumed to occur by the solidification cracking mechanism, according to Uddin *et al.* [3]. On the contrary, with a preheated powder bed at 500°C, the microstructure appears to be crack-free, refined, and free of melt pool boundaries (see **Figure 2-21b**). The preheated microstructure did not feature the melt pool boundaries, typically observed in L-PBF, indicating that, the melt pool was very large due to the powder bed heating at 500 °C. Moreover, large noncoherent Al-Si-O dispersoids were identified to be homogeneously distributed in the preheated microstructure [3].

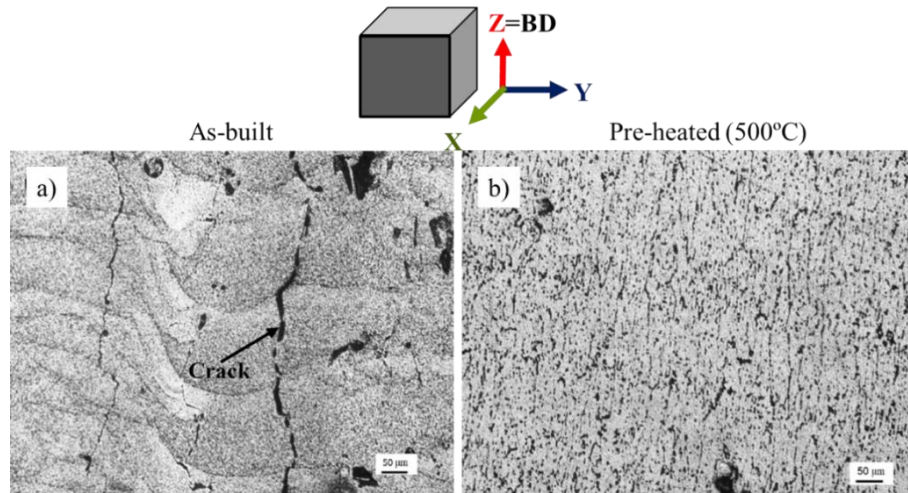


Figure 2-21 a) Optical micrograph of as-built 6061 Al-alloy and b) after preheating the powder bed at 500°C, adapted from [3].

According to Uddin *et al.* [3] the powder heating system (AconityONE induction heating-TruHeat HF series) employed in their work, diminished the available build area of fabrication. The fabricated samples were restricted in terms of dimensions to around 200 mm in width. Similarly, due to the pre-heating of the powder bed, the water-cooled system was necessary for the build chamber to avoid problems arising from self-ignition. Thus, it is true that preheating was able to produce crack-free samples, however, there were concerns related to the maximum produced dimensions of the sample and the safety [3]. Moreover, since it was induction heating from the base plate, it is also not sure until what building height the effect of preheating will occur. No further study has been reported to also understand the mechanism that causes crack mitigation due to preheating, apart from the fact that thermal gradients were diminished due to preheating.

- **Effect of double lasers (welding)**

Drezet *et al.* [97] studied the effect of twin lasers on successfully welding crack-free 6xxx Al-alloy. They used a system of twin lasers in comparison to conventional laser beam welding. Drezet *et al.* [97] used a primary laser source of continuous CO₂ laser and a secondary laser (pulsed Nd:YAG) positioned at a specific distance (δx) before the primary laser to achieve crack-free 6xxx alloy (see **Figure 2-22a**). The distance between the two laser beams was identified as the key factor that was optimized based on the effective melt pool geometry and was found to be $\delta x=3\text{mm}$ [97].

Using such a combination of lasers, they showed that microstructure in the fusion zone is highly refined, causing columnar to equiaxed transition (CET). For example, when using just the continuous CO₂ laser the microstructure contained columnar grain and cracks (see **Figure 2-22c**), highlighted red square of b)). Whereas by using just the secondary laser, it is not enough to melt the alloy (see **Figure 2-22c**), highlighted

blue square in the transition zone). And finally, when the combination of two lasers was employed, the resultant microstructure possessed equiaxed grains without the presence of cracks (see **Figure 2-22c**), highlighted green square).

Drezet *et al.* [97] attributed such an observation of crack-free samples to low strain localizations. Fine equiaxed grains are known to withstand the deformation compared to the columnar grains, and, they have higher permeability [97]. They concluded that, due to the combination of lasers, the effective thermal gradients were lowered and so does the effective strain localization. This leads to a higher level of liquid feeding in the mushy zone causing crack-free 6xxx Al-alloy [97]. A similar effect by just using a single pulsed laser beam was identified to reduce the cracking during laser welding of 6061 Al-alloy by Zhang *et al.* [101].

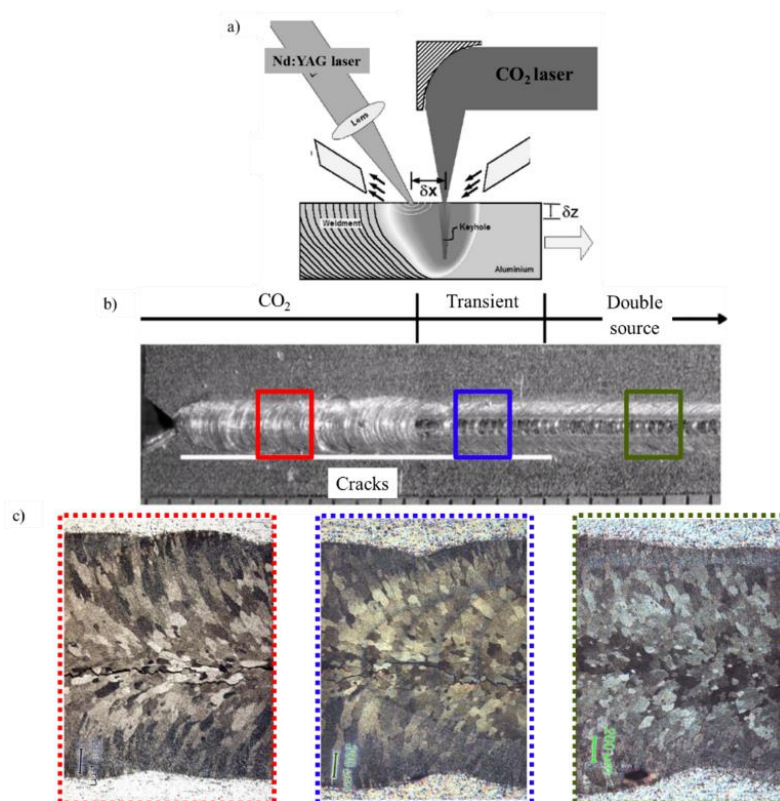


Figure 2-22 Effect of twin lasers in welding a 6XXX Al-alloy, adapted from [97].

- **Effect of ultrasound to refine the microstructure (L-PBF)**

Todaro *et al.* [102] studied the effect of high-intensity ultrasound (see **Figure 2-23a**) in Ti-6Al-4V alloy produced using laser powder deposition. They showed that by employing high-intensity ultrasound the columnar grain structure (**Figure 2-23b**) can significantly be altered into equiaxed grains (**Figure 2-23c**).

Using this technique, equiaxed grains were achieved without the addition of external nucleating agents. Even though this technique was employed to other systems of alloys, Todaro *et al.* [102] suggest that this technique can be applied to other light alloys producing columnar grains (like for instance structural Al-alloys) during additive manufacturing.

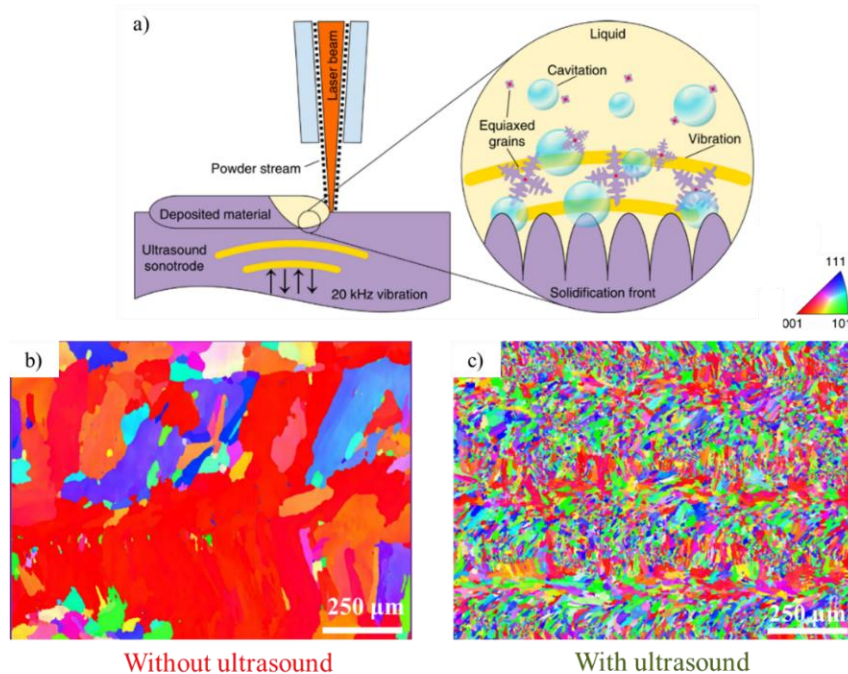


Figure 2-23 Effect of high-intensity ultrasound employed in laser powder deposition for the Ti-6Al-4V alloy, adapted from [102].

As shown in **Figure 2-23a**), due to the inclusion of high-intensity ultrasound (sonotrode vibrating at 20kHz) during the fabrication process, there is a creation of acoustic cavitation. The acoustic cavitation during solidification agitates the nuclei originally present in the alloy to form the equiaxed grains (**Figure 2-23c**)). Knowing the fact that grain refinement is known to increase the permeability of the mushy zone and accommodate the deformation, such a processed-based grain refinement can be considered as a possible strategy to mitigate cracks.

2.5.2. Grain refinement through external nucleating agents.

Another strategy that has been reported frequently to induce grain refinement is by the addition of external nucleating agents [4,103,104]. Martin *et al.* [4] demonstrated the usefulness of the addition of ZrH₂ nanoparticles on the powder surface to promote equiaxed grain structure to mitigate cracking in 6061/7075 alloys produced by L-PBF. The selection of ZrH₂ was preferred due to its similar lattice misfit,

similar atomic arrangement with the Al-crystallographic planes, and thermodynamic stability [4]. The addition of such particles on the powder surface allowed the formation of the Al_3Zr nucleating phase. Around 1% vol nanoparticles were added electrostatically on the powder surface to create pre-alloyed powders. Finally, the pre-alloyed powders produced fine equiaxed grains from the Al_3Zr nucleating phases to produce strain tolerant and crack-free microstructure (see **Figure 2-24**). By such heterogeneous nucleation, the typical columnar grains observed in L-PBF of 6061/7075 Al-alloys were transformed to crack-free equiaxed grains.

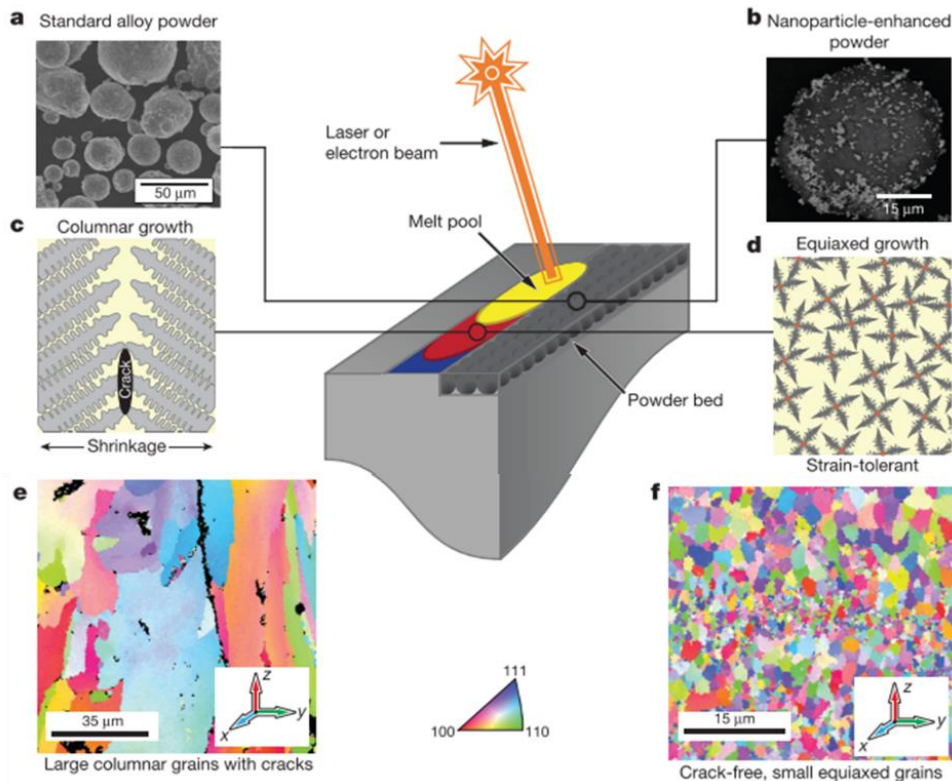


Figure 2-24 Effect of ZrH_2 nanoparticles addition on the powder surface to mitigate cracking in 6061/7075 Al-alloys, adapted from [4].

However, the equiaxed grain in the microstructure was not homogeneously distributed. A duplex microstructure was obtained that contained equiaxed grains near the melt pool boundaries and fine columnar grains growing within the melt pool. Such a duplex microstructure is frequently reported in Sc/Zr modified Al-alloys, including the Scalmalloy[®] [54,105]. A similar observation was reported by Opprecht *et al.* [104]. They added ZrO_2 particles using YSZ (Yttria stabilized zirconia) (4 vol%) on the 6061 Al-alloy powder surface to produce crack-free 6061 Al-alloys using L-PBF. Opprecht *et al.* [104] observed that based on the quantity of ZrO_2 (1-4 vol%) added on the powder surface, the resulting fraction of equiaxed grains in the melt pool and the crack density was affected. By increasing the nucleating agents, the quantity of Al_3Zr responsible for heterogenous nucleation also increased, causing a strain tolerant, crack-free microstructure [104].

Another study reported by Carluccio *et al.* [106] was focused on exploring the traditional grain refinement principles used in casting and implementing them in additive manufacturing. They used two types of grain refiners namely Scandium (Sc) and TiBor (4wt% Ti and 1wt% B, balance Al). In literature, Sc is known to produce Al_3Sc that acts as a nucleating site for the Al to grow, due to its low lattice parameter mismatch of only 1.6% with Al [106]. Similarly, Al-Ti-B refiners are also well known in casting literature for their refinement ability due to the formation of TiB_2 particles on the thin Al_3Ti substrates. Using these refiners, Carluccio *et al.* [106] casted the alloys by adding 0.33wt% TiBor and 0.4 wt% Sc in the 6061 Al-alloy. They showed that, by laser melting the casted alloys, both the refiners produced the expected grain refinement. TiBor was more effective in homogeneously nucleating the equiaxed grains (see **Figure 2-25b**) and on the contrary, a mixture of columnar and equiaxed grains was obtained for the Sc addition (see **Figure 2-25c**).

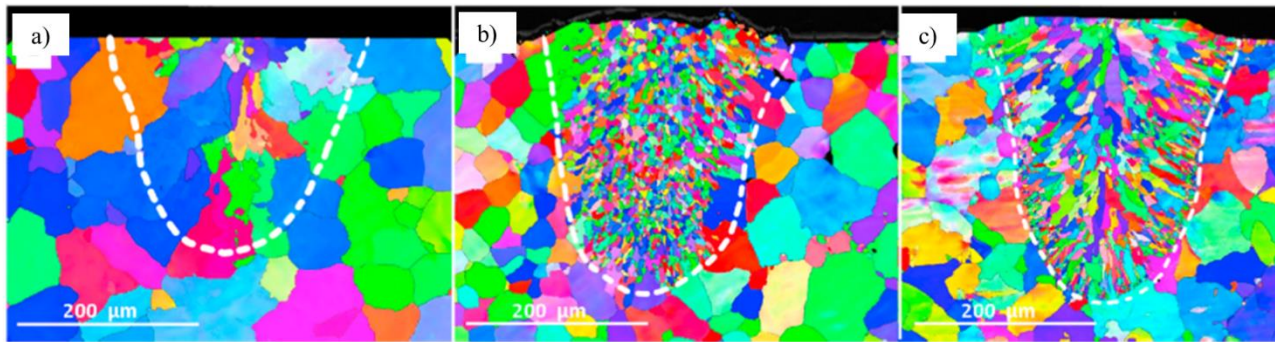


Figure 2-25 Effect of TiBor and Sc addition in the laser melted 6061 Al-alloy. a) EBSD of laser melted 6061 Al-alloy melt pool, b) with 0.33 wt% TiBor addition and c) 0.4 wt% Sc addition, adapted from [106].

Thus to summarize, grain refinement principles used in the casting literature can be implemented in the framework of additive manufacturing to induce grain refinement of Al-alloys. This approach has been widely studied in the AM literature and has proven efficient to produce crack-free Al-alloys. However, there are concerns due to the cost issues of the refiners like Sc- a rare earth element.

2.5.3. Solute composition modification.

So far we have reviewed the process-based and external nucleating agent based cracking mitigation strategies. However, in literature, there are also a few instances, where solute composition modification has been reported as a cracking mitigation strategy. The only solute modification reported in AM literature to produce crack-free 7075 Al-alloy is done by Sistiaga *et al.* [5]. 7075 is a high strength Al-alloy having Zn-Cu-Mg as its major alloying elements, with ~ 0.7 wt% Si. Sistiaga *et al.* [5] varied the silicon content in the 7075 base alloy to mitigate cracking (see **Figure 2-26**). Crack density was found to decrease, with Si addition ranging from (1-2 wt%); whereas for 3-4wt% Si addition, crack free 7075 were produced by L-

PBF [5]. In casting literature, Si is usually added to improve the processability of the alloy since it acts in reducing the melting temperature, improving the melt fluidity, and reducing the thermal expansion coefficient. Moreover, the addition of Si results in the formation of low melting point eutectics that could result in backfilling the cracks present in 7075 Al-alloy, as also observed in ref. [107].

Si addition in 7075 Al-alloy resulted in cracking mitigation and also refined grain structure, however, its applicability to other structural Al-alloys is not clear. For example, Giraud *et al.* [73] in their constrained solidification studies reported that, by increasing the Si content in the 6061 Al-alloy up to 2-3 wt%, the crack density increased compared to the standard 6061 Al-alloy. Thus it is not clear, whether the Si addition to the 6061 will benefit or not, since literature dealing with solute composition modification in 6061 Al-alloy in the framework of AM is quite rare.

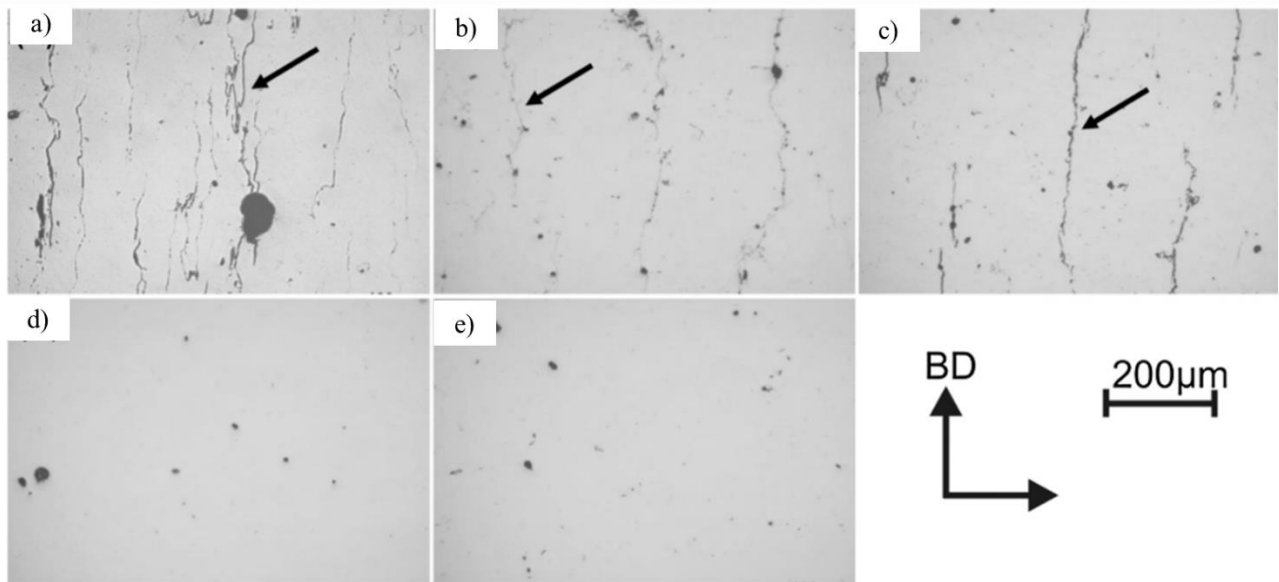


Figure 2-26 Building direction microstructure of Si modified 7075 Al-alloy. a)-e) Si content added 0, 1, 2, 3, 4 wt%, respectively, adapted from [5].

It is known in the welding literature [18,24,25] that 6061 alloy tends to liquation cracking, as shown in **Figure 2-27a)**. Huang & Kou [94], studied the liquation cracking sensitivity of 6061 Al-alloy during welding by using different filler metals namely, with 5356(Al-5Mg) and 4043 (Al-5Si). Filler alloys in welding are used mainly during the joining process to avoid cracking and also to maintain the mechanical properties of the weld [95]. It is also known in literature [108] that, the dilution (% of base metal in the resultant weld metal) affects the feasibility of the welding process. A crack-free weld was obtained by Huang & Kou [94], when a filler alloy 4043 with 68% dilution was used to weld the 6061 Al-alloy (see **Figure 2-27b)**). The composition of the 4043 filler (Al-5Si) is shown in **Table 2-7**. The 4043 filler majorly contains 5wt% Si, 0.8wt% Fe, and a very low amount of Mg compared to the standard 6061 Al-alloy.

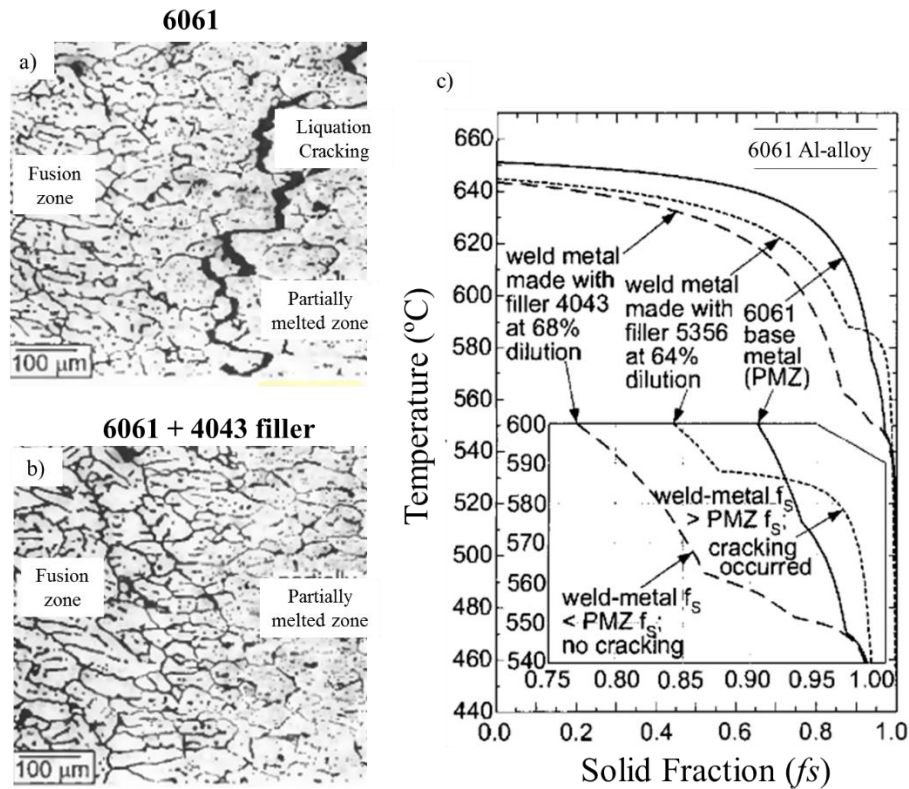


Figure 2-27 a) Welded microstructure of standard 6061 Al-alloy showing fusion zone and PMZ, b) Welded microstructure of 6061 with a filler of 4043 alloy. c) Temperature vs solid fraction curves for standard 6061 alloy, with 4043 filler and with 5356 filler alloy, adapted from [94].

Huang & Kou [94] showed that depending on the solid fraction of the partially melted zone (PMZ) compared to the fusion weld metal, cracking sensitivity will be affected. They compared their thermodynamic predictions to the experiments and concluded that liquation cracking will occur if the weld metal has a higher solid fraction than the PMZ. As shown in **Figure 2-27c**), three temperature vs solid fraction curves are shown for 6061 Al-alloy (which will be majorly in PMZ), 6061+4043, and 6061+5356. The curves with filler alloy represent the fusion weld metal region. Thus according to Huang & Kou [94], since for 6061+4043 filler, the solid fraction of weld metal is $<$ the PMZ solid fraction, cracking will not occur. And on the contrary for 6061+5356 filler, the solid fraction of weld $>$ than the solid fraction of PMZ, indicating the presence of cracks with 5356 filler (Al-5Mg).

Thus to summarize, by using filler alloys during welding, locally the weld composition is altered. The change in weld composition affects the cracking sensitivity of the 6061 Al-alloy. Filler alloy 4043 is proved in welding literature to be effective in reducing liquation cracking in 6061 Al-alloy. However, the use of 4043 compositions to mitigate the solidification cracking is not yet reported. In addition, the use of filler with base alloy can deviate the composition from the actual composition of the 6061 Al-alloy.

Table 2-7 Composition of 4043 filler used in the welding of 6061 alloy, adapted from [94].

	Al	Si	Mg	Fe	Cu	Cr	Ti	Mn	Zn
6061 [67]	Bal.	0.4- 0.8	0.8- 1.2	<0.2	0.15- 0.4	0.04- 0.35	<0.15	<0.15	<0.25
4043 [95]	Bal.	5.2	0.05	0.8	0.3	0.001	0.2	0.05	0.1

2.5.4. Summary

Thus, to summarize, most of the reviewed approaches either aimed at refining the microstructure by rare earth elements or by reducing the thermal stresses through processing. However, the direct link between the root cause of cracking and these solutions is still unclear for L-PBF of 6061-grade. In the literature, several strategies have been explored to overcome cracking issues affecting the 6061 Al-alloy, either by process variation or compositional changes. The most common process-based strategy involves playing with first-order parameters such as laser power and speed [61]. Less common but efficient strategies consist of preheating the substrate [3], use pulsed laser beam [101], or twin laser beams [97]. These approaches aim to avoid hot cracking sensitivity by reducing the thermal gradients and thus thermal strains acting on the solid-liquid zone in the melt pool. Grain refinement, which can be achieved by using ultrasound [102] or laser re-scanning [109], is also considered as a possible way to minimize hot cracking. However, for the case of structural Al-alloys, no such process-based grain refinement has been proven to fully avoid cracking.

On the contrary, compositional variation has proved to be efficient in inducing grain refinement to mitigate cracking. For example, the addition of nucleation agents to refine the microstructure is often reported in refs. [4,110,111][106] to produce crack-free parts. The addition of Si (4wt%) in the 7xxx alloy proved to be beneficial, however, its applicability on the 6061 alloys is not reported and needs to be understood. Thus, the effect of solute composition changes in the framework of AM of 6061 alloy needs research efforts in linking the causes of cracking to predicting crack-free compositions.

Also besides, compared to compositional variation, the processing path still needs opportunities for enhancement. Despite the success of preheating [3] from the processing point of view, no other method was able to eliminate cracking or provide guidelines in 6061 Al-alloy during L-PBF.

3. Powder Characterization

In this chapter, the 6061 Al-alloy powder characteristics are detailed. The powder chemical composition, size distribution, and morphology are reported.

Two batches of 6061 Al-alloy powders from two different suppliers were analyzed in the present study. The first batch was from TLS Technik© and the other one was from second manufacture (Powder-2). Both powder batches were pre-alloyed and gas atomized by respective suppliers. The two sets of 6061 alloy powders were analyzed and only one was selected to perform the elementary experiments. The selected 6061 Al-alloy powder was used to perform process optimization studies (reported in **Chapter 4**) by various elementary experiments (single and multiple laser tracks) and to fabricate 3D cubes. The current Chapter is divided into the three following sections, the objective is to get a full description of the as-received powder batches:

- **Chemical composition;**
- **Powder size distribution;**
- **Powder morphology and flowability.**

3.1. Chemical composition.

The chemical composition analysis of the powders was carried out at Elektrowerk GmbH using Inductively coupled plasma-optical emission spectrometry (ICP-OES) with DIN-EN-14242 standards [112]. The powder samples preparation needed the following steps:

- The samples were taken in a glove box after mixing the powder canister for around 2-5 minutes.
- A small quantity is then taken in an airtight stainless steel container.
- The powder was then sent for analysis.
- For each series of analyses, 2 samples were prepared separately.

The compositions of the two powder batches are given in **Table 3-1**. Both the powder compositions are within the ranges imposed by the standard for the 6061 Al-alloy [67].

Table 3-1 Chemical composition of the 6061 Al-alloy powder used in the present study in (wt %). The standard is also given for comparison.

	Al	Si	Mg	Fe	Cu	Cr	Ti	Mn	Zn
Standard [67]	Bal.	0.4- 0.8	0.8- 1.2	<0.2	0.15- 0.4	0.04- 0.35	<0.15	<0.15	<0.25
TLS Powder	Bal.	0.78	0.95	0.14	0.25	0.16	0.01	0.003	0.007
Powder-2	Bal.	0.8	1.04	0.2	0.23	0.15	<0.01	<0.01	<0.01

3.2. Powder size distribution

The procedure used was as per the ASTM standard B822 – 10 [113]. Particle size analysis was performed on a Mastersizer 2000 laser particle size analyzer (by Malvern Instruments ©) equipped with a hydro liquid analysis module. The liquid used was ethanol. Two representative samples of each powder were analyzed ten times each with and without the use of ultrasounds (for 2 minutes). The purpose of using ultrasounds is to break down agglomerates due to the strong cohesion of the powder particles. An analysis corresponds to a series of 5 measurements without ultrasounds and 7 measurements with (of which only the last 5 are kept) per sample. The reported size distribution is the one after a series of 10 measurements. The powder samples stored in the glove box were used after mixing the container for 2-5 minutes and placed in a plastic container. Once out of the glove box, the powder was analyzed immediately.

Based on the laser granulometry analysis shown in **Figure 3-1**, the size distribution for the two powder batches is summarized in **Table 3-2**. According to the size distribution, the powder from the second manufacture (Powder-2) appears to have a smaller size distribution compared to the TLS powder. The size distributions for both the powder batches are within the recommended range for L-PBF Al-alloys [12].

Table 3-2 Powder size distribution of the two 6061 Al-alloy powders.

	TLS powder	Powder-2
Size distribution	D10= 27 μm D50= 41 μm D90= 63 μm Refer to Figure 3-1a)	D10= 10 μm D50= 24 μm D90= 50 μm Refer to Figure 3-1b)

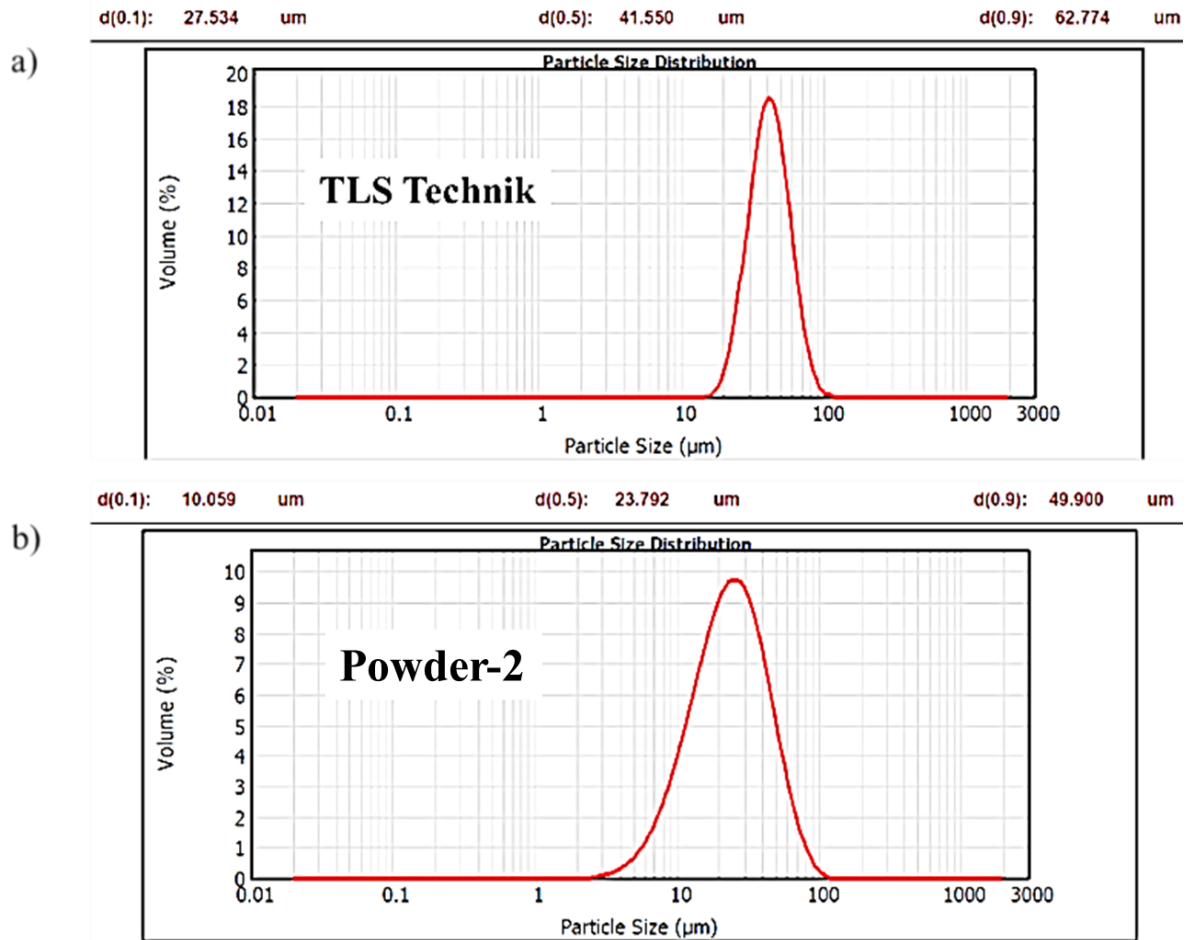


Figure 3-1 Powder size distribution determined using Mastersizer 2000 (laser particle size analyzer). a) TLS Technik powder batch and b) Powder-2 batch.

3.3. Powder morphology and flowability

3.3.1. Morphology

The morpho-granulometric analysis was performed using a Morphologi G3S morpho-granulometer (Malvern Instruments ©). A 7 mm³ sample representative of each powder batch was observed at x20 magnification. The analysis was carried out on roughly ~80,000 particles. Two filters were used. The first one eliminates agglomerates and the second allows dust particles to be removed: all particles having Circle Equivalent Diameter (CED) < 2 μm are discarded from the analysis. The aspect factor is defined as the ratio of the width to the length of the particle. A long and thin particle will have an aspect ratio close to 0, whereas a spherical particle will have an aspect ratio close to 1. Apart from quantifying the morphology of the powders, the powder particles were also observed in a scanning electron microscope using secondary electrons (SE) and back-scattered electrons (BSE) contrast.

Based on the powder morpho-granulometry analysis shown in **Figure 3-2**, the aspect ratio of the two powder batches is summarized in **Table 3-3**. According to the quantitative morpho-granulometry analysis, both powder particles of each batch appear to be spherical in nature with an aspect ratio close to 1 for the majority of the particles.

For the TLS powder, **Figure 3-3a) & b)** SEM observations show that the as-received powder exhibits spherical shape with few satellites. Microstructure of the powder particles is polycrystalline in nature as revealed by the BSE-SEM contrast micrograph and grain map shown in **Figure 3-3c) & d)** respectively. For the Powder-2 batch, **Figure 3-3e)** shows that the as-received powder exhibits also spherical particles with the presence of agglomerated particles. The powder-2 batch also exhibits a polycrystalline structure; see **Figure 3-3f)**.

Table 3-3 Powder morphology (aspect ratio) of the two 6061 Al-alloy powders.

	TLS powder	Powder-2
Morphology (aspect ratio)	0.95 for 90% of the number powder distribution. Refer to Figure 3-2a)	0.95 for 65% of the number powder distribution. Refer to Figure 3-2b)

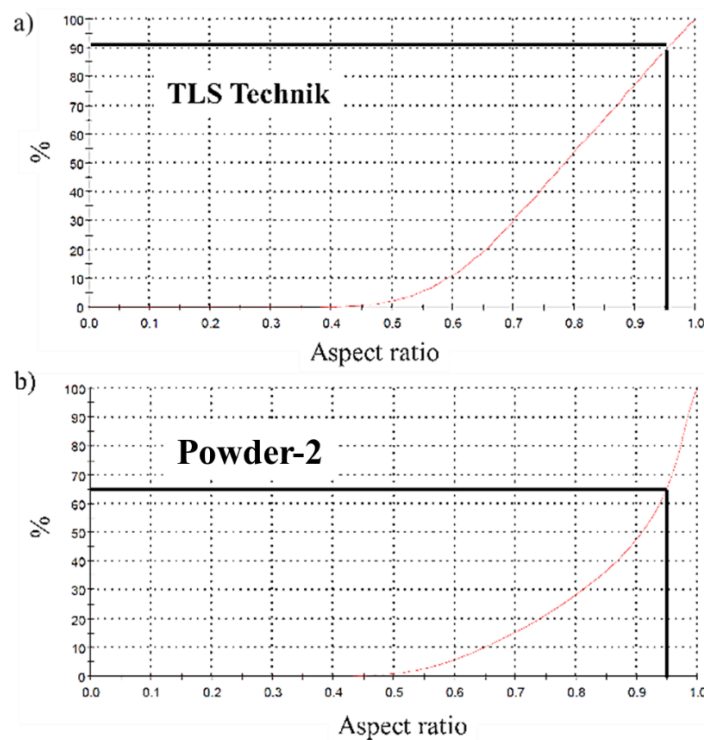


Figure 3-2 Morpho-granulometry of the a) TLS Technik powder batch and b) Powder-2 batch, determined using a Morphologi G3S morpho-granulometer.

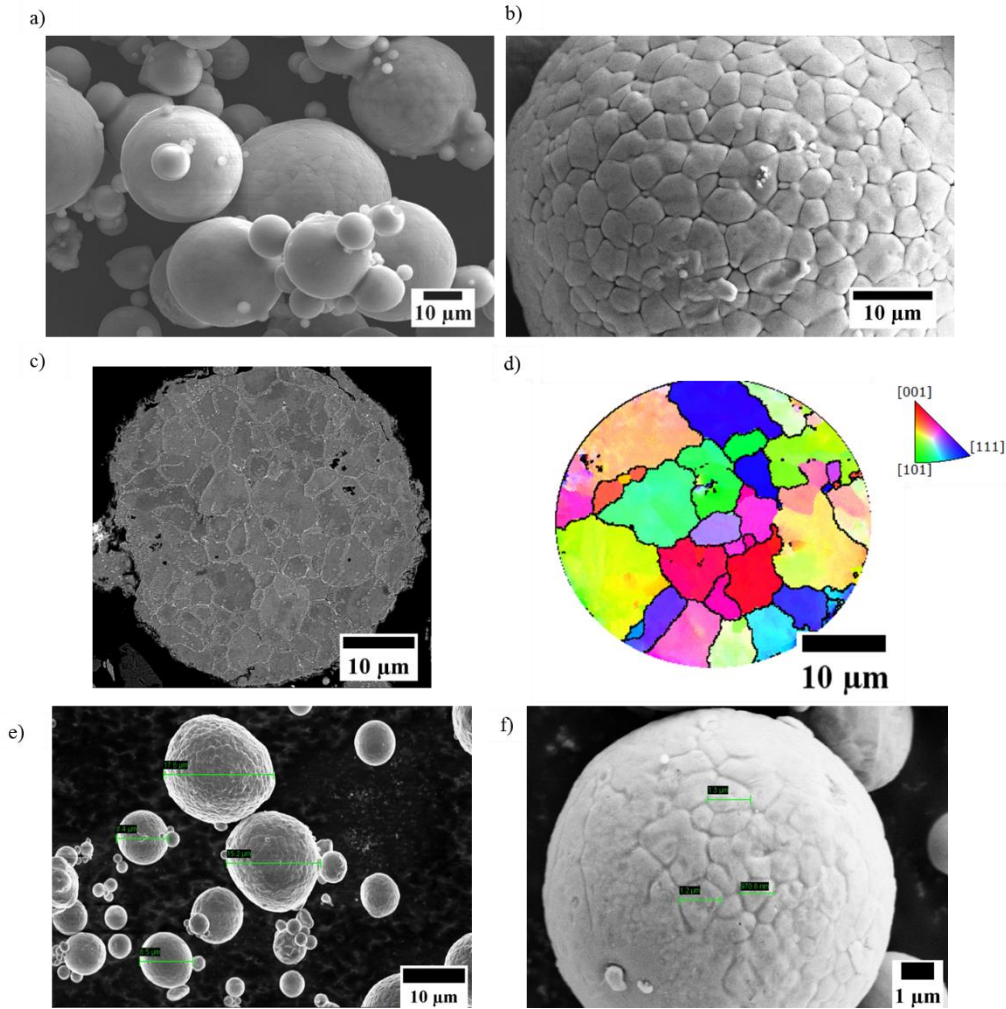


Figure 3-3 TLS Technik powder: a) & b) Powder morphology at different magnification observed using SEM-SE micrographs. c) Cross-section of the powder showing different grains (SEM-BSE contrast). d) Grain map of the powder cross-section measured using EBSD. **Powder-2 batch:** e) & f) Powder morphology at different magnification, respectively.

3.3.2. Flowability

The powder flowability was characterized by two methods. The first one using the angle of avalanche. The avalanche angle measurements were done in a rotating drum avalanche measurement system from Mercury scientific instruments, as illustrated in the schematic of **Figure 3-4**. The rotating drum has a volume of 125 cm^3 that rotates and measures the angle at which the powder starts to fall, i.e. the angle of avalanche. A default revolution speed of 0.3 revolutions per minute was used and the build-in camera took images at 30 fps. Around 150 avalanches were analyzed to obtain the average avalanche angle for the two sets of powder used.

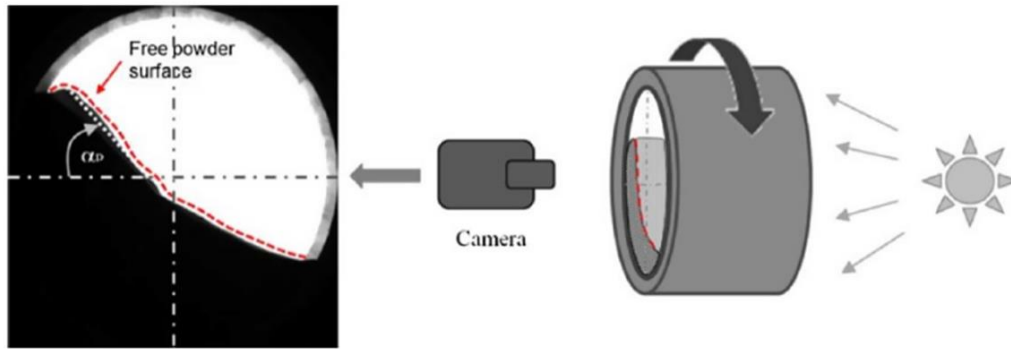
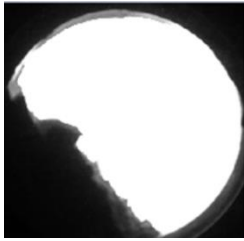
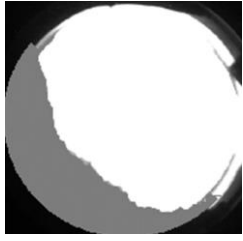


Figure 3-4 Schematic of the rotating drum used for avalanche angle measurement [114].

The second method to quantify the flowability was using the Hausner ratio [115]. It is a ratio of tapped density over the apparent density. The measurement of the tapped density of a powder consists of filling a graduated burette with a known mass of powder (thus obtaining the apparent density of the powder) and after a certain number of taps, the powder quantity stabilizes, giving the tapped density. The instrument used was the AutoTap (Quantachrome Instrument ©). The measurement was conducted in air and around 2000 taps were used for the volume of powder to stabilize, with the tapping rate at 250 taps per minute. Thus, according to the Hausner ratio classifications mentioned in ref [115], the powder flowability can be classified as excellent (1-1.1), good (1.12-1.18), and fair (1.19-1.25).

The Powder flowability results are summarized in **Table 3-4**. Higher avalanche angle indicates poor flowability. With an avalanche angle of 48.9° for the TLS and 68.2° for the Powder-2 batch, the TLS powder has relatively better flowability compared to Powder-2. The Hausner ratio analysis also indicates a similar trend of poor flowability for the Powder-2 batch. This poor flowability of the Powder-2 batch can be attributed to the high amount of moisture content. **This allowed us to select the TLS powder owing to its better flowability for performing powder layer experiments, which is reported in the next chapter. Chapter 4 is focused on performing process parameter optimization using the TLS powder to identify the stable melting conditions to fabricate 3D cubes by L-PBF. Similarly, the microstructural characterizations on the as-built cubes are also detailed.**

Table 3-4 Powder flowability of the two 6061 Al-alloy powders.

	TLS powder	Powder-2
Flowability (Avalanche angle)	 $48.9 \pm 5^\circ$	 $65.2 \pm 3^\circ$

Flowability (Hausner ratio)	Mass: 298 g Apparent volume: 249 ml Tapped volume: 219 ml Hausner ratio: 1.13 (Good)	Mass: 342 g Apparent volume: 245 ml Tapped volume: 195 ml Hausner ratio: 1.25 (Fair)
--	--	--

4. Process parameter optimization and microstructural observations

In this chapter, the stable processing parameter regime in L-PBF is identified based on elementary experiments consisting in laser single and multiple adjacent tracks on a powder bed. Moreover, the cracking pattern and its sensitivity to processing conditions are studied. The chapter hosts the study related to resolving the ambiguity related to the cracking mechanism occurring in 6061 Al-alloy during L-PBF. A detailed microstructural study of the as-built 6061 Al-alloy is also presented identifying the nature of second-phase particles and the key microstructural features in comparison to conventional manufacturing processes.

This chapter is divided into two parts: Process optimization and Microstructural characterization.

4.1. Process Optimization

Fabrication of Al-alloys by L-PBF has many challenges like high reflectivity and high thermal conductivity [5]. Al-alloys have a thermal conductivity of 167W/m-K compared to steel which has only 24.3 W/m-K [78]. In addition to that, Al-alloys require a lot of energy for melting (the high latent heat of fusion of 378 kJ/kg), compared to 272 kJ/kg (Fe) and 297 kJ/kg (Ni) [78]. This high energy density can cause evaporation of low boiling point elements like Zn and Mg, often creating gas porosities [116]. Moreover, Al-alloys have moisture absorption ability, for instance the solubility of H₂ in molten Al is almost ~20 times higher than in solid Al, which causes an increase in H₂ induced porosities [116]. Despite these issues, while processing Al-alloys, the Al-Si-Mg alloys (AlSi10Mg/AlSi7Mg) are easy to process by L-PBF compared to high strength Al-alloys (6xxx and 7xxx). The (AlSi10Mg/AlSi7Mg) alloys are frequently reported to be crack-free due to their high Si content, compared to the structural alloys like 6061 and 7075 during L-PBF [1,4,5]. Due to severe cracking in 6061 Al-alloy along with the challenges mentioned above, processing of 6061 alloy is a difficult task in Aluminum L-PBF industry.

4.1.1. Introduction

Process parameter optimization is done based on the stable fusion processing parameters identified on the bulk 6061 Al-alloy substrates and using the powder layer experiments, those will be used to fabricate 3D-cubes. In all the powder experiments, TLS powder was used. To identify the processing window for the 6061-alloy, which will ensure stable melting conditions, a bottom-up strategy was employed, as shown in **Figure 4-1**.

This bottom-up strategy employed in the present work will allow to:

- Identify the various regimes within the explored processing range: stable vs unstable fusion conditions (Unstable fusion due to high laser speeds and high energy density, or stable fusion) with single tracks on single and multiple powder layers.
- Investigate if the cracks can be mitigated by the variation of the first-order melting parameters like Power (P) and laser speed (v_{laser}).
- Validate our thermal calculations by comparing the melt pool size and morphology characterized experimentally with the one obtained through thermal calculations for various processing parameters (**Chapter 5**).

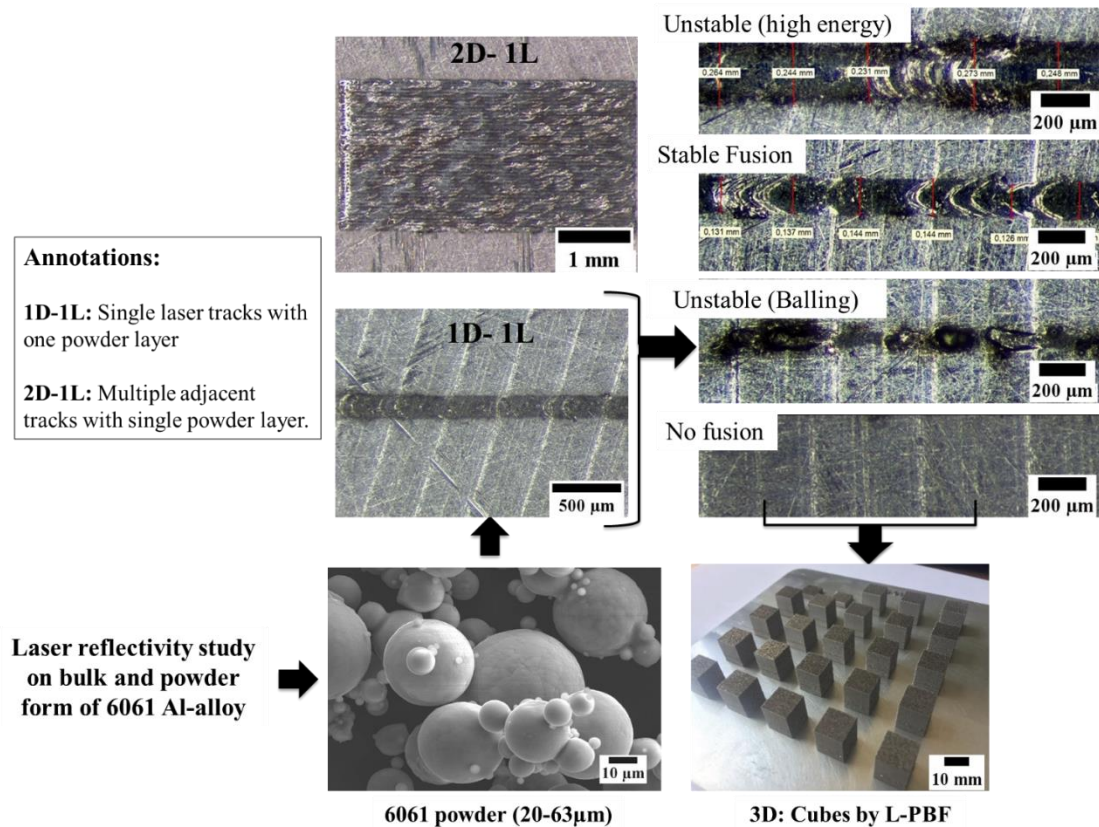


Figure 4-1 Experimental strategy employed to identify stable melting conditions.

This part of the Chapter is divided into the following subsections:

- i. **Laser reflectivity of the bulk substrate and powder:** the reflectivity of the two forms of 6061 Al-alloy used in the study (the bulk substrate and the powder) are investigated.
- ii. **Powder layer experiments:** Single tracks (1D) and multiple tracks (2D) with a single powder layer. L-PBF process involves layer-by-layer deposition of powder. This section also investigates the stability of the molten tracks at different intermediate levels (with several powder layers).
- iii. **Fabrication of 3D cubes by L-PBF:** Based on the identified regimes from the powder layer experiments, 3D cubes were fabricated. The behavior of these parameters on the cracking sensitivity and porosity during L-PBF is reported and an optimized parameter for best relative density is determined. Here the optimized parameters refer to the parameters leading to stable molten tracks that reduce the occurrence of lack-of-fusion defects and thus increase the relative density of the as-built samples. However “optimized parameters” do not necessarily mean that the samples were found to be crack-free.

4.1.2. Reflectivity of the bulk-substrate and the powder

Bulk 6061 Al-alloy in the as-machined state were produced by Impol Aluminum industries. The surface of the as-machined bulk substrate was very smooth ($R_a=1.2\mu\text{m}$). This caused issues related to high laser reflectivity, as already reported in ref [5]. The bulk substrate and the TLS powder were investigated for their laser reflectivity.

- **Methods used to measure reflectivity/surface roughness:**
 - i. **Reflectivity:** The total reflectivity analysis was performed on a Lambda 950 laser spectrophotometer (Perkin Elmer ©). For each measurement, three samples were analyzed. The bulk substrate samples were directly placed in the spectrophotometer, while the powder samples were placed in a quartz sample holder. For the case of the powder sample, the total reflectivity had contributions from the powder and the quartz sample holder. Thus to obtain the powder reflectivity alone, the pre-measured reflectivity of the quartz needed to be subtracted from the reflectivity measurements. For the bulk substrates, the obtained reflectivity was solely from the sample. The analysis range used was 250 to 1500 nm with a step size of 5 nm. The total reflectivity measured for a laser wavelength of 1064 nm was used for comparing the materials used in the study.
 - ii. **Roughness on bulk substrates:** The profilometry analysis was done with an infinite focus microscope (that measures the roughness) to monitor the variation in the roughness of the bulk substrates. The average roughness (R_a) was used for comparing different surface states of the bulk substrates.

- **Reflectivity comparison (bulk substrate and powder):**

The as-machined bulk substrate reflectivity as a function of wavelength is reported in **Figure 4-2** (blue curve). For the laser wavelength used in the present work (1064 nm), the as-machined bulk substrate reflectivity was around $\sim 80\%$. In other words, it means that only 20% of the energy input is absorbed by the materials. This suggests that the present surface state of the bulk substrate was highly reflective and needs to be roughened to achieve a better absorptivity since surface roughness can help to achieve a better absorption as reported in ref [1].

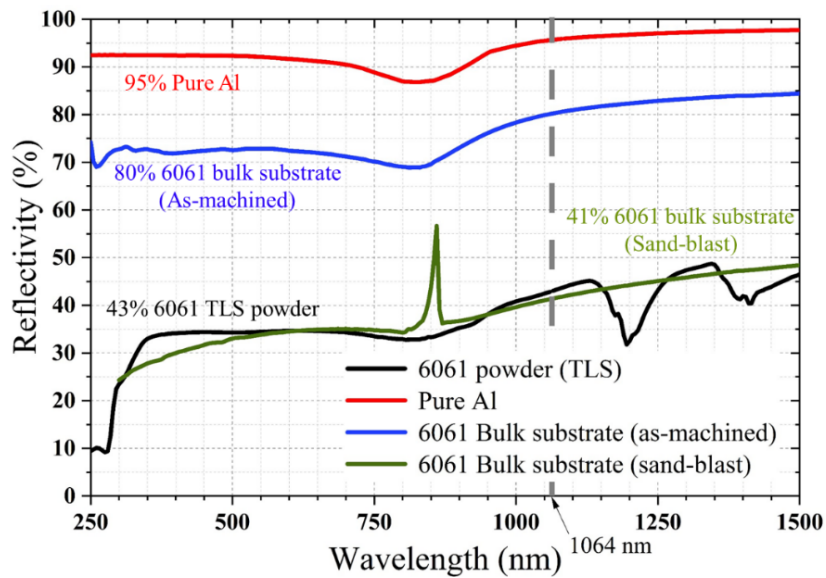


Figure 4-2 Reflectivity measured on the 6061 bulk substrates and the 6061 powder (TLS Technik) using the laser spectrophotometer. The reflectivity of pure Al is also shown for reference.

Another surface state of bulk substrate was analyzed, which was sand-blasted. The sandblasting was done using manual sandblast, which uses a stream of abrasive material to bombard the sample surface, making it rough. **Figure 4-3a)** shows the roughness measurements on the as-machined substrate. The Ra (average roughness) was around $1.2 \mu\text{m}$ before sandblasting and post sandblasting the Ra increased to $6.3 \mu\text{m}$, with 10-15 minutes of sandblasting (see **Figure 4-3b)**). The average roughness increased (~ 5 times) by sand blasting and this led to a decrease in reflectivity of the sand blast bulk substrate, refer to the green curve in **Figure 4-2**. The sand blast reflectivity was around 41%, around half the reflectivity obtained with the as-machined bulk substrate.

The 6061 Al-alloy powder (from TLS Technik manufacturer) used in the present study had $\sim 43\%$ reflectivity for the same laser wavelength (1064nm), refer to the black curve in **Figure 4-2**. The obtained total reflectivity for the powder ($\sim 43\%$) is almost half the reflectivity obtained for the as-machined bulk substrates ($\sim 80\%$). Moreover, the powder reflectivity shows a similar profile for reflectivity when the surface state of the bulk substrate is sand-blasted with a roughness of $Ra=6.3 \mu\text{m}$. These results are also compared with the pure Aluminum reflectivity profile, adapted from Tissot *et al.* [117]. Compared to the pure Al reflectivity of 95%, the 6061 powder had comparatively low reflectivity ($\sim 43\%$), but still, this was higher compared to reflectivities encountered in powders made of other alloys (Ti-6Al-4V: 26%, 316L: 30%) [118].

To summarize, the as-received powder showed better absorptivity compared to the as-machined bulk substrate. This suggests that, it is better to utilize the powder in comparison to the bulk-substrate for the process parameter optimization. Moreover, studies dealing with the utilization of powders can represent the actual L-PBF process in comparison to the bulk-substrate experiments. This helped us to

concentrate the process optimization studies using the as-received powder, and the results will be presented in upcoming sections. Preliminary process parameter optimization performed on the bulk substrates (1D-2D) experiments are reported in **Appendix**. The latter ones were interesting but not very representative of the L-PBF process.

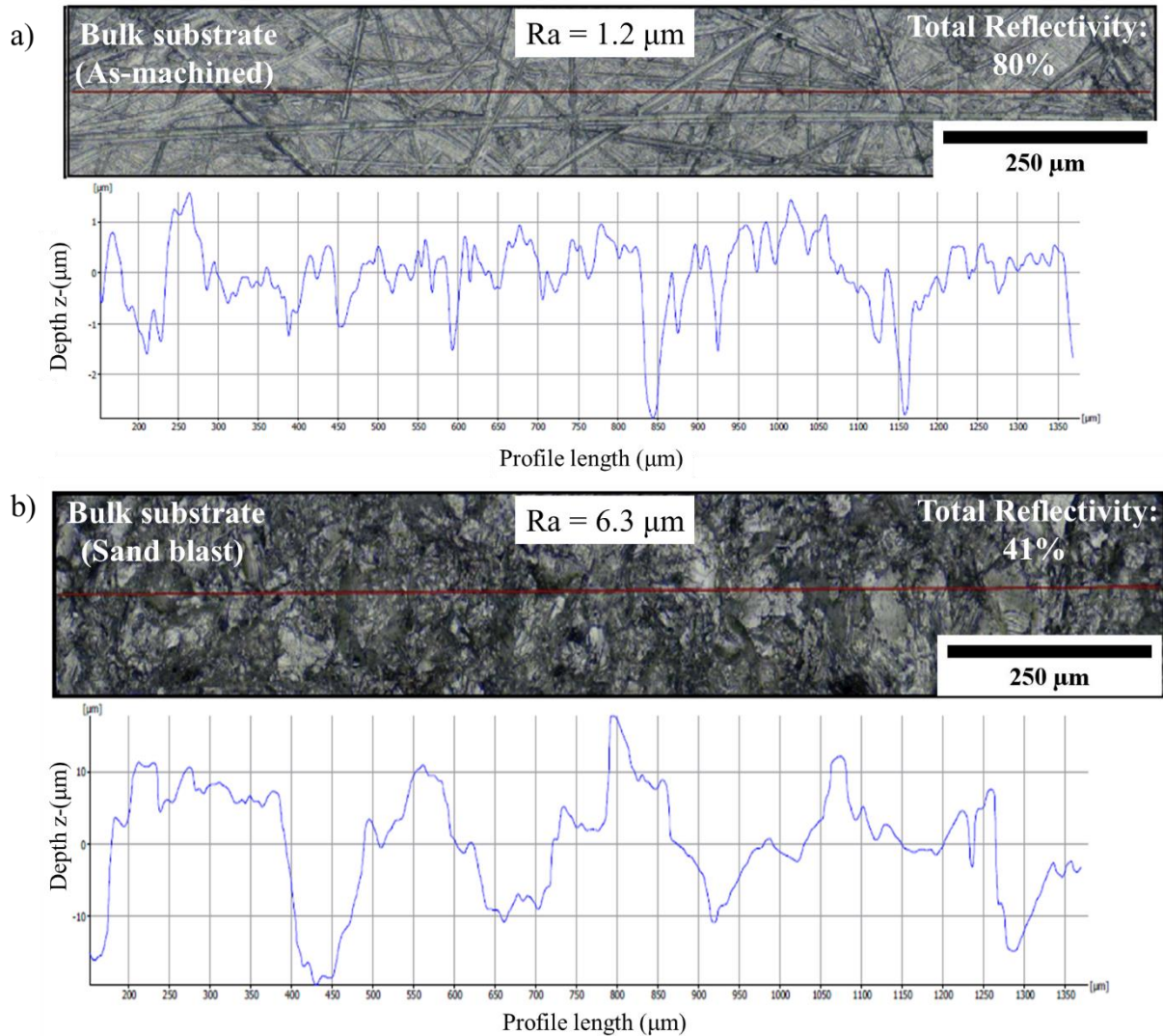


Figure 4-3 Profilometry analysis to measure the mean roughness of the a) as-machined bulk substrate and b) sand-blasted bulk substrate.

4.1.3. Elementary powder layer experiments

Several experiments using the actual 6061 powder (20-65μm) from TLS Technik were carried out to determine the stable processing window. The TLS powder was preferred to perform experiments because of its good flow nature. Experiments dealing with single-tracks on a single powder layer (1D-1L), multiple

adjacent tracks on a single powder layer (2D-1L), and multiple tracks on five powder layers (2D-5L) were performed to evaluate the effect of laser speed and power on the stability of the tracks during laser scanning while the laser spot size was kept constant and equal to 70 μm . By these experiments, just with a single or several powder layers, stable processing regime without the evidence of discontinuity in melting can be identified. Such a strategy helps saving time and amount of powder consumed to fabricate the 3D L-PBF samples.

- **1D experiment: Single tracks on a single powder layer (1D-1L)**

A ProX 200 L-PBF machine from 3D Systems (see **Figure 4-4**) was used to perform laser scanning experiments on the powder layers for process optimization and consequently to fabricate 3D cubes. The machine incorporates a Fiber laser operating at a near-infrared spectrum ($\lambda=1064\text{ nm}$). With the ProX 200 machine, the maximum laser power (P) was about 274W. The laser power was varied from 10% (27.4W) to 100% (274W). The laser speed (v_{laser}) was varied from 200 mm/s to 2200 mm/s. The laser spot size was kept constant to 70 μm . To estimate the density of energy received by the powders as a function of processing parameters, the linear energy density defined as $E_L = P/v_{laser}$ was used.



Figure 4-4 ProX 200 L-PBF machine from 3D systems [119].

Figure 4-5 shows the top view of the 1D tracks scanned on a single powder layer. Three sets of power (137W, 219W, and 274W) are shown with the laser speed varying from 200 mm/s to 2200mm/s. Based on the top view images displayed in **Figure 4-5**, stable (continuous) laser tracks and unstable laser tracks (discontinuous) are identified. The stable continuous tracks were observed for $P=219/274\text{W}$ from 1100-2000 mm/s.

Similarly, according to **Figure 4-5**, the unstable tracks were classified into two different categories: (i) unstable tracks due to high energy density and (ii) unstable tracks due to low energy density. The instability

occurring due to high energy density is referred to the condition of the melt pool track that appears to be uneven due to an excessive heat input. This can occur due to intense convective flows caused by a high energy input, which increases the recoil pressure in comparison to the surface tension and hydrostatic pressure of liquid metal [76]. This kind of high energy instability was observed mainly for smaller laser speeds (<1000 mm/s) and high powers (>210 W). To identify the difference between the unstable (high energy) and the stable molten tracks, please refer to the yellow and green regions highlighted in **Figure 4-5**.

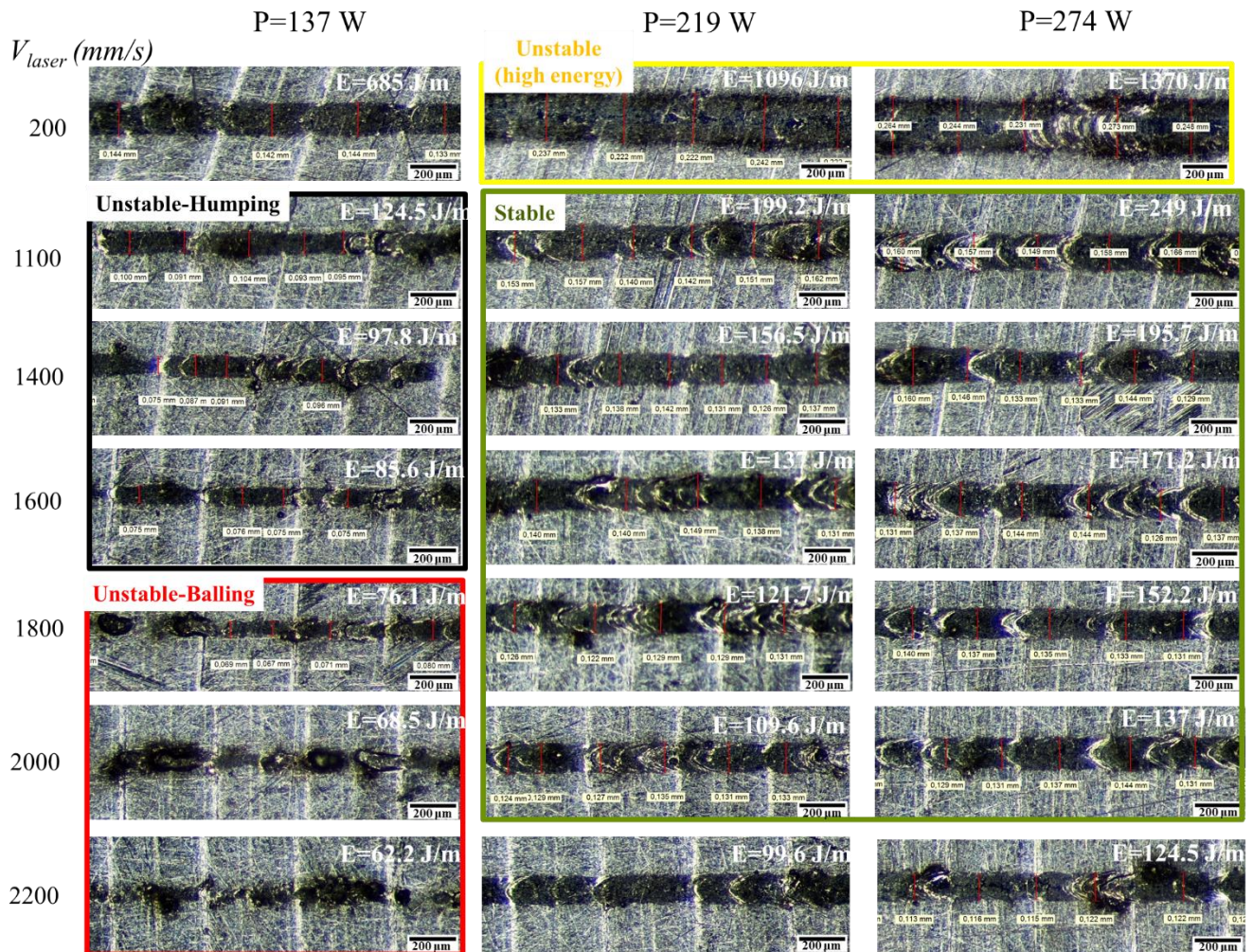


Figure 4-5 Single tracks for various processing parameters carried out on a single powder layer.

Instability of laser tracks can also occur due to very low energy density. For the low power of 137W, humping (v_{laser} in the range of 1100-1600mm/s) and balling (v_{laser} in the range of 1800-2200mm/s) was observed. The optimum laser speeds at which a stable track can convert into an unstable track thus needs to be identified. Although high laser speeds mean less time for fabrication, they have some drawbacks. Higher speeds can often cause lowering of the melt pool temperature and increase in melt viscosity of the liquid metal making it difficult to flow and giving rise to lack-of-fusion defects between layers. According to DebRoy *et al.* [120], when the laser speed increases, the melt pool length often

increases creating elongated melt pools along its length. This situation might create the breaking of melt pools into various smaller regions, which causes discontinuity. These discontinuities are often qualified as humping and balling.

- **Humping:** Humping usually occurs at high laser speeds (1100-1600mm/s). The top view morphology is often classified as broken beads having open unfilled spots, as shown in **Figure 4-6**. The mechanism of its occurrence is majorly due to the hydrodynamic instability caused by the difference in buoyancy force to shear force at the surface of melt pools [120]. The black highlighted region of **Figure 4-5** shows the typical humps/broken beads formed in the present study.
- **Balling:** At even higher-speeds (1800-2200mm/s), balling can occur. Compared to instability like humping, the mechanism of occurrence of balling is slightly different. During high speeds, the melt pool becomes elongated along its length and starts to separate from the tracks in the form of the spherical balls to maintain the minimum capillary pressure inside the melt pools (see **Figure 4-6**). The maximum allowable length of melt pool above which balling can occur is based on the Plateau-Raleigh capillary instability criterion: $L/w > \pi$ (where L and w are the length and width of melt pool) [120]. The red highlighted region of **Figure 4-5** shows the typical laser tracks of balling phenomena occurring in the present study.

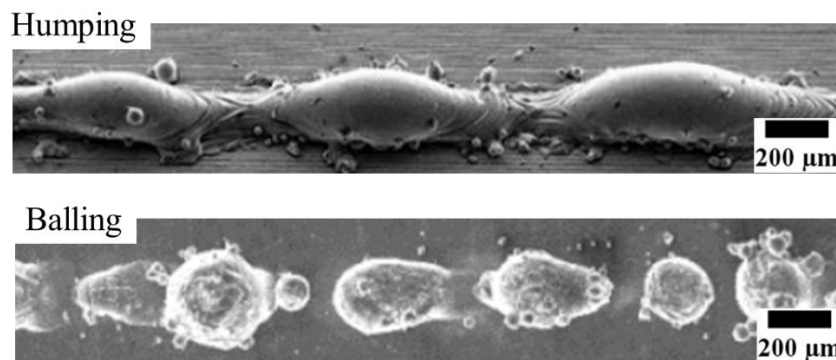


Figure 4-6 Single tracks showing the typical signature of humping and balling, adapted from [12,121].

To understand the limit at which balling or humping occurs using the Plateau Raleigh capillary instability criterion for the case of 6061 Al-alloy powders, dimensional analysis of the melt pool tracks was performed over the studied range of parameters. As shown in **Figure 4-7a) &b)**, the average melt pool widths (w) and lengths (L) were estimated (based on the top view of melt pools in **Figure 4-5**) as a function of linear energy density. The increase in melt pool width is expected as a function of linear energy density, as shown in **Figure 4-7a)**. However, the length of the melt pool (shown in **Figure 4-7b)**) shows a decreasing behavior when the input energy density increases. This is because as the laser speed increases (i.e. lower energy density), the melt pool tends to be elongated along its length, making its length to increase for low E_L .

With the help of these dimensions (widths and lengths), their ratio can be used to identify the critical point at which balling/humping can occur. As shown in **Figure 4-7c**), the length/width ratio is calculated for various energy densities. The L/w ratio curve shows a rectangular hyperbola. For $E_L < 200$ J/m, the L/w ratio shows a rapid increase. Whereas for higher energy densities, the L/w ratio stabilizes around 0.75-1 value. **The transition point at which the identified parameter starts to show characteristics of balling/humping, corresponds to a L/w ratio approaching a value of 3.** Thus, in the present study, we are quite close to the value predicted by the Plateau Raleigh capillary instability criterion ($L/w > \pi$). **Figure 4-7d**) shows the identified top view of the single tracks for the selected L/w ratio in **Figure 4-7c**). The stable region is shown in green square for a L/w ratio of 0.7, whereas, humping and balling tracks are identified for a L/w ratio of 3.1 and 4.25, respectively. Thus, based on the L/w ratio analysis for the 6061 Al-alloy powder, it suggests that to be in the stable region and avoid humping/balling, the L/w must be kept < 3 . For the unclassified parameters in **Figure 4-5**, $v_{laser} > 2000$ mm/s and $P = 219/274$ W, premature signs of humping behavior can be observed, which is less severe compared to the humping region observed for low power of 137W. According to DebRoy *et al.* [120] the occurrence of humping is even possible at high powers when the laser speed is sufficiently high enough.

Finally, a processing map is generated to identify the different regimes based on laser power and speeds. As shown in **Figure 4-8a**), the processing parameter map allows different regimes to be identified, namely: unstable due to high energy (yellow), stable fusion (green), unstable due to humping/balling (black) and no fusion (red). No fusion/unfused refers to the laser tracks that did not absorb enough input energy to melt the material. The x-axis shows the studied laser speed range in *mm/s* and the y-axis shows the laser power in W. **Figure 4-8b**) shows the typical forms of the identified regimes from the top (XY plane).

Out of the studied parameters, the single track analysis on one powder layer shows that the stable continuous tracks were observed for the green zone marked in **Figure 4-8a**). This regime corresponds to the $P > 164$ W with speeds ranging from 500-2000 mm/s. Instabilities due to high energy density were observed for $P > 220$ W and low scanning speeds, around 400-700 mm/s. Moreover, parameters with low power ($P < 135$ W) were repeatedly found to be having unfused tracks. In addition to the observed regimes, balling/humping regimes were classified for process parameters having laser speeds > 1500 mm/s (as highlighted in black in **Figure 4-8a**)). **This indicates that to avoid the balling/humping phenomena, the laser speeds must be kept lower than 1500 mm/s, which will ensure the L/w ratio of the melt pool < 3 .** It must be noted that this critical speed of 1500mm/s is identified for a $P = 150$ W. As Power increases, this critical speed also shifts to a higher value (see **Figure 4-8a**)), this is due to an increase in energy density that will increase the tolerance towards the L/w ratio.

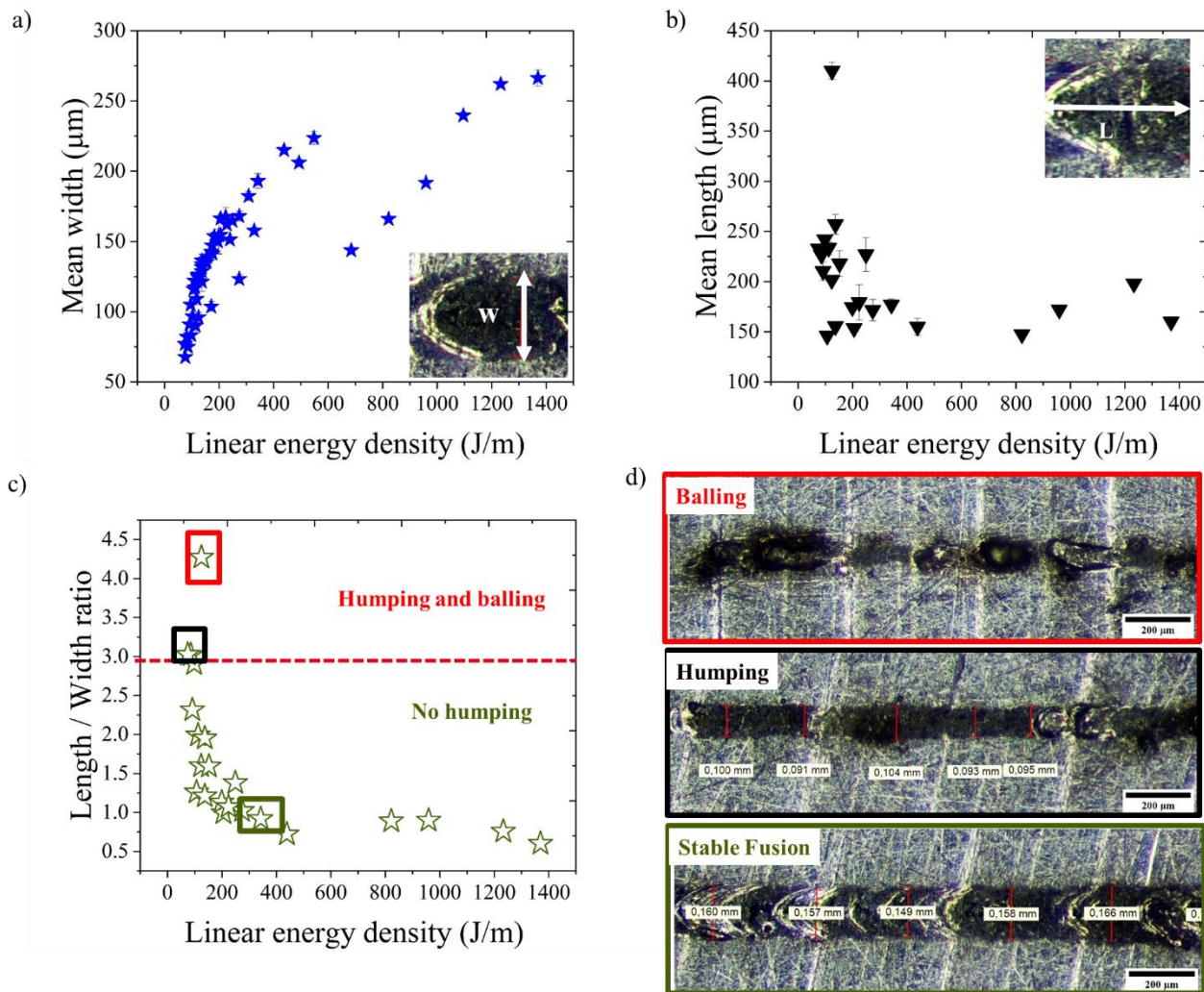


Figure 4-7 Analysis of single tracks to identify the criterion for humping/balling. a) Melt pool width, b) Melt pool length, c) Length/Width ratio, and d) Top view of the single tracks for the parameters marked in figure c).

To summarize, a stable melt pool track regime was identified based on the stability map shown in **Figure 4-8** and also based on the L/w ratio analysis of **Figure 4-7**. In comparison to the bulk substrate analysis reported in **Appendix A**, the powder layer experiment goes a step further in identifying a stable regime without the occurrence of balling and humping, which were not identified in bulk substrate experiments (basically due to the absence of powder particles used in the bulk substrate experiments). The stable regimes from the bulk substrate experiments (sand blast, $R_a = 6.3 \mu\text{m}$) are quite similar to the ones found with the powder experiments, probably due to the similar reflectivity profiles for the powder and the bulk substrates (sand-blast), see **Figure 4-2**. Moreover, the minimum power required to not have lack-of-fusion tracks was around 137W for the powder layer experiment, whereas for the bulk substrates (as-machined, $R_a 1.2\mu\text{m}$) it was $\sim P=200\text{W}$. This was majorly due to the high reflectivity in the case of the as-machined bulk substrate (refer to **Figure 4-2**).

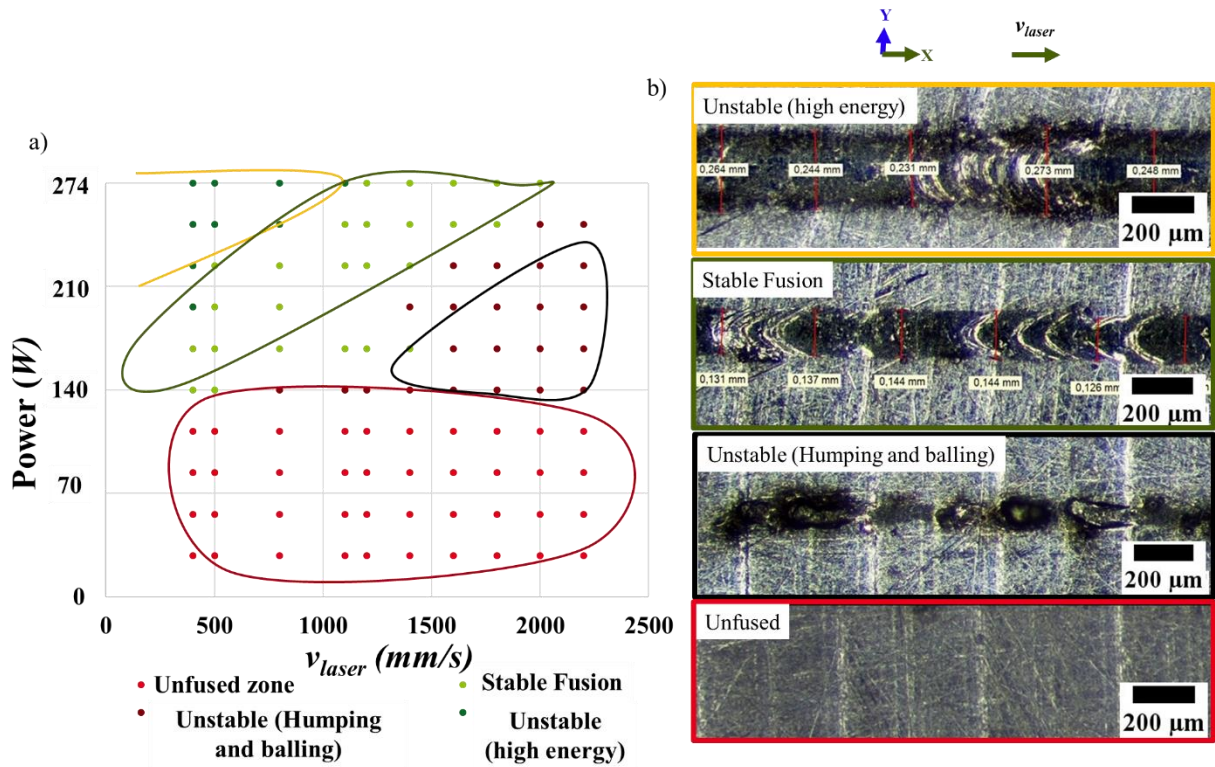


Figure 4-8 a) Processing map for the single tracks experiments performed on a single powder layer. b) Observation of typical regimes identified in the processing map.

The measured melt pool widths across the studied parameters during the single track analysis with powder can also be compared to the melt pool widths obtained with bulk substrates. **Figure 4-9** shows the measured melt pool widths across the different forms of 6061 Al-alloy. For the case of a single powder layer, the measured melt pool widths show an increase with increasing energy density. A similar trend is observed for the bulk substrates (sand-blasted). Moreover, there is not a huge difference in the measured melt pool widths between the powder tracks and the tracks performed on the bulk substrate (sand-blasted), majorly due to similar laser reflectivity (**Figure 4-2**). On the other hand, the bulk substrates (as-machined), which were not sand-blasted show quite small melt pools due to lack of laser absorption, as they had a higher reflectivity ($\sim 80\%$) compared to the powder ($\sim 43\%$). This comparison shows that the bulk substrate (sand-blasted) melt pools can be considered as a representative of the actual melt pool tracks observed with the powder layer experiment. In **Figure 4-9**, only the width of the melt pools were compared, however, to get a full picture of the melt pool dimensions, measurement of the depth is also desirable. This comparison was just to have an idea about the use of bulk substrate melt pool dimensions, to where they are when considering actual powder tracks dimensions. This will also help to use the bulk substrate melt pool dimensions in updating the thermal simulations done as a part of the present study that will be presented in **Chapter 5**.

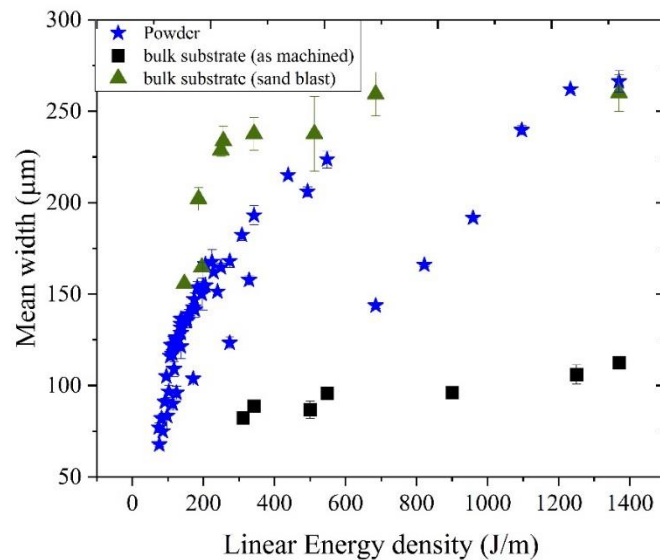


Figure 4-9 Comparison of mean width's for different lasing conditions: powder, rough bulk substrate (sandblast, $R_a = 6.3\mu\text{m}$), and bulk substrate (as-machined, $R_a = 1.2\mu\text{m}$).

- **2D experiments: Multiple adjacent tracks on a single powder later (2D-1L) and five powder layers (2D-5L)**

Until now, with the single laser tracks on a single powder layer, the stable regime of parameters was identified, which was also quite similar to the one identified with the bulk substrate experiments when using a sand-blasted substrate (shown in **Appendix**). This section focuses on scanning multiple adjacent tracks on a single powder layer and the motivation behind such experiment is to go a step closer to the actual 2D scans and identify the regions of stability based on the top view of the laser tracks. This will help us to understand, how the stability regime is affected when multiple tracks are scanned compared to the single track experiments.

A 2D region of $5 \times 3\text{ mm}^2$ was used to study the effect of multiple adjacent laser tracks on the powder layer. Similarly, the same first order process parameters were used from the 1D-1L experiment ($P: 27\text{ W}$ - 274 W and $v_{laser}: 200\text{-}2200\text{ mm/s}$) with the spot size kept constant to $70\mu\text{m}$ and a layer thickness of $20\mu\text{m}$. Multiple adjacent tracks with a hatch spacing of $100\mu\text{m}$ were found to possess stable melting conditions compared to a hatch spacing of $50\mu\text{m}$. This behavior was identical to the ones observed in bulk substrate experiments, where a $50\mu\text{m}$ hatch spacing caused a similar unstable molten tracks (due to high energy), based on top view observations. With smaller hatch spacing of $50\mu\text{m}$, the overlap between neighboring melt pools was more and resulted in the agitation of molten tracks making it unstable. Thus, all the multiple

tracks experiments carried out on the powder layer (2D-1L and 2D-5L) were done with a higher hatch spacing of 100 μm .

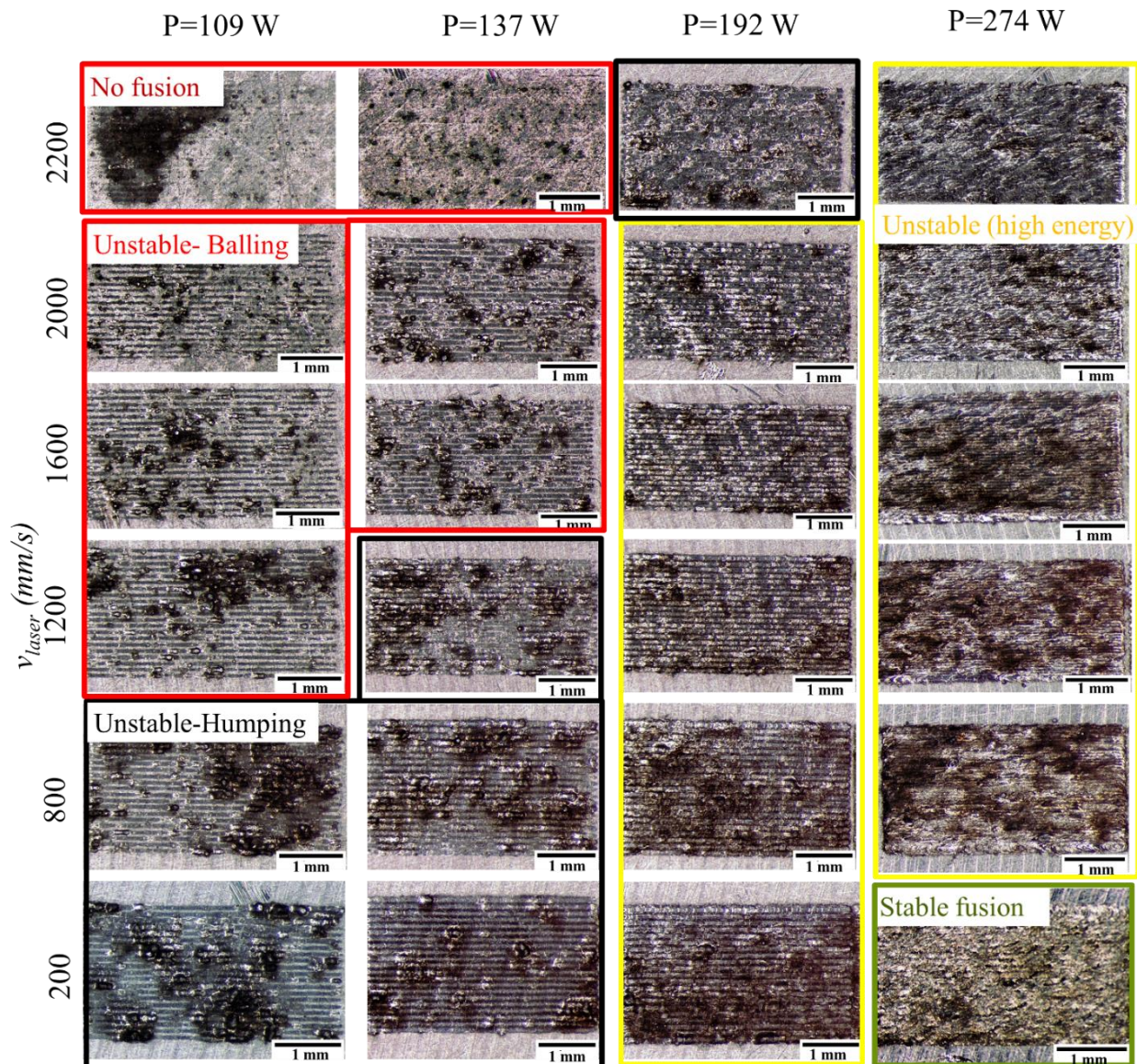


Figure 4-10 Top views of the 2D region scanned with multiple adjacent tracks on a single powder layer.

With a 100 μm hatch spacing, the top view of the 2D tracks for various parameters can be visualized in **Figure 4-10**. The combination of low powers (109W and 137W) and high laser speeds 2200 mm/s was found to have no fusion (laser tracks hardly visible). Similarly, for these powers and laser speeds 1200-2000 mm/s (balling) and 200-1200 mm/s (humping) were also observed. Balling can be identified by the red highlighted region where molten tracks are discontinuous, whereas humping is associated with broken beads highlighted by black regions, in **Figure 4-10**. This is in correlation with the single track experiments (1D-1L) where for 137 W, throughout the range of laser speeds balling/humping was detected, as shown in **Figure 4-5**. Similarly, in **Figure 4-10** for P=192W, the evidence of humping was observed for high laser speed 2200 mm/s, similar to the single track experiment where humping was observed even at high powers. For the maximum power of 274W, unstable multiple tracks caused by high energy input were

observed in the laser speed range (800-2200 mm/s), with few instances showing stable continuous molten tracks for low laser speeds (<800 mm/s).

Similar to the single-track experiments, a stability map (**Figure 4-11**) of multiple tracks on a single powder layer for various processing parameters were established. Note that the boundaries between various regimes are not accurately determined since for few parameters, classification was difficult. In comparison with the single-track laser scans on the powder layer of **Figure 4-8**, the stable tracks process parameters with multiple laser tracks in **Figure 4-11** have shifted to higher laser power and lower laser speeds. This is probably due to the inter-track consolidation behavior caused by the multiple adjacent tracks for a given hatch spacing of 100 μm . For example, for a single track, the stability of the track was considered just based on one single track, however, when considering a 2D region for its stability, the inter-track consolidation behavior and the denudation zone (powder free zone ahead of melt pool due to spattering [120]) can also play a role in determining the melt pool stability. For instance, consider the top view images in **Figure 4-10** for a $v_{laser}=200\text{mm/s}$. As power increases from 109W to 274W, the spacing between the tracks starts to disappear, indicating better consolidation. Thus, a higher energy density might be required to form a stable 2D region in addition to forming a stable 1D track. This explains why the region of stability shifted to higher powers and lower speeds for the case of 2D multiple tracks on a powder layer. The stable fusion parameters (highlighted in 'green') were restricted to lower laser speeds ($v_{laser}<800$ mm/s) for $P>233\text{W}$. Similarly, in **Figure 4-11**, the instability occurring due to the high energy was identified for higher powers ($>250\text{W}$) and higher speed ($>1000\text{mm/s}$) contrary to what was identified at low laser speeds during the single-track experiments. This is probably due to improper overlapping between the neighboring tracks at high laser speeds. When speed is low, even though it is high energy, the inter-layer overlapping for the 2D tracks makes the instability disappear. This explains why the unstable (high energy) region was identified for high powers and high speeds for the multiple tracks. For $109\text{W}<P<219\text{W}$ and $v_{laser}>1000$ mm/s, balling/humping was typically predominant, as highlighted in 'black' of **Figure 4-11**. As power decreases below 109W, unfused tracks starts to become predominant, similar to what was observed in the work done by Olakanmi *et al.* [122] on Al-Si process optimizations during L-PBF.

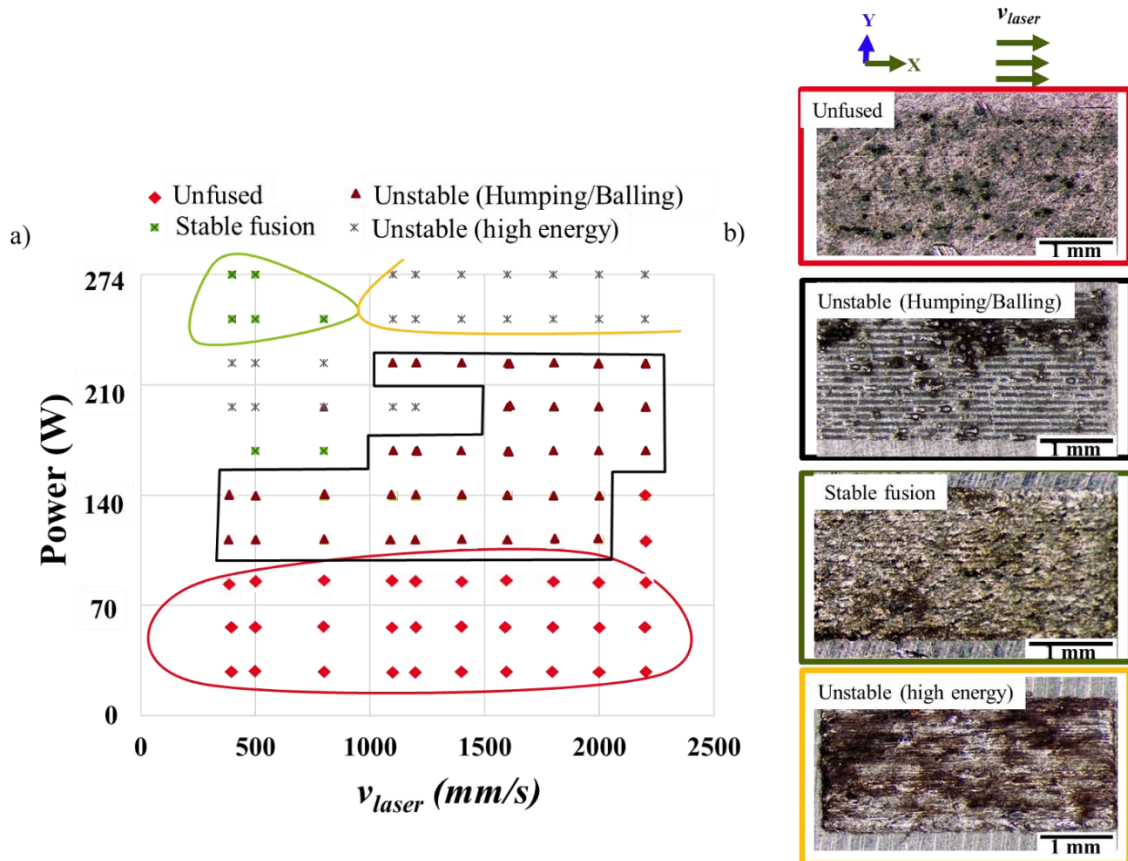


Figure 4-11 a) Processing map for the 2D multiple tracks on a single powder layer. b) Observation of typical regimes identified in the processing map.

Moving further with the analysis to identify the fusion parameters, 2D laser scanning on five powder layers were also performed. With the same process parameters as in the 2D tracks on a single powder layer, the motivation to understand how the regimes of stability are affected by the layer-by-layer powder deposition technique. In this experiment, multiple laser tracks were performed after each layer deposition to mimic the actual L-PBF process. The final stability regimes were identified after examining the top surface laser tracks on the last powder layer. **Figure 4-12** shows the stability map for the processing conditions yielding the stable continuous fusion after five layers of powder deposition and subsequent laser scanning. Compared to the 2D-1L experiment, the stable fusion zone for five powder layer 2D tracks was identified with some flexibility in the laser speed range. With a single powder layer, the stable fusion was identified for small laser speeds (<800 mm/s), whereas, with the successive scanning on five powder layers the speed range for stable tracks has widened up to 1200 mm/s. This tolerance of the laser speed is probably due to the inter-layer consolidation of the powder layers, achieved with the five powder layers deposited on top of each other. Another consequence of this possible inter-layer consolidation with five powder layer deposition was the humping/balling region was reduced and restricted to $109\text{W} < P < 160\text{W}$, in comparison to single powder layer 2D tracks where balling was also observed for higher powers up to 219W. These

observations suggest that, stacking of powder layer on top of each other can be beneficial to heal some of defects.

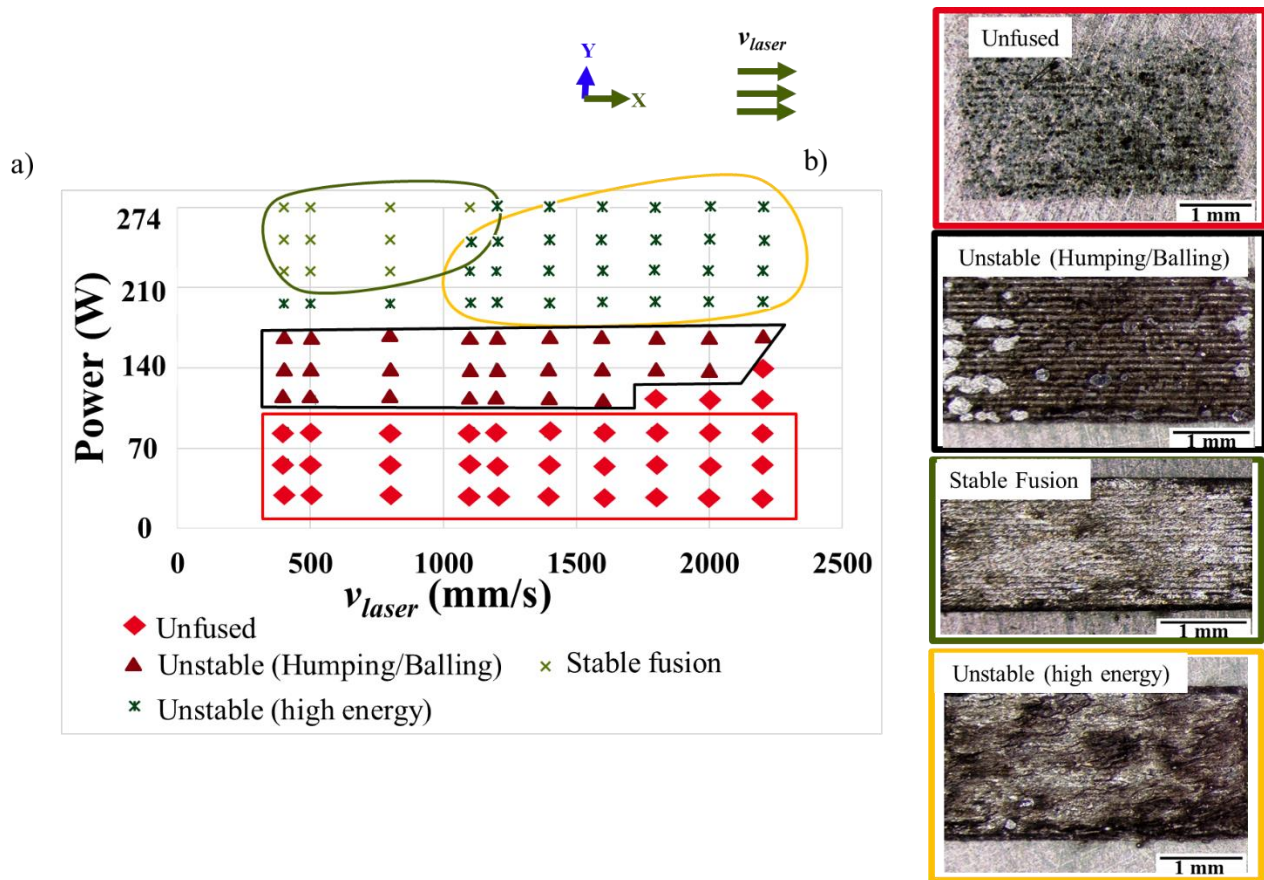


Figure 4-12 a) Processing map for the 2D multiple tracks on five successive powder layers. b) Observation of typical regimes identified in the processing map.

After five rounds of powder deposition and subsequent laser scanning, the stable fusion parameters were identified for $P > 210$ W, $400 < v_{laser} < 1200$ mm/s, hatch: $100\mu\text{m}$, layer thickness: $20\mu\text{m}$ and spot size: $70\mu\text{m}$. The identified laser speed range for the stable fusion was similar to the ones reported by Uddin *et al.* [3] (v_{laser} : 500-1400 mm/s), but they used a wider power range (150-500W). Similarly, Olakanmi *et al.* [122] and Louvis *et al.* [55] proposed to use high powers > 150 W to have better consolidation behavior of the 6061 Al-alloy, since with their processing parameters (P : 50-150W, v_{laser} : 80-420 mm/s and hatch spacing $> 300\mu\text{m}$) problems related to delamination and a low relative density $\sim 88\%$ were reported. Thus, the identified stable parameters in the present study are far away from the parameters causing delamination and lack-of-fusion defects such as reported in the study of Louvis *et al.* [55].

Moreover, by using laser speeds less than 1200 mm/s, we are also sure that single track balling/humping will not occur. Since in 1D-1L experiments we saw that L/w ratio < 3 for laser speeds less than 1500 mm/s. Since these several layer deposition and subsequent laser scanning experiments are thought to be

very close to the actual L-PBF process, the identified stable parameters were then selected to fabricate cubes using L-PBF. These results will be presented in the upcoming sections.

Moreover, in all the powder layer/bulk substrate experiments, cracking was always observed (except for the parameters that did not lead to fusion), see **Figure 4-13**. **Figure 4-13a)** and **b)** show evidence of cracking inside the melt pool cross-sections of the bulk substrates. For more details, refer to **Appendix**. The work done on bulk substrate also suggests that over the investigated range of process parameters (P : 180-274W, v_{laser} : 200-1400 mm/s), cracking cannot be avoided but rather crack density was found to decrease as a function of increasing energy density (see **Figure A-7c)**). For the powder layer experiments, **Figure 4-13c)** and **d)** show the typical cracking location from the top view. Cracks are systematically located in the center of the laser tracks, following the laser scanning direction, similar to the ones reported in the welding literature [97].

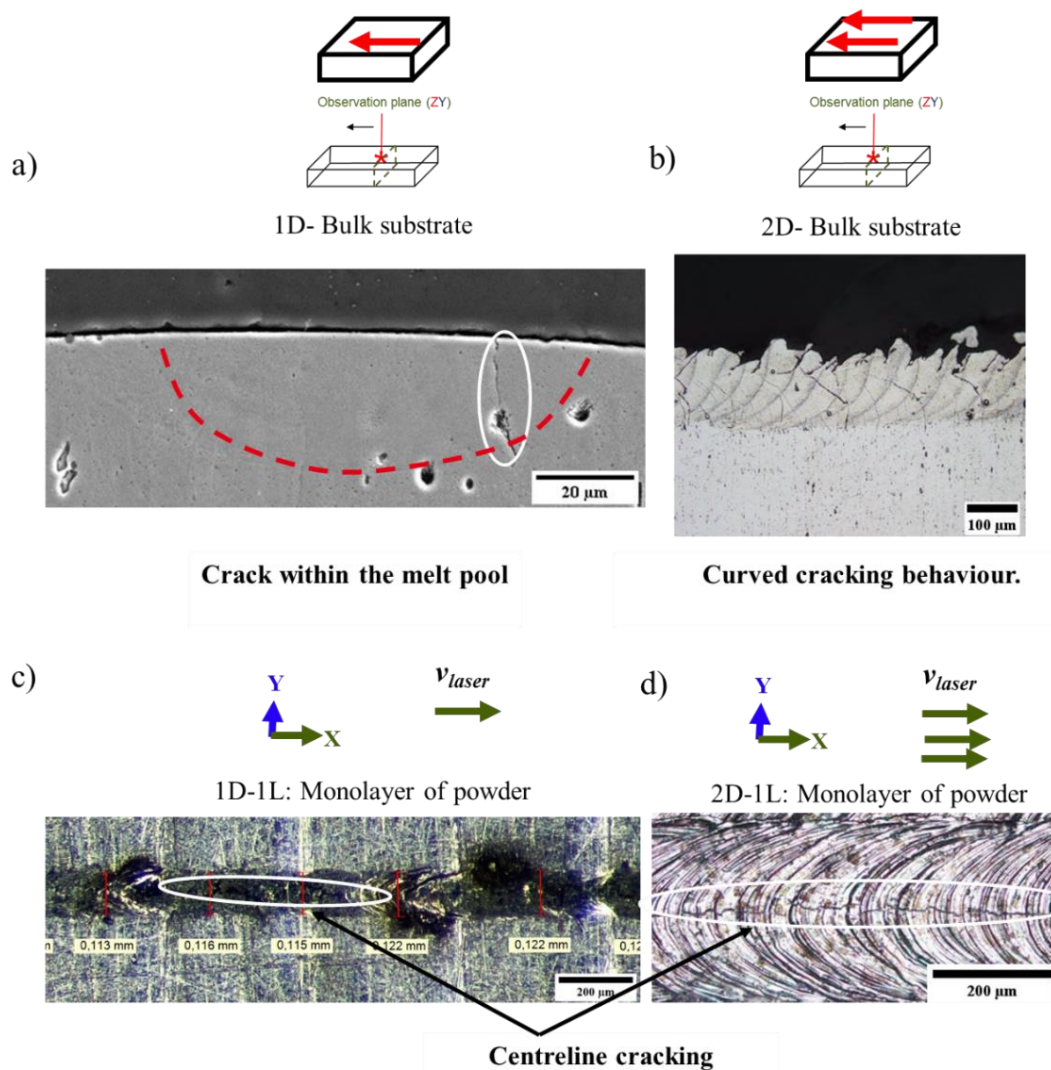


Figure 4-13 Cracking observation in a) 1D-bulk substrate, b) 2D-bulk substrate, c) Single tracks on a single powder layer, d) multiple tracks on a powder layer.

4.1.4. Fabrication of 3D cubes by L-PBF.

The powder experiments allowed us to quantify the length/width ratio of the melt pool to identify instabilities such as humping and balling. Similarly, stable continuous process parameters on single and multiple powder layers were also identified. These experiments played a major role in identifying the stable regime of parameters to fabricate L-PBF cubes.

- **Processing parameters:**

From the stable fusion process parameters from the elementary powder layer experiments, the final processing parameters for the L-PBF experiments were selected. **The final 3D cubes (10mm x 10mm x 10mm) were fabricated with parameters ranging from (P: 164W-274W and v_{laser} : 400-1400 mm/s) with a hatch spacing of 100 μ m, a layer thickness of 20 μ m and a laser spot size of 70 μ m, kept constant.** Although the identified stable parameters suggested by powder experiments were ($P > 210$ W and v_{laser} : 400-1200 mm/s), the final parameters of 3D cubes were fabricated with some tolerance. For example, the speeds were restricted to less 1500mm/s to avoid balling/humping, the power was kept above 164W since below that lack of fusion (unfused regions) were identified and also Olakanmi *et al.* [122] suggested to keep power greater than 150W. Similarly, a simple parallel scan strategy without rotation between layers was chosen as shown in **Figure 4-14**, to obtain ‘simple’ microstructures that can be easily interpreted without having influence due to scanning strategy. A simple microstructure can be just an epitaxially grown columnar grains. Thus, without the rotation between the layers, a simple strategy will be helpful to observe the melt pools and interpret the microstructure, in comparison to the strategies consisting of melting islands with 67° of rotation between layers.

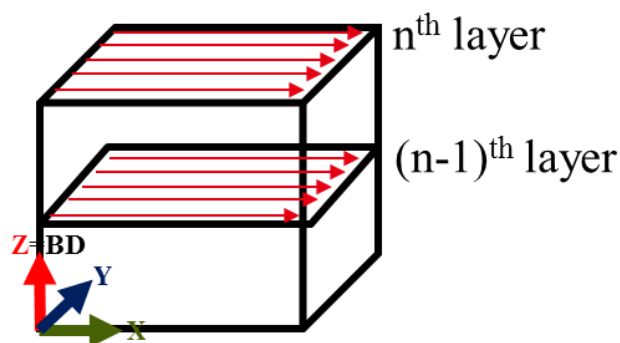


Figure 4-14 Parallel scanning strategy without rotation between layers used to fabricate L-PBF cubes.

- **Experimental procedures to characterize 3D cubes:**
 - i. **Estimating the relative density:** The relative density for the 3D cubes was estimated using the Archimedes principle according to ASTM B311-13. Polished samples were used for the measurement. The density of the cubes was performed using a YDK01LP density measurement kit and a LA310S balance (Sartorius ©) having a precision of 0.001g. The measurement consists of taking two consecutive weighing's: the first consists of taking the mass of the dry sample, then in immersion in a liquid. The liquid used for this measurement can be water, ethanol, or isopropanol. In our case, we used ethanol. The density of the liquid was checked by regularly measuring the mass of standard quartz (around every 20-25 min). The liquid was placed at the point of measurement one hour before at least so that it is at room temperature. Each mass measurement was performed 3 times to be able to give an average value of the density of the as-built samples. The density of the sample was estimated using $Density = (M_a \cdot D_{liquid}) / (M_a - M_{liquid})$, where M_a is the weight of the sample in air, D_{liquid} is the density of the liquid (at room temperature) and M_{liquid} is the weight of the sample submerged in the liquid. Finally, the relative density was obtained by dividing the obtained density by the reported density (2.7 g/cm^3) of the 6061 Al-alloy in ref. [3].
 - ii. **Quantifying cracking density/porosity:** To measure the crack density on the 3D cubes, polished cross-sections were used to be able to detect cracks. The crack density was estimated using ImageJ software in an area of $\sim 2.7 \text{ mm}^2$ in four different locations of the YZ planes (along the building direction, Z). This allowed us to estimate the average number of cracks per mm^2 for samples with different processing conditions. This method was selected to quantify cracks as it was frequently used in refs. [71,73]. Similarly, for the porosity estimation, ImageJ software was used. The polished micrographs of samples were converted to a binary image to which thresholding was used to identify the pores. In this way, porosity in an area of 2.7 mm^2 and its size distribution could also be estimated.

- **3D cubes fabrication: results and discussion**

All the 3D cubes were fabricated without any technological issues, except for the high energy density cubes having $v_{laser} < 600 \text{ mm/s}$. The high energy density cubes (marked in red, in **Figure 4-15a**) were not completely fabricated. Due to the high energy input of the laser, the powder spreader was occasionally blocked by the solidifying alloy during fabrication, as shown in **Figure 4-15b**). Thus, the analysis of the cubes was restricted to only parameters ranging from P: 164-274W and v_{laser} : 600-1400 mm/s.

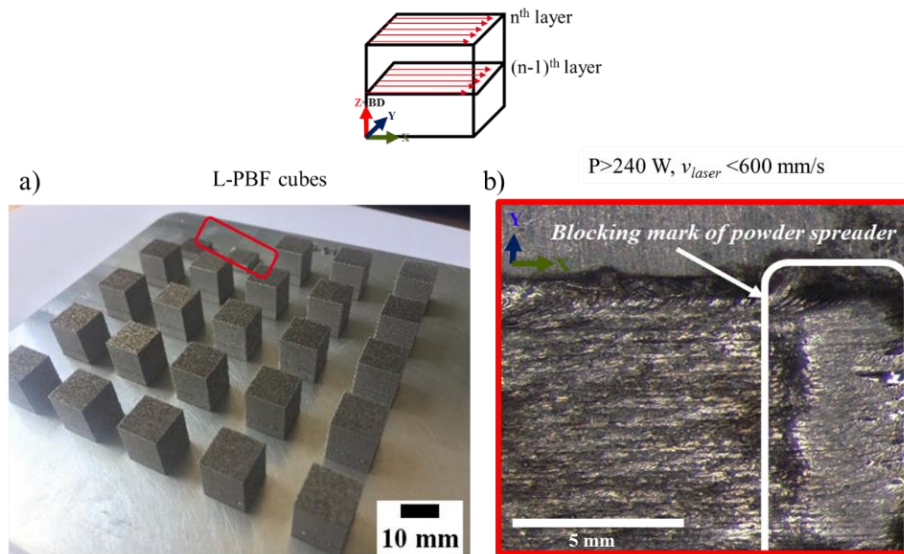


Figure 4-15 a) 6061 Al-alloy cubes made using L-PBF. b) Surface state of unfinished cube due to blocking of powder spreader, when excessive energy input is used ($E_L > 400 \text{ J/m}$)

As shown in **Figure 4-16a**), the relative density of the fabricated cubes was estimated using the Archimedes method. The as-built cubes showed an increase in relative density when increasing the laser linear energy density. **The maximum relative density achieved was 98.5% for $E_L = 400 \text{ J/m}$ ($P = 240 \text{ W}$, $v_{laser} = 600 \text{ mm/s}$).** This was the processing condition that was optimized for having a better relative density compared to the work done by Uddin *et al* [3], which reported 97% relative density (without powder bed heating). Uddin *et al.* [3] also obtained a high relative density of 98.7% by employing powder-bed preheating temperature of 500°C along with a combination of high power (400-500W) and laser speeds (1400-1600 mm/s). Similarly, the maximum relative density reported by Louvis *et al.*[55] was only 88.7% for the L-PBF of 6061 Al-alloy for the parameters (P : 100-150W, v_{laser} : 80-420 mm/s).

Figure 4-16a) also shows the porosity evolution as a function of linear energy density for the TLS powder cubes. The porosity termed here refers to the lack-of-fusion defects since within the pores there were evidences of unmelted powder particles (see **Figure 4-16d**)). As the laser energy density increases, the porosity measured based on optical micrographs taken in a plane containing the build direction tends to decrease. The process parameter ($E_L = 400 \text{ J/m}$) had minimum porosity of 0.3%. The porosity was estimated using image processing by analyzing an area of $\sim 1500 \mu\text{m}^2$ of different cubes. Since cracks were present in the microstructure, as shown in **Figure 4-16c**), they were discriminated from the estimation of porosity using image processing tools. Even though cracks are considered as defects, they were not taken into consideration to determine the porosity content in the cubes. This means that the sample with optimized processing conditions had very few lack-of-fusion defects but cracks were still present in the sample. To visualize the micrographs of the optimized processing conditions, please refer to **Figure 4-16c**). On the contrary, the processing condition ($E_L = 117 \text{ J/m}$) had the highest lack-of-fusion porosity

(2.6%) and the least relative density ($\sim 96\%$). The optical micrograph of this low energy sample is shown in **Figure 4-16d**). This is similar to what was observed for the 3D cubes of 6061 Al-alloy fabricated by Louvis *et al.* [55]. They attributed this lack of fusion porosity due to low energy density.

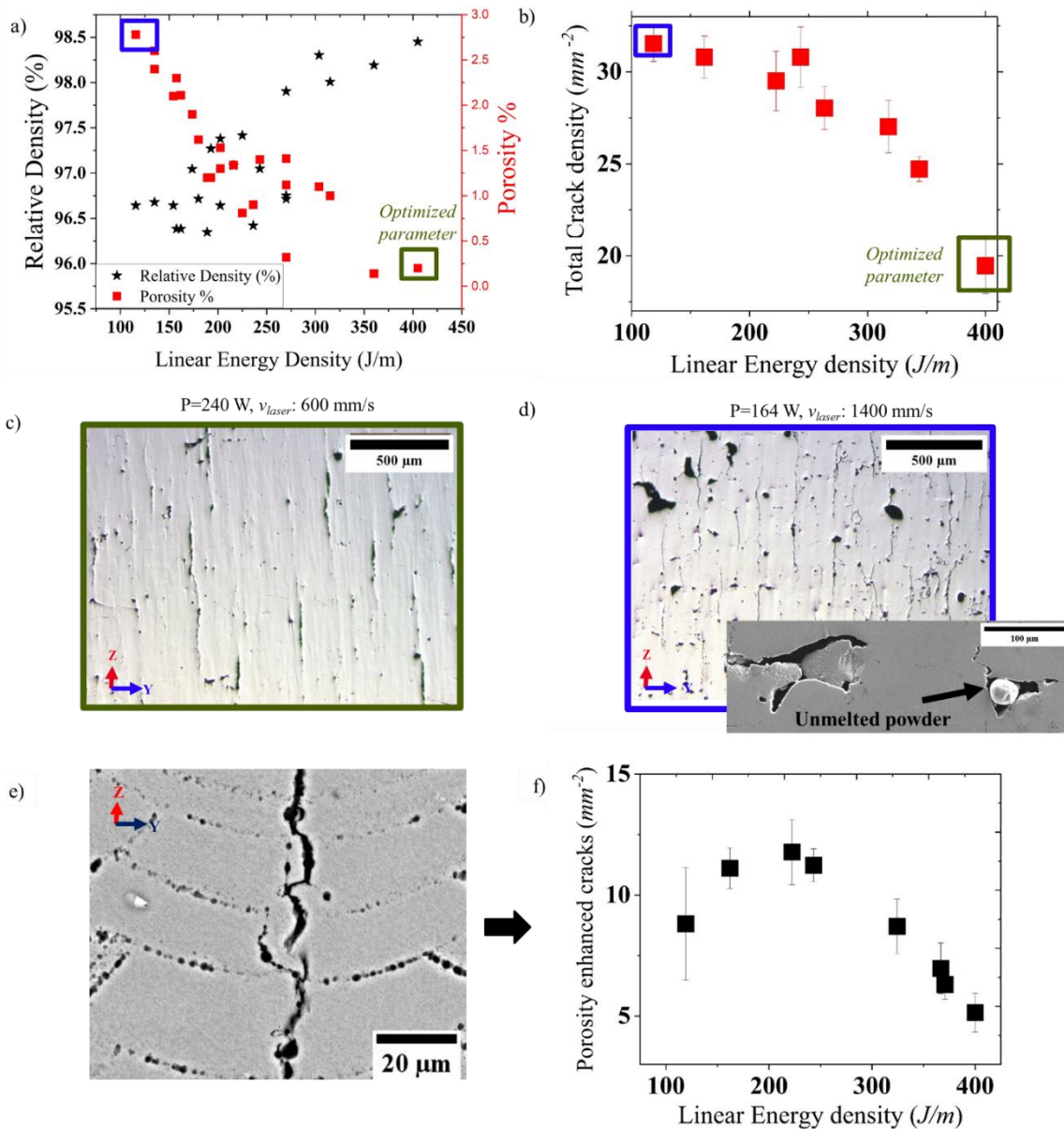


Figure 4-16 a) Relative density and porosity as a function of laser energy density for cubes fabricated using TLS powder. b) Variation of crack density with laser energy density. c) and d) Optical micrographs of the samples with $E_L=400\text{ J/m}$ and $E_L=117\text{ J/m}$, respectively. e) Optical micrograph showing porosity enhanced cracking. f) Variation of porosity enhanced crack density with linear energy density.

This observed trend of decrease in lack-of-fusion porosity with increasing energy density is opposite to the trend observed in bulk substrate melt pools, where metallurgical pores (H_2 induced porosity) increased with the increase in linear energy density (see **Figure A-7a**). The lack-of-fusion pores identified in the

3D cubes were much larger due to the embedded unfused powder particles, compared to the metallurgical pores (few microns) identified in the bulk substrate melt pools. The mechanism of formation of these two different types of pores is different, thus it is reasonable to expect a difference in their variation compared to the change in laser energy density. For example, as input energy density decreases, there is a higher chance for the powder particles to not melt and form a lack-of-fusion defects. On the contrary, for smaller melt pools with low energy density, there will be less amount of H₂/other gases trapped in the melt pool. This explains the opposite variations of the two types of porosities with the input energy density.

In addition to the observed porosities, cracks were also found throughout the processing parameter range investigated in the current work. As illustrated in **Figure 4-16b**), the average total number of crack per unit area shows a decreasing trend with the increasing linear energy density. The highest crack density (31.5 cracks per mm²) was observed for an energy input of $E_L = 118.5 \text{ J/m}$ ($P = 166\text{W}$ and $v_{laser} = 1400 \text{ mm/s}$) while the lowest crack density was measured for the highest energy ($E_L = 400 \text{ J/m}$). This observed trend is consistent with the reported literature, which reports that cracking can be reduced but not avoided by increasing the energy input, see ref. [34]. A similar trend of decreasing cracking density was also observed during the bulk substrate experiments (see **Figure A-7c**)).

Besides, there were a few instances where some of the cracks have metallurgical porosities located along their propagation path (see **Figure 4-16e**)). This observation suggests that there is a significant connection between cracks and gas-entrapped pores. This interaction between the cracks and pores was recently identified by synchrotron X-ray imaging techniques in the 6061 Al-alloy, see ref [123]. According to Kouraytem *et al.* [123], pre-existing pores (metallurgical or keyhole) are the preferred sites for cracks to initiate. These porosities probably help the cracks to propagate. In addition, Kouraytem *et al.* [123] also observed that, when laser beam passes through the cracks, metallurgical pores tend to form along the crack propagation path. Thus the observations reported by Kouraytem *et al.* [123], support the observation of the present study seen in **Figure 4-16e**). The porosity enhanced cracking density as shown in **Figure 4-16f**) was also found to decrease as a function of linear energy density. However, a similar trend for increasing energy density ($E_L > 400 \text{ J/m}$) is difficult to expect, since keyhole porosities can also form [76]. It is known in the literature that, as laser energy density increases, there are chances of keyhole melting mode and keyhole regime can also give rise to additional keyhole porosities [76], which might be detrimental to the build sample mechanical properties.

In all the studied parameters of the bulk substrate and powder experiments (P: 180-274W, v_{laser} : 200-1400 mm/s), the melting mode was classified as conduction mode (since melt pool depth/width ratio was systematically found to be <1 , see **Figure A-6c) and not as keyhole mode.** The parameters used to fabricate 3D cubes ($P: 164\text{W}-274\text{W}$ and $v_{laser}: 400-1400 \text{ mm/s}$) are also far away from the **typical keyhole regime reported in the literature for: 6061 Al-alloy (P: 500W, v_{laser} : 16 mm/s)** [124] **and other Al-alloys (P: 450-750W, $v_{laser} < 100 \text{ mm/s}$)** [76,125]. Moreover, we also tried to estimate the typical normalized enthalpy ($\Delta H/hs$) using **equation 4.1**, as suggested by Kiss *et al.* [126], since it was frequently used as a parameter to compare conduction and keyhole melting mode [127–129]. The normalized enthalpy is estimated in **Table 4-1** for the melting parameters (in the present study) and the one that leads to keyhole from ref. [124]. For the melting parameters used in the present study, a

normalized enthalpy of 5.4 was estimated which is comparatively lower than the normalized enthalpy of 24.5 (calculated for keyhole melting parameters reported in ref. [124] for the same 6061 Al-alloy). According to Bertoli *et al.* [129], a conduction melting mode will occur in most of the metals, when the normalized enthalpy is less than 6. **Thus, our analysis (low normalized enthalpy) suggests that the melting mode employed in the present study is only by conduction melting and not by keyhole melting. This is in agreement with what was observed in the bulk substrate experiments (Appendix) with the hemispherical morphology of the melt pool.** The normalized enthalpy of 24.5 found for the keyhole regime in 6061 Al-alloy, is less than the ones observed for stainless steel ($\Delta H/h_s = 30$) [126] and higher than for Ti-6Al-4V ($\Delta H/h_s = 17$) [130]. However, it is highly possible that, the critical normalized enthalpy (conduction to keyhole transition) for the 6061 Al-alloy can be less than 24.5, since it is very rare to find literature on 6061 Al-alloy, reporting that critical normalized enthalpy.

$$\frac{\Delta H}{h_s} = \frac{\eta P}{\pi \rho C_p T_{liquidus} \sqrt{\alpha v_{laser}} r^3} \quad \text{equation (4.1)}$$

Where, ΔH is the specific enthalpy, h_s is the enthalpy at melting, η is the absorptivity coefficient (assumed 0.6, based on the powder reflectivity of 6061 alloy, see **Figure 4-2**, P is the laser power, ρ is the density, C_p is the specific heat capacity, $T_{liquidus}$ is the liquidus temperature, α is the thermal diffusivity, r is the laser spot size and v_{laser} is the laser scan speed.

Table 4-1 Constants used to estimate the normalized enthalpy for the two melting modes observed in 6061 Al-alloy.

Constants for 6061 alloy	Conduction mode (optimized parameter)	Keyhole mode (Ref. [124])
Laser speed (v_{laser})	600 mm/s	16 mm/s
Laser Power (P)	240 W	500 W
Absorptivity (η)	0.6	
Specific heat capacity (C_p)	897 J/(kg K) [131]	
Density (ρ)	2700 kg/m ³ [131]	
Thermal diffusivity (α)	6.89 x 10 ⁻⁵ m ² /s [131]	
Laser spot size (r)	70µm	140µm
Liquidus ($T_{liquidus}$)	925K	
Normalized enthalpy ($\Delta H/h_s$)	5.4	24.5

Note that, the powers ($\geq 500W$) used to obtain the keyhole mode (shown in **Table 4-1**) are way higher than the maximum 274W achieved by the ProX200 machine used in the present study. Similarly, low laser

speeds of 16 mm/s can significantly affect the low production rates and also affect the powder spreading ability. Thus by further increasing the energy density ($> 400\text{J/m}$), technological issues, unstable (high energy) melt pool morphology observed in powder layer experiments and evaporation of low boiling point elements (Zn, Mg) [26] can become predominant.

Finally, based on the best relative density of 98.5%, the least lack of fusion porosity (0.3%) and the least crack density (~ 19 cracks/ mm^2) obtained, the sample with process parameter (P: 240W, v_{laser} : 600 mm/s) was considered as “optimized” and will be utilized for further advanced microstructural characterization in the upcoming section.

4.2. Multi-scale characterization of the as-built microstructure (optimized parameters)

The second part of the chapter details the multiscale characterization of the samples produced using the optimized parameters. A multiscale analysis of the microstructure was performed, starting with the macrostructure (grain structure) to nano-scale microstructure to better understand the as-built 6061 Al-alloy. A detailed microstructural study allowed us to identify the as-built microstructural features, including the cracking pattern and its mechanism. This part of the chapter is divided into various subsections:

- i. **Experimental procedures**
- ii. **Macrostructure.**
- iii. **Cracking pattern:** Identification of cracking pattern with respect to the microstructure.
- iv. **Cracking mechanism:** The section will concentrate on identifying the underlying cracking mechanism occurring in the 6061 Al-alloy fabricated by L-PBF.
- v. **Observation of the microstructure by SEM/TEM.**
- vi. **Discussion on the as-built microstructural observations.**

4.2.1. Experimental procedures

The macrostructure was observed using the scanning electron microscopes (SEM) and for understanding of the microstructure, standard characterizations like electron back-scattered diffraction (EBSD) was also used. The details of the sample preparation needed to use each technique, as well as the operating conditions of the instruments are detailed below.

- **Sample preparation**

For microstructural observation, the as-built samples were cut in YZ and XZ planes respectively, X being the laser scan, Y the direction transverse to the laser scan, and Z the build direction. The

specimens were ground using silicon carbide paper until P4000 grit size and polished down to a finishing step with a $0.03\ \mu\text{m}$ colloidal silica solution. To observe the melt pool boundaries, samples were etched using Keller's reagent (2.5% nitric acid, 1.5% hydrochloric acid, 1% hydrofluoric acid in water) for $\sim 10\text{-}15$ sec. To perform EBSD analysis, the samples needed an additional vibratory polishing step to get rid of the deformation caused by grinding. The vibratory polishing was done on the Buehler Vibromet 2 machine. The samples were stuck to the sample holder with a double adhesive tape. Using a microfloc disk and the colloidal silica solution along with Alumina (the combination exists as Master met solution 200ml), the samples were polished with a subjected weight of 100-200 g for a minimum of three hours at 60% of vibration.

- **XRD / SEM/ EBSD**

The as-built optimized cube was analyzed using X-ray diffraction (XRD) to detect the presence of different phases/second-phase particles formed and also to determine the texture. The analysis was performed using Brücker D8 Advance. Polished samples of the as-built cubes and powders were characterized by using the Cu K- α radiation.

The microstructure along the building direction (BD) was observed using the secondary electron (SE) and back-scattered (BSE) modes in the ZEISS Gemini SEM500 FEG-SEM at 5kV accelerating voltage. To have detailed information about the sample crystallographic information, misorientation, microtexture, and grain size, electron backscattered diffraction (EBSD) was used in the present study. EBSD maps at 20kV accelerating voltage in an $500\times 400\ \mu\text{m}^2$ area acquired with a step size of $0.3\ \mu\text{m}$, were collected on the XZ/XY-plane of the as-built sample. Post-processing was done using ESPRIT and HKL Channel-5 softwares, in which the columnar grain width was measured using the intercept method.

4.2.2. Macrostructure: grain structure

To get insights into the macrostructure of the as-built 6061, the cube with optimized parameters (with $E_L=400\ \text{J/m}$ ($P: 240\text{W}$, $v_{laser}: 600\ \text{mm/s}$)) was selected for further analysis. **Figure 4-17a)** shows the low magnification image taken in a plane containing the build direction (along Z-axis). Cracks are oriented along the build direction. Similarly, the melt pool boundaries are revealed using Keller's reagent. The average melt pool width (w) is measured to be about $152\pm 4\ \mu\text{m}$ and depth (d) about $66\pm 6\ \mu\text{m}$. Since the d/w ratio < 1 , it confirms once again that the selected sample has been processed under a conduction mode of melting, in line with the analysis of normalized enthalpy displayed in **Table 4-1**. For a similar process parameter, compared to the bulk substrate experiments, the depth found here is comparatively smaller, this is due to the small layer thickness of $20\ \mu\text{m}$. However, the width is comparable to the ones observed in the bulk substrate as well as the powder layer experiments performed using $E_L=400\ \text{J/m}$. In **Figure 4-17a)**, the melt pools can penetrate inside the melt pools from the previous powder layer. Good

adhesion between successive layers was observed. Moreover, due to the good adhesion, there was no trace of interlayer defects such as delamination or lack of fusion defects located in between consecutive layers. Thus, good consolidation behavior of the fabricated part was observed.

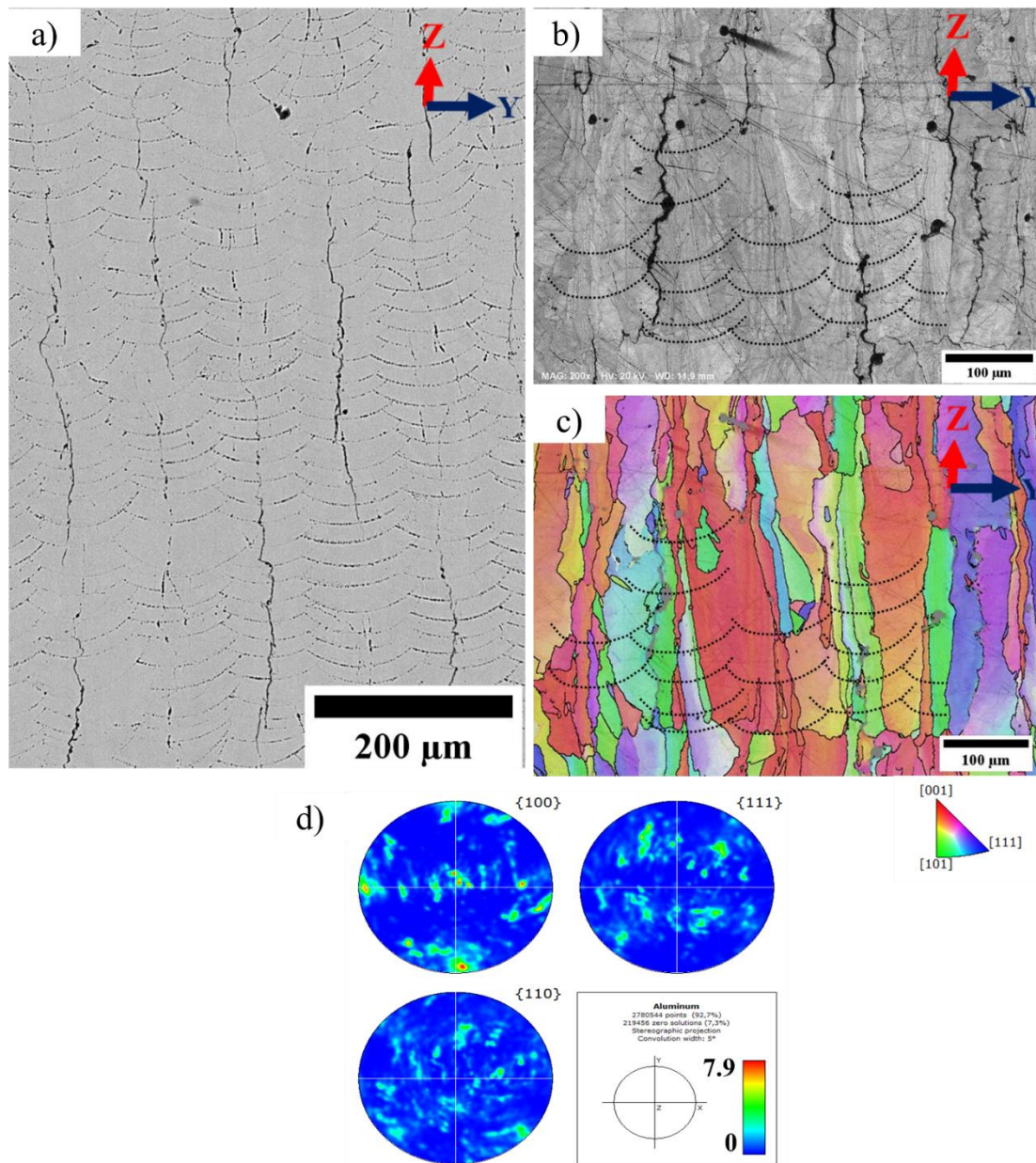


Figure 4-17 a) Low magnification optical micrograph along the build direction (etched with Keller’s reagent) taken from a cube fabricated with optimized parameters ($E_L=400$ J/m). b) Pattern quality image measured using EBSD. c) IPF-EBSD map of the 6061 cube sample normal to the X-direction of the cube sample. d) (100), (111) and (110) Pole figures determined over the map shown in c).

Figure 4-17b) shows a high magnification pattern quality image from EBSD acquired in the plane containing the building direction. For the sake of clarity, some melt pools are highlighted with black dotted lines. **Figure 4-17c)** shows the Inverse Pole Figure (IPF) map of the same region of interest extracted

from the as-built microstructure. To visualize the grain structure with respect to melt pool boundaries, crystallographic orientations were determined on the exact same region as shown in **Figure 4-17b**). Based on the IPF map, the microstructure consists of columnar grains oriented towards the Z-axis (build direction), with an average width of about 60-70 μm , estimated based on the intercept method. The grains are found to be crossing several melt pools along the building direction. The columnar grains stretch along the building direction over several hundreds of microns in length typically about $\sim 400 \mu\text{m}$. The sample shows a significant number of cracks at grain boundaries. Therefore, cracking can be qualified as ‘intergranular cracking’. Since cracks follow the grain boundaries, cracks do also propagate over several hundreds of microns.

During solidification, due to the local solidification conditions, there can be a preferred orientation of some grains compared to other, i.e. formation of crystallographic texture. Generally, FCC metals having $\langle 001 \rangle$ direction perpendicular to the melt pool boundaries grow faster than the other orientations [72]. According to the pole figure obtained using EBSD analysis in **Figure 4-17d**), the sample exhibits a predominant micro-texture along the $\langle 001 \rangle$ direction, this direction being aligned with the build direction (Z-axis), similar to the ones reported in refs [3,132]. The observed texture is due to the epitaxial growth of the columnar grains along the $\langle 001 \rangle$ direction, since powder layers are built on top of each other and the thermal gradient is mainly oriented along the building direction. A similar maximum texture intensity (7.9) to the ones observed in the present study was reported by ref [133]. However, the observed value is comparatively higher than the ones reported in ref [32], since in our case we rather used a simple scanning strategy (without rotation between layer), whereas in ref [32] a rotation between layers was employed, which possibly affected the texture intensity.

4.2.3. Cracking pattern

To understand the cracking sensitivity to grain boundary misorientation, a statistical analysis was performed. Typical grain boundaries (GB's) shown in the IPF map of **Figure 4-18a**) were classified according to their misorientation, based on measurements carried out at ~ 45 cracked grain boundaries. The grain boundaries were classified as high angle grain boundaries (HAGBs), characterized by a misorientation angle $\theta > 15^\circ$ and highlighted in ‘black’ in **Figure 4-18b**). Similarly, low angle grain boundaries (LAGBs), defined as having a misorientation angle between 5° and 15° are marked in ‘white’ in **Figure 4-18b**). Misorientation angle less than 5° was not considered. **The statistical analysis shown in Figure 4-18c) shows that cracking occurs systematically along HAGBs. Moreover, LAGBs are always found to be crack-free.** This observation corroborates previous reports made for other alloy systems, see e.g. [89][134].

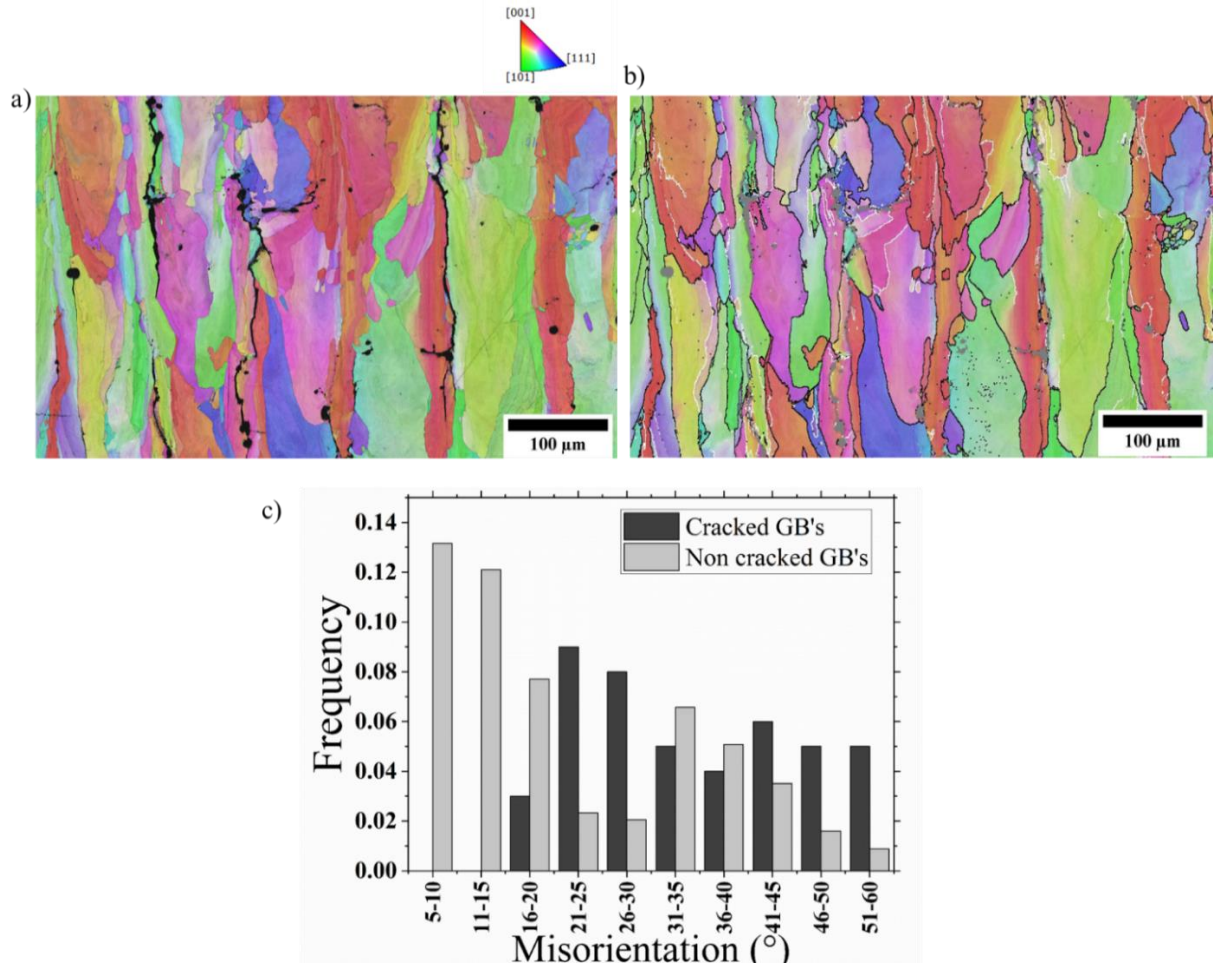


Figure 4-18 a) IPF-EBSD map normal to the X-direction of 6061 cube sample, showing intergranular cracking. b) IPF-EBSD map showing non-cracked low angle grain boundaries ($5^\circ < \text{LAGB} < 15^\circ$) marked in white and high angle grain boundaries ($\text{HAGB} > 15^\circ$) marked in black. c) Distribution of misorientation angle for cracked and non-cracked grain boundaries.

It is also noticeable that cracking at grain boundaries is not systematic since many high angle grain boundaries remain crack-free. **Figure 4-19a)-b)** show that cracking occurs preferentially in the central region of the melt pool. A similar trend is observed in the top surface XY plane, as shown in **Figure 4-19c)**. The average spacing between the cracks is found to be $98 \pm 10 \mu\text{m}$, which is comparable to the hatch spacing set to $100 \mu\text{m}$ in our experiments. **This suggests that the solidification conditions at the center of the melt pool are the most susceptible to cause hot cracking at GBs. Thus, another key parameter identified for cracking is the spatial location of HAGBs with respect to the melt pool.**

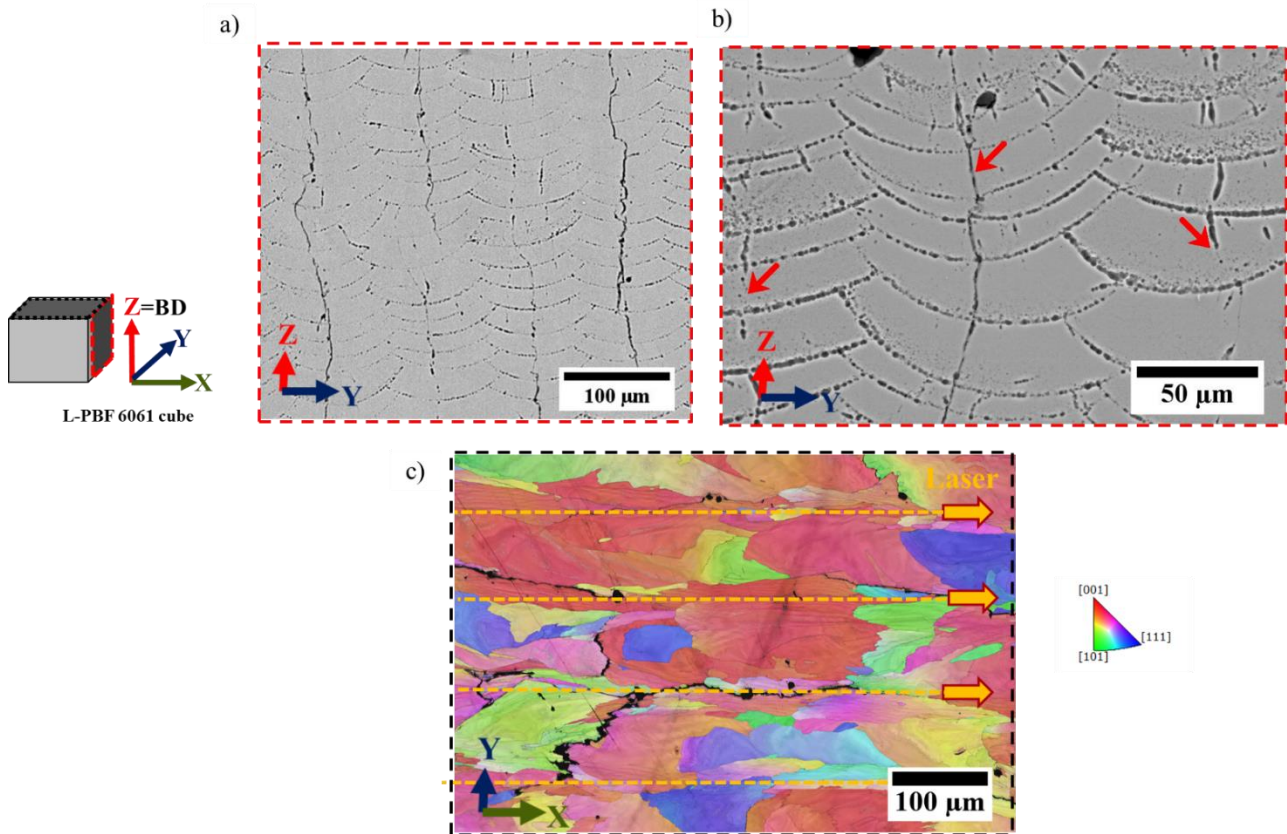


Figure 4-19 a) & b) BSE-SEM contrast micrographs of the as-built 6061-alloy using the optimized processing conditions ($P = 240\text{W}$ and $v_{laser} = 600\text{ mm/s}$). b) IPF-EBSD map of 6061 cube sample in XY plane.

The observation of cracking in the central region found in the current study, shows some striking similarities with what has been reported in laser welding of Aluminum alloys, see e.g. [97][135][136]. The centerline cracking observed in welding literature is due to the lack of liquid feeding in central dendrite regions of the mushy zone [97][137]. According to Campbell [138], the orientation of dendrites located in the central region can be detrimental to the cracking susceptibility, with a lack of ability to sustain tensile strains. Similarly, the sensitivity of HAGBs to cracking is also reported in numerous refs [89][134] and the coalescence undercooling model of Rappaz *et al.* [6,85] can be utilized to explain its occurrence. According to Rappaz *et al.* [6,85] cracking can be influenced by the coalescence of dendritic arms. For highly misoriented dendrites, their mutual coalescence can be delayed, compared to the dendrites belonging to the same grains. This causes the liquid in the inter-dendritic region along the GB's to be in the form of thin continuous film, which is vulnerable to thermal induced strains. However, this theoretical model of coalescence undercooling can be used to rationalize the HAGB cracking in the present study, only if the cracking mechanism occurs by solidification cracking. The investigation of the cracking mechanism will be discussed in **section 4.2.4**.

To elucidate the local strain state of the as-built samples, the misorientation plots of the XY/ZY plane are also generated with the EBSD technique. Such an analysis will provide the location within the microstructure which is deformed compared to other locations. For example, as shown in **Figure 4-20a)** & b), the grain average misorientation (GAM) map is shown for the XY plane and ZY plane, respectively. In GAM maps, the misorientation of a given point with reference to the average misorientation of all the points belonging to that particular grain can be observed. These kinds of maps are particularly used to identify recrystallized grains and “strain-free” grains. The lower the deviation of misorientation at a given point, the lower will be the strain associated. Thus, in **Figure 4-20a)&b)**, the green/yellow zones denote the high degree of strain in the vicinity of cracked grain boundaries. Along the region where the laser tracks pass in **Figure 4-20a)**, there is high misorientation, indicating a highly strained region near the grain boundaries coinciding with the laser tracks.

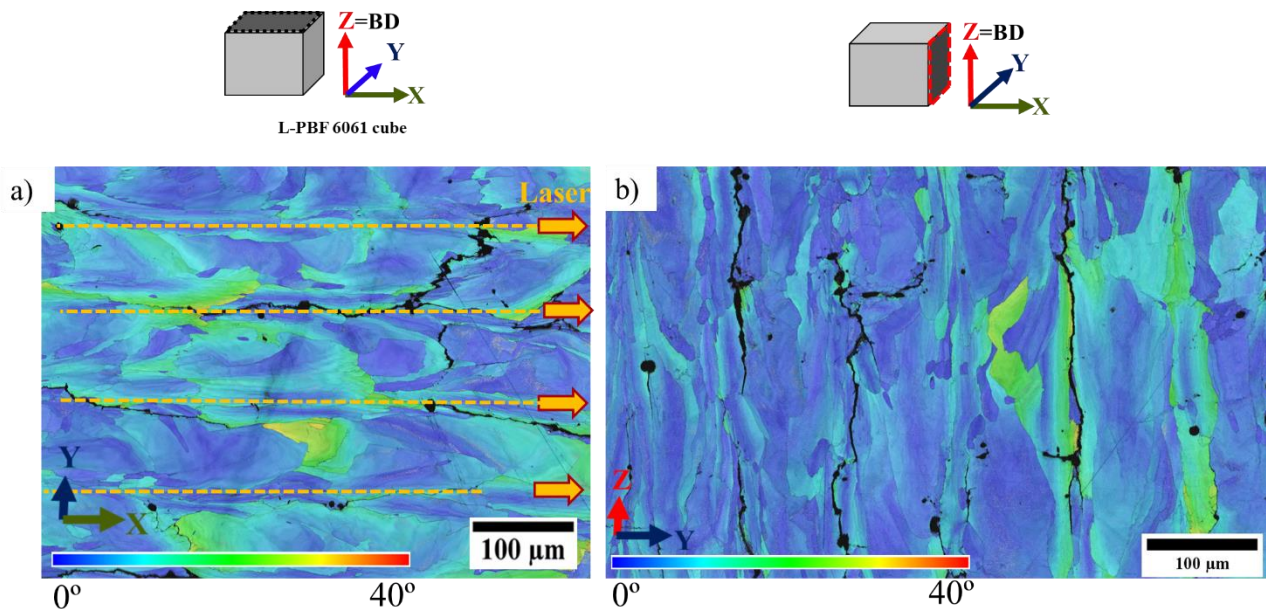


Figure 4-20 a) & b) Grain average misorientation map of the XY and ZY plane, respectively.

4.2.4. Cracking mechanism

As already reported in the literature section, cracking mechanisms are classified into two categories: (i) hot cracks and (ii) solid-state cracks [81]. Hot cracks form due to the presence of liquid films associated with shrinkage and tensile strain in the mushy zone. The typical fracture surface of hot cracks shows a dendritic morphology, demonstrating the evidence of trapped liquid films. Solid-state cracking occurs without the presence of liquid films, contrary to the previous mechanism. One simple way to distinguish the type of cracking is through the observation of the surface state around cracks. To do so, small tensile coupons

with dimensions (10mm x 10mm x 1mm) have been machined from the as-built L-PBF cube samples. The tensile coupons were not machined as dog-bone shaped (typically used for tensile testing), since studying tensile properties was not the objective of the study but rather to reveal the key features regarding the cracking mechanism based on fracture surface observations. The coupons were subjected to tensile loading in the direction perpendicular to the BD, as shown in the schematic of **Figure 4-21a**). Those coupons were loaded in tension to open the cracks and examine the fracture surface with the SEM.

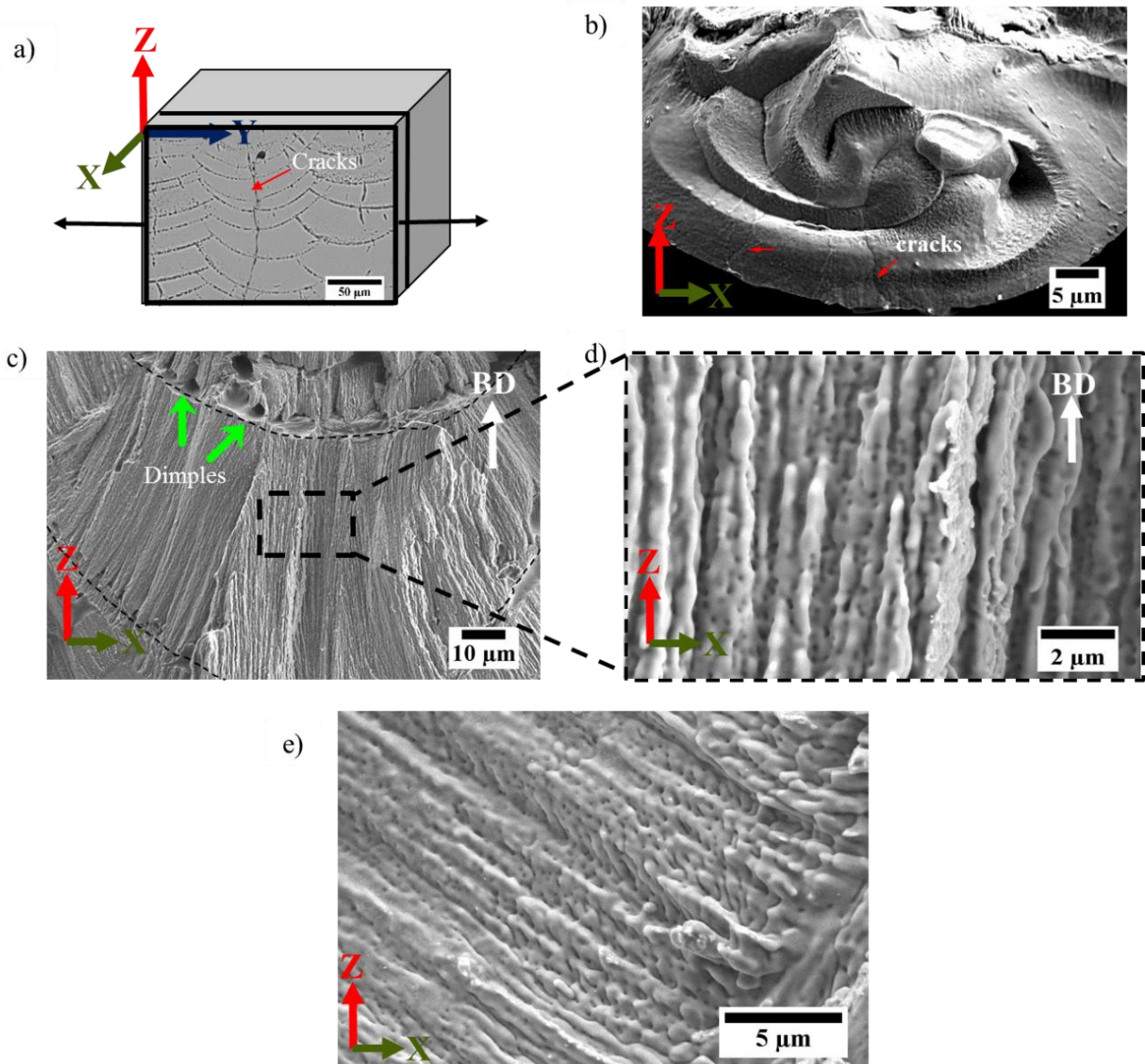


Figure 4-21 a) Schematic showing how the tensile coupons were extracted from cube samples. b) Micrograph of fracture surface demonstrating Marangoni convection inside the melt pool c) Low magnification SE-SEM contrast micrograph of the melt pool. d) & e) High magnification SE-SEM contrast micrograph at the surface of cracks.

Figure 4-21b) shows the fracture surface after the tensile test, showing the low magnification image of the melt pool. **Figure 4-21b)** shows the experimental evidence of the Marangoni convection [139] happening during the solidification inside the melt pool. Cracks are seen to originate at the bottom of the melt pool. Similarly, **Figure 4-21c)** shows the fracture surface after the tensile test. Few regions at the boundary between melt pools, indicated by green arrows, exhibit dimples, which are characteristic of ductile fracture. However, more importantly, a cellular/dendritic morphology is observed in almost the entire fracture surface. This suggests that cracking occurred in the presence of liquid films trapped in the growing columnar dendrites during the L-PBF fabrication. With this evidence of dendritic/cellular morphology, the cracking mechanism is identified without ambiguity as hot cracking. **Figure 4-21d) & e)** also confirm the cellular dendritic morphology in the central location of the melt pool, where cracking is predominantly observed. **Cellular dendrites with very limited secondary dendrite arms can be seen in the vicinity of cracks. The average spacing between two primary dendrite trunks (PDAS) is found to be about $\sim 0.6 \mu\text{m}$. Interestingly, note that the average spacing between the secondary dendrite arms (SDAS) is of the same order of magnitude.**

In the literature, hot cracking can further be classified as solidification cracking and liquation cracking. Solidification cracking occurs in fusion zones of melt pools, whereas liquation cracking occurs in the heat-affected zone [18]. To clarify this point, **Figure 4-22** shows the topmost layer of the L-PBF cube. Hot cracks are observed inside the topmost melt pools (marked with ‘red’ dashed lines in **Figure 4-22**), which are not re-melted in comparison with the melt pools from previous layers (marked with ‘black’ dashed lines). **This suggests that hot cracks originate inside the fusion zone during the solidification, thus qualifying the cracking mechanism as solidification cracking.** The identified solidification cracking mechanism in the 6061 Al-alloy fabricated by L-PBF, will further allow us to rationalize the HAGB cracking with the help of the coalescence undercooling model of Rappaz *et al.* [6,85]. This will be discussed in **Chapter 5**, which is dedicated to developing a cracking sensitivity criterion using the Rappaz, Drezet, and Gremaud (RDG) model [7].

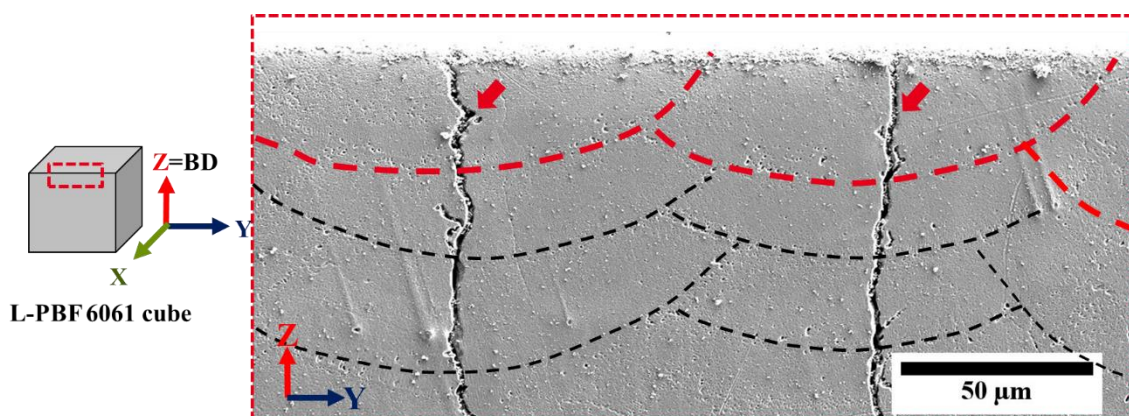


Figure 4-22 Optical micrograph of the topmost layer of L-PBF cube sample along the building direction. The cracks are denoted by the red arrows, and the topmost melt pools by red dashed lines.

Summary

So far we have analyzed the cracking pattern, its location with respect to the melt pool and its sensitivity to high angle grain boundaries. The fact that the 6061 Al-alloy is sensitive to cracking under welding operations is known for years. However, the literature about the fundamentals mechanisms at the root cause of cracks does not unanimously agree on a given mechanism: solidification cracking or liquation cracking. Without experimental evidence of the present work, both may operate according to the welding literature [18,140]. In the current work, this ambiguity regarding the governing mechanism for the fabrication of the 6061 Al-alloy by L-PBF is resolved. The upcoming sections will be focused on detailed microstructural characterizations at an intra-granular level to identify the key features of the as-built 6061 Al-alloy.

4.2.5. Microstructure

- **SEM observations**

In the literature of 6061 alloy during L-PBF, not much information regarding the microstructure and in particular the nature of the second-phase particles has been reported. Since the major issue with this alloy is its cracking sensitivity, most of the literature was focused on solving the cracking issue rather than understanding microstructure formation in detail in the context of fabrication by L-PBF [3,4]. For example, out of the reported work on L-PBF of 6061 Al-alloys, only Uddin *et al.* [3] reported the presence of ~200 nm dispersoids of Al-Si-O in the as-built samples. However, their claim was only based on energy dispersive X-ray spectrometry (EDS) analysis performed in SEM and would deserve further analyses to be confirmed.

The as-built microstructure of 6061 Al-alloy fabricated by L-PBF revealed by chemical etching is shown in **Figure 4-23**. Several BSE-SEM images with different magnifications acquired in the plane containing the build direction are shown for the sample built with optimized conditions ($E_L=400$ J/m). The L-PBF microstructure shows a lot of cracks along the grain boundaries as shown in **Figure 4-23a**). Moreover, several second-phase particles revealed thanks to chemical etching appear in dark **Figure 4-23b-d**). Those second phase particles are homogeneously distributed throughout the sample. These second-phase particles are present in the grains as well as along the grain boundaries, see **Figure 4-23c-d**), similar to what was observed by Uddin *et al.* [3]. These second-phase particles exhibit a rather spherical morphology. Similarly, their size ranges from 50-450 nm with the majority of the particles belonging to the 0-50 nm size group. The average spacing between these particles is roughly ~200-300 nm. Similarly, according to **Figure 4-23b-c**), the primary dendrite arms can also be observed growing along the build direction. The PDAS from the microstructure was found to be ~0.5-0.6 μm , similar to what was observed in the fracture surface observation of **Figure 4-21**. There are also other type of particles, observed with a brighter contrast in the BSE image shown in **Figure 4-23c**). Compared to the dark second-phase particles, these white particles are fewer, coarser (typical size of about 200nm), and not homogeneously distributed within the

microstructure. The fact that they appear white in the BSE contrast image, indicates that those are composed of heavy solutes present in the 6061 Al-alloy.

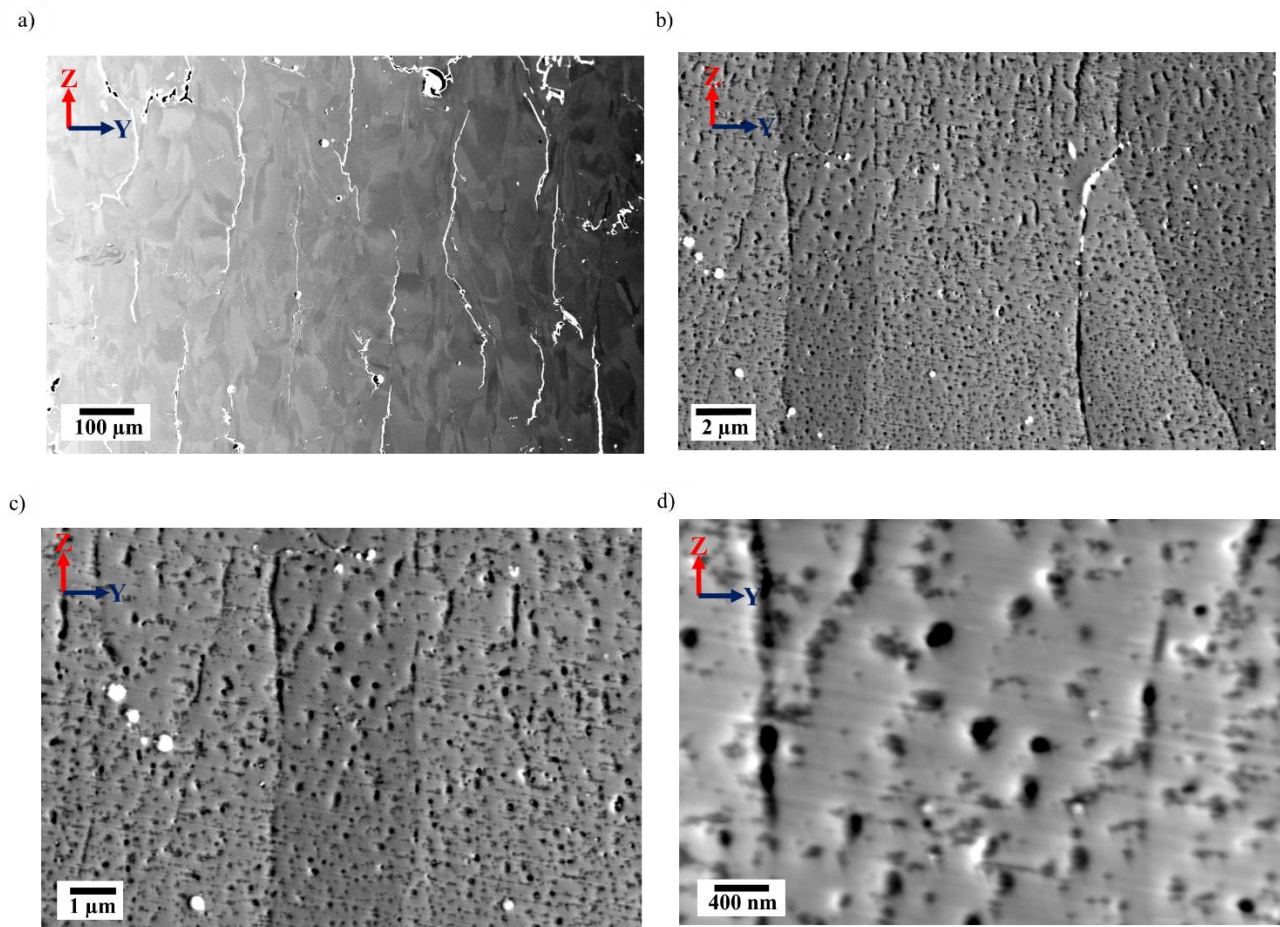


Figure 4-23 a)-d) Typical 6061 Al-alloy L-PBF as-built microstructure revealed by chemical etching (BSE-SEM contrast) at various magnifications extracted in the plane containing the build direction.

Since these dark second-phase particles observed in the as-built etched microstructure seem to be numerous, X-ray diffraction (XRD) was carried out in an attempt to get some insights regarding their crystallographic nature. **Figure 4-24** shows the XRD pattern from an analysis performed in the XY plane. The diffraction peaks from the powder are also shown for comparison.

The diffraction pattern of the as-built samples, along with the one of the as-received powder, shows the presence of FCC-Aluminum (see **Figure 4-24**). No other peaks corresponding to the second phase particles were detected, probably due to the small size of the second-phase particles and/or their relatively low volume fraction. Similar peaks were also reported by Uddin *et al.* [3], where they were not able to detect the presence of second-phase particles using XRD. A similar set of diffracting planes is also observed for the 6061 powder (TLS), indicating that no other phase can be detected by XRD in the powder neither. However, comparing the intensity of the as-built and powder sample XRD peaks, the (200) from the as-built cube has higher intensity. This indicates that the as-built sample has a predominant texture

with most of its planes belonging to $\{100\}$ family of planes as already revealed in the EBSD-IPF maps displayed in **Figure 4-17d**).

To summarize, despite the presence of second-phase particles in the as-built microstructure, classical laboratory XRD was not able to detect those phases. To further investigate these phases, TEM imaging combined with chemical analyses with EDX was carried out. This will help to collect information regarding the nature of the solutes contained in those second-phase particles and will be presented in upcoming section.

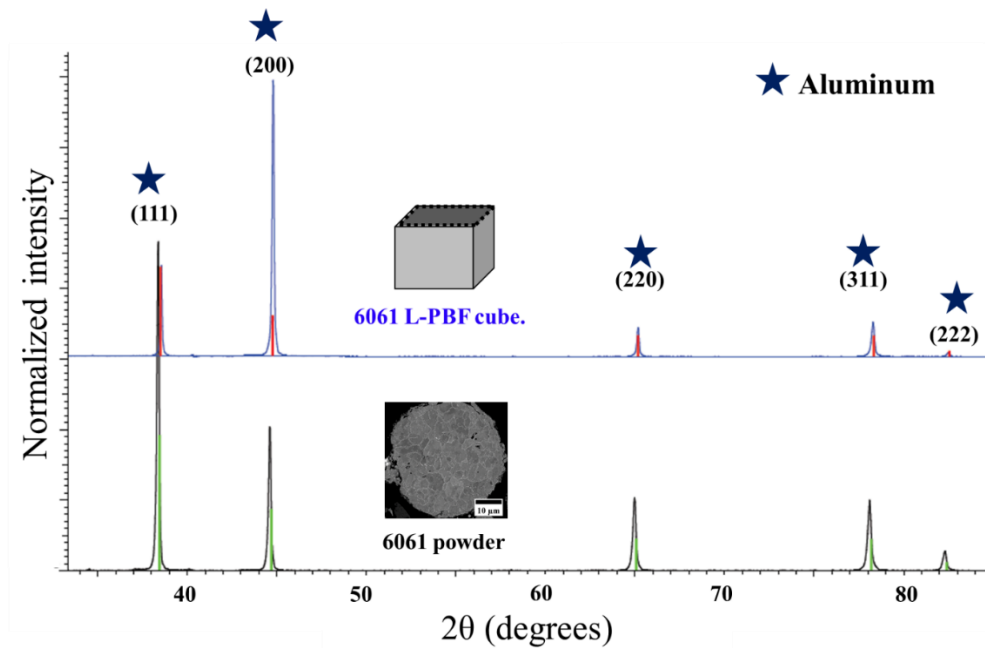


Figure 4-24 X-ray diffraction analysis on the as-built cube (XY plane)-top and the gas atomized TLS powder – bottom.

- **TEM observations**

To date, it is very rare to obtain experimental evidence related to second-phase particles in the framework of 6061 Al-alloy microstructures produced using L-PBF. The objective of using transmission electron microscopy (TEM) is to identify which solutes are enrichment in those second-phase particles already revealed in **Figure 4-23** and also detect possible segregation of elements along the GB's.

Focused Ion Beam (FIB) lift-out method using a Thermo-Fisher Strata 400S FIB-SEM instrument was used in the study. The advantage of FIB is that the region of interest can be selected to prepare the lamellas. Using the FIB lamellas, the TEM characterizations were performed on the Thermo-Fisher Osiris Tecnai instrument, having an Extreme field emission gun (X-FEG) operating at 200 kV. Energy dispersive X-ray (EDX) analysis was performed in STEM mode, with the TEM equipped with four Silicon Drift Detectors

technology. The resolution depends on the size of the electron probe used; here in our study, we used a spot size of 0.1 nm.

The plane containing the build direction of the sample with optimized processing conditions was used to extract the FIB sample as shown in **Figure 4-25**. Vibratory polishing was used to prepare the sample for FIB extraction. **Figure 4-25** shows the micrographs of the location of 'TEM sample with respect to the cracks and melt pool locations. Two types of grain boundaries (cracked and non-cracked) were selected to be part of the FIB sample (indicated by 'black square' in **Figure 4-25b**). These two types of GBs were purposefully selected to investigate the possible difference in segregation or the nature of the second-phase particle. Both of these GB's were HAGBs.

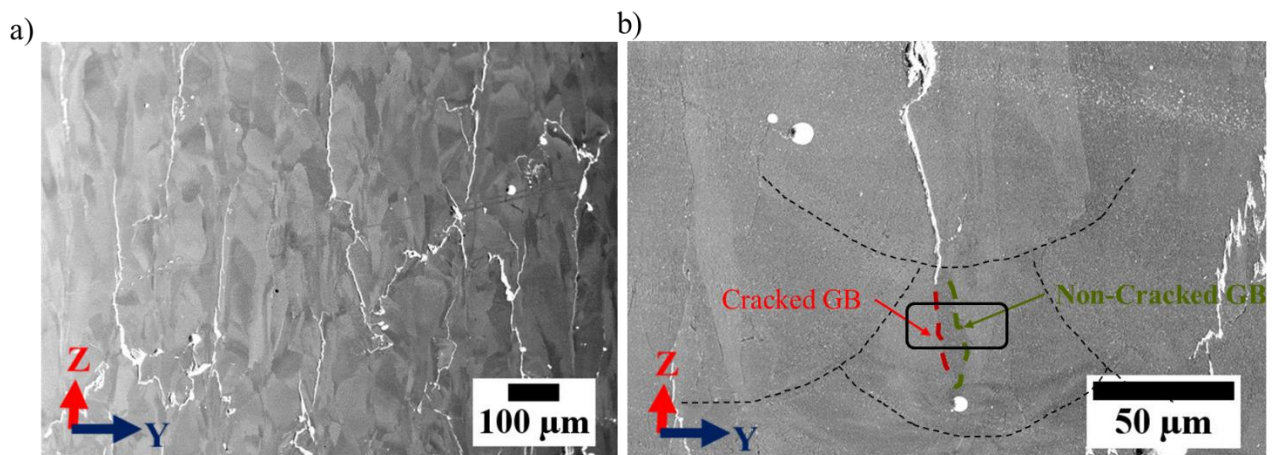


Figure 4-25 a)-b) SEM-BSE micrographs (not chemically etched) taken along building direction with increasing order of magnification. The FIB sample was extracted in the location indicated by the 'black square' in b).

Figure 4-26a)-c) shows different micrographs acquired during the process of FIB lamella preparation. The length of the prepared lamella was around 20 μm with a thickness around 110 nm. The two grain boundaries: non-cracked and cracked are highlighted in green and red in the prepared FIB lamella, see **Figure 4-26c**).

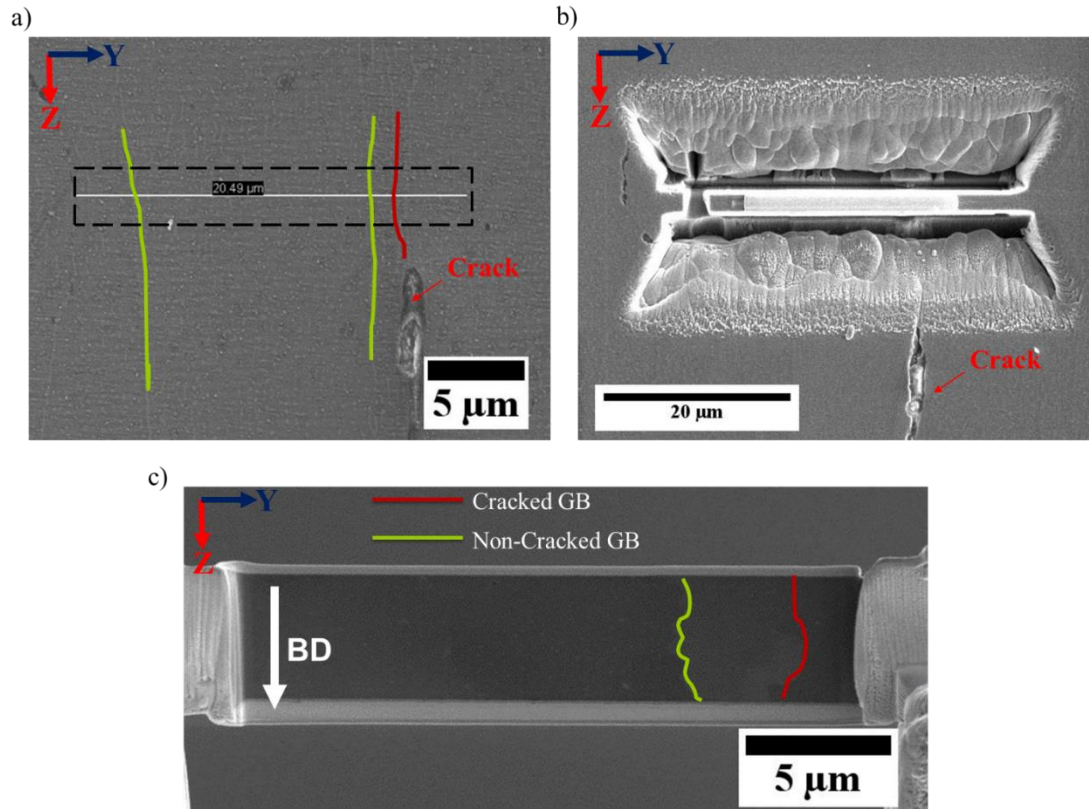


Figure 4-26 a) & b) SEM-SE micrographs (not chemically etched) showing the location of FIB sample with cracked GB (marked in red) and non-cracked GB (marked in green). c) FIB lamellas having a cracked GB and non-cracked GB.

Corresponding to these non-cracked and cracked GB of the FIB lamella in **Figure 4-27a**), a low magnification first view TEM images were obtained as shown in **Figure 4-27b) & c)**. **Figure 4-27b)** shows the entire view of non-cracked GB along with the surrounding matrix using a HAADF image (left) and a BF image (right). Similarly, **Figure 4-27c)** shows the HAADF and BF images of the cracked GB. In both **Figure 4-27b) & c)**, the respective GB's are highlighted in green and red dashed-lines. Both GB's, the non-cracked GB in **Figure 4-27b)** (HAADF image), the cracked grain boundary in **Figure 4-27c)** (HAADF image), appear with a brighter contrast in comparison with the FCC-Al matrix. This observation indicates that some heavy elements are segregating at the GB's. Another observation from HAADF images of **Figure 4-27** is that there are evidences of the presence of bright second-phase particles inside the grains. These are the same second-phase particles which appeared to be dark due to etched sample state in the BSE-SEM image shown in **Figure 4-23**. This suggests that chemical etching caused the particles to appear in dark in BSE-SEM image because those are likely to be dissolved. However in reality, those particles are enriched with heavy elements. These fine second-phase particles inside the grains have mostly a spherical morphology, an average size of roughly ~ 100 nm and are separated by roughly ~ 200 nm.

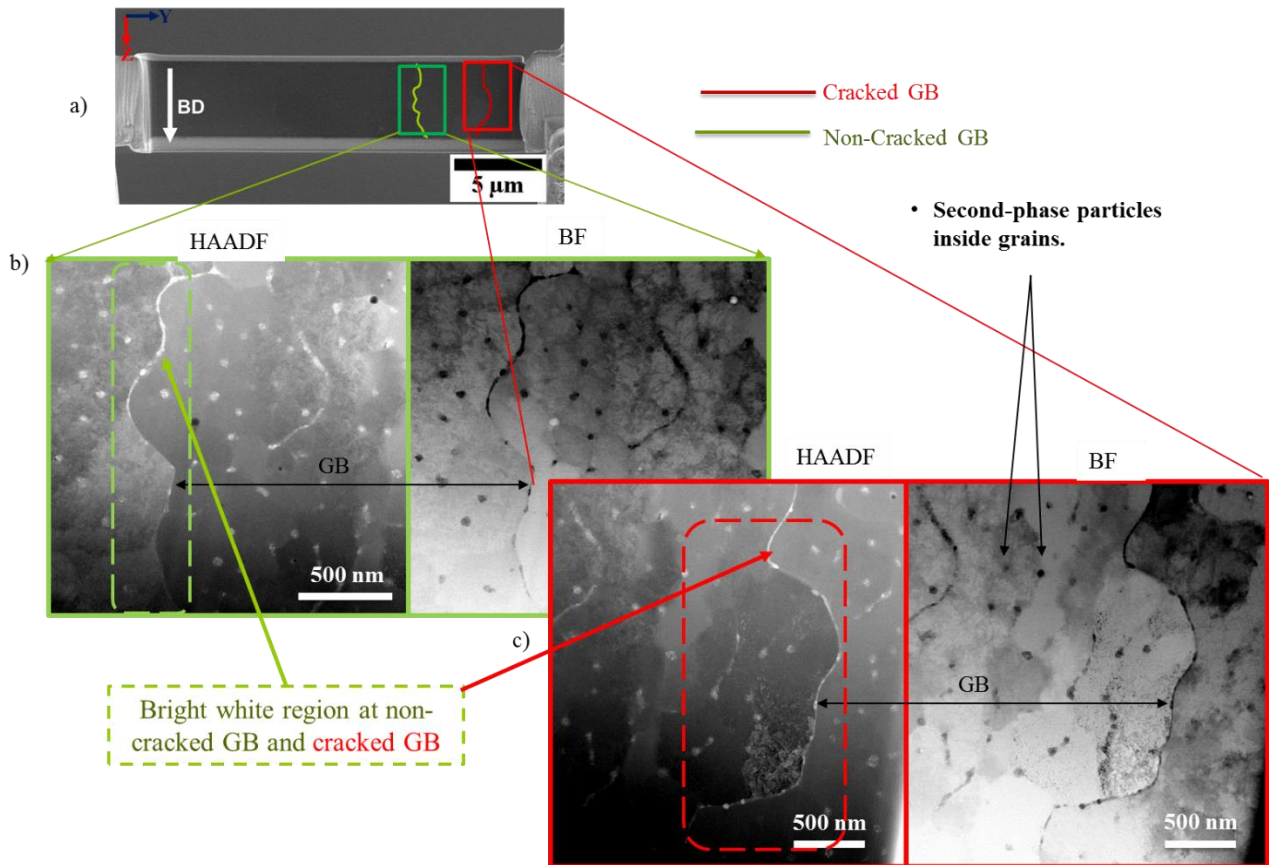


Figure 4-27 a) FIB lamella with cracked (red) and non-cracked GB (green). b) & c) HAADF (left) image and BF (right) image taken from a region including the non-cracked GB and cracked GB, respectively.

(i) Cracked GB

Figure 4-28a) shows the overview of the cracked GB along with HAADF and BF images. **Figure 4-28b) & c)** shows the magnified top and bottom region of the cracked GB, respectively. The HAADF image of the top region (**Figure 4-28b)** shows a continuous bright film decorating the GB. Besides, certain bright second-phase particles are also observed along the GB. Similarly, on the magnified image of the bottom region (**Figure 4-28c)**), the HAADF image shows the presence of bright-contrasted second-phase particles along the GB.

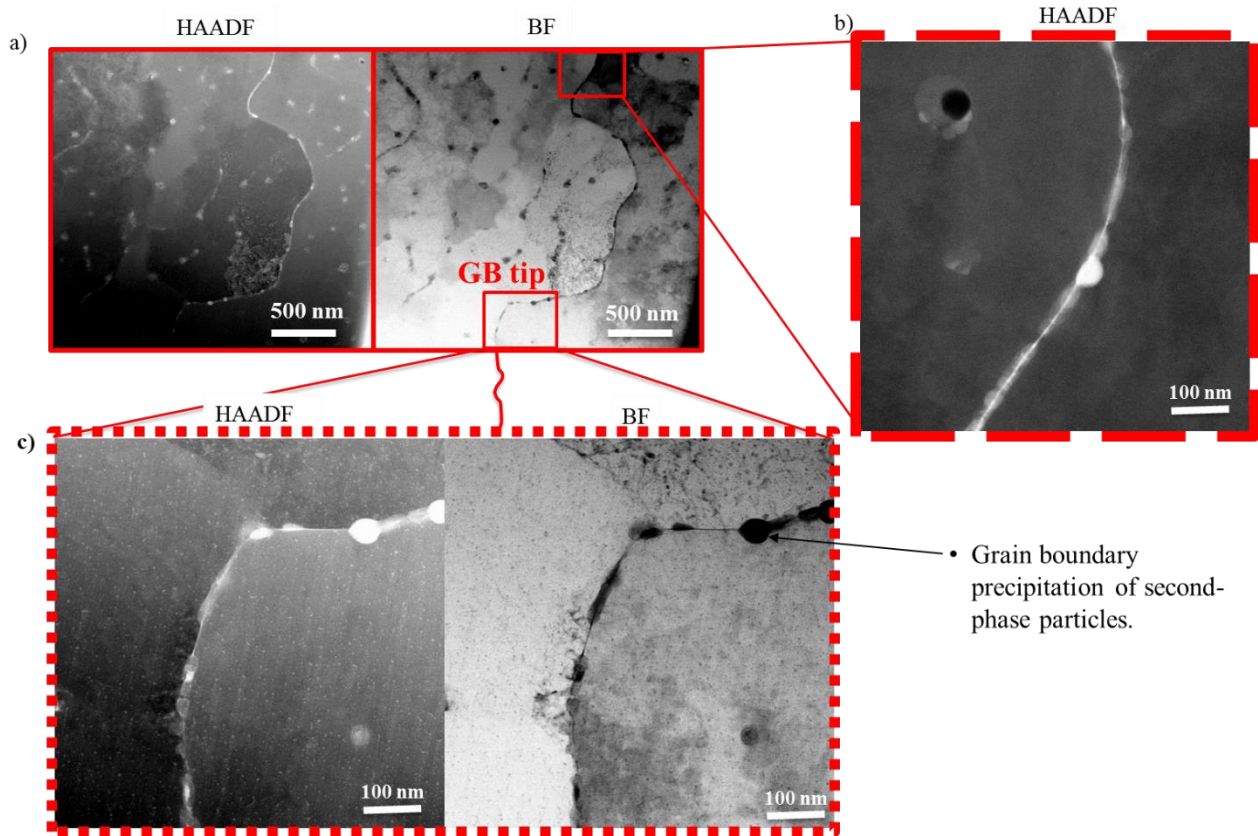


Figure 4-28 a) HAADF (left) image and BF (right) image of the cracked GB. b) HAADF image of the top region of the cracked GB. c) HAADF (left) image and BF (right) image of the bottom region of the cracked GB.

The STEM-EDX maps of **Figure 4-29** extracted from the cracked GB, show the distribution of different solute elements Si, Mg, Cu, Fe, Cr. There is high enrichment of Si/Mg/Fe along the GB. Similarly, Cu/Cr segregation is also observed along the cracked GB. **Moreover, the white rich second-phase particles along the GB observed in the HAADF image are identified as Si-Mg-Fe enriched particles along the grain boundary with few instances of Cu-rich particles as well.** These Cu-rich precipitates were only observed along the GB's and not in the Al-matrix. These Cu-rich phases are not perfectly circular, they are oval and have their size ranging between 40-60 nm. **Similarly, the homogeneously distributed second-phase particles in the matrix are majorly composed with Si/Mg/Fe with little Cu surrounding them.** These are also the elements that were found to decorate the GB's. Thus, no significant difference was observed between the second-phase particles along the GB's and inside the grain, except for the fact that Cu-rich second-phase particles were predominantly observed along the GB's. Moreover, we also see little evidence of oxygen, surrounding these second-phase particles. The presence of oxygen around these particles was probably the reason why Uddin *et al.* [3] concluded that these were Al-Si-O dispersoids. However, in reality, oxygen is not present in majority in comparison to Si/Mg/Fe elements in those second-phase particles. Thus, these majority of the second-phase particles are not in agreement with the Al-Si-O dispersoids reported by Uddin *et al.* [3].

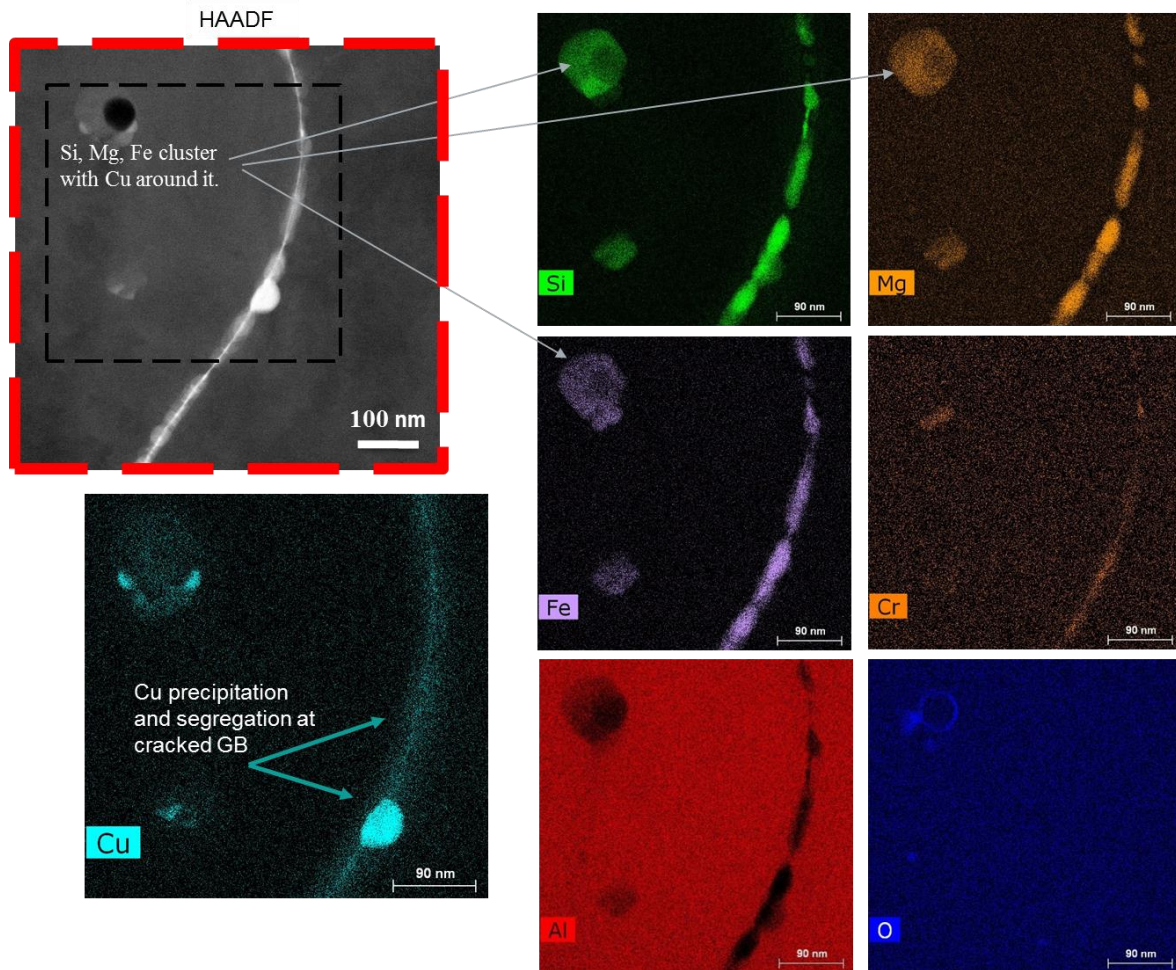


Figure 4-29 HAADF image of the top region of the cracked GB and the corresponding STEM-EDX maps showing various solute elements.

At another location within the cracked GB as shown in **Figure 4-30**, exactly similar segregations to the ones revealed in **Figure 4-29** were observed. Si, Mg, and Fe were found to segregate along the GB. Similarly, slight segregation of Cu and Cr was also observed in lines with the ones revealed in **Figure 4-29**. This indicates that the cracked GB was uniformly segregated along its entire observed length. In addition, a similar Cu-rich second-phase particle was observed along the cracked GB.

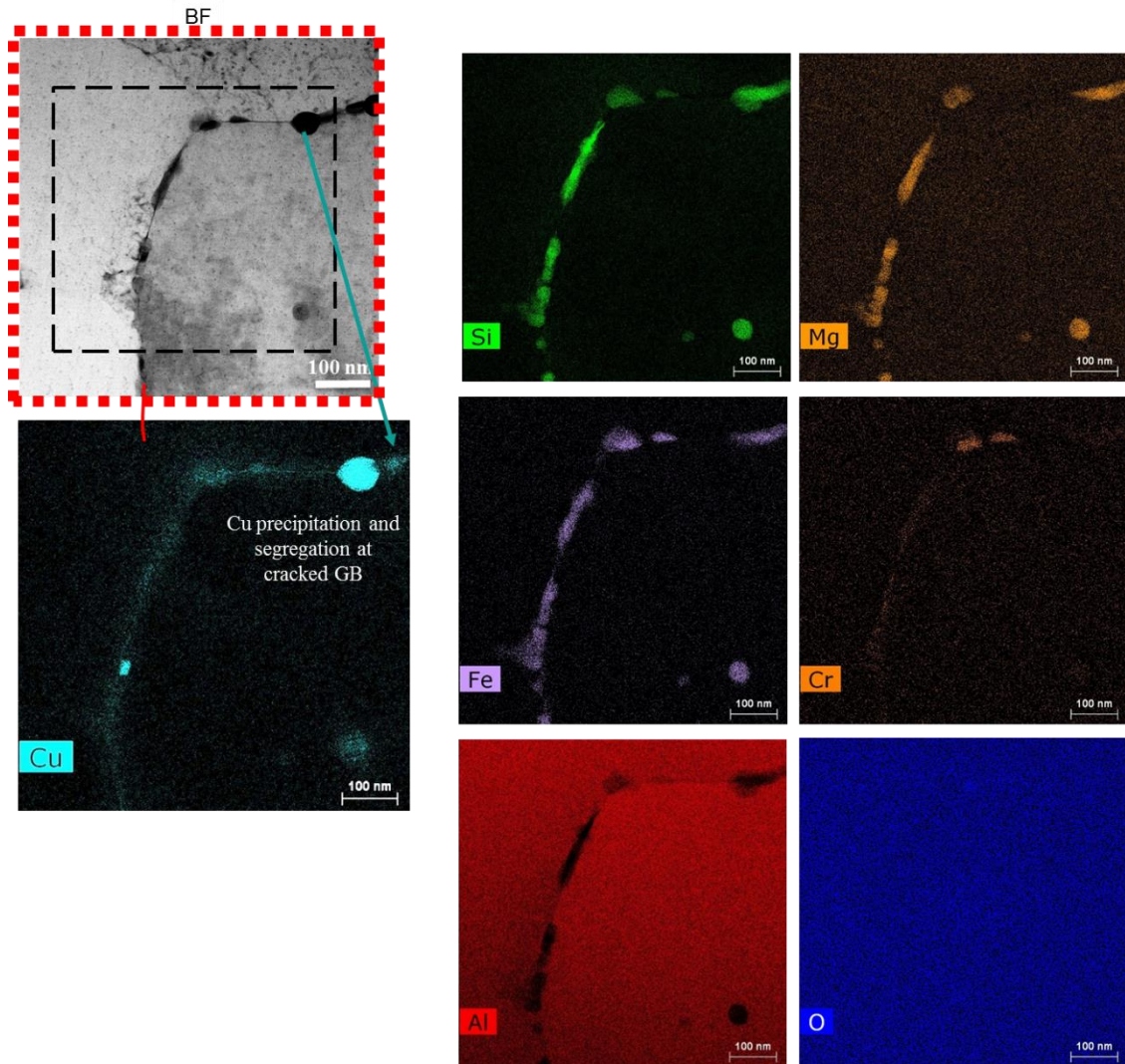


Figure 4-30 BF image of the bottom region of cracked GB and the corresponding STEM-EDX maps showing various solute elements.

(ii) Non-Cracked GB.

Figure 4-31a) shows the overview of the non-cracked GB and **Figure 4-31b)** gives a magnified image of its bottom region. The decoration of the non-cracked GB in the magnified image of **Figure 4-31b)** appears to be non-uniform, i.e. the bright region in the HAADF image is not continuous. However, looking at the low magnification HAADF image in **Figure 4-31a)**, the top region of the GB appears to be brighter than the bottom region. This explains why a non-uniform bright region in the magnified bottom part of the non-cracked GB was observed. It seems that the bright region observed along the GB in the HAADF image can be location specific and extracting conclusions must be dealt with care.

The top region of the non-cracked GB has some second-phase particles along its GB (see HAADF of **Figure 4-31a**) and the bottom region of the GB has no evidence of these particles (see HAADF of **Figure 4-31b**). However, to be able to validate these observations, further statistics would be required. For example, several non-cracked GB's must be studied to consolidate the results in terms of segregation and decoration by second-phase particles.

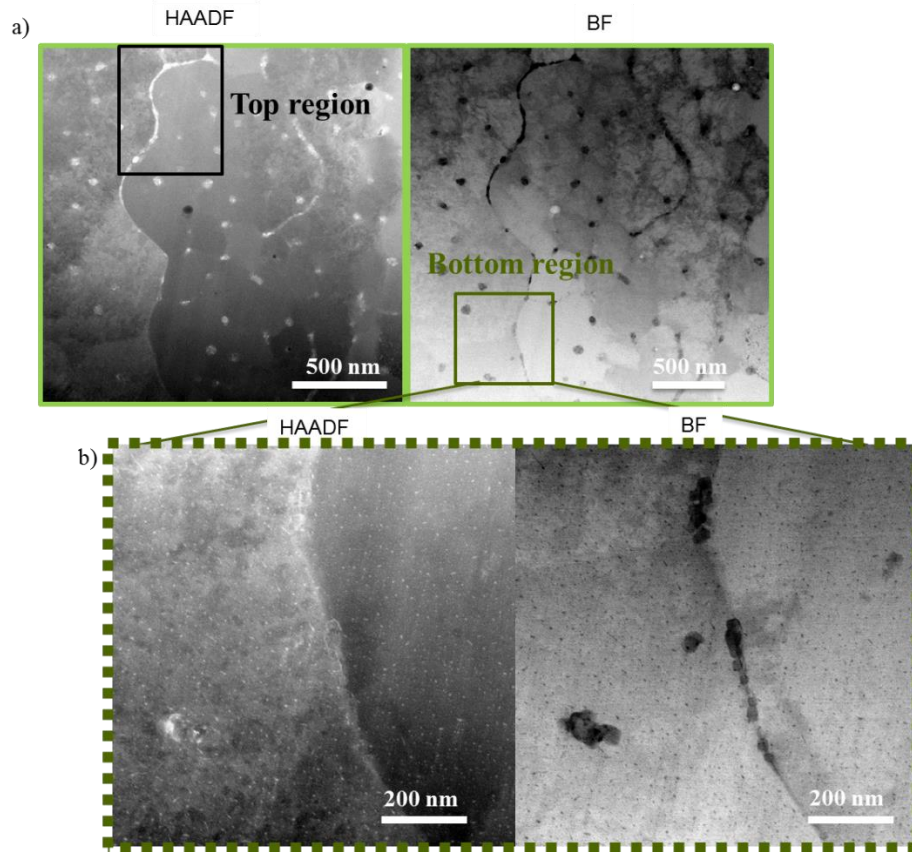


Figure 4-31 a) HAADF (left) image and BF (right) image of the non-cracked GB. b) High magnification region of the non-cracked GB, HAADF (left), and BF (right).

To verify the extent of solute segregation, STEM-EDX mapping for several solutes was performed on bottom part of the non-cracked GB, as shown in **Figure 4-32**. Of the solutes present in 6061 Al-alloy, Si/Mg/Fe were found to segregate along the non-cracked GB, but, non-uniformly. Again, this non-uniformity is arising due to the location where this EDX analysis was performed on the non-cracked GB. If the STEM-EDX analysis was performed on the top region of non-cracked GB, probably we would have seen exactly similar trend like the one observed for the cracked GB. This is also one of the reason for a lower level of Cu/Cr segregation observed in **Figure 4-32**, since the bottom region of non-cracked GB appears to be less segregated compared to the top. Thus, as raised previously, further statistics might be necessary. The second-phase particles present inside the grains (near the non-cracked GB) as seen in **Figure 4-32**, show the exact same chemistry as the one observed for the matrix in the vicinity of cracked GB's (see **Figure 4-29**). These second-phase particles inside the grain are always enriched in Si, Mg, and

Fe with Cu surrounding them. Thus to conclude, based on observations on only two GB's (cracked and non-cracked) we did not detect any significant differences in the nature of the second-phase particles.

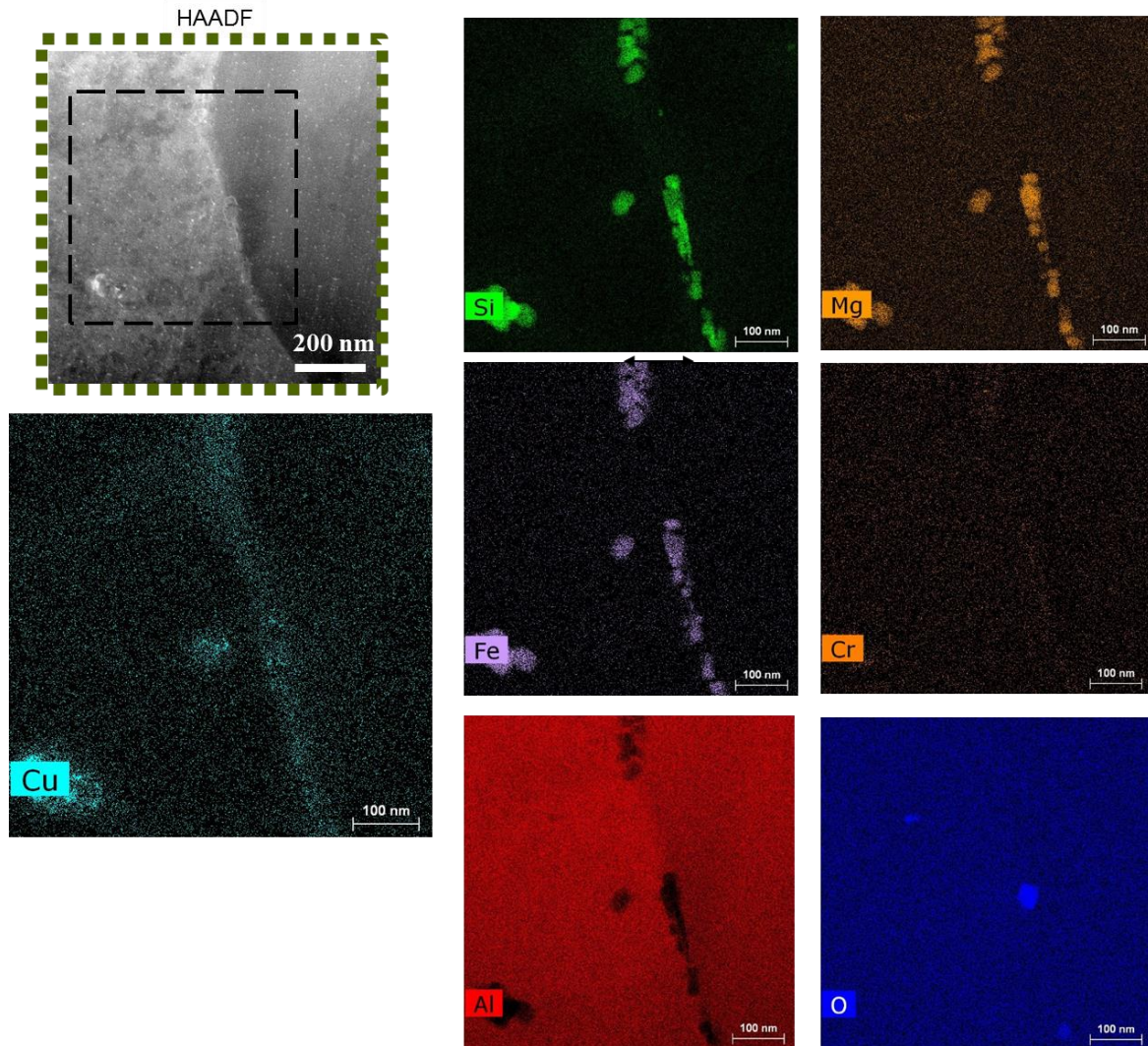


Figure 4-32 HAADF image of the non-cracked GB and the corresponding EDX maps showing various solute elements.

4.2.6. Microstructure: Discussion

According to the as-built microstructure presented in **Figure 4-23**, at first glance, it appears to be quite different compared to the casting and welding microstructures of **Figure 2-5** and **Figure 2-6** reported in the literature section of **Chapter 2**. The L-PBF microstructure contains a lot of cracks along high angle grain boundaries as shown in **Figure 4-23a**). Moreover, there is no evidence of the Chinese script morphology of second-phase particles along the grain boundaries. Also besides, the primary dendrite arm

spacing is smaller ($\sim 0.5\text{-}0.6\ \mu\text{m}$) compared to the other conventional processes ($100\text{-}200\ \mu\text{m}$)[141], this is due to the high cooling rates associated with the L-PBF process.

The multi-scale characterization study employed on the as-built 6061 Al-alloy going from macrostructure to microstructure was the first of its kind. In comparison to the reported literature on 6061 L-PBF, the present work reports various interesting features that were not reported before:

- Cracking location with respect to melt pools and their sensitivity to HAGBs positioned in the central region of the as-built 6061 Al-alloy. The centerline cracking and the HAGB cracking was well known in welding literature but not in the framework of L-PBF.
- The presence of second-phase particles located inside the grain and along the GB in the as-built microstructure was observed. Those are rich in Si/Mg/Fe with very less evidence of Cu are mainly present in Al-matrix. The ones along the GB's are enriched with similar elements: Si/Mg/Fe with presence of Cu-rich second-phase particles. These observations were based on TEM analysis along the GBs and not on SEM-EDX analysis as in the work of Uddin *et al.* [3] that claims the presence of Al-Si-O particles.
- Evidence of grain boundary segregation in the as-built 6061 Al-alloy was rarely reported prior to the present work. In comparison to the AlSi10Mg L-PBF microstructures, where only Si is found to readily segregate along the GB's, our observations for the 6061 Al-alloy suggest that other solutes (Mg, Fe, Cu and Cr) can also segregate along the columnar GB's. This observation is in agreement with the calculation done as a part of the study to estimate the partition coefficient of different solutes. Si, Mg, Fe, Cu and Cr were found to have a partition coefficient less than 1, suggesting their affinity to segregate in the interdendritic regions and along the GBs. In line with the literature, these solutes have a partition coefficient ($k=C_S/C_L < 1$) in Al, indicating less solubility in solid compared to liquid [142][141].

Speaking in terms of the possibility of these second-phase particles observed in 6061 alloy literature [72][73], the frequently reported phases are: $\alpha\text{-AlFeSi}$ ($\alpha\text{-Al}_3\text{Fe}_2\text{Si}$), Mg_2Si , and Al_2Cu . In the present study and the 6061 L-PBF literature (as-built condition), the presence of strengthening phases like Mg_2Si phase (β'' and β') was not observed. This probably resulted into a lower hardness ($\sim 55\text{-}60\text{HV}$) of the as-built 6061 Al-alloy, which is far less than the T6-condition hardness of 119 HV (refer to **Table 2-2**). According to the differential thermal analysis (DTA) analysis performed by Giraud *et al.* [73] on 6061 Al-alloy, the Fe containing phases were identified to form before any other phases (like Mg_2Si), during the solidification. Similarly, Cu-rich particles were observed along the GB's during the TEM analysis. In the literature, there are several instances where Al_2Cu second-phase particles have been reported in Cu-containing Al-alloys, see refs [143,144]. Thus, the observed Cu-rich second phase particles along the GB's in **Figure 4-29** could be the Al_2Cu phase. However, to be sure about all these possibilities, the diffraction pattern of these particles must be carefully analyzed.

4.3. Summary of Chapter 4.

- Using the powder layer experiments (1D-2D tracks), the processing regime was identified based on the stable fusion parameters without the presence of balling/humping. This was the first of its kind of process parameter optimization done for the 6061 Al-alloy in the L-PBF framework. No other reports in literature were found to perform such bottom-up optimization studies on the 6061 Al-alloy in the framework of L-PBF.
- Using the identified stable processing regime, cubes were fabricated using L-PBF. The sensitivity of defects (cracks and porosity) to processing conditions was performed and it was found that crack density tends to decrease with increasing linear energy density. Also besides, different types of porosities (metallurgical and lack of fusion) were identified in the as-built cubes and their sensitivity to processing conditions were discussed. The highest relative density of 98.5% was obtained for the process parameter (P: 240W, v_{laser} : 600mm/s, hatch: 100 μ , layer thickness: 20 μ , laser spot size: 70 μ) using a parallel scan strategy without rotation between the layers and thus was considered as “optimized”. The optimized parameters led to no lack of fusion defects but cracks were still present.
- Multi-scale characterization of the optimized 3D cube was performed. Inter-granular columnar cracking was observed and cracks were found to occur only along at HAGB's ($\theta > 15^\circ$). Cracks were systematically found to be in the central GB region, inside the melt pool.
- The ambiguity regarding the governing mechanism occurring during L-PBF of the 6061 Al-alloy was finally resolved. The cracking mechanism was identified as solidification cracking, thanks to the cellular dendritic morphology observed in the fracture surface as well as the occurrence of cracks in the topmost melt pool.
- Detailed microstructure analysis of the as-built 6061 microstructure was performed on several length scales using SEM/TEM analysis. Several second-phase particles were identified in the as-built samples in addition to GB segregation.

5. Developing cracking sensitivity criteria (based on RDG model)

In the previous chapter, we have resolved the ambiguity about the cracking mechanism and shown evidence of solidification cracking. Experimentally, we have identified two criteria for cracking to occur, namely, a) cracks specifically propagate along HAGB's and LAGB's are crack-free, b) cracks must be located along the central GB inside the melt pool.

This chapter focuses mainly on rationalizing experimental observations about cracking through thermal modeling and the use of hot cracking criterion. The chapter details the methodology used to provide the reasoning for cracking in 6061 grade during the L-PBF process and consequently establishes a cracking sensitivity criterion based on Rappaz, Drezet & Gremaud (RDG) model.

5.1. Rappaz, Drezet & Gremaud (RDG criterion)

Since the L-PBF of the 6061 Al-alloy encounters a solidification cracking mechanism as discussed in **section 4.2.4**, the RDG criterion is employed to evaluate the hot cracking sensitivity in the current study. Compared to various hot cracking models reported in the literature section, the Rappaz-Drezet-Gremaud (RDG) model is selected, since it can take into account the material parameters (solidification path: $f_s(T)$) and L-PBF process parameters (thermal gradients: G , solidification velocity: v).

The RDG criterion has been widely addressed in cracking issues of laser welding, see e.g. [89][96]. Rappaz *et al.* [7], proposed a hot tearing criterion that mainly deals with liquid films trapped inside the growing columnar dendrites. The criterion quantifies the pressure drop in the liquid located in the inter-dendritic region, which if falls below a critical cavitation pressure, can nucleate a void and eventually cause hot cracking. The total pressure drop (ΔP_{total}) results from two contributions: contraction of the solid with cooling (thermal strains), and shrinkage due to the difference of density between the solid and the liquid. As the liquid has no mechanical resistance, nucleation of a cavity in the presence of thermal strains leads to hot cracks. Thus, hot cracking can occur when the total pressure drop (ΔP_{total}) as mentioned in **equation 5.1**, exceeds a critical value ($\Delta P_{critical}$), i.e. no longer has the capacity to be fed by the liquid. **As a result, the hot cracking sensitivity can be directly related to the pressure drop in the liquid.** This pressure drop is given by:

$$\begin{aligned} \Delta P_{total} &= \Delta P_{deformation} + \Delta P_{shrinkage} \\ &= \frac{180(1+\beta)\mu}{\lambda^2 G} \int_{T_{gc}}^{T_l} \frac{E(T)f_s(T)^2}{(1-f_s(T))^3} dT \\ &+ \frac{180v\beta\mu}{\lambda^2 G} \int_{T_{gc}}^{T_l} \frac{f_s(T)^2}{(1-f_s(T))^2} dT \quad . \end{aligned} \quad (\text{equation 5.1})$$

$$\text{with } E(T) = \frac{1}{G} \int_{T_{gc}}^T f_s(T) \dot{\epsilon}(T) dT$$

$$L = \frac{T_l - T_{gc}}{G} \quad (\text{equation 5.2})$$

where ΔP_{total} is the total pressure drop in the liquid film, $\Delta P_{deformation}$ the pressure drop caused by thermal strains and $\Delta P_{shrinkage}$ the pressure drop due to shrinkage; β is the solidification shrinkage coefficient, μ the dynamic viscosity, λ the characteristic length of the microstructure (typically the secondary or primary dendrite arm spacing); G the thermal gradient, v the solidification front velocity, $f_s(T)$ is the fraction of solid as a function of temperature, **T_{gc} the coalescence temperature beyond which the feeding problem is no longer considered because the liquid film has collapsed into small drops (no continuous liquid films)**, T_l the liquidus temperature; $\dot{\epsilon}$ the strain rate of the solid normal to the dendrite growth direction (which will be assumed to be temperature independent in our calculations), and, L is the length of the mushy zone. According to the definition of the mushy zone, it is defined as $T_l - T_{solidus}$,

however, here we define it as $T_1 - T_{gc}$ because we consider that once the temperature reaches T_{gc} , the liquid remains only as liquid pockets.

The integrals in **equation 5.1**, runs from the temperature of T_{gc} to T_1 , which are considered here as the bounds to define the mushy zone. Thus, the length of the mushy zone (L) that is embedded between these bounds, is given by its temperature difference divided by the thermal gradient, as mentioned in **equation 5.2**.

The model input parameters are the solidification path (given by the solid fraction f_s as a function of temperature for the 6061 Al-alloy), the thermal gradient G and solidification front velocity v , the characteristic length of the microstructure (primary or secondary dendrite arm spacing λ), and, the coalescence temperature T_{gc} . These inputs, in the current study, will be best rationalized in the following sections by taking into account the experimental observations (cracking along HAGBs and position of the crack within the melt pool) and utilizing the solidification conditions typical of L-PBF with the help of the Rosenthal calculations.

5.2. Thermodynamic calculations.

In our study, the software FactSage [145] with the *Equilib* module was used to run the solidification calculations on the 6061 Al-alloy chemical composition, provided in **Table 3-1**. Using an *FTlite* element database, the Scheil –Gulliver model was used to predict the solidification path and understand the phase formation. Several compounds and solution phases were excluded, to retain only phases that were reported in the literature [146]. Thus, only α -Al, Mg₂Si, and Si were retained in our calculations describing the solidification of the 6061 alloy. Using Scheil-Gulliver assumptions [63] which assume infinite diffusion in liquid, no diffusion in solids, and equilibrium at the solid/liquid interface. The theoretical understanding of the model is detailed below.

5.2.1. Introduction to Scheil-Gulliver Model.

During solidification of an alloy in liquid state having a uniform composition, the final solid is barely with a uniform composition. The solutes present in the alloy tend to redistribute themselves, and this redistribution depends on the alloy thermodynamics, phase diagram, fluid flow, etc [81]. Thus to best describe the thermodynamics of the L-PBF process, we used the Scheil Gulliver model, which does not take into account the diffusion in solid and considers infinite diffusion in liquid.

At the beginning of solidification, the first solid to form has kC_0 as its composition, where k is the partition coefficient defined as ($k = C_s/C_L$), where C_s refers to solid composition, C_L is liquid composition and C_0 is the composition of alloy. The value of k depends on the temperature. It also depends on the

solidification velocity [147], but to obtain k as a function of solidification velocity needs important research efforts, which is considered out of the scope.

At an intermediate temperature, the solid and liquid have C_S and C_L composition, respectively. Since diffusion in solid is neglected, the solid composition rises from kC_0 to C_S , while the liquid stays homogenized at C_L . It must be noted that C_L and C_S will also vary as a function of temperature according to the given phase diagram, and thus they vary as a function of the solid fraction (f_s). During solidification, the amount of solute must be conserved, i.e. the content of solute in liquid and solid, should equal the initial content of solute in liquid before the solidification starts. By performing such mass balance, one can obtain **Equation 5.3**, which is referred to as the Scheil equation [81].

$$C_S = kC_0 (1 - f_s)^{k-1} \quad \text{or} \quad C_L = C_0 (1 - f_s)^{k-1} \quad (\text{equation 5.3})$$

Equation 5.3 can be written as **Equation 5.4** to obtain the solid fraction (f_s) as a function of given temperature, since $C_L(T)$ and $C_S(T)$.

$$f_s = 1 - \left[\frac{C_0}{C_L} \right]^{\frac{1}{1-k}} \quad (\text{equation 5.4})$$

It must be pointed out that, in comparison to equilibrium solidification, where at any moment in time, the composition of solid and liquid is uniform, the Scheil model always predicts the solute segregation (depending on the value of k). Moreover, solute trapping is also not considered with the Scheil-Gulliver model.

Finally, the Scheil-Gulliver model can be applied to the multi-component system like 6061 Al-alloy. With the help of the Scheil model and its implementation in FactSage software, it is possible to estimate:

1. Solidification path of the alloy, $f_s(T)$
2. The sequence of phase formation.
3. Composition of liquid and solid as a function of solid fraction.
4. Composition of phases as a function of solid fraction.

5.2.2. Solidification path of 6061 Al-alloy (f_s)

Figure 5-1 shows the predicted temperature as a function of the solid fraction for the alloy investigated in this work. The liquidus temperature is $T_{\text{liquidus}}(f_s=0) = 652^\circ\text{C}$, the coalescence temperature is $T_{\text{gc}} = 558^\circ\text{C}$, taken here at $f_s=0.97$ (fraction of coalescence determined experimentally for the 6061 Al-alloy, see [73]) and the solidus temperature is $T_{\text{solidus}}(f_s=1) = 510^\circ\text{C}$. These data will be used as input in the RDG

model. Using Scheil-Gulliver assumptions, the solidification temperature range $T_1 - T_{\text{solidus}}$ is about 142°C and with equilibrium solidification, it is around 67°C .

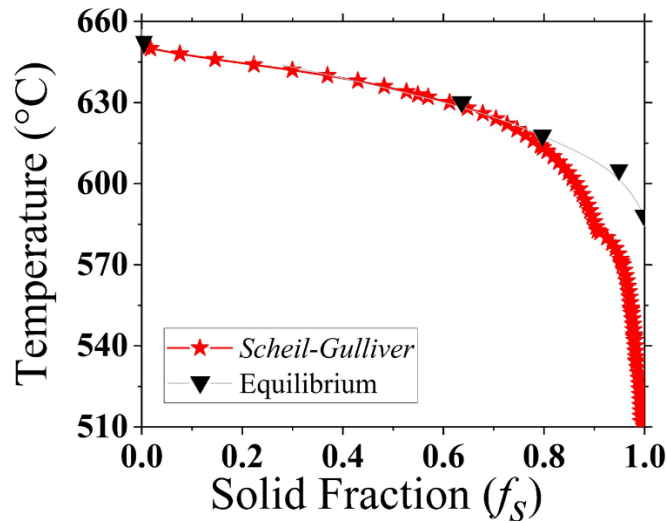


Figure 5-1. Solidification path of the 6061 Al-alloy, showing the solidification path $T(f_s)$ using Scheil-Gulliver assumptions (no diffusion in solid and infinite diffusion in liquid).

5.3. Rationalizing cracking at HAGB's

According to **equation 5.1**, to predict the cracking sensitivity by estimating the pressure drop, it is necessary to get an estimation of T_{gc} . The standard RDG model does not consider the role of grain boundaries misorientation on the hot cracking sensitivity. Since the RDG model was formulated for a growing dendrite. As shown in refs [6,85], the presence of high angle grain boundaries makes liquid film stables at lower temperatures. To include this effect, we apply the theoretical coalescence model during the last stages of solidification, see the pioneering work in [6].

5.3.1. Coalescence undercooling

The Coalescence model developed by Rappaz *et al.* [6] predicts that for a grain boundary with high misorientation (HAGB), the coalescence temperature will undergo an additional undercooling that will further decrease its coalescence point. This coalescence undercooling denoted by $\Delta T_{\text{undercooling}}$, is responsible for lowering of T_{gc} , strongly depends on the grain boundary energy (γ_{gb}) and solid-liquid interface energy ($\gamma_{\text{s-l}}$).

The coalescence undercooling ($\Delta T_{\text{undercooling}}$) is often described as the difference between the coalescence temperature for attractive GB and repulsive GB. Here, the term ‘attractive GB’ refers to the boundaries that do not require any energy to bridge; as soon as they are near each other (within the thickness of the solid-liquid interface, δ), they coalesce. In other words, an attractive GB do not need any undercooling for bridging whereas a ‘repulsive GB’s’ needs further activation energy in the form of undercooling to bridge themselves. These boundaries are therefore classified according to their grain boundary energies (γ_{gb}) based on the following conditions mentioned in [6]:

- attractive GB: $\gamma_{\text{gb}} < 2 \cdot \gamma_{\text{s-l}}$,
- repulsive GB: $\gamma_{\text{gb}} > 2 \cdot \gamma_{\text{s-l}}$.

To explain the above relations, consider the case for repulsive GB’s and where the thickness of liquid film (h) is diminishing, between the two grains of different misorientations, as shown in **Figure 5-2**. When the liquid film thickness (h) is high, i.e. the solid-liquid interfaces are separated by a distance ‘ h ’, the excess free energy of the system is denoted by the two contributions from two solid-liquid interfaces, adding the total to $2 \cdot \gamma_{\text{s-l}}$. When the liquid film thickness gets closer to 0 ($h \rightarrow 0$), i.e. the coalescence happening between the two dendrites from neighboring grains, the excess free energy equals the grain boundary energy (γ_{gb}). Since it is the case for misoriented grains, i.e. $\gamma_{\text{gb}} > 0$, an additional undercooling is required to make the liquid film unstable and promote coalescence. However, for the case where dendrites belonging to the same grain ($\gamma_{\text{gb}} = 0$), i.e. no mutual misorientation, as soon as the liquid film thickness reaches the critical value δ , there is a gain in the energy of the system, which is utilized to solidify the last liquid film. Thus, making it ‘attractive’ in nature. Thus depending on the misorientation of dendrites between two neighboring grains, they can be classified as attractive or repulsive.

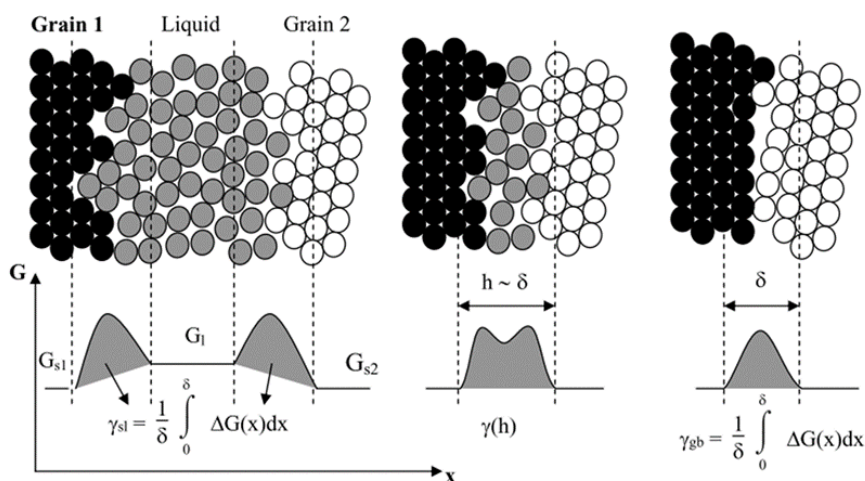


Figure 5-2. Atomistic view of liquid film thickness diminishing between the two neighboring grains ($\theta \neq 0$) during coalescence and schematic of excess free Gibb’s energy as a function of location, adapted from [85].

As shown in **Figure 5-3a**), typically γ_{gb} increases as a function of the misorientation angle θ until reaching a given misorientation (without considering the coincident site lattice (CSL) grain boundaries or Σ GB's). Therefore, $\Delta T_{\text{undercooling}}$ also depends on the misorientation. As shown in **Figure 5-3b**), two coalescence temperatures can be considered for dendrites belonging to the attractive boundaries or repulsive boundaries. For the dendrites belonging to the same grain (attractive GB), i.e. the mutual misorientation is low enough for them to coalesce immediately when the temperature reaches T_{gc} . On the other hand, for dendrites belonging to different grains (repulsive GB), i.e., having high mutual misorientation, they will coalesce at a later stage. This delay in coalescence for dendrites from two different grains, with high misorientation (HAGB's) makes the liquid film persist at temperatures below T_{gc} .

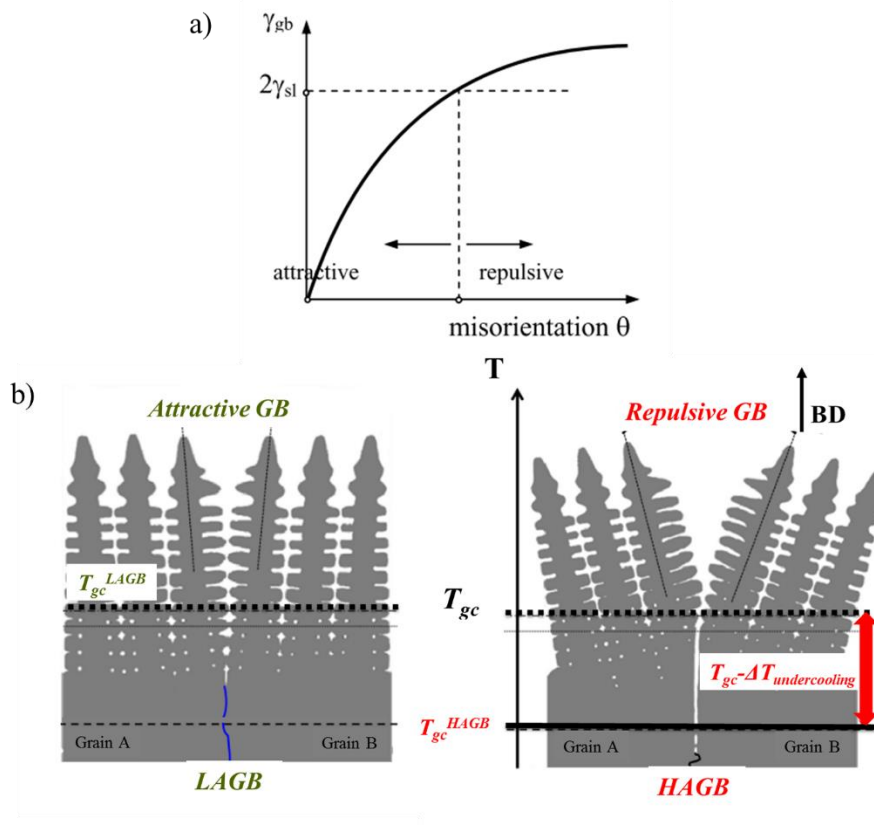


Figure 5-3 a)Schematic of grain boundary energy as a function of misorientation angle (θ) [85]. b) illustration showing the columnar dendrites growing with different misorientation, adapted from ref.

As a result, according to Rappaz's coalescence model, the HAGBs will bridge at a lower T_{gc} due to this coalescence undercooling, compared to LAGBs. Introducing this coalescence undercooling in the RDG criterion allows the influence of GB misorientation on cracking sensitivity to be evaluated. Here, we assume that the coalescence for the 6061 Al-alloy happens at a given temperature estimated based on the solidification path taken at $f_s = 0.97$ [73], and the additional contribution arising from this coalescence undercooling effect is estimated using **equation 5.5**.

$$\Delta T_{\text{undercooling}} = \frac{\gamma_{gb} - 2\gamma_{s-l}}{\Delta S_f \delta} \quad (\text{equation 5.5})$$

where, γ_{gb} is the grain boundary energy; γ_{s-l} is the solid-liquid interfacial energy; ΔS_f is the entropy of fusion, and δ is the thickness of solid-liquid interface. However, to predict the coalescence undercooling, a better estimation of grain boundary energy as a function of misorientation angles is needed. The following sections will discuss the methods analyzed to obtain the $\gamma_{gb}(\theta)$.

5.3.2. Estimating grain boundary energy $\gamma_{gb}(\theta)$

To estimate the grain boundary energy (γ_{gb}) as a function of the misorientation angle, various methods have been reported. N. Wang *et al.* [89] used the theoretical model of Read-Shockley [148] which is based on dislocation theory. Grain boundary is a defect in the crystal orientations, which has excess free energy per unit area. Read and Shockley [148], came up with an idea of assessing the grain boundary anisotropy. They considered the tilt grain boundary to be composed of several edge dislocations. Since edge dislocations possess certain energy, the energy of the tilt grain boundary is nothing but the individual sum of energies of each dislocation along with their interaction energy. By increasing the misorientation, the number of edge dislocations will increase linearly, thereby increasing the energy of the GB. However, the model of Read-Shockley does not take into account the intra dislocation interactions and thus needs a high separation between neighboring edge dislocations to neglect their contribution. This makes the model only valid for small misorientation less than 15° . **Equation 5.6**, denotes the grain boundary energy according to the dislocation model of Read-Shockley [148].

$$\gamma_{gb} = \frac{G_s b \theta}{4\pi(1-p)} * \left(1 - \ln \frac{\theta}{\theta_m}\right) \quad (\text{equation 5.6})$$

where, γ_{gb} is the grain boundary energy; b is the burgers vector; G_s is the Shear modulus, p is the Poisson's ratio and θ_m is the misorientation angle at which γ_{gb} is maximum. Thus, depending on the selected θ_m , the γ_{gb} can be estimated as a function of θ until θ reaches θ_m . **Table 5-1** summarizes the constants used to estimate γ_{gb} using the Read-Shockley model.

Table 5-1 Constants for pure Al used to estimate grain boundary energy (Read-Shockley model [148])

Constants	Value
b (Burgers vector)	2.85×10^{-10} m [149]
G_s (Shear modulus)	2.6×10^{10} N/m ² [149]

ν (Poisson's ratio)	0.33 [149]
-------------------------	------------

Figure 5-4 shows the estimated grain boundary energy for 6061 Al alloy using **equation 5.6**. For increasing values of θ_m , the $\gamma_{gb}(\theta)$ increases, similar to the schematic of **Figure 5-3**. Thus, Read-Shockley is an option to be employed in present study but the model is valid only for small misorientation angles. To obtain data reporting the GB energy vs misorientation for Aluminum, further literature was looked upon.

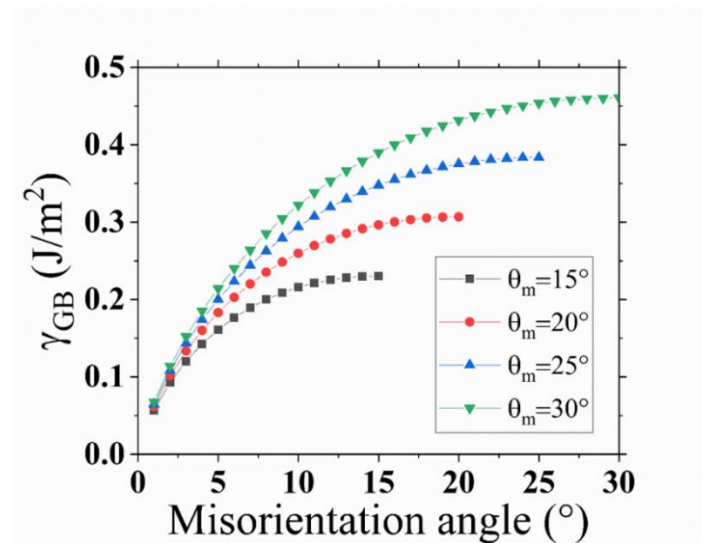


Figure 5-4 Grain boundary energy as a function of misorientation angle (based on estimation using the Read-Shockley model)

Another method to calculate the grain boundary energy is using atomistic simulations. M. A Tschopp *et al.* [150] employed atomistic simulation to estimate $\gamma_{gb}(\theta)$ for pure Aluminum, which can be applied even in the high misorientation regime. Since the current study deals with sensitivity towards HAGB, $\gamma_{gb}(\theta)$ for pure Aluminum was adapted from the simulations mentioned in refs [150][151], as shown in **Figure 5-5** (a). The grain boundary energy $\gamma_{gb}(\theta)$ is plotted for various tilt boundaries oriented in different directions. **There is a transition from attractive GB to repulsive GB when: $\gamma_{gb} = 2 \cdot \gamma_{s-l}$, which corresponds, for Aluminum, to a misorientation of roughly $\theta_{a-r} = 5^\circ$ ($\gamma_{s-l}(\text{Al}) = 0.12 \text{ J/m}^2$). θ_{a-r} is defined as the misorientation angle corresponding to the transition from attractive to repulsive interfaces.** Thus, two regimes can be distinguished in the $\gamma_{gb}(\theta)$ curve: (i) attractive GBs for misorientation $< 5^\circ$, and, (ii) repulsive GBs for misorientation larger than 5° . It should be also noted that the $\gamma_{gb}(\theta)$ reaches a plateau for misorientations close to 20° . Note that the averaged $\gamma_{gb}(\theta)$ from **Figure 5-5a**) is not far from the one

predicted by the Read-Shockley model in **Figure 5-4** for $\theta_m=30^\circ$. **The averaged fitting of the three tilt boundaries shown in Figure 5-5a) was finally used to define $\gamma_{gb}(\theta)$.**

To estimate the coalescence temperature for repulsive GBs using **equation 5.5**, parameters given in **Table 5-2** (for pure Al) were used along with $\gamma_{gb}(\theta)$ taken from **Figure 5-5a)**. It is also important to point out that, the presence of solutes affect the quantities mentioned in **Table 5-2** and **Figure 5-5a)**, due to multiple effects such as segregation effects. It cannot be excluded either that the segregation extent might depend on misorientation (especially in the misorientation range from 5 to 15° , regime in which the grain boundary energy varies substantially), and it certainly affects interface energy values (γ_{gb} but also γ_{s-l}). However, taking these factors into account is a very difficult task requiring important research efforts that have been considered out of the scope of the current study.

Table 5-2 Constants used to estimate coalescence undercooling.

Constants	Values /empirical law
γ_{s-l} (S/L interfacial energy)	0.12 J/m^2 [152]
ΔS_f (Entropy of fusion)	$1.11 \times 10^6 \text{ J/m}^3\text{K}$ [153]
δ (thickness of solid-liquid interface)	10^{-9} m [89]

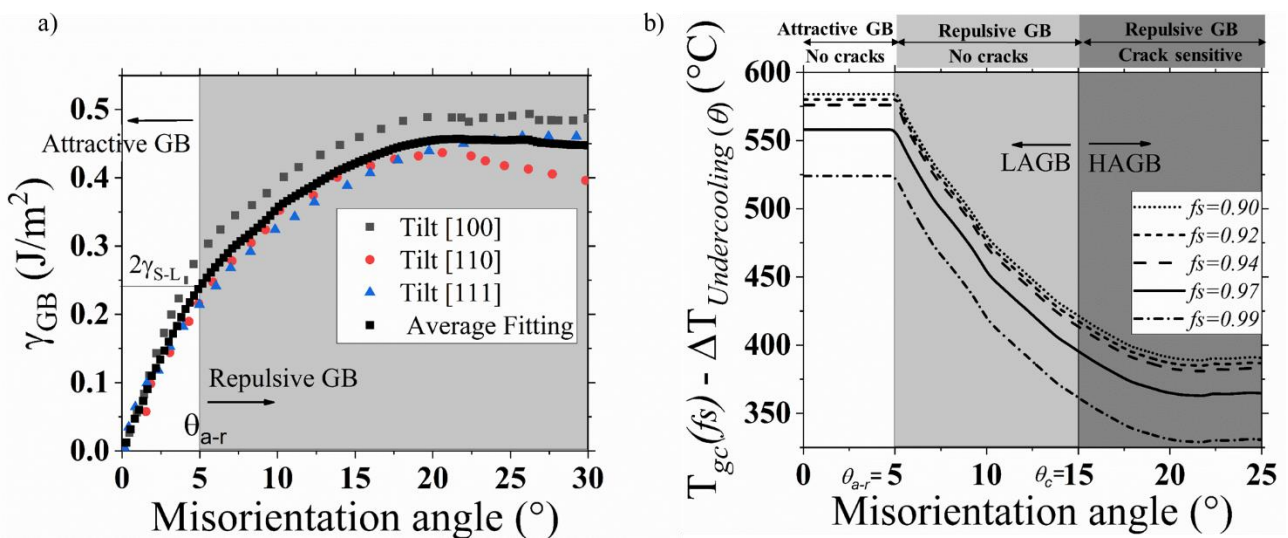


Figure 5-5. a) Grain boundary energy of pure Aluminum for different tilt boundaries as a function of misorientation angle [150][151]. b) Effect of misorientation on the dendrite coalescence temperature.

The lowering of the grain coalescence temperature due to the coalescence undercooling is shown in **Figure 5-5b**). The coalescence temperature for attractive GBs ($\theta < 5^\circ$) was estimated using the solidification path shown in **Figure 5-1**, for various solid fractions ($0.90 \leq f_s \leq 0.99$) in the critical temperature range (last stages of solidification). As discussed previously, the lowering of T_{gc} , happens only for repulsive GB's ($\theta > 5^\circ$). Thus, with the help of estimated $T_{gc}(\theta)$, the lower bound of the integrals in **equation 5.1**, can be updated to include the dendrite coalescence undercooling that changes with misorientation to predict the cracking sensitivity of HAGB using the RDG criterion. To summarize, with the help of coalescence undercooling of HAGB's, the effective coalescence temperature at $f_s=0.97$ as mentioned in **Figure 5-5b**), is used as an input to define $T_{gc}(\theta)$; thereby including the misorientation aspect into the RDG criterion.

5.4. Estimating solidification conditions typical of L-PBF (thermal gradient and solidification velocity)

Apart from material inputs like solidification path and coalescence temperature, process inputs are also needed to apply the RDG criterion in the context of AM. The solidification process inputs mentioned in **equation 5.1** are thermal gradients (G) and solidification velocity (v). However, the L-PBF process is controlled by the first-order melting parameters, namely the laser power (P) and speed (v_{laser}). Thus, it is important to make a direct link between these first-order melting parameters (P, v_{laser}) and the solidification conditions(G, v). To do so, the Rosenthal analytical solution was implemented.

5.4.1. Introduction to Rosenthal analytical solution.

An analytical Rosenthal solution [28] is used in the current study and implemented on COMSOL Multiphysics software [154]. This solution captures the basic physics required to estimate the solidification parameters (thermal gradient and solidification velocity) as a function of the laser energy input. The Rosenthal model was chosen over other more complex numerical models, the idea being to capture the correct order of magnitude. Thus to simplify, the solution was applied on a laser scanned bulk 6061 Al-alloy substrate and not on the powder bed. The analytical solution evaluates the temperature field in a bulk substrate when it is subjected to a moving point heat source. **Equation 5.7** gives the temperature field of a point location (x, y, z) with respect to the moving heat source (along x-direction), here in our case, the laser.

$$T(x, y, z) = T_0 + \frac{\eta P}{2\pi k \sqrt{x^2 + y^2 + z^2}} \times e^{\left(\frac{-v_{laser}(x + \sqrt{x^2 + y^2 + z^2})}{2\alpha}\right)} \quad (\text{equation 5.7})$$

Where, T is the temperature, (x, y, z) is the position in the (X, Y, Z) coordinate system, T_0 is the temperature of the substrate, P is the laser power, η is the absorptivity coefficient, k is the thermal conductivity, v_{laser} is the laser scanning speed and α the thermal diffusivity of the material.

The thermal properties used for the study are assumed to be constant and independent of temperature. This equation ignores the effect of the latent heat of fusion as well as heat fluxes in the liquid (convection).

The term $\sqrt{x^2 + y^2 + z^2}$ in **equation 5.7**, refers to the radial distance of the point from the laser beam; whereas, 'x' denotes the distance of the point from the laser beam along the scanning direction. Optimized processing parameters P and v_{laser} , mentioned in **section 4.1.4** are used as inputs in the Rosenthal equation to compute the thermal fields considered as typical of L-PBF. T_0 refers to the initial temperature of the bulk substrate, which in the case of 'no preheating', is taken as 293 K.

From the temperature fields, the thermal gradient (G) within the melt pool and the mushy zone is estimated using the gradients in all three dimensions, for a given point. The thermal gradient (G), is expressed as:

$$G(x, y, z) = \sqrt{[G_x(x, y, z)]^2 + [G_y(x, y, z)]^2 + [G_z(x, y, z)]^2} \quad (\text{equation 5.8})$$

where, G_x , G_y , and G_z are the thermal gradients along x, y, and z-direction, respectively. The next useful solidification parameter is the solidification velocity (v), which is geometrically related to the laser scanning speed (v_{laser}), and melt pool shape [155], as:

$$v(x, y, z) = v_{laser} \cdot \cos(\theta(x, y, z)) = v_{laser} \cdot \frac{G_x(x, y, z)}{G(x, y, z)} \quad (\text{equation 5.9})$$

where θ is the angle between laser scanning direction and the solidification front velocity (velocity of the liquidus isotherm), as shown in **Figure 5-6**. Since v_{laser} is along the x-direction, $\cos(\theta)$ is substituted to G_x/G , as mentioned in **equation 5.9** to compute the solidification velocity.

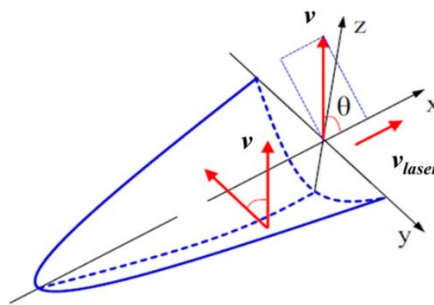


Figure 5-6 Geometrical relation between the solidification velocity and the laser scanning speed, on a melt pool schematic, adapted from [120].

5.4.2. Rosenthal simulations

The thermal gradient (G) and solidification velocity (v) corresponding to **the optimized L-PBF melting parameters namely: $P= 240W$ and $v_{laser}= 600$ mm/s are estimated.** Table 5-3 gives all the parameters used to perform the Rosenthal calculations based on **equation 5.7**. The melt pool boundaries are estimated from the temperatures predicted by the Rosenthal equation. Key temperatures in the mushy zone (all the combinations of x,y,z points satisfying: $T_s < T(x, y, z) < T_l$) can also be plotted considering the temperatures estimated based on the Scheil-Gulliver solidification calculations.

Table 5-3 Constants used for Rosenthal analytical simulations.

Constants	Values
Laser speed (v_{laser})	600 mm/s
Laser Power (P)	240 W
Thermal conductivity (k)	167 W/(m K) [131]
Specific heat capacity (C_p)	897 J/(kg K) [131]
Density (ρ)	2700 kg/m ³ [131]
Thermal diffusivity ($\alpha = \frac{k}{\rho C_p}$)	6.89 x 10 ⁻⁵ m ² /s

Since the analytical solution was applied on a bulk substrate, it is important to calibrate the Rosenthal model to obtain the correct melt pool dimensions. The laser scanned bulk substrates (sand-blast), (see **Appendix**) were used to compare the melt pool depth estimated using Rosenthal solution. To remind, the measured total reflectivity of the rough ($Ra=6\mu m$) sand-blasted bulk substrates was $\sim 41\%$ (for a $\lambda=1064nm$) and was quite close to the reflectivity of the powder sample, as shown in **Figure 4-2**.

The measured melt pool depth for the bulk substrate was found to decrease with the increasing laser speed. Comparing the measured maximum melt pool depths to the ones estimated using Rosenthal analytical solution for different v_{laser} : 200 mm/s, 600 mm/s and 1000 mm/s as shown in **Figure 5-7**, the effective power transferred to the material was about 60% of the 240W, **giving an absorptivity coefficient of 0.6**, similar to the reported value in ref. [156]. This estimated absorptivity to update the thermal simulations is also in line with the measured absorptivity ($100-41(\text{reflectivity})= 59\%$) for the bulk substrate, see **Figure 4-2**. This sensitivity analysis helps to better replicate the actual melt pool formed during laser melting.

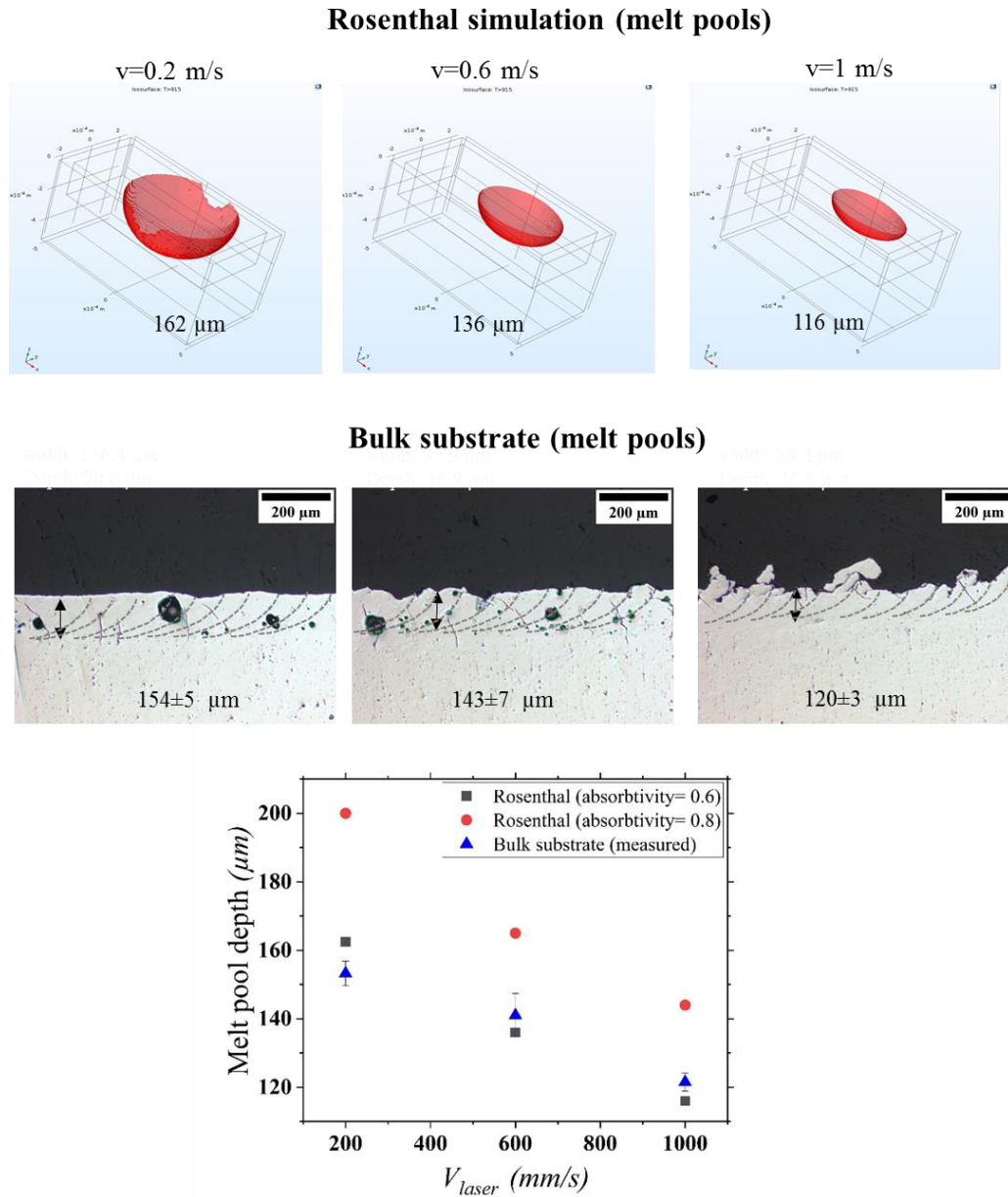


Figure 5-7 (Top) Estimated melt pool depths using Rosenthal simulation and experimentally verified melt pool depths on the bulk substrate (middle) for different laser speeds (v_{laser}). The bottom graph shows the variation in melt pool depth as a function of v_{laser} for different absorptivity coefficients (η): 0.8 and 0.6.

Using the obtained absorptivity coefficient of 0.6 along with the constants mentioned in **Table 5-3**, thermal gradients (G) fields in different planes (ZX , XY , and ZY) were obtained as shown in **Figure 5-8**. The thermal gradients were obtained according to **equation 5.8**. The three planes can be categorized with respect to the Cartesian coordinate system in which the laser direction is along the X -axis. The XY -plane denotes the top surface of the substrate and the ZX plane (longitudinal) denotes the cross-section of the XY -plane at $Y=0$, meaning the central cross-section along the direction of the laser. Similarly, if we make

cross-sections of the ZX-plane at different X- coordinate, we can obtain various-ZY planes (transverse) in which the laser is supposed to move perpendicularly to the ZY-plane.

On each contour, various iso-temperature dotted lines are marked, namely: red for T_{liquidus} at ($f_s=0$) = (652°C), green for T_{gc} at ($f_s=0.97$) = (558°C) and black for T_{solidus} at ($f_s=1$) = (510°C). These temperature dashed contour lines help to visualize the melt pool. Since the laser moves along the X-direction, the region on the right extremities of the G-contours tends to have higher thermal gradients compared to the left extremities, as shown in **Figure 5-8**. Thus, indicating the right extremities to be in the process of melting and left one to be solidifying. The thermal gradients are in the range of 10^6 - 10^8 K/m in both the XY and ZX-planes. However, depending on the location of the cross-section in ZX-plane, the transverse ZY plane can have varying G values. For example starting from the cross-section plane ZY near to the laser spot (denoted by highest G, in the red spot) and moving away from the melting zone, the thermal gradients continuously show a decreasing trend. Moreover, the maximum depth of melt pool, calculated on the $f_s=1$ 'black dashed line', also diminishes in ZY-plane located at left extremities (i.e. **Figure 5-8c**) compared to the ZY-plane where melting is predominant (i.e. **Figure 5-8f**). It should be also noted that, in all the planes, the maximum (G_{max}) is inside the liquid, i.e. when $T > T_{\text{liquidus}}$.

Similarly, a study has been done to evaluate the solidification velocity (v) for $P=240\text{W}$ and $v_{\text{laser}}=600$ mm/s, in all the different planes, as shown in **Figure 5-9**. Solidification velocity (v) has been computed inside the melt pool bound by the solidus temperature (T_{solidus}), using **equation 5.9**. As the name suggests, solidification velocity is the velocity of the solidification front, or in other words the velocity of the liquidus contour. Contrary to the thermal gradients, solidification velocity is only restricted within the liquid state ($T \geq T_{\text{liquidus}}$) and mushy zone ($T_{\text{solidus}} < T < T_{\text{liquidus}}$). In addition, according to **equation 5.9**, based on the direction thermal gradient in X-direction (G_x), the solidification velocity can be positive (G_x along +X direction, during solidifying) or negative (G_x along -X direction, during melting). Since cracking happens during end of solidification, only positive values of v are plotted in **Figure 5-9**.

Concerning the solidification velocity magnitude for the given laser parameters ($v_{\text{laser}}= 600$ mm/s, $P=240\text{W}$), it ranges from 0 to 0.6 m/s in all the planes. Contrary to the G contours in **Figure 5-8**, the solidification velocity is least in the transverse ZY-plane near the laser and shows an increasing trend when moved away from the laser. It should be also noted that, in the XY plane, the solidification velocity is maximum in the center of the melt pool, along the laser scanning direction (x-axis). The solidification and thermal gradient contours provide useful information in terms of the trend in which they vary inside the melt pool. **Since the coalescence is considered to happen at $f_s=0.97$ [73], it is important to estimate the G and v quantitatively around the temperature associated to a solid fraction of 0.97 ($f_s=0.97$), see dashed green line in **Figure 5-8** and **Figure 5-9**.**

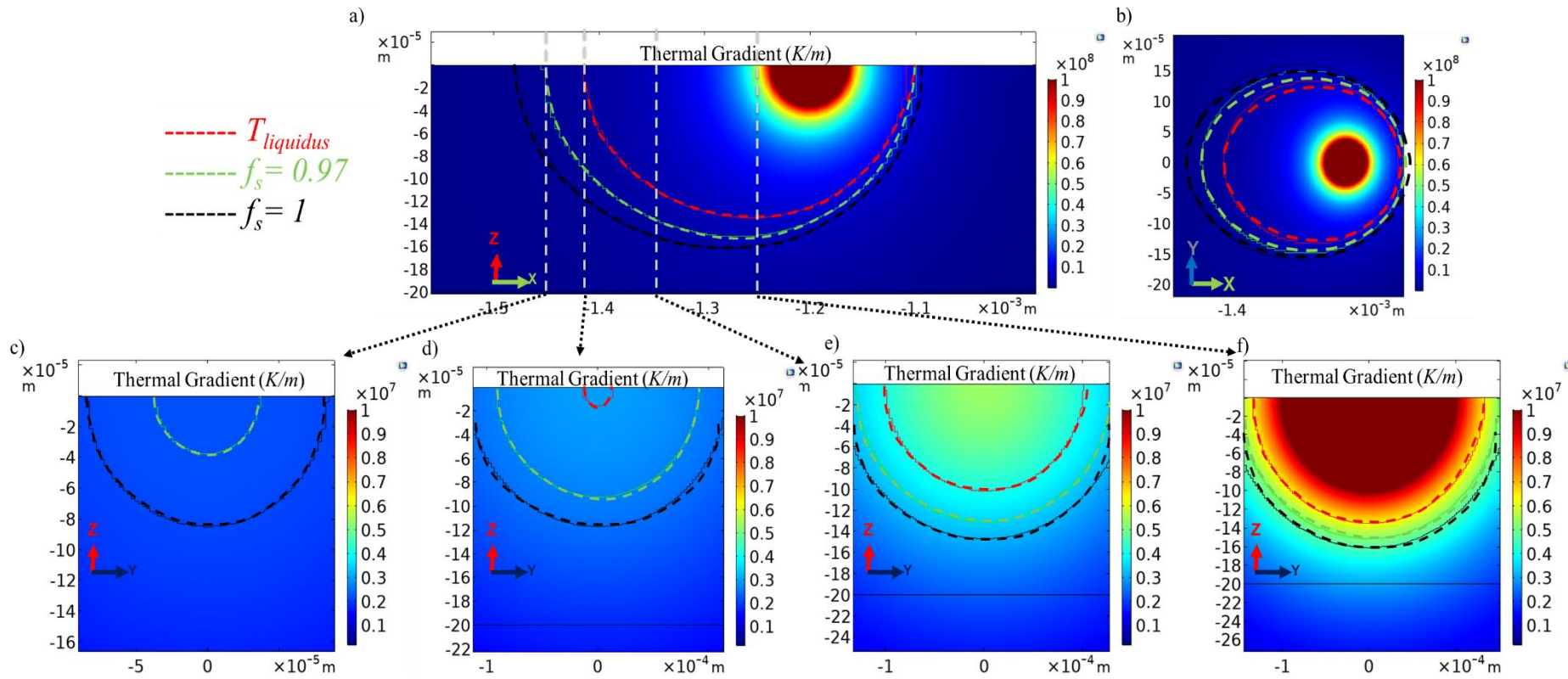


Figure 5-8 Thermal Gradient (G) contours for $P=240$ W and $v_{laser}=600$ mm/s in different plane (a) ZX-plane, b) XY-plane and c)-f) ZY-plane at different cross sections of ZX-plane.

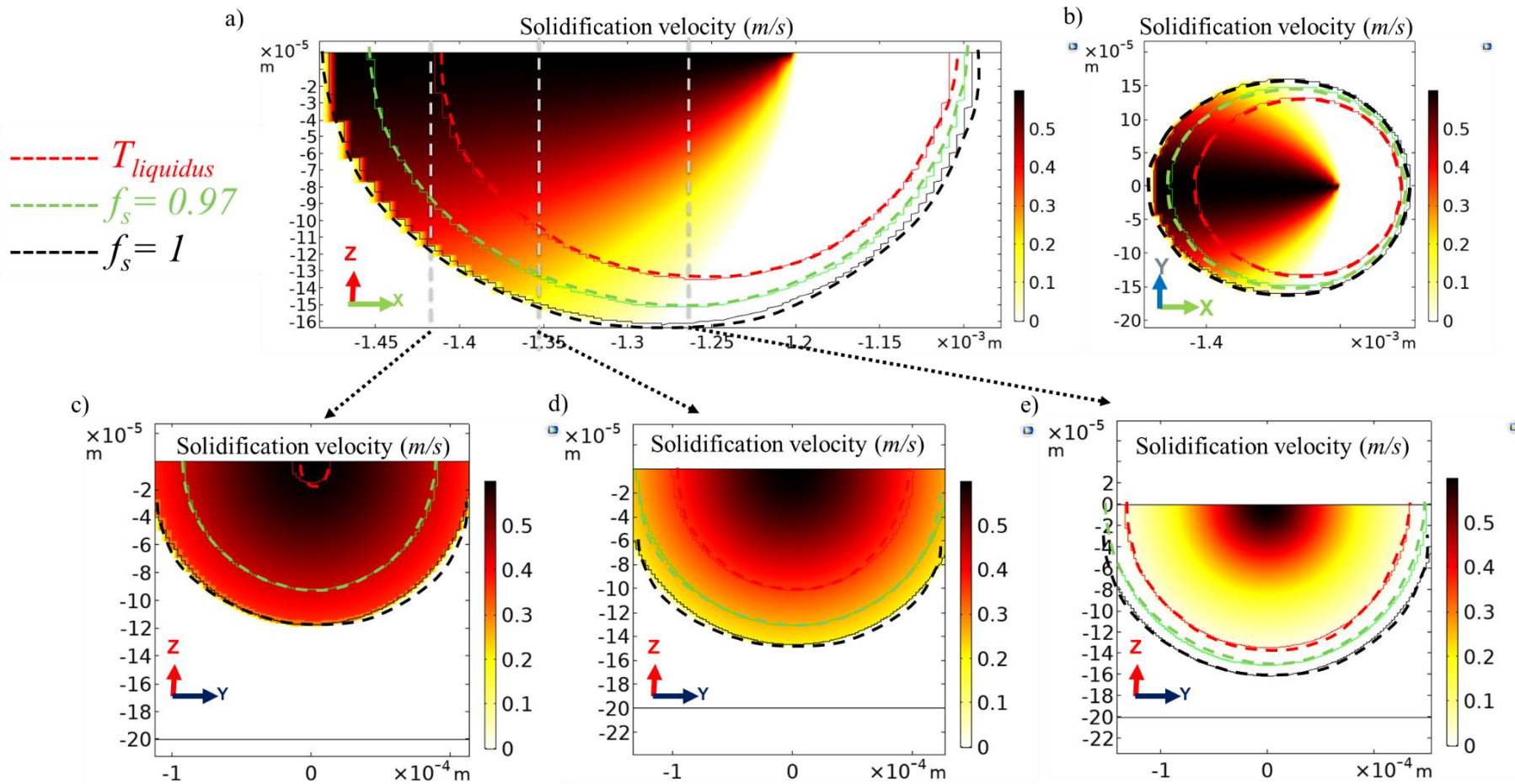


Figure 5-9 Solidification velocity (v) contours for $P=240$ W and $v_{laser}=600$ mm/s in different plane (a) ZX-plane, b) XY-plane and c)-e) ZY-plane at different cross-sections of ZX-plane.

For the transverse YZ-plane (see **Figure 5-10b**), the location of this cross-section was selected at the frontier of the melt pool as shown by the ZY red arrow in **Figure 5-10a**). As a consequence, no liquidus contour can be observed in the YZ-plane. Since the central section of the melt pool is the most prone to hot cracking, the values of G and v are extracted in the YZ-plane, as shown in **Figure 5-10b**). The solidification parameters are estimated as a function of the melt pool depth, as shown in **Figure 5-10c**) for both, longitudinal XZ and transverse YZ-planes. For the XZ-plane, the G & v are computed along the $T(f_s=0.97)$ isothermal contour (indicated with ‘star markers’ in **Figure 5-10a**)), whereas for the YZ-plane it is computed along the melt pool centerline (indicated with ‘square markers’ in **Figure 5-10b**)).

For both planes, the thermal gradient inside the melt pool increases with the depth and reaches a maximum value at the bottom part of the melt pool. On the contrary, the solidification velocity shows a decreasing profile along with the melt pool depth. In both the XZ and YZ-planes, the thermal gradients are of the order of 10^6 K/m, whereas the solidification velocity is always smaller than the laser speed $v_{laser} = 0.6$ m/s. **The average values measured at the isotherm T_{gc} are : $G = 2.8 \cdot 10^6$ K/m and $v = 0.3$ m/s. These values were then selected as inputs to apply the RDG criterion.**

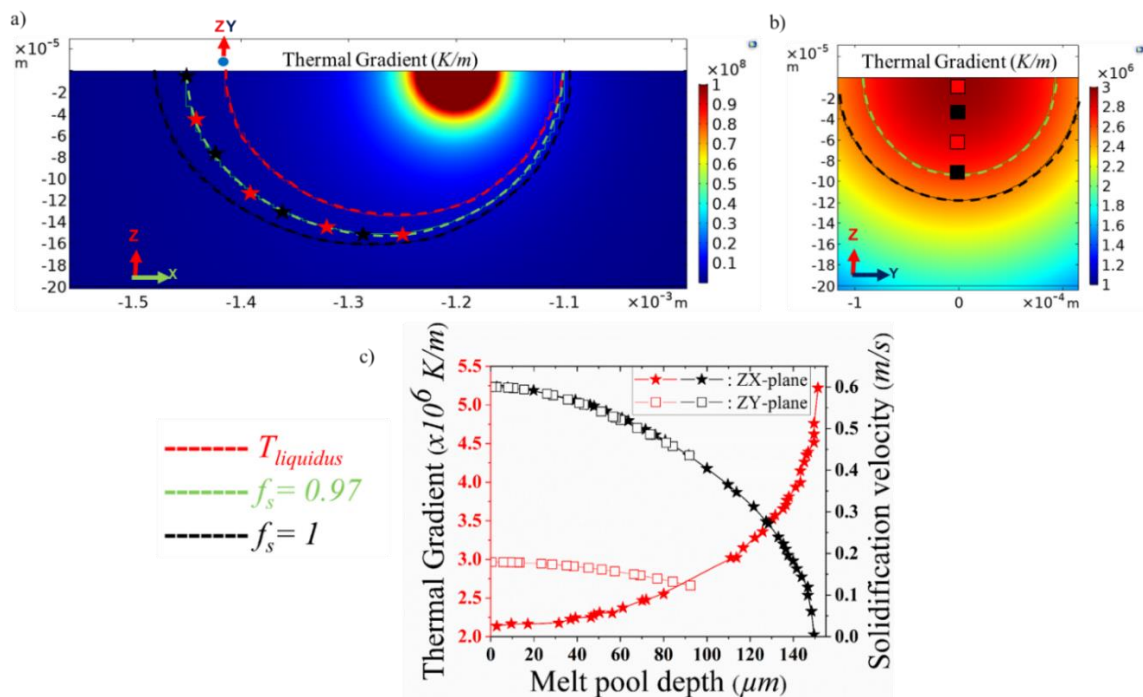


Figure 5-10 a) and b) Thermal gradients inside the melt pool (XZ-plane and YZ-plane) computed using Rosenthal analytical solution when a bulk 6061 Al alloy substrate is subjected to laser power of 240W and laser speed of 600 mm/s (optimized conditions suppressing lack-of-fusion defects). c) Variation of thermal gradients (G) and solidification velocity (v) along the melt pool depth.

5.4.3. Rationalizing centerline cracking

We have been able to consider the cracking sensitivity at HAGB's by using the coalescence undercooling concept described in **section 5.3** and using it as inputs into the RDG criterion. The central location of cracking still needs to be addressed. To do so, as described in **equation 5.2**, the length of the mushy zone can be used as a parameter to identify cracking sensitive locations inside the melt pool. Depending on the length of the mushy zone, we can qualitatively estimate the region the most susceptible to cracking.

Let us now consider the temperature contour in the ZX-plane as shown in **Figure 5-11a**). According to **equation 5.2**, to estimate the length of the mushy zone (L), two input temperatures are required: (i) T_{liquidus} (652°C), and (ii) T_{gc} , the coalescence temperature which is a function of f_s and misorientation (θ). Knowing that the dendrite coalescence temperature is affected by the coalescence undercooling, the mushy zone is defined as the temperature range between T_l and $T_{\text{gc}}(\theta = 15^{\circ})$. Using such a definition, the length of the mushy zone (L) can be estimated using **equation 5.2**, by updating the T_{gc} at $\theta = 15^{\circ}$ and using the thermal gradient estimated using Rosenthal calculations. Such an analysis will help us to determine the location that has the maximum possibility to crack.

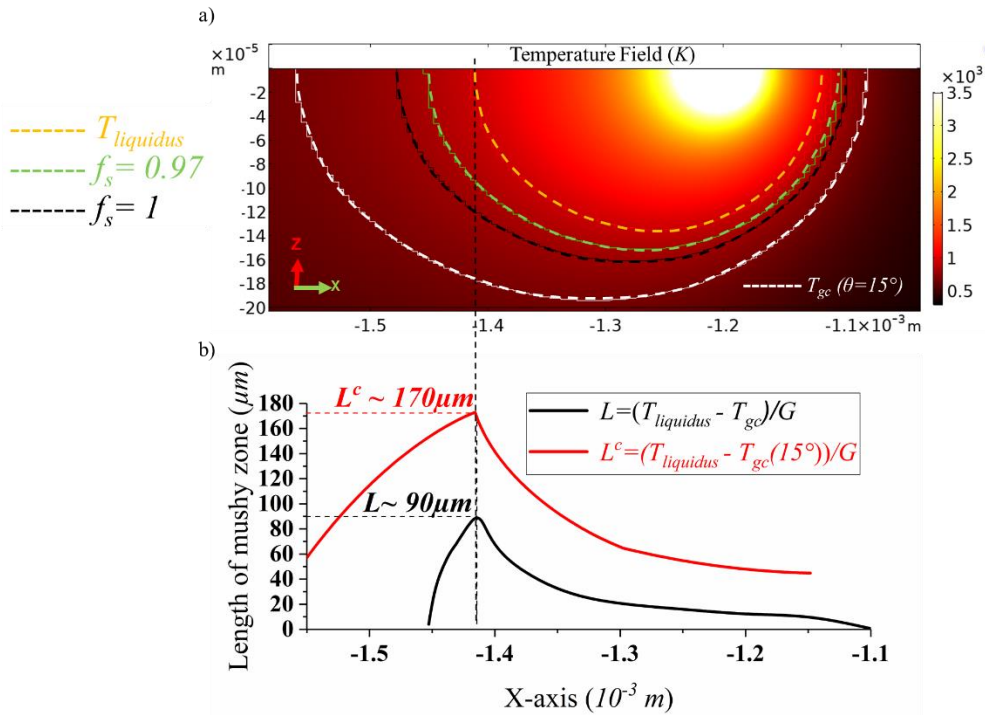


Figure 5-11 a) Temperature field inside the melt pool computed using Rosenthal simulation in the XZ-plane. b) Evolution of length of the mushy zone along the laser scanning direction (X-axis) using the T_{gc} ($f_s=0.97$): black curve and another using the coalescence temperature of $T_{\text{gc}}(f_s=0.97$ and $\theta=15^{\circ}$): red curve.

Thus, another temperature contour ‘dashed white’ is marked in **Figure 5-11a**), which takes into account the effect of coalescence undercooling due to misorientation at $\theta=15^{\circ}$. This new T_{gc} ($f_s=0.97$ & $\theta=15^{\circ}$) was calculated using the data from **Figure 5-5b**).

Finally, as shown in **Figure 5-11b**), two curves are generated for the length of the mushy zone as a function of laser scanning direction: (i) Black curve- without considering misorientation undercooling (case of attractive GB's) and (ii) Red curve- considering misorientation undercooling at $\theta=15^\circ$ (case of repulsive GB's). For the first case, $T_{gc}(f_j=0.97)=558^\circ\text{C}$ was used in **equation 5.2** to compute the length of the mushy zone (L). For the second case, $T_{gc}(f_j=0.97 \ \& \ \theta=15^\circ)=395^\circ\text{C}$ was used to estimate the length of the mushy zone denoted by L^c . For both, the variation of the curve along the X-direction in **Figure 5-11b**), there exists a maximum at a given x-coordinate where the liquidus contour begins, as highlighted in **Figure 5-11a**). Moreover, the important point is that, considering the misorientation undercooling, the L^c (red curve) is always higher than the case where dendrites do not need an additional undercooling to coalesce, i.e. L (black curve). **This suggests that GB that require additional undercooling to coalesce by the virtue of their relative misorientation tend to have a higher length of mushy zone compared to their counterpart attractive GB.** In addition, within those repulsive GB's, there exists a maximum length of mushy (maximum $L^c \sim 170\mu\text{m}$) zone along the scanning x-direction (see the red curve in **Figure 5-11b**). This indicates, in the ZX-plane, there exists a location where a repulsive GB is more sensitive to cracking compared to other repulsive ones. This way, we were qualitatively able to highlight the location the most sensitive to cracking for repulsive GB in the ZX-plane.

Thus, to understand centerline cracking, a similar analysis can be done for other planes as shown in **Figure 5-12**. **Figure 5-12a), b), c)** shows the temperature field in the XY, ZX, and ZY-planes respectively. Based on **Figure 5-12a)**, one can see that there is a critical location in the XY-plane, where L^c reaches a peak. This is the location where the laser passes and cracks are observed. To prove that the central ZX-plane is cracking sensitivity A similar analysis can be done for different XZ-planes at different Y-coordinates, starting from $Y = 0$ (denoting the central XZ-plane) and $Y = -100 \mu\text{m} / -150 \mu\text{m}$ (denoting the planes away from the central location). **Figure 5-12d)** shows that L^c reaches a maximum for the central plane at $Y = 0$. **With this analysis, the extent of the mushy zone can be qualitatively compared in the top (XY-plane) and also along the Z-axis. This helps us to explain, why the center of the melt pools is the region the most sensitive to cracks.**

Summary

We have addressed the key inputs needed to apply the RDG model. Starting from generating solidification path ($f_j(T)$), rationalizing cracking at HAGB's by using the concept of coalescence undercooling, and finally understanding the solidification process parameters typical of L-PBF, namely thermal gradients and solidification velocity with the help of Rosenthal simulations. Moreover, by the concept of the extent of the mushy zone, we were able to qualitatively justify the centerline cracking in 6061 grade processed by L-PBF. All these inputs will be necessary to further apply the RDG model in the context of the fabrication by L-PBF, this will be detailed in the next sections.

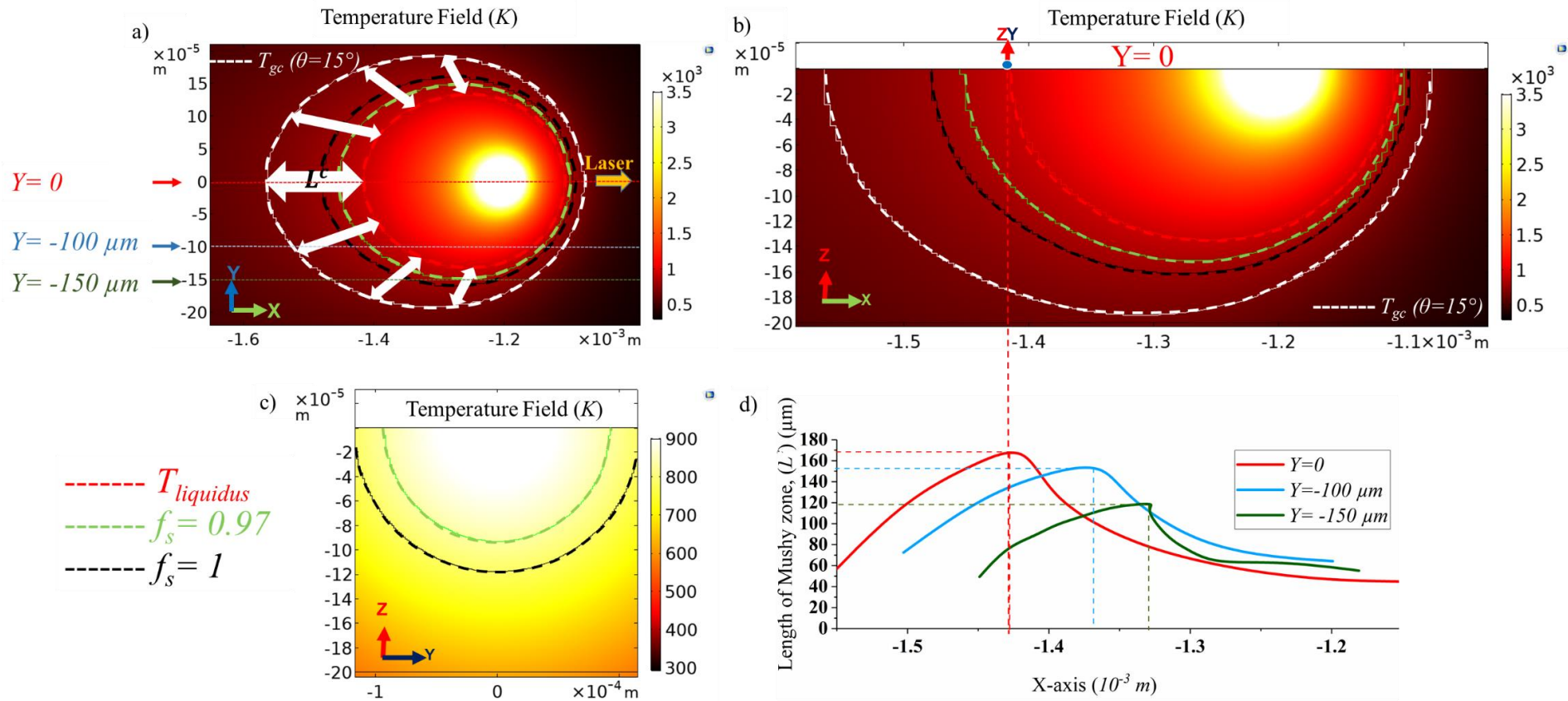


Figure 5-12 a), b) and c) Temperature field inside the melt pool (XY, ZX plane, and ZY plane) computed using Rosenthal analytical solution when a bulk 6061 Al alloy substrate is subjected to laser power of 240W and laser speed of 600 mm/s (optimized conditions suppressing lack-of-fusion defects). d) Variation of the length of the mushy zone (L^c) in the ZX-plane, inside the melt pool, as a function of laser scanning direction for different Y-coordinate values to rationalize the central location of cracking.

5.5. Predicting critical pressure drop

By taking into account the additional undercooling caused by the presence of HAGB's, the RDG criterion finally allows estimating the total Pressure drop (ΔP_{total}) corresponding to our experimental observations. Various constants required to run the RDG criterion are summarized in **Table 5-4**. In the original formulation of the RDG criterion, the characteristic length of the microstructure is taken as the secondary dendrite arms spacing (SDAS). **However, in the current work, according to Figure 4-21, as the secondary arms are not fully developed, and as the order of magnitude of the primary (PDAS) and secondary arm spacing (SDAS) is similar, we have used the primary dendrite spacing as the characteristic length in the RDG criterion.** It is known that PDAS depends on the cooling rate, i.e. the product of solidification process parameters ($G \times v$) according to ref. [15]. If the cooling rate is high enough like in the L-PBF, there is no proper development of secondary dendrite arms and as a result, only primary trunks are seen. To have a better prediction of PDAS, the empirical formula based on ref. [15] was further used in the RDG model. The empirical formula to estimate $\text{PDAS} = 43.2 * (G * v)^{-0.324}$ (μm) was chosen, since the predicted PDAS's matched the experimental PDAS for typical L-PBF cooling rates ranging from (10^5 - 10^7 K/s) for the AlSi10Mg alloy [15]. According to this empirical formula, for given laser parameters ($P=240\text{W}$ & $v=600$ mm/s) and the corresponding averaged solidification parameters ($G=2.8 \cdot 10^6$ K/m and $v=0.3$ m/s), the obtained PDAS is roughly around $0.6 \mu\text{m}$. This obtained PDAS is close to the actual PDAS measured (~ 0.5 - $0.6 \mu\text{m}$), based on surface images revealing the dendrite trunks (see **Figure 4-21**).

Note that the dynamic viscosity (μ) is temperature-dependent and can be affected due to the presence of solutes in alloys. According to [157], **the dynamic viscosity, estimated at melting temperature for pure Al was used in the current study**, assuming that the effect due to temperature variation is not significant.

Another important parameter in **equation 5.1** is the strain rate ($\dot{\epsilon}$). Determining the ($\dot{\epsilon}$) felt by the growing dendrites in L-PBF conditions, is a difficult task. Tensile tests conducted at temperatures very close to the dendrite coalescence temperature would be needed to estimate the strain rate sensitivity but this would require important research efforts. **Here, to make a crude estimation, the strain rate equation mentioned in Table 5-4 is used to get rough values.** Similar to the PDAS estimation, the strain rate is considered to be dependent on the solidification parameters (G, v) according to ref. [97]. Unlike the use of $G_{f_s=0.98}$ as reported in ref [97] to estimate strain rate, in our study we evaluated G at $f_s=0.97$ (which corresponds to the coalescence solid fraction chosen for 6061 Al-alloy).

Table 5-4 Constants used as inputs for RDG criterion.

Constants	Values /empirical law
Shrinkage factor (β)	0.065 [158]
Dynamic viscosity (μ)	$1.4 \times 10^{-3} \text{ Pa}\cdot\text{s}$ [157]
λ = Primary dendrite arm spacing (PDAS)	$43.2 * (G * v)^{-0.324} (\mu\text{m})$ [15]
Thermal expansion coefficient (α)	$23.4 \times 10^{-6} \text{ K}^{-1}$ [159]
Strain rate ($\dot{\epsilon}$)	$\alpha * G_{fs=0.97} * v (s^{-1})$ [97]

Finally, after having obtained all the input parameters required to run the RDG model, the definite integrals mentioned in **equation 5.1** needs to be calculated to estimate the total pressure drop. The numerical integration was done for each of the integrals, namely the $\Delta P_{deformation}$ & $\Delta P_{shrinkage}$.

Note that, depending on the misorientation, the T_{gc} needs to be updated in the lower bound of the integrals. Thus, for a particular misorientation, the coalescence temperature (T_{gc}) can be estimated using **Figure 5-5b**). However, to obtain the pressure drop value, each of the integrand functions in **equation 5.1** must be analyzed in the range of temperature limits (T_1 to T_{gc}). The higher the integration value of these functions, the higher will be the pressure drop. According to Drezet *et al.* [96], sensitivity to hot cracking was analyzed for different alloys based on the integration value of the integrand function corresponding to shrinkage only. They did not consider the deformation integrand function, since they mentioned that the deformation integrand function would vary in a similar way as the shrinkage. **In the present study, the integration values for both these integrand functions (deformation and shrinkage) are taken into consideration to estimate the total pressure drop.** **Figure 5-13** shows the behavior of integrand function corresponding to the deformation and shrinkage terms of **equation 5.1** in the given temperature limits. For example, for an attractive GB bridging at $fs=0.97$, the estimated $T_{gc}(0 < \theta \leq 5^\circ)$ is 558°C and for the repulsive GB it is $T_{gc}(\theta_c = 15^\circ) = 395^\circ\text{C}$. In **Figure 5-13** only two important misorientations are considered: (i) denoting transition from attractive to repulsive ($\theta_{a-r} = 5^\circ$), as shown in **(Fig a-c)** and (ii) critical misorientation after which cracking occurs ($\theta_c = 15^\circ$), as shown in **(Fig d-f)**.

From **equation 5.1**, the first integral evaluated is the $E(T) = \int_{T_{gc}}^T fs(T) dT$, since it is the subpart of the deformation integrand function. Here for the sake of simplicity, we considered only the integration part of $E(T)$ for the analysis, since G and $\dot{\epsilon}$ are assumed independent of temperature. The limits for $E(T)$ vary from (T_{gc} to T), i.e. to visualize the evolution of $E(T)$ as a function of T , the upper limit will be successively varied and the lower limit will be updated corresponding to the angle of misorientation. The plots in

Figure 5-13a) & d), calculates the $E(T)$ integration value as a function of temperature, for $\theta_{a-r} = 5^\circ$ and $\theta_c = 15^\circ$, respectively. The integral value tends to show a decreasing trend as the temperature is lowered. Moreover, the integration returns zero when $T = T_{gc}$, since the upper limit of $E(T)$ becomes equal to the lower bound.

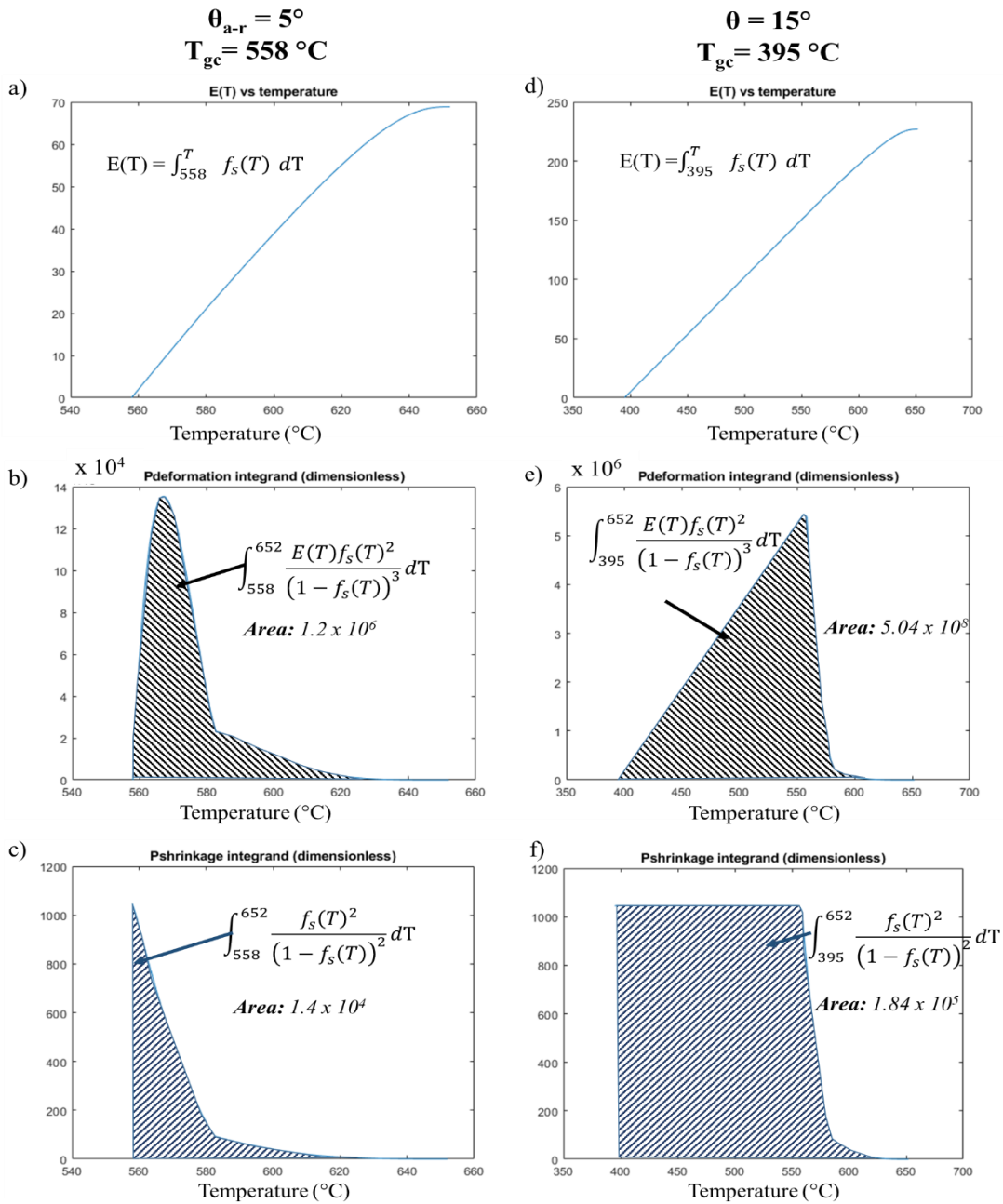


Figure 5-13 a)-c) Calculation of the different integrand functions used to define the shrinkage and deformation part of RDG criterion as a function of the temperature bounds ($T_{liquidus}$ to $T_{gc}(f_s=0.97)$), for the case of attractive boundaries (since $\theta \leq \theta_{a-r}=5^\circ$). **d)-f)** For the case of repulsive boundaries those are HAGB at $\theta=15^\circ$.

Now, considering the deformation integrand function in **equation 5.1**, as shown in **Figure 5-13b) & e)**, the integrand function is composed of the $E(T)$ and other terms depending on the $f_s(T)$. This integrand function tends to increase and reaches a peak as the temperature decreases, however when $T \rightarrow T_{gc}$, the function decreases rapidly to zero since $E(T)$ approaches zero as well. Finally, after having the evolution of the deformation integrand function, the area under the curve within the limits (T_1 to T_{gc}), will give us the definite integration value corresponding to the deformation term. **From Figure 5-13b) & e), the integration value calculated using numerical integration gives a higher value for $\theta_c = 15^\circ$ compared to $\theta_{a-r} = 5^\circ$. An increase of two times the order of magnitude can be seen, suggesting deformation is more likely for HAGB.**

A similar exercise for shrinkage integrand function is done in **Figure 5-13c) & f)**, where the function only depends on the $f_s(T)$ terms. The function tends to increase as the solidification progresses. Note that, for all the $\theta > 5^\circ$, further undercooling makes the T_{gc} goes below $T(f_s=1)$, this will make the denominator of all the integrand functions tend to zero (because of ' $1-f_s$ ' term, since $f_s \rightarrow 1$). Hence all these functions need to be controlled for the value of $f_s(T)$, so that they return a valid function value. **Thus, it was assumed that $f_s(T)$ will always return a value of 0.97 (corresponding to coalescence solid fraction) for all $T < T_{gc}(\theta=5^\circ, f_s=0.97) = 558^\circ\text{C}$.** This is the reason why the integrand function in **Figure 5-13f)**, returns a constant function value for $T_{gc}(\theta=15^\circ)=395^\circ\text{C} \leq T < T_{gc}(\theta=5^\circ)=558^\circ\text{C}$. **The physical significance of this assumption is that the liquid film will persist up to lower temperature until the coalescence takes place, and thus maintaining the solid fraction values to be constant.** Eventually, the area under the curve for shrinkage is estimated and it turns out that, the integration value is higher for the HAGB's compared to the attractive GB's. However, the increase is only by one order of magnitude compared to the increase in the case of the deformation terms. This suggests that the misorientation has a higher impact on the deformation across the dendrites in comparison with the impact on shrinkage. In addition, the area under the curve for the shrinkage part is always less than the deformation part, irrespective of the misorientation. Thus, such an analysis for the variation of integrand functions helps us to understand the weightage of different integrand functions, misorientation angle on estimating the deformation and shrinkage integrals in the RDG criterion.

Having estimated the integration values, these values must be multiplied by their respective constants mentioned in **Table 5-4** according to **equation 5.1**. This will allow us to estimate the total pressure drop, which is the addition of the contributions from the deformation and shrinkage respectively. As seen previously, each misorientation is associated with its corresponding T_{gc} , which helps to return a unique total pressure drop value.

The updated coalescence temperature ($T_{gc}(\theta)$) which takes into account the grain coalescence undercooling, helped us to compute the total pressure drop as a function of misorientation, $\Delta P_{total}(\theta)$. **Figure 5-14** shows the pressure drop evolution as a function of misorientation for different fractions of coalescence. To understand the relative weight of contribution due to deformation and shrinkage, respective pressure drops are also shown in **Figure 5-14a) and b)** and their addition gives us the total pressure drop as shown in **Figure 5-14c)**. The total pressure drop shows a sudden increase from $\theta_{a-r} = 5^\circ$

($\gamma_{\text{gb}} = 2 \cdot \gamma_{\text{s-l}}$) indicating that the hot tearing sensitivity increases continuously with grain boundary misorientation until reaching a misorientation of roughly 20° . Experimentally cracking was only observed for $\theta > 15^\circ$ while lower misorientation grain boundaries were found to be crack-free, see **Figure 4-18**. Note that for misorientation $\theta_{\text{a-r}} = 5^\circ < \theta < 15^\circ$, the dendrite coalescence undercooling model of Rappaz indicates that we have repulsive boundaries. However, our experimental results rather suggest that this dendrite coalescence undercooling seems not significant enough to induce cracking. **Based on our experimental observations, for cracking to occur, it is rather thought that one needs to reach a critical coalescence undercooling determined when $\theta = \theta_c = 15^\circ$. This allows the critical pressure drop ($\Delta P_{\text{critical}}$) above which a GB will be crack sensitive to be estimated. Thus, the critical pressure drop, $\Delta P_{\text{critical}} (\theta_c = 15^\circ, f_s = 0.97)$, is taken equal to 2.45 GPa and can be considered as the cracking sensitivity criterion.** We have deliberately chosen a fraction of coalescence of $f_s = 0.97$ as it was the values experimentally determined in [73] for the 6061 Al-alloy. **This magnitude of pressure drop is relatively high, compared to the ones reported in welding literature, see e.g. [89,96], certainly because of the characteristics of the L-PBF process (small λ , high G and relatively high v).** Note that this value is a crude estimate and that we should rather consider relative hot cracking sensitivity and not take the pressure drop values as absolute values. Also, note that such critical pressure is of the same order of magnitude as the cavitation pressure (P_c) estimated using molecular dynamic simulations in pure aluminum ($P_c = -670 \text{ MPa} = 0.67 \text{ GPa}$), see ref [160]. It can also be highlighted that, even if we assume a larger critical misorientation, the impact on the critical pressure drop would be limited. For instance, taking $\theta_c = 25^\circ$, the critical pressure drop is about 3.1 GPa . This observation is due to the grain boundary energy and the dendrite coalescence undercooling, which stabilizes for misorientation ranging from 20° to 30° , as shown in **Figure 5-5**.

Using the RDG criterion, we can rationalize the experimental observation of misorientation dependent cracking, using $\Delta P_{\text{total}}(\theta)$. **In Figure 5-14, we illustrate that the pressure is extremely sensitive to the coalescence temperature during the last stage of solidification.** Indeed, the pressure drop is about 0.1 GPa when taking a coalescence temperature corresponding to a solid fraction of $f_s = 0.90$, however, this pressure drop reaches 2.45 GPa for a coalescence temperature corresponding to a solidified fraction of $f_s = 0.97$ and $\sim 46 \text{ GPa}$ for a fraction of coalescence of $f_s = 0.99$. **Finally, one should note that experimentally, we observe cells, i.e. dendrite trunks but with very limited secondary arms (see Figure 4-21), this should be pointed out because geometrically this suggests that the coalescence temperature is likely associated with very high solid fractions.**

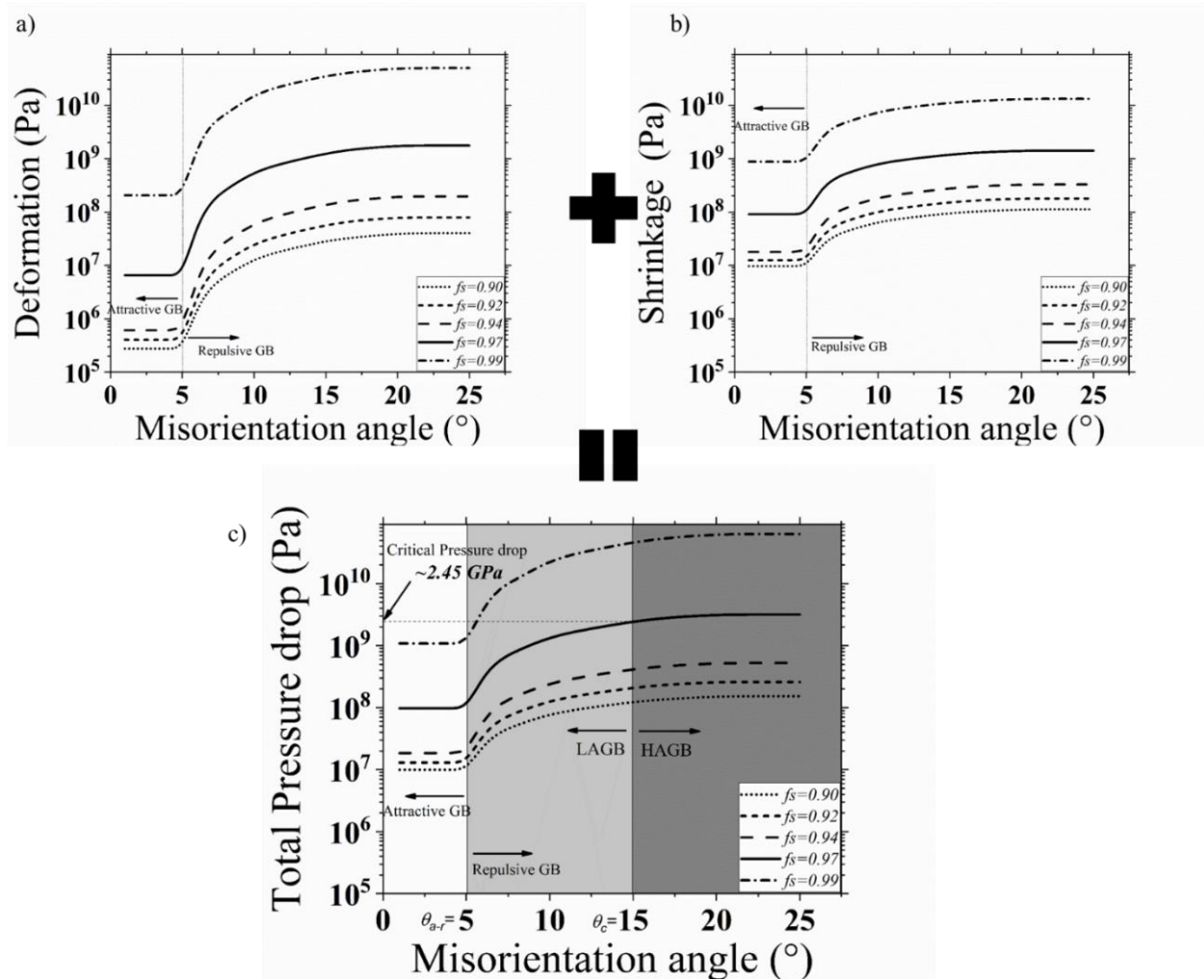


Figure 5-14 a) Pressure drop due to deformation, b) Pressure drop due to shrinkage and c) Total pressure drop for a given $G = 2.8 \times 10^6$ K/m and $v = 0.3$ m/s, typical values extracted from our Rosenthal simulations for $P = 240$ W and $v = 600$ mm/s.

Speaking in terms of the individual contribution of the deformation and shrinkage terms to the total pressure drop, **Figure 5-13** showed that the trend observed for the area under the curve for deformation is quite high compared to shrinkage at a given coalescence $f_s = 0.97$, irrespective of the misorientation changes. However, as mentioned previously, after multiplying the different constant to these estimated integration values, the actual behavior of the $\Delta P_{deformation}$ and $\Delta P_{shrinkage}$ can be known, as shown in **Figure 5-14a)** and **b)**. From **Figure 5-14a)** and **b)** it is evident that, for attractive grain boundaries ($\theta \leq 5^\circ$), irrespective of the considered coalescence f_s , the $\Delta P_{shrinkage} > \Delta P_{deformation}$. This is contrary to the values of the integrand function in **Figure 5-13**, where deformation integrand function had higher value compared to shrinkage integrand function for a given misorientation. Thus, multiplying constants mentioned in **Table 5-4** according to equation 5.1 reverses the trend observed in **Figure 5-13** and finally makes the $\Delta P_{shrinkage} > \Delta P_{deformation}$ (see **Figure 5-14a)** and **b)** for $\theta \leq 5^\circ$).

However, if we consider repulsive grain boundaries ($\theta \geq 5^\circ$) in **Figure 5-14a) and b)**, the inequalities ($>$ or $<$) between $\Delta P_{shrinkage}$ and $\Delta P_{deformation}$ becomes unclear.

To understand the trend clearly, **Figure 5-15**, decodes the weightage of pressure drop contribution as a function of both misorientation and f_s . Consider **Figure 5-15a)**, for a given coalescence $f_s=0.92$, the deformation pressure drop contribution (marked in 'black') is always lower than the shrinkage one (marked in 'light grey'), regardless the misorientation. This suggests that, when the mushy zone undergoes coalescence at an early stage of solidification (at $f_s=0.92$), the contribution due to shrinkage is predominant. However, in this case, the total pressure drop always remains under the critical pressure drop $\Delta P_{critical}$, thereby less prone to cracking. For $f_s=0.97$ (see **Figure 5-15b)**, the deformation contribution remains lower until a given misorientation is reached. For $\theta \geq 15^\circ$, the deformation starts to dominate the shrinkage, indicating that contribution arising from deformation is highly sensitive to misorientation and coalescence solid fraction. Considering even higher coalescence $f_s=0.99$ (see **Figure 5-15c)**, the deformation contribution starts to dominate from an even lower misorientation of $\theta \geq 10^\circ$. **This indicates that, when coalescence is delayed at a later stage of solidification, the deformation at the growing dendrites becomes so high that it dominates the shrinkage and in reality can induce cracking even at lower misorientation.**

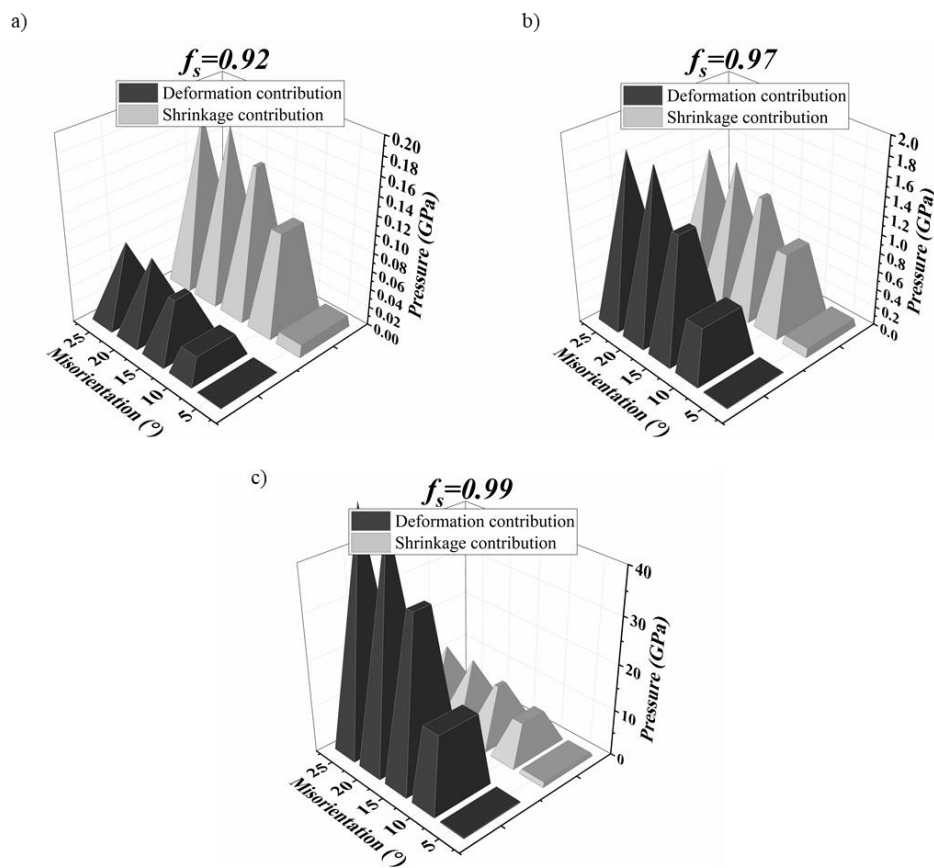


Figure 5-15 Effective contribution of deformation and shrinkage terms as a function of misorientation angle for different coalescence solid fraction: a) $f_s=0.92$, b) $f_s=0.97$ and c) $f_s=0.99$.

A similar exercise can be done, by fixing the misorientation angle and verifying the shrinkage and deformation contribution as a function of solid fraction. **Figure 5-16a)-c)** shows the contribution from the two terms for fixed misorientation of 5° , 10° , and 15° , respectively. We know that, as misorientation increases the magnitude of the two pressure terms also increases, as demonstrated in **Figure 5-14**. A similar trend is observed as a function of solid fraction, shown in **Figure 5-16**. However, a key thing to notice in **Figure 5-16 b) & c)** is that, as solidification approaches the end ($f_s > 0.97$), the deformation contribution starts to dominate the shrinkage contribution. For lower values of solid fraction and misorientation, it is the shrinkage that dominates the deformation contribution.

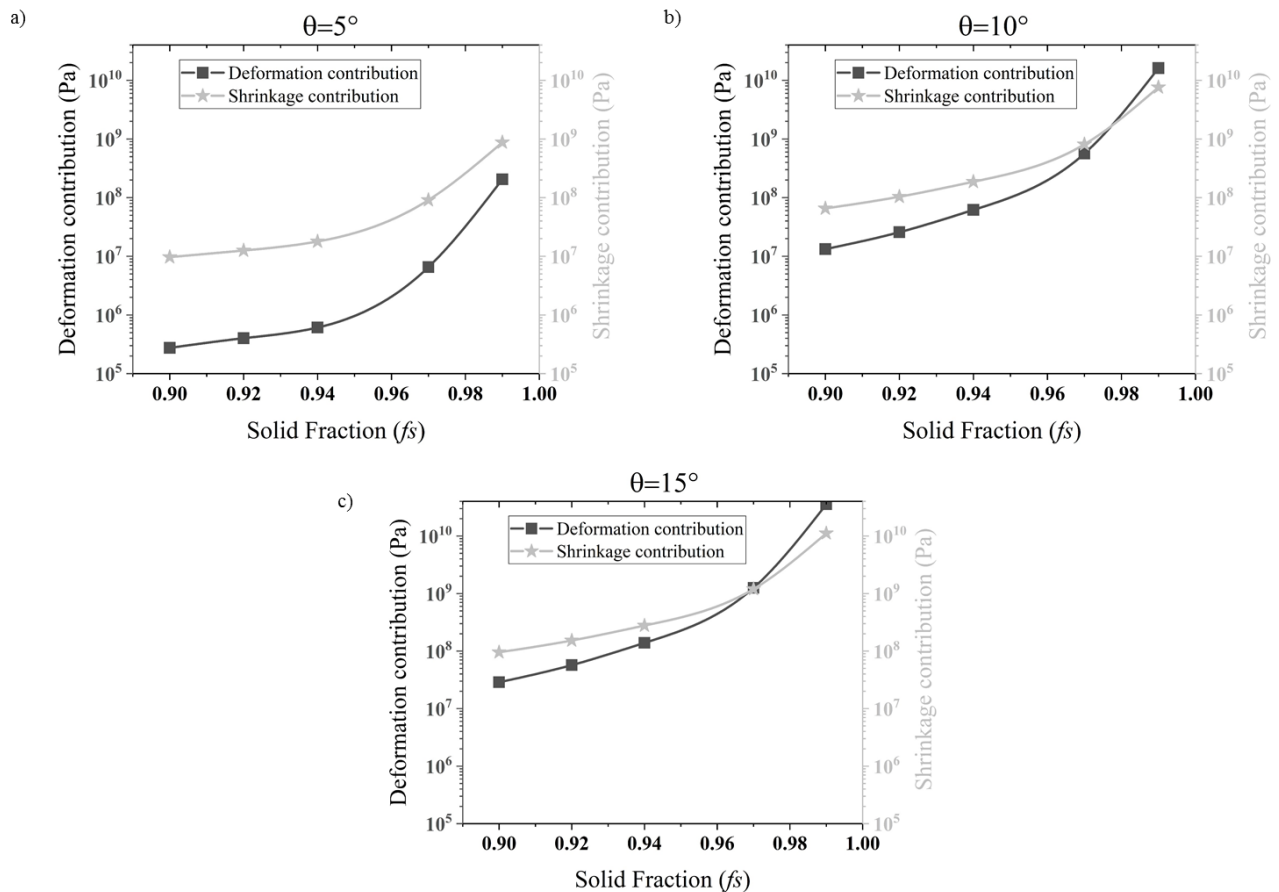


Figure 5-16 Effective contributions of deformation and shrinkage terms as a function of solid fraction for different misorientation angles: a) $\theta=5^\circ$, b) $\theta=10^\circ$ and c) $\theta=15^\circ$.

To summarize, there exist differences in the behavior of shrinkage and deformation integrand functions depending on the coalescence f_s and misorientation changes. It is recommended to consider both contributions (deformation and shrinkage) to have a reliable cracking sensitivity prediction. Such an analysis helps us to visualize the competition between deformation and shrinkage in inducing cracking, in the light of L-PBF of the 6061 Al alloy, and provides us useful insights into the occurrence of cracking.

5.5.1. Region with critical pressure inside the melt pool.

After having estimated the critical pressure drop, the pressure drop can be estimated locally at the melt pool scale. This way, regions sensitive to cracking inside the melt pool can also be identified based on the magnitude of the pressure drop, in addition to the length of mushy zone exercise done in **section 5.4.3**. Thus, another way to demonstrate the sensitivity of the central region of the melt pool is by estimating the pressure drop inside the melt pool. In **Figure 5-17a**), the pressure drop is estimated inside the XY-plane melt pool (refer to **Figure 5-12a**)). Note that, for each position (x, y) , inside the melt pool, the pressure drop according to **equation 5.1** depends on $T(x, y)$ and the solidification conditions $(G(x, y), v(x, y))$ inside the melt pool. Thus, according to **Figure 5-17a**), the pressure inside the liquidus contour is 0 and as temperature decreases below the liquidus, the pressure drop shows an increase in magnitude. The black region in **Figure 5-17a**) indicates the critical pressure region, having $\Delta P_{\text{total}} > 2.45$ GPa. Note that the magnitude of pressure drop in some locations can be higher than the selected critical value (2.45 GPa) since in this analysis it is the local rather than average values of G and v , which were used to estimate the pressure drop.

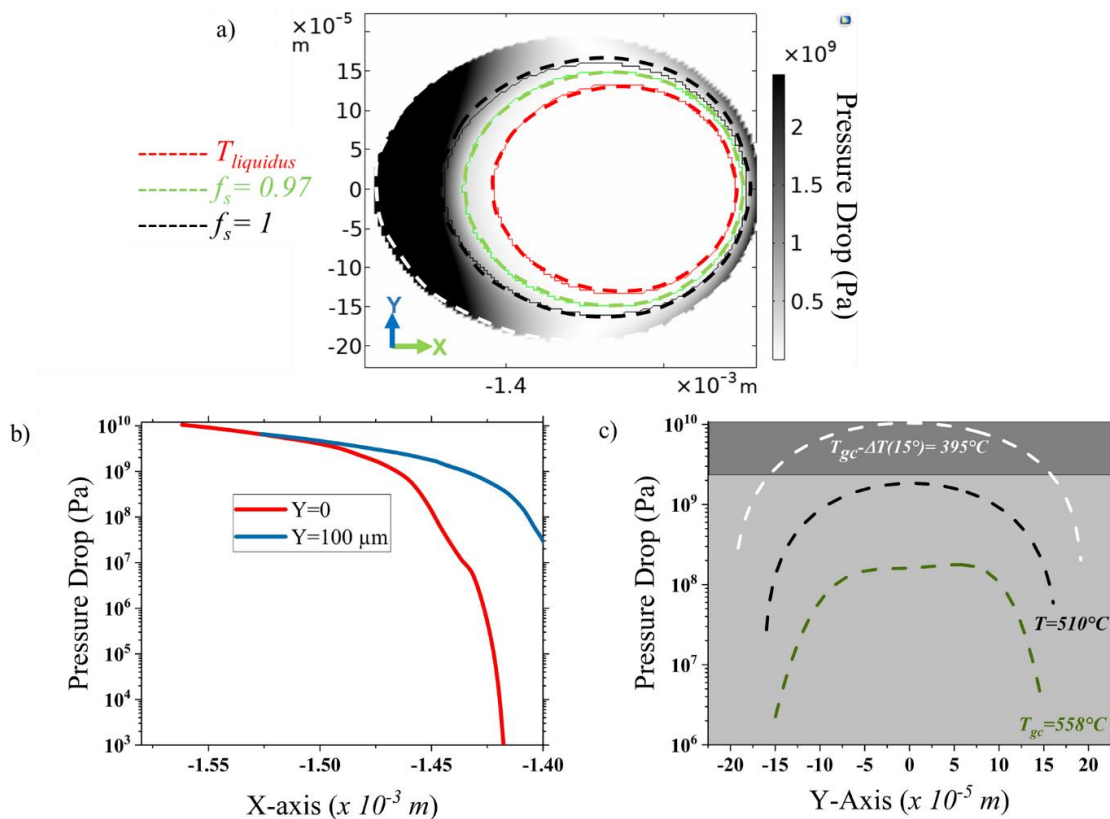


Figure 5-17 a) Shows the pressure drop map inside the XY plane melt pool. b) Evolution of pressure drop along the X-axis for different Y-coordinates. c) Pressure drop variation as a function of the Y-axis for different temperature contours inside the XY-plane melt pool.

However, in this pressure map of **Figure 5-17a**), it is very difficult to locate the transition and region most susceptible to cracking. To have a better visualization of the pressure drop evolution, consider **Figure 5-17b**). The pressure drop is plotted as a function of the X-axis for different Y-coordinate ($Y=0$ representing the central region, and $Y=100\mu\text{m}$ representing a region away from the central region). It is evident to notice that, for $Y = 0$, the pressure drop from a temperature just below the liquidus to the T_{gc} goes from 1KPa to 10GPa. This is because, the pressure is very sensitive to the temperature at a given position (x, y) . And comparatively, the $Y=100\mu\text{m}$ the evolution in pressure drop along the X-axis is not as steep compared to the central region ($Y=0$).

In **Figure 5-17c**), the pressure drop is estimated for different temperature contours inside the XY-plane melt pool namely, $T_{gc}=558^\circ\text{C}$, $T=510^\circ\text{C}$ and $T_{gc} - \Delta T_{undercooling}(\theta = 15^\circ) = 395^\circ\text{C}$. As we move along a given temperature curve, the position (x, y) also varies. As solidification progresses from 558°C (green curve) to 395°C (white curve), the pressure drop increases by orders of magnitude due to the inclusion of coalescence undercooling in estimating the pressure drop. **Moreover, for a fixed temperature, the local variation in $G(x, y)$ and $v(x, y)$ makes the pressure drop increase and reach a maximum for $Y=0$ (central region). Away from this central region, the pressure drop decays symmetrically on either side. In other words, the pressure drop is also sensitive to the location inside the melt pool.** With such an analysis on the melt pool scale, we show that the local mechanical solicitation can cause a higher pressure drop in the center of the melt pool, increasing its cracking sensitivity. Thus in agreement with the extent of the mushy zone (**Figure 5-12d**), the pressure drop inside the melt pool also demonstrates the higher cracking sensitivity of the central region of the melt pool.

5.6. Summary

According to **Chapter 4**, two conditions are required for a grain boundary to be cracked: (i) being a HAGB, and, (ii) being located at the central position of the melts pools. Those two conditions were discussed using the RDG hot tearing criterion. The RDG criterion was updated to include the effect of coalescence undercooling to rationalize the effect of misorientation. Similarly, to address the centerline cracking observed in the experimental section, the concept of length of the mushy zone was used. The length of the mushy zone is maximum in the center of the melt pool, thus qualitatively rationalizing the cracking sensitivity of the central grain boundaries.

Various inputs were generated to run the RDG criterion like solidification path ($f_s(T)$) of 6061 grade, solidification parameters namely thermal gradients (G) and solidification velocity (v) were estimated for the L-PBF process using the Rosenthal Analytical solution. With these inputs, the RDG criterion was used to estimate the pressure drop in the mushy zone. It was found that the pressure drop is sensitive to the grain boundary misorientation and increases rapidly when there is a transition from attractive to repulsive grain boundaries at $\theta_{a-r} = 5^\circ$. The effect of the fraction of coalescence on the pressure drop was also investigated and our sensitivity analysis demonstrates that this is the key factor controlling the hot tearing

sensitivity. Having the coalescence of dendrites at an early stage is beneficial to reduce the total pressure drop and thus can be an effective way to avoid solidification cracking in 6061 grade.

Finally corresponding to the coalescence solid fraction ($f_s=0.97$) of 6061 Al alloy and the misorientation angle of 15° , the estimated pressure drop was considered as 'critical', above which cracking is highly probable. Using this cracking sensitivity criterion, the effect of process parameters and the effect of chemical composition can be studied to provide key insights and possible guidelines to avoid cracking.

6. Effect of processing parameters on hot cracking sensitivity

In the previous chapter, the critical pressure drop above which grain boundaries are sensitive to cracking is estimated based on the RDG criterion applied in the framework of L-PBF.

This chapter focuses on using this criterion and analyzing the effect of first-order melting parameters of L-PBF on cracking sensitivity. In addition, it also discusses the possible ways to mitigate cracking via other process modifications. The chapter identifies key parameters affecting cracking based on process modifications and presents their sensitivity analysis to understand their effect on hot cracking.

6.1. Introduction

Now that we have rationalized the cracking sensitivity of HAGB and the position of the cracked HAGB using the RDG criterion, we propose to evaluate the effects of processing parameters (melting conditions and preheating) on the hot cracking sensitivity. Studying these various effects will allow us to provide guidelines to limit cracking sensitivity based on the crude estimation of the critical pressure drop $\Delta P_{\text{critical}} = 2.45 \text{ GPa}$.

6.2. Evaluating cracking sensitivity for L-PBF melting parameters.

The laser power (P) and laser scanning speed (v_{laser}) are often considered as the first-order parameters used to optimize the processing conditions to obtain a high relative density of the fabricated parts. In order to establish the cracking sensitivity based on these first-order parameters, the solidification parameters corresponding to them must be estimated. Since P and v_{laser} are not the direct inputs to the RDG criterion, they can be introduced into the model using their G and v . The thermal gradients and solidification velocities corresponding to different laser linear energy densities ($E_L = P/v_{\text{laser}}$) are evaluated using the Rosenthal analytical solution. For each combination of P and v_{laser} , the average values of G and v (taken along the isotherm associated with the fraction of coalescence $f_s = 0.97$) are calculated, similar to the analysis done for **Figure 5-10c**). Similarly, both the strain rate and the primary dendrite arm spacing are updated according to the empirical formula given in **Table 5-4** and based on the various combinations of G and v corresponding to different E_L , i.e. melting parameters (P and v_{laser}). Such an approach will help to provide insights into the effect of first-order melting parameters on hot cracking.

The thermal gradient varies from 10^6 - 10^8 K/m and the solidification velocity varies up to 0.7 m/s over the range of experimentally investigated melting parameters (P : 164-274W, v_{laser} : 600-1400 mm/s) mentioned in **section 4.1.4**. The hot cracking sensitivity (HCS) maps shown in **Figure 6-1** illustrates the effect of these solidification parameters on the ΔP_{total} estimated using **equation 5.1**, taking into account the coalescence undercooling $T_{\text{gc}}(\theta)$ at $\theta = 5^\circ, 15^\circ$ & 25° . The black lines indicate iso-pressure drop levels and the black region (marked with a red dashed line) in the HCS map displayed in **Figure 6-1** indicates the pressure drop values higher than 2.45 GPa . **Thus, this black region can be defined as the cracking sensitive region, since the pressure drops in this region are considered as critical.** It is also important to point out that, as the misorientation increases, the region sensitive to cracking ($\Delta P_{\text{total}} > 2.45 \text{ GPa}$) increases; thus indicating a higher sensitivity to HAGB's for various melting parameters. **This is an original way to represent the cracking sensitive region including the L-PBF process parameters and the coalescence undercooling behavior.**

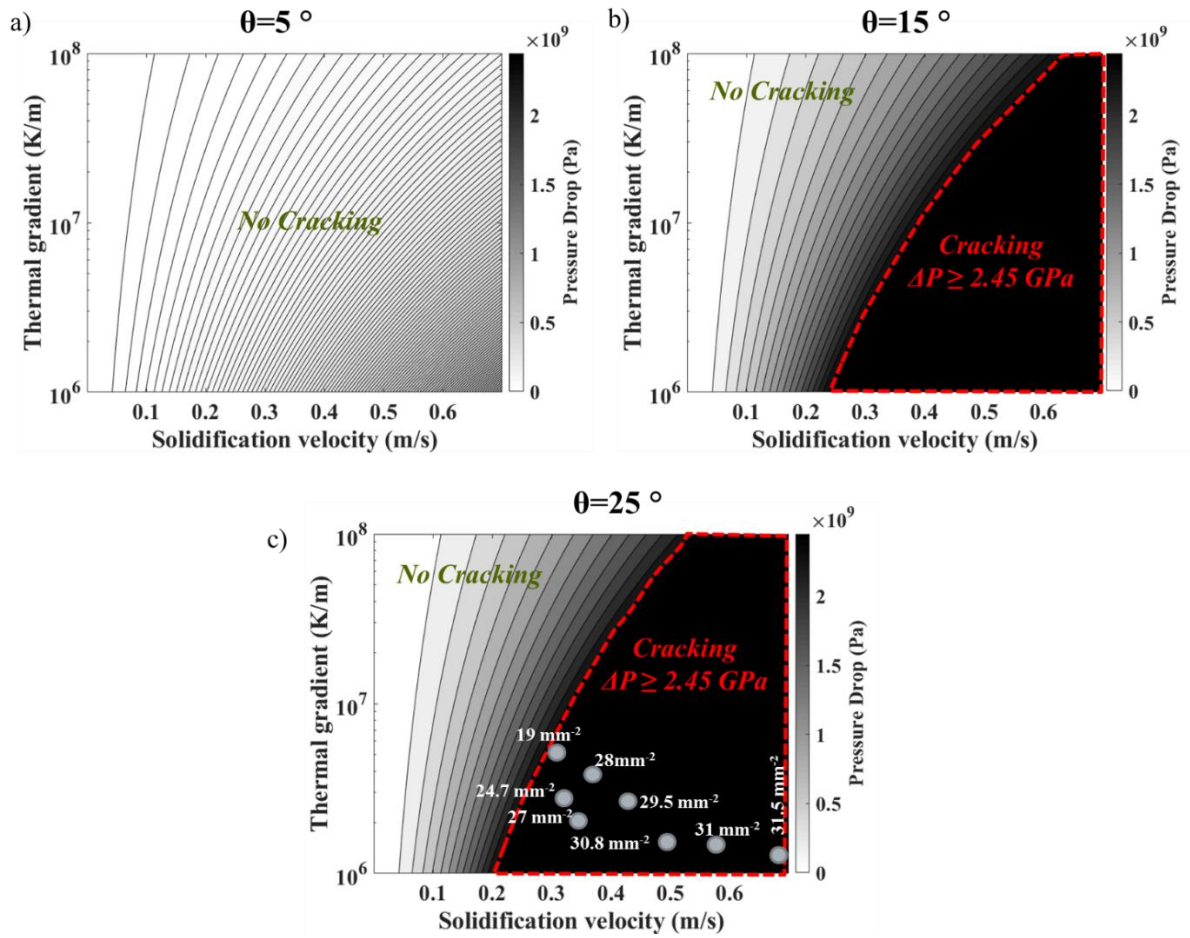


Figure 6-1 a) b) & c) Hot cracking sensitivity (HCS) map for $\theta = 5^\circ$, $\theta = 15^\circ$ & $\theta = 25^\circ$ respectively. Mean crack density (measured experimentally) is also superimposed on the HCS map of figure c).

Similarly, as seen in the experimental section that LAGB were free of cracks, the HCS map of **Figure 6-1a** gives a justification for this observation since there is no black crack sensitive region for $\theta=5^\circ$. Another important aspect of the HCS maps in **Figure 6-1**, is that, for a given thermal gradient, there exists a critical solidification velocity above which, $\Delta P_{\text{total}} > 2.45 \text{ GPa}$, i.e. cracking is probable. Thus for **Figure 6-1c**), a critical solidification velocity above which cracking can occur, can be estimated, suggesting that there is still some room to achieve a crack-free zone, in particular when solidification velocity is substantially decreased to $v=0.1-0.2 \text{ m/s}$. To obtain such solidification velocities ($0.1-0.2 \text{ m/s}$), which to remind are the average values along the $f_s=0.97$ contour, we need to employ slow laser speeds typically $\sim 200-400 \text{ mm/s}$. This can be inferred that, if we sufficiently reduce the solidification velocity below 0.2 m/s for the extreme case of $\theta=25^\circ$ (**Figure 6-1c**)), we could still achieve crack free region even under L-PBF conditions. In other words, even for HAGB despite the coalescence undercooling, decreasing sufficiently the solidification velocity can potentially help to decrease the cracking sensitivity.

As shown in **Figure 4-16b**), the mean crack density in the samples was found to vary as a function of the linear energy density. In order to compare the experimental trend (**Figure 4-16b**)), their corresponding solidification parameters (G, v) were linked to the crack density, and these data points were superimposed on the HCS map of **Figure 6-1c**). All samples are found to lie in the predicted hot cracking sensitive

region. The crack density tends to decrease as the solidification velocity decreases. Interestingly, the lowest crack density (19 mm^{-2}) is found the closest to the transition limit defined by the critical pressure drop, while the data point for the highest crack density (31.5 mm^{-2}) is positioned far away from the boundary between the crack sensitive and non-crack sensitive regions. This suggests that the prediction is qualitatively in agreement with the experimental measurements of crack density and thus can be seen as a first step towards the validation of our predictions. To further validate our approach and to refine the prediction of the crack sensitive region, one may want to also investigate solidification conditions giving rise to crack-free samples.

However, achieving low laser speeds tend to increase the linear energy density. **Figure 6-2**, illustrates the effect of linear energy density (Power and v_{laser}) on the ΔP_{total} . The pressure drop shows a decreasing trend for high energy density. This suggests that to be less cracking sensitive, it is imperative to implement melting parameters (mainly low v_{laser}) that give high laser energy densities $\geq \sim 500 \text{ J/m}$. From **Figure 6-2**, it must be also highlighted that, when low linear energy densities (115-400 J/m) are employed like the ones experimentally tested in the current study, these melting conditions will always lead to cracking sensitive regions. Their mean crack densities (found experimentally) are superimposed in **Figure 6-2**. All the cracking parameters found experimentally, lie in the cracking sensitive region predicted with our modeling approach. This indicates that the RDG model can capture the cracking trend found experimentally.

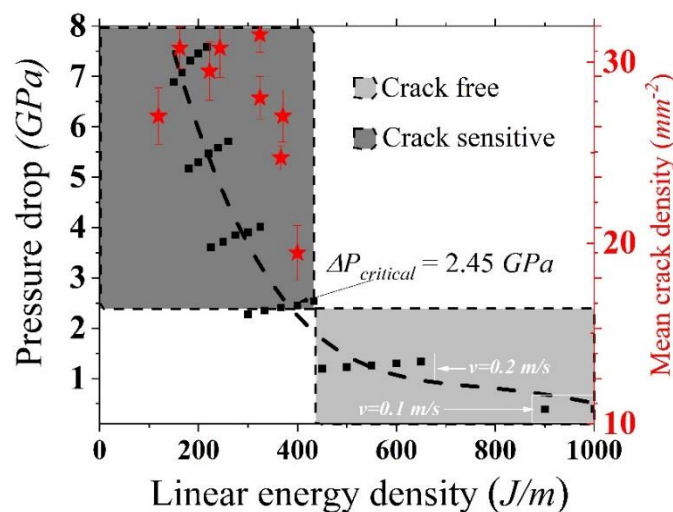


Figure 6-2 Shows the total pressure drop as a function of melting parameters (linear energy density). Mean crack density (found experimentally) is also superimposed to qualitatively compare the predictions and experimental observations.

The HCS maps and the pressure as a function of linear energy density indicates that it will be very challenging to achieve a crack-free zone, at least over the range of parameters investigated in this work. Therefore, it is important to understand which solidification parameter (G or v), makes these low linear energy densities return a higher pressure drop. In other words, which solidification parameter has an

impactful effect on ΔP_{total} . From **equation 5.1**, it is straightforward to notice that, $\Delta P_{\text{Shrinkage}}$ varies as a function of v/G , however, PDAS (λ) and strain rate ($\dot{\epsilon}$) are also dependent on G and v , in our modelling approach. Thus to take that into account, their empirical relations mentioned in **Table 5-4** must be substituted in **equation 5.1** to know the eventual dependence of G and v on ΔP_{total} . Assuming, $G_{f_s=0.97}$ is roughly equal to G at any f_s , the pressure contribution from deformation ($\Delta P_{\text{deformation}}$) in **equation 5.1** is found to be directly proportional to $(v^{1.648}/G^{0.352})$, see the calculation of **equation 6.1**. A similar exercise done for $\Delta P_{\text{shrinkage}}$, yields the same dependence on G and v . **Thus, the eventual dependence of total pressure drop (ΔP_{Total}) is also directly proportional to $(v^{1.648}/G^{0.352})$.** This suggests that v has a strong influence on the (ΔP_{total}) compared to G , and thus explains why increasing solidification velocity (decreasing E_L), will eventually lead to high (ΔP_{total}), predicting cracking, as shown in **Figure 6-2**.

$$\Delta P_{\text{deformation}} = \frac{180 (1 + \beta)\mu}{\lambda^2 G} \int_{T_{gc}}^{T_l} \frac{E(T) f_s(T)^2}{(1 - f_s(T))^3} dT$$

$$\Delta P_{\text{deformation}} = \frac{180 (1 + \beta)\mu \dot{\epsilon}}{\lambda^2 G \cdot G} \int_{T_{gc}}^{T_l} \frac{f_s(T)^2 \int_{T_{gc}}^T f_s(T) dT}{(1 - f_s(T))^3} dT \dots \text{substituting for } E(T)$$

$$\Delta P_{\text{deformation}} = \frac{180 (1 + \beta) (\alpha \cdot G \cdot v)}{\lambda^2 G} \int_{T_{gc}}^{T_l} \frac{f_s(T)^2 \int_{T_{gc}}^T f_s(T) dT}{(1 - f_s(T))^3} dT \dots$$

substituting for $\dot{\epsilon} = \alpha \cdot G \cdot v$, (assuming $G_{f_s=0.97} = G$)

$$\Delta P_{\text{deformation}} = \frac{180 (1 + \beta)\mu (\alpha v)}{(43.2 * (G \cdot v)^{-0.324})^2 G} \int_{T_{gc}}^{T_l} \frac{f_s(T)^2 \int_{T_{gc}}^T f_s(T) dT}{(1 - f_s(T))^3} dT \dots \text{substituting for } \lambda$$

$$\Delta P_{\text{deformation}} = \frac{180 (1 + \beta)\mu \alpha}{43.2^2} \frac{v^{1.648}}{G^{0.352}} \int_{T_{gc}}^{T_l} \frac{f_s(T)^2 \int_{T_{gc}}^T f_s(T) dT}{(1 - f_s(T))^3} dT \quad (\text{equation 6.1})$$

The effect of laser speed can also be observed by estimating the pressure drop inside the melt pool regions. To estimate the spatial distribution of pressure drop ($\Delta P_{\text{total}}(x,y)$) as a function of laser speed, RDG model was applied inside the melt pool corresponding to the location specific $G(x,y)$ and $v(x,y)$ in the XY plane (top surface), similar to **Figure 5-17a**). According to **Figure 6-3**, for a given laser P=240 W and varying laser speeds, the solidification velocity is the most affected parameter compared to the thermal gradients inside the melt pool. For example, for v_{laser} of 600 mm/s and 1000 mm/s, the maximum solidification velocity is 0.6 m/s and 1 m/s, respectively; whereas the thermal gradients are barely affected. Correspondingly for each set of $G(x,y)$ and $v(x,y)$, the $\Delta P_{\text{total}}(x,y)$ was estimated by implementing the RDG criterion inside the melt pool. It must be noted that temperature variation inside the melt pool ($T(x, y)$) was also considered in estimating the $\Delta P_{\text{total}}(x,y)$.

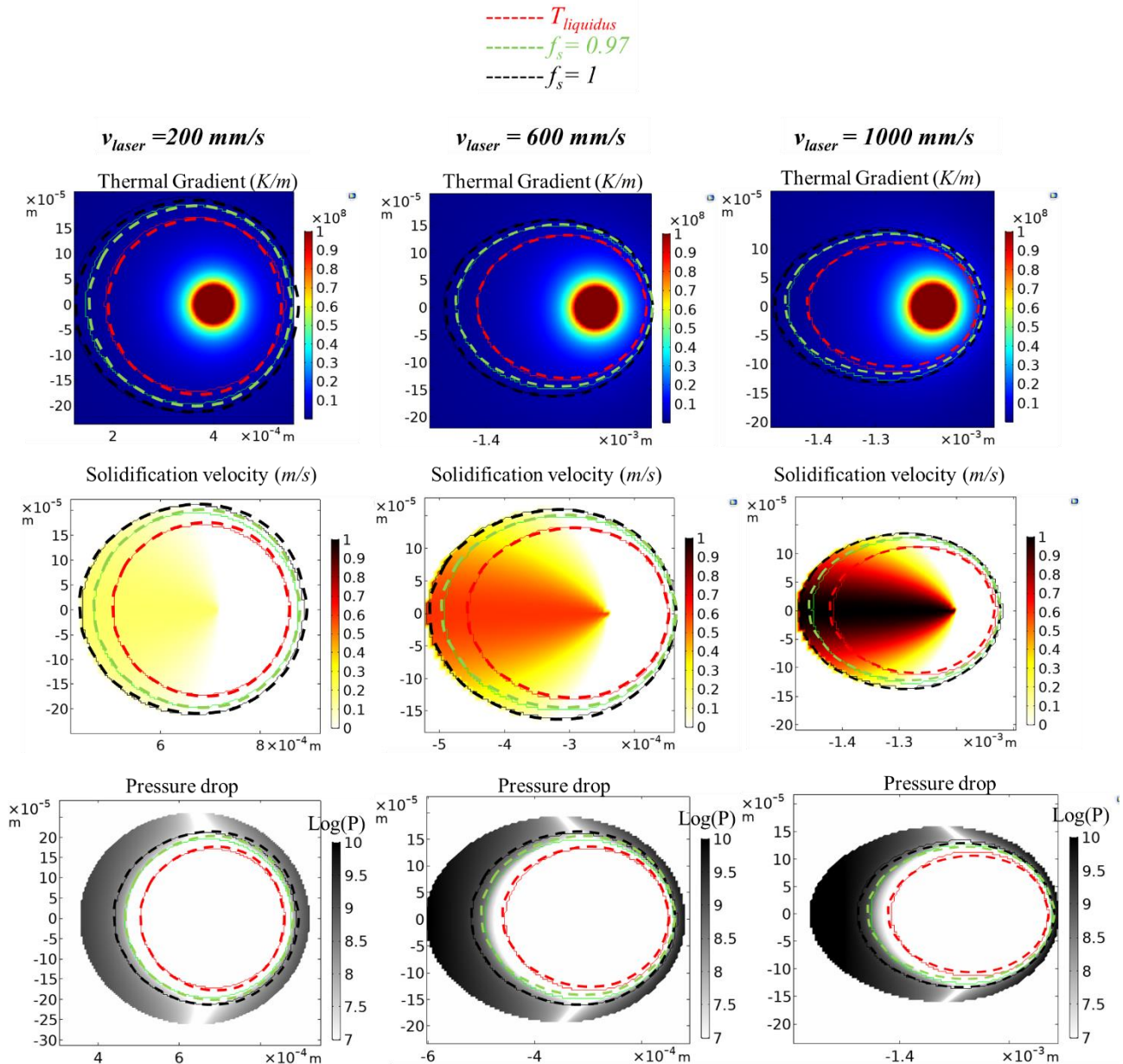


Figure 6-3 Effect of laser scanning speed (v_{laser} : 200, 600, 1000 mm/s) on the spatial distribution of pressure drop inside the melt pool in the XY-plane. The first two rows show the thermal gradients and solidification velocity inside the melt pool corresponding to a constant laser power of 240 W. Pressure drop is estimated inside the melt pool by implementing RDG criterion based on the location specific solidification parameters (G, v).

For the $v_{laser}=200$ mm/s, the maximum $\Delta P_{total}(x,y)$ is $\sim 10^8$ Pa, whereas for the other two speeds (600 & 1000 mm/s) it exceeds more than $\sim 10^9$ Pa and $\sim 10^{10}$ Pa, respectively in the central region of the melt pool. For the central location of the melt pool, where the laser is passing, the $\Delta P_{total}(x,y)$ is maximum (better visualized in pressure map for $v_{laser}=1000$ mm/s). **Thus, application of RDG criterion inside the melt pool as shown in Figure 6-3, gives two important messages: (i) cracking sensitivity**

increases as the laser scanning speed and (ii) the central location of the XY plane melt pool has the highest $\Delta P_{\text{total}}(x,y)$.

The HCS map in **Figure 6-1**, the pressure drop for different energy densities in **Figure 6-2** and pressure drop inside the melt pool in **Figure 6-3**, all point to the same inference that it would be very challenging to achieve a crack-free zone, at least over the range of investigated melting parameters (P : 164-274W, v_{laser} : 600-1400 mm/s). **One would need solidification velocities below a critical value estimated to be about 0.2 m/s to produce less cracking sensitive L-PBF parts.** This inference, that reducing laser scanning speed will decrease the tendency for the 6061 Al-alloy to crack, is in correlation with the results reported in ref [34], which also reports a similar link between cracks and v_{laser} for Al-Cu-Mg alloys fabricated by L-PBF. However, reducing laser-scanning speeds and consequently increasing the E_L has its shortcomings. Indeed, when, $v_{\text{laser}} < 200\text{-}400$ mm/s was employed to fabricate samples by L-PBF, technological issues related to powder spreading onto the building platform were encountered (ProX200 machine). The roller used for spreading powder was occasionally blocked due to the overheating of the samples causing sample deformation at high E_L . Besides, for low laser speed, productivity might decrease significantly. Similarly, other physical issues related to keyhole porosity or spattering might become predominant due to low scanning speeds [76]. Another consequence of high linear energy density can be the evaporation of key alloying elements such as Mg, which might induce melt pool instabilities and alter the post-fabrication chemical composition of the 6061 Al-alloy. Thus, decreasing $v_{\text{laser}} < 200\text{-}400$ mm/s might be beneficial to reduce cracking sensitivity when the 6061 Al-alloy is fabricated by L-PBF, but, it might raise other technological or physical issues.

Another quantity that will be affected by the process parameters is the length of the mushy zone (L^c , see **section 5.4.3**), which we have not addressed so far. The length of the mushy zone can also varies inside the melt pool for a given set of parameters (P , v_{laser}), see **Figure 5-11b**). Considering the maximum length of the mushy zone ($\max L^c$) for a combination of (P , v_{laser}), and evaluating the effect of various linear energy densities (E_L) on ($\max L^c$), will permit us to visualize the trend in cracking location. **Figure 6-4** shows the effect of linear energy density on maximum L^c . In contradiction to **Figure 6-2**, the length of mushy zone increase as a function of linear energy density (see **Figure 6-4**), since higher laser energy densities impart larger melt pools depths. **The two concepts (ΔP_{total} and L^c) indeed seem to give a contradiction with respect to their variation as a function of energy densities.** However, it must be noted that, cracking occurs by the virtue of increase in pressure drop and the concept of extent of mushy zone can only guide us qualitatively to determine its most probable location. The length of mushy zone is not ‘the criterion’ to predict cracking, it is just a qualitative indication to expect the most probable location, given that ΔP_{total} for those particular locations exceeds 2.45 GPa. Thus, just considering the concept of length of mushy can be misleading and hence must be dealt with due care. **The pressure drop criterion must be given the priority to predict cracking in comparison to the length of mushy zone.**

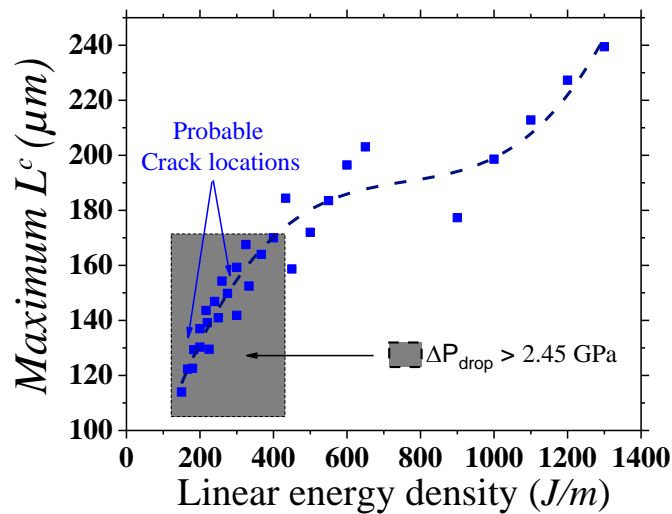


Figure 6-4 Maximum length of mushy zone (L_c) as a function of laser linear energy density. The maximum length of mushy zone was estimated using the concept of coalescence undercooling at $\theta=15^\circ$ for a the studied process parameters (P , v_{laser}).

Summary

The effect of first-order melting parameters (P , v_{laser}) was evaluated for cracking sensitivity based on the RDG criterion. It was concluded through the analysis of Hot cracking sensitivity (HCS) maps that, it is mandatory to reduce the solidification velocity ($v < 0.2$ m/s) to be less cracking sensitive. Solidification velocity is also found to be a highly influential factor compared to the thermal gradients. To achieve solidification velocities less than 0.2m/s, the laser speeds must be lowered to 200-400 mm/s. This lowering of laser speeds increases the linear energy density and can lead to different technological issues (spattering, keyhole porosities, blocking of powder spreading & Mg evaporation). **Thus based on our modelling approach, by varying the first-order melting parameters during L-PBF it will be very difficult to achieve a crack-free zone in 6061 Al alloy, similar to the experimental observations reported in Chapter 4.**

6.3. Effect of preheating conditions.

The previous section has shown that one way of minimizing hot cracking is to decrease the laser speed (affecting the solidification velocity). However, this might cause other issues as described previously. Here, we investigate other proven methods (mainly preheating [3]), which can modify solidification parameters (in particular the thermal gradient G) without giving any additional technological (powder spreading) or physical problems (keyhole porosity, spattering). Thus, to investigate the preheating effect, the substrate

temperature was varied from $T_0 = 20^\circ\text{C}$ (no preheating) to $T_0 = 500^\circ\text{C}$, in the Rosenthal analytical solution mentioned in equation 5.7. Figure 6-5 a)-b), illustrate the effect of preheating temperatures on the thermal gradients and solidification velocities, respectively. These solidification parameters are estimated along the melt pool contour of $f_s=0.97$ using the Rosenthal equation. It can be noticeable in Figure 6-5a) that, the thermal gradient $G_{f_s=0.97}$ can be decreased by 1 or 2 orders of magnitude when high temperature preheating is employed. For $T_0 = 500^\circ\text{C}$, the thermal gradient varies from $\sim 10^4$ - 10^5 K/m in comparison to 10^6 - 10^7 K/m when no preheating is applied. On the contrary, as shown in Figure 6-5b), solidification velocities do not drastically change due to preheating.

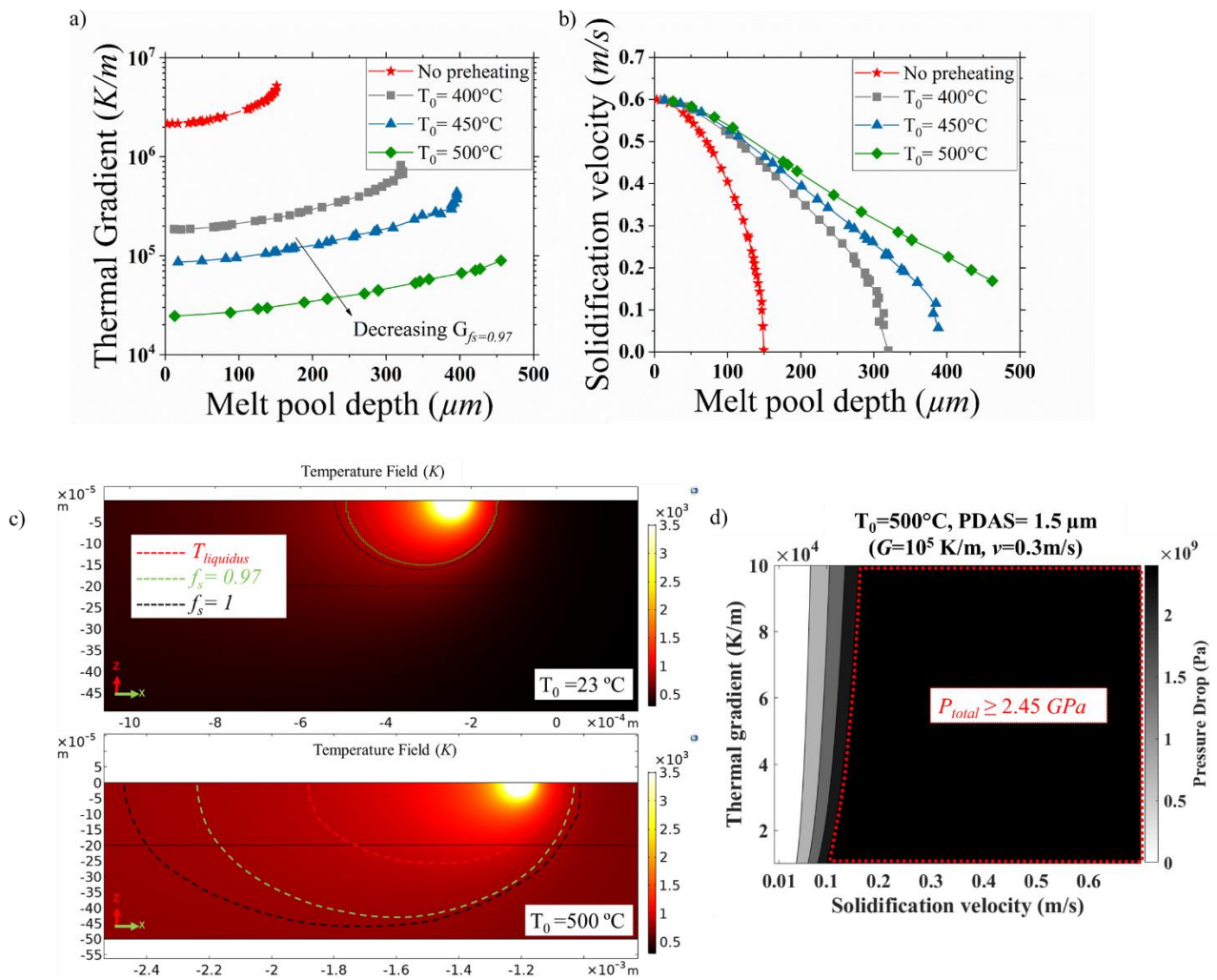


Figure 6-5 a) Effect of the preheating temperature on thermal gradients along the $f_s=0.97$ contour of the respective melt pools (for $P = 240\text{W}$ and $v_{\text{laser}} = 600$ mm/s). b) Effect of the preheating temperature on solidification velocities along the $f_s=0.97$ contour. c) Typical melt pools in ZX-plane for different preheating temperatures ($T_0=23^\circ\text{C}$ and $T_0=500^\circ\text{C}$). d) HCS map ($T_0 = 500^\circ\text{C}$) estimated using the updated G and v of the preheated melt pools and updated PDAS using the empirical formula ($\lambda = 43.2 (G \cdot v)^{-0.324}$).

For $P = 240\text{W}$ and $v_{laser} = 600\text{ mm/s}$, the melt pool depth will increase as a function of T_0 (see **Figure 6-5c**). This results in a slight change in the magnitude of the solidification velocity at a particular melt pool depth for different preheating temperatures in **Figure 6-5b**). However, as compared to thermal gradients, the solidification velocity order of magnitude is not affected by preheating. More importantly, the results presented in **section 6.2**, suggest that decreasing the solidification velocity can be an efficient way of reducing the hot cracking sensitivity.

Using these updated values of G and v obtained when preheating is applied; the total pressure drop can be estimated (assuming that coalescence undercooling and the parameters mentioned in **Table 5-4** are not affected by preheating). Note once again that both the strain rate and PDAS are updated based on the calculated values of both G and v . The HCS map displayed in **Figure 6-5d**) shows the effect of $T_0 = 500^\circ\text{C}$ on the total pressure drop using the updated solidification parameters, G (10^4 - 10^5 K/m) and v (0.3 m/s). **Since preheating does not drastically alter the solidification velocity but decreases substantially the thermal gradient, the RDG criterion predicts a higher pressure drop when preheating is applied. Such a dependence can be explained using the equation 6.1 ($\Delta P_{Total} \propto (v^{1.648}/G^{0.352})$), where decreasing the G and non-altering v , does increase the pressure drops.**

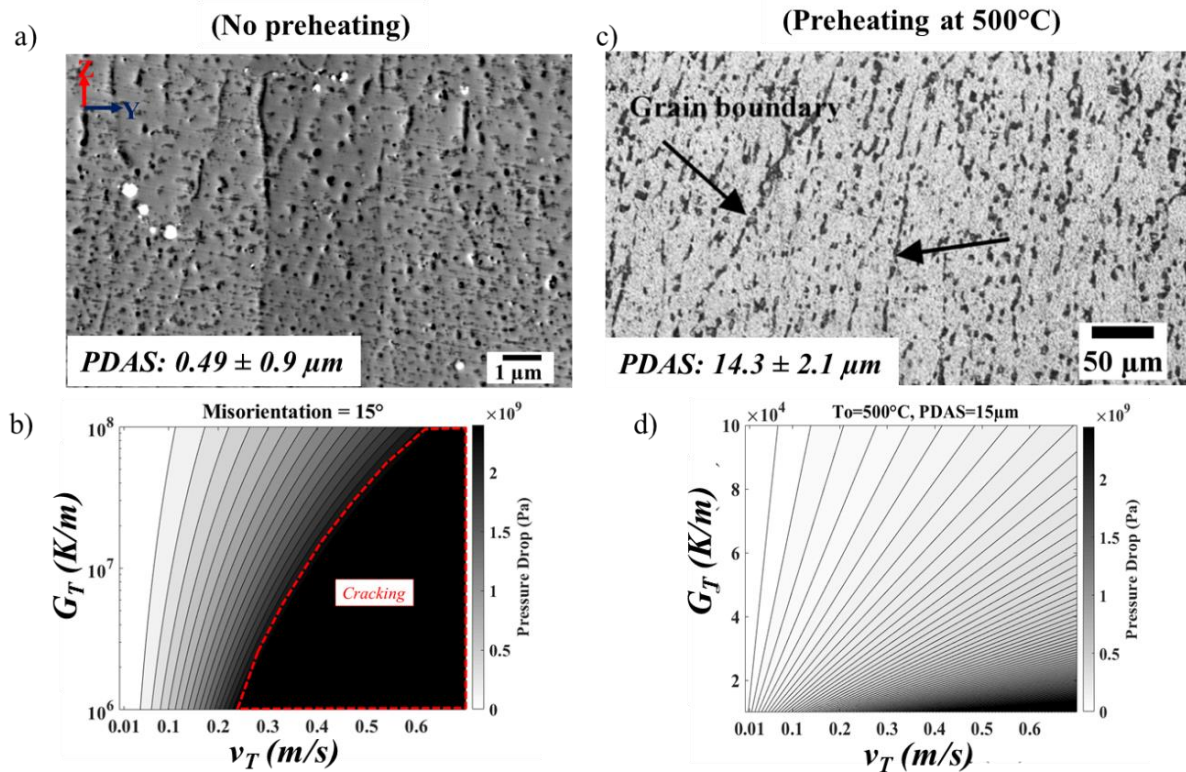


Figure 6-6 a)- b) SEM micrograph and corresponding HCS map, respectively, of 6061 Al alloy fabricated under L-PBF ($P: 240\text{W}$, $v_{laser}: 600\text{ mm/s}$) with ‘no preheating’. **c)-d)** Optical micrograph (adapted from ref. [3]) and corresponding HCS map, respectively, of 6061 Al alloy fabricated under L-PBF with ‘preheating $T_0 = 500^\circ\text{C}$ ’.

Such a result of predicting higher sensitivity to cracking due to preheating at $T_0 = 500^\circ\text{C}$, is not consistent with the results published by Uddin *et al.* in [3]. They showed that cracking can be suppressed with a preheating temperature of 500°C . To discuss this contradiction between our predictions using the RDG criterion and the experimental results of Uddin *et al.* [3] obtained in the case of preheating; we have roughly estimated the PDAS of the preheated samples at 500°C based on the micrographs published in the study of Uddin *et al.* [3]. **Figure 6-6a)** shows the etched micrographs for the case of ‘no preheating’ (present study). The primary dendrite arm spacing estimated from this micrograph is roughly $0.49\ \mu\text{m}$, which is similar to the one predicted using the empirical formula: $(\lambda = 43.2 (G.v)^{-0.324})$. **Figure 6-6b)** shows the corresponding HCS map (where PDAS was updated using the empirical formula). Similarly, **Figure 6-6c)** shows the ‘preheated’ micrograph from the work of Uddin *et al.* [3] and **Figure 6-6d)** shows its corresponding HCS map (considering the actual PDAS of $\sim 15\ \mu\text{m}$ from the **Figure 6-6c)** and not via the empirical formula).

It was found that in ref. [3] (see **Figure 6-6c)**), the PDAS was $\sim 15\ \mu\text{m}$ whereas the empirical formula used in the present work ($\lambda = 43.2 (G.v)^{-0.324}$ as suggested in [15]) would give a PDAS of about $1.5\ \mu\text{m}$ for a preheating temperature of 500°C ($G = 10^5\ \text{K/m}$ and $v = 0.3\ \text{m/s}$). **Thus, in comparison to the case without preheating (PDAS $\sim 0.49\ \mu\text{m}$), the PDAS is significantly increased to $\sim 15\ \mu\text{m}$ when the preheating temperature of 500°C is employed.** This last result further suggests that the empirical equation used for estimating the PDAS is likely not relevant to extrapolate values over a large range of solidification conditions, in particular when preheating is applied. At the same time, one should acknowledge that the total pressure drop is inversely proportional to the square of the PDAS ($\Delta P_{total} \propto \frac{1}{\lambda^2}$, see **equation 5.1**). It means that the PDAS strongly affects the pressure drop. The total pressure drop was then calculated using the PDAS measured to be equal to $15\ \mu\text{m}$ based on the micrographs published by Uddin *et al.* [3] and **Figure 6-5d)** was subsequently updated to **Figure 6-6d)**. Considering a PDAS of $15\ \mu\text{m}$ demonstrates that the cracking sensitivity of the 6061 Al-alloy will strongly decrease when preheating (by comparing **Figure 6-6b)** and **Figure 6-6d)**). Thus, it is very important to use accurate information concerning the different inputs of the RDG criterion, to relatively compare different solidification conditions.

Finally, it is also important to point out that the ratio G/v is known to control the morphology of the solidification front. It means that a decrease in this ratio can help to break down the cellular front and to promote the development of dendrite secondary arms. Here, it was shown that a preheating stage allows a decrease in the thermal gradient (G), and therefore the G/v ratio. Such a decrease might help to promote the development of dendrite secondary arms. It is thought that such a morphological change of the solidification front might also lead to an improvement of the coalescence behavior by breaking down the continuous liquid films.

Summary

The RDG criterion was used to evaluate the effect of pre-heating the substrate to predict the cracking sensitivity. Using Rosenthal analytical solution, thermal gradients and solidification velocities were

estimated for a preheating condition of 500°C. It turns out that, G is significantly lowered to 10^4 - 10^5 K/m, and whereas the order of magnitude of v is not altered. Using these inputs for the preheating case, and the actual PDAS corresponding to the micrograph reported by Uddin *et al.* [3] for the preheating case, the RDG criterion was able to estimate lower pressure drops, indicating beneficial effects of preheating to the cracking sensitivity.

6.4. Sensitivity studies for different parameters.

Depending on the inputs of **equation 5.1**, the total pressure drop can vary and significantly deviate. Hence, it is important to carry out a sensitivity analysis for the key input parameters of the RDG model. This section deals with varying the input parameters and understanding the effect on the total pressure drop. It also discusses the methods needed for controlling these inputs parameters, to avoid the cracking tendency.

6.4.1. Primary dendrite arm spacing (λ)

The first important microstructure parameter which depends on the solidification process is the primary dendrite arm spacing (PDAS). In the original formulation of the RDG criterion, the characteristic length of the microstructure is considered as the secondary dendrite arm spacing (SDAS) and not PDAS. The dependence of SDAS on pressure drop calculation in the RDG criterion comes from the concept of permeability (comparing **equation 5.1** and **equation 6.2**). By definition, permeability is the ease of liquid flow through a porous medium. The RDG criterion relies on the Carman-Kozeny relation (see **equation 6.2**), which shows that the ease of liquid flow (i.e. the permeability) in the mushy zone depends on the shape of the solid skeleton (i.e. it will depend if the mushy zone has primary arms or secondary arms) and also the solid fraction [161]. According to the fracture surface micrographs of **Figure 4-21**, the dendritic morphology gives evidence of mainly the primary arms and secondary arms are barely seen or are in the stage of initiation. Having said that, thus it is important to use the permeability of liquid in the presence of solid skeleton, which has mainly the primary arms. **According to Poirier [162], if the liquid flow is parallel to the columnar dendrites, the permeability depends only on the PDAS and not on SDAS.** Thus in the current study, the use of PDAS instead of SDAS in the RDG model can be justified according to ref [162]. Moreover, one could even derive geometrically the permeability, which is solely depending on the primary trunks than the complex dendrites.

$$K = \frac{\lambda^2 (1 - f_s(T))^3}{180 f_s(T)^2} \quad (\text{equation 6.2})$$

Where K is the permeability of the mushy zone, λ is the characteristic length of the microstructure (typically the secondary or primary dendrite arm spacing) and $f_s(T)$ is the fraction of solid as a function of temperature.

As seen previously that depending on the preheating conditions, PDAS can be significantly affected. PDAS can also be affected due to different solidification processes. **Table 6-1** compares the G and v for casting, welding and L-PBF processes. The typical PDAS's for these processes are estimated using the empirical formula: $\lambda = 43.2 (G.v)^{-0.32}$ [15]. The choice of this relation is detailed in **section 5.5**. It must be kept in mind that the empirical relation to estimating the PDAS was experimentally verified for the cooling rates typical of L-PBF (10^5 - 10^7 K/s) in ref [15]. For other processes like welding and casting that have comparatively low cooling rates, the relation must be used with care. Here in this section, the sensitivity study was just to have a rough estimate of the PDAS variation between different processes, thus the same empirical formula for PDAS was retained. To visualize how the PDAS changes with (G, v) , see **Figure 6-7a**). The PDAS increases rapidly for a decreasing G and v , i.e. casting and welding regimes will have higher PDAS compare to L-PBF.

Table 6-1 Estimated PDAS for various processes based on solidification parameters.

	Casting [82]		Welding [83]		L-PBF	
$v(m/s)$	0.001	0.001	0.001	0.1	0.1	10
$G(K/m)$	10	10^4	10^5	10^5	10^6	10^8
$PDAS(m)$	1.92×10^{-4}	2.05×10^{-5}	9.72×10^{-6}	2.19×10^{-6}	1.04×10^{-6}	5.24×10^{-8}

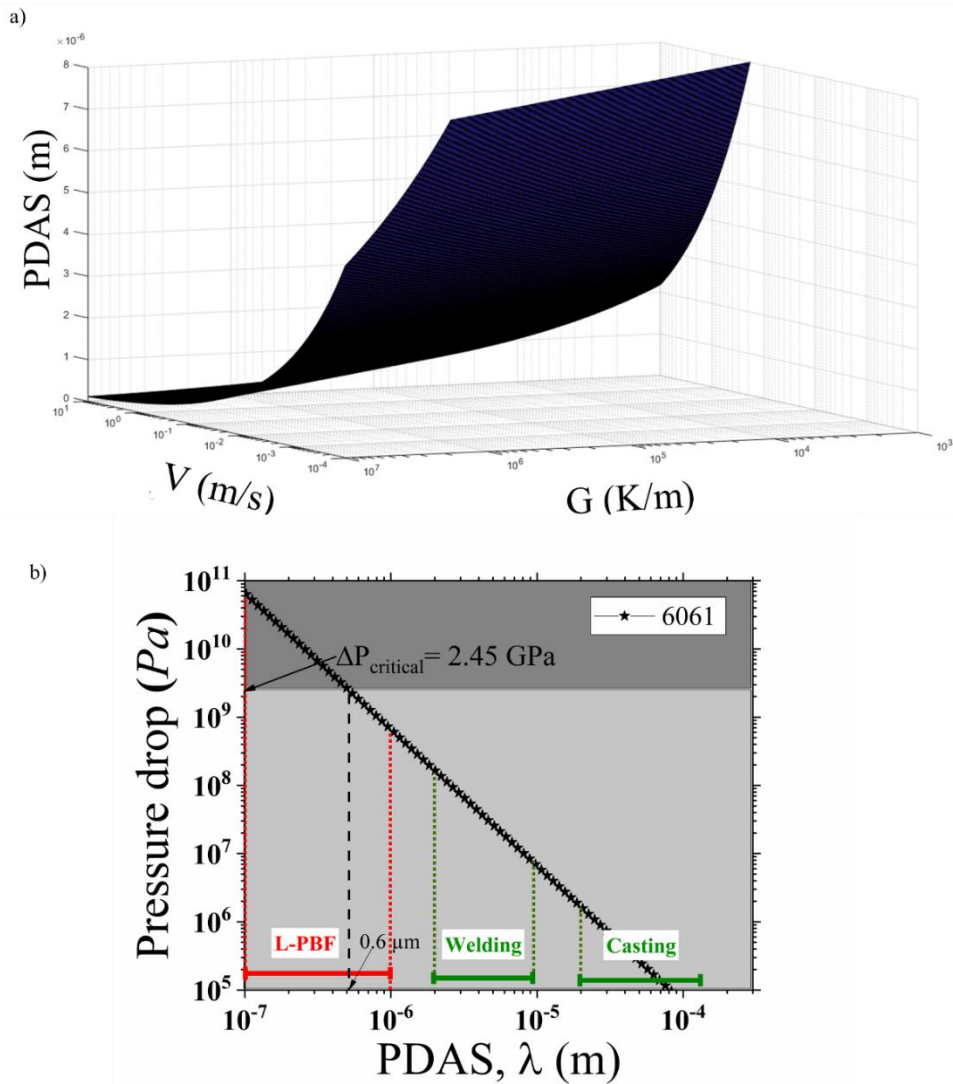


Figure 6-7 a) Evolution of PDAS as a function of thermal gradient and solidification velocity (according to $\lambda = 43.2 (G \cdot v)^{-0.324}$). b) Sensitivity analysis for variation in primary dendrite arm spacing (PDAS). The effect of PDAS variation on pressure drop is shown assuming all other input parameters to be not affected ($G=2.8 \times 10^6$ K/m and $v=0.3$ m/s, for $\theta=15^\circ$).

According to **equation 5.1**, $\Delta P_{total} \propto 1/\lambda^2$, the pressure drop decreases rapidly for an increasing PDAS, also confirmed by the sensitivity analysis of **Figure 6-7b**). Here, the sensitivity analysis for PDAS was done by varying it from 10^{-7} to 10^{-4} m, to understand the resulting variation in total pressure drop. The graph appears to be linearly decreasing due to the logarithmic scale. The λ corresponding to the critical pressure drop is around $0.6 \mu\text{m}$ and increasing it slightly to $1 \mu\text{m}$ can relatively decrease the pressure drop. Hence to understand which solidification process can capture such an increasing trend of λ , the typical PDAS corresponding to different process regimes from the values in **Table 6-1** are then superimposed on **Figure 6-7**, to know their relative cracking sensitivity tendency, in a qualitative way. It should be noted that the pressure drop calculation for **Figure 6-7b**) does not take into account the individual solidification parameters (G , v) corresponding to the different solidification processes, it only alters the λ to see its

effect on pressure drop for the G, v corresponding to optimized L-PBF condition ($P: 240W$ and $v_{laser}: 600mm/s$). According to **Figure 6-7b**), the characteristic length corresponding to casting regime and welding regime estimate relatively lower pressure drop values compared to λ 's of the L-PBF regime. This indicates that one way to decrease the cracking sensitivity in L-PBF conditions is to somehow concentrate on increasing the PDAS. Physically it means that the permeability of the mushy zone will be high for increased PDAS, resulting in better liquid feeding. However, permeability also depends on the morphology of the dendrites. Since in the present work only cellular dendritic morphology was observed, the role of morphology will not be much relevant and thus the magnitude of PDAS will control the permeability behavior.

Addressing the solidification parameters needed to achieve a crack-free zone under L-PBF conditions has been already addressed in **section 6.2**. However, to give a bigger picture of the HCS map, which includes different solidification processes (with updated G & v), is presented in **Figure 6-8**. PDAS corresponding to the different solidification process was estimated using the empirical law ($\lambda = 43.2 (G.v)^{-0.324}$), to generate the HCS map. The black region in **Figure 6-8** denotes the $\Delta P_{total} > 2.45$ GPa and thus indicating cracking sensitivity for the L-PBF process. Even in L-PBF, there is still a region, which is less cracking sensitive. This region can be achieved by reducing solidification velocity, similar to the conclusion of **section 6.2**. Similar to **Figure 6-7b**), the HCS map predicts lower cracking sensitivity to the casting and welding compared to L-PBF

However, as seen in the literature section, 6061 Al alloy is also reported to be cracking during welding. As mentioned previously, the cracking sensitivity criterion is based on pressure drop for L-PBF process considering the experimental observations of HAGB cracking. Several assumptions have gone into establishing this critical pressure drop like the coalescence solid fraction taken at $f_s=0.97$ and the undercooling at $\theta=15^\circ$, constant viscosity, crude approximation of strain rate etc. Thus comparatively to other processes, the pressure drop criterion will just provide a relative idea about the cracking sensitivity. In order to be sure and absolute for the cracking sensitivity in welding like process, the critical pressure drop corresponding to welding must be computed by taking inputs specifically observed during welding. For example, knowledge of following factors is necessary to estimate the cracking criterion during welding:

1. Microstructure: Welding can cause significant microstructural changes compared to L-PBF microstructure.
 - Microstructural inputs like PDAS must be accurately predicted for the welding process since the PDAS empirical relation used in the present study is experimentally verified only for the L-PBF processing conditions.
 - Misorientation based cracking must be investigated in welding. Whether the HAGB are susceptible to cracking? If HAGB are susceptible, coalescence undercooling specifically for welding must be evaluated.
2. Solidification parameters (G, v) estimated during the welding (inside the melt pool).
 - Melt pool geometry, i.e. the dimension can be significantly different compared to L-PBF, since cooling rates are quite different.

- Mechanical constraints need to be considered when predicting the cracking during welding. These constraints during welding can cause restrictions to the material's expansion or contraction, which is not the case in L-PBF. Their presence during welding can significantly affect the residual stress state and level of distortions in the material.

Thus to better estimate the cracking sensitivity using the RDG criterion, experimental feedback is important to accurately determine the cracking sensitivity criterion. A similar methodology employed in the present study might be useful to predict a critical pressure drop corresponding to the welding processes, beyond which the alloy becomes crack sensitive.

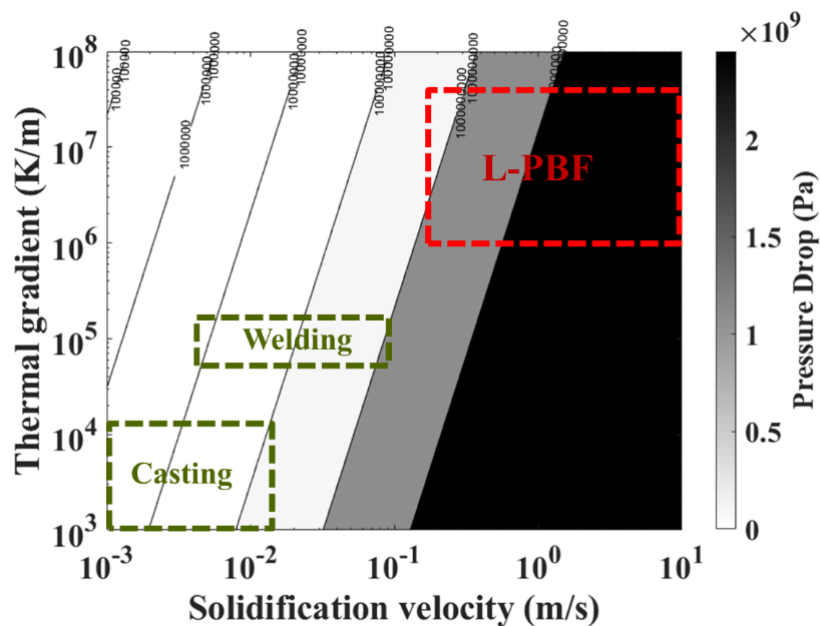


Figure 6-8 Hot cracking sensitivity map showing three different process regimes: casting, welding, and L-PBF marked in 'colored dashed squares'. The pressure drop was calculated assuming inputs from **Table 5-4** and at coalescence undercooling of 15° .

Speaking about the typical PDAS in the L-PBF framework, it can vary from $0.05 \mu\text{m}$ - $1 \mu\text{m}$ (estimated based on the PDAS empirical relation). Similarly, a way to control the PDAS of 6061 Al-alloy during L-PBF is by the utilization of preheating. With preheating of 500°C , the PDAS can increase to $\sim 15 \mu\text{m}$ (see **section 6.3**). Such an increase of PDAS is only possible due to preheating, which can significantly reduce the cracking sensitivity. In other words, the variation of PDAS shown in **Figure 6-7b** is highly possible in the framework of L-PBF. Investigation of variation in PDAS by other processing methods apart from the preheating must be examined (for example, double lasers, use of ultrasound etc).

6.4.2. Strain rate ($\dot{\epsilon}$)

Another important input of the RDG criterion is the strain rate. In the original formulation of the RDG model, the deformation is considered to occur perpendicular to the direction of dendrite growth. The rate at which deformation in the mushy zone takes place is by the virtue of local solidification parameters (G , v). Thus, depending on the deformation rate, the pressure drop in the mushy zone can vary and affect the cracking sensitivity. This section deals with understanding the effect of strain rate sensitivity on total pressure drop.

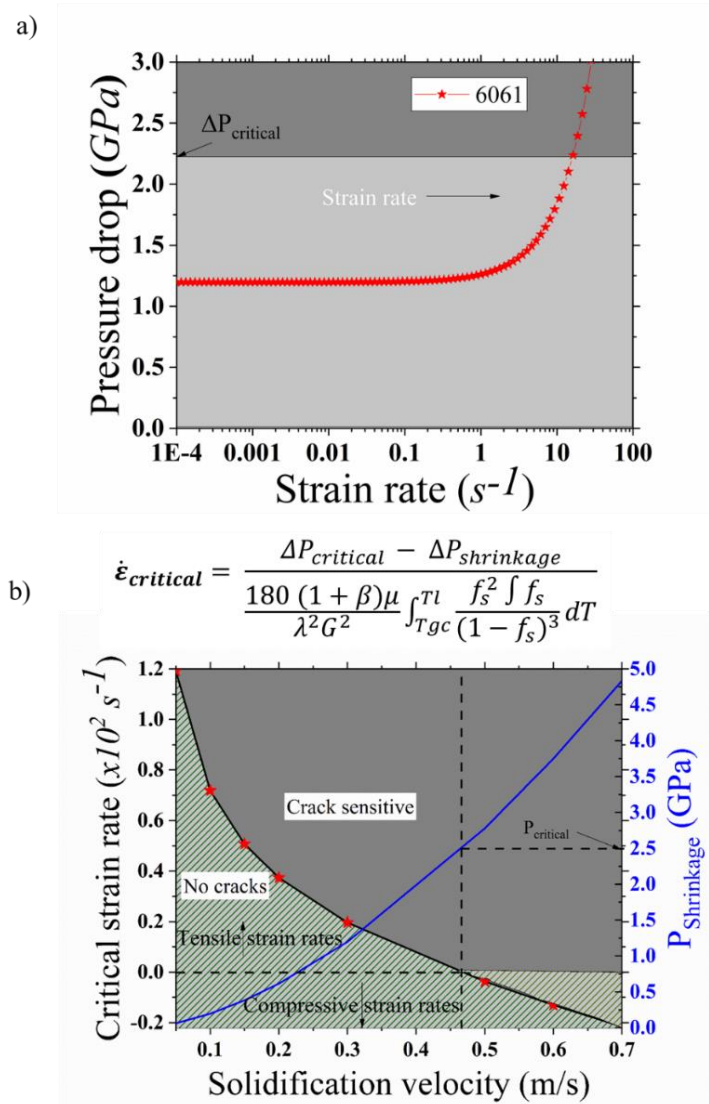


Figure 6-9 a) Shows the effect of strain rate sensitivity on total pressure drop estimated for $G=2.8 \times 10^6$ K/s and $v=0.3$ m/s & $\theta=15^\circ$. b) Effect of solidification velocity on the critical strain rate (beyond which cracking is highly probable), considering the $\Delta P_{critical}=2.45$ GPa.

In our study, the strain rate was assumed to depend on the local solidification parameters using the crude estimation ($\dot{\epsilon} = \alpha * G_{fs=0.97} * v$), as reported in ref [97]. In the current sensitivity analysis, the strain rate

was varied from 10^{-4} to 10^2 s^{-1} , and the total pressure drop was estimated as a function of strain rate, as shown in **Figure 6-9a**). The higher the strain rate, the higher will be the deformation causing cracking sensitivity. For instance in **Figure 6-9a**), the total pressure drop increases rapidly after a given strain rate in the range of ($\dot{\epsilon} = 1$ to 10 s^{-1}) and reaches the critical pressure drop around $\dot{\epsilon} \sim 19 \text{ s}^{-1}$. For $\dot{\epsilon} < 1 \text{ s}^{-1}$, there is negligible influence of strain rate on the pressure drop. This indicates that, to have higher pressures drops reaching critical value, a high strain rate ($> 1 \text{ s}^{-1}$) might be needed. Such high strain rates are typical of L-PBF and thus weakens the ability of the mushy zone to resist the thermal strains during the last stage of solidification. This suggests that, it is imperative to increase the ability of the mushy zone to resist high strain rates.

Another way to look at the deformation problem inside the mushy zone is by considering the critical strain rate ($\dot{\epsilon}_{critical}$). The $\dot{\epsilon}_{critical}$ is defined as the strain rate beyond which, $\Delta P_{Total} > \Delta P_{critical} = 2.45 \text{ GPa}$, i.e. the point at which, the maximum capacity of the mushy zone to bear the strain rate has been reached. Beyond the critical strain rate, cracks can nucleate and further weaken the mushy zone. The critical strain rate can be estimated using **equation 6.3**, at the critical pressure drop.

In the previous section, it was concluded that reducing solidification velocity will be beneficial for cracking sensitivity. To see how the critical strain rate is varied as a function of v , please refer to **Figure 6-9b**). The critical strain rate decreases as the solidification increases. This suggests that, for lower v , the critical strain rate will be higher, making the mushy zone more resistant to the deformation, in comparison to the high solidification speeds. This is another reason why lower solidification velocity is beneficial for avoiding cracking. Moreover, two regimes can be identified in **Figure 6-9b**), the region above the critical strain rate curve, 'grey region' is referred to as cracking sensitive and the region below 'green area' is considered as less sensitive/crack free. For each solidification velocity, there exists a strain rate beyond which cracking is highly probable (i.e. the $\dot{\epsilon}_{critical}$).

It must be also noted that the critical strain rate shows a transition from positive values (tensile strains) to negative values (compressive strains) when solidification velocity is high enough ($\sim 0.46 \text{ m/s}$). This happens because the $\Delta P_{shrinkage}$ increase as a function of v (see the blue curve of **Figure 6-9b**) and reaches a value of 2.45 GPa at $v = 0.46 \text{ m/s}$. This makes the numerator of **equation 6.3** \rightarrow zero, i.e. when $\Delta P_{critical} = \Delta P_{shrinkage} = 2.45 \text{ GPa}$ for the $v = 0.46 \text{ m/s}$; the resultant critical strain rates are 'compressive'. It is known that cracks are triggered due to the strains that are 'tensile' in nature and not by the 'compressive'. However, for high v , the critical strain rate is compressive in nature. To explain cracking for high v regime, please refer to the $\Delta P_{shrinkage}$ curve. Consequently, the shrinkage dominates the deformation, as the $\Delta P_{shrinkage} > \Delta P_{critical} = 2.45 \text{ GPa}$ (for $v > 0.46 \text{ m/s}$). That is the reason why the area enclosed within ($\dot{\epsilon}_{critical} < 0$ and $v > 0.45 \text{ m/s}$) do not lead to cracking due to deformation, however, in reality cracking occurs for such high solidification velocities due to the dominant shrinkage contribution.

$$\dot{\epsilon}_{critical} = \frac{\Delta P_{critical} - \Delta P_{shrinkage}}{\frac{180(1+\beta)\mu}{\lambda^2 G^2} \int_{T_{gc}}^{T_l} \frac{f_s^2 \int f_s}{(1-f_s)^3} dT} \quad (\text{equation 6.3})$$

It is highly important to control the strain rate since slight fluctuation can result in attaining the critical strain rate, beyond which cracking is most probable. However, reliably predicting the cracking sensitivity based on the RDG model, it is necessary to have a rough estimate of the strain rates in the mushy zone. In the framework of L-PBF, it is very rare and difficult to measure the strain rate during the high cooling rates associated with the process. The strain rates reported in literature dealing with the application of the RDG criterion to alloys fabricated during L-PBF, use the strain rates obtained in the welding literature, see ref [163]. In the present studies, we tried to make a crude estimation, similar to ref. [97] and found a strain rate for L-PBF conditions could be in the range of $1-19 \text{ s}^{-1}$. These values are comparatively higher than the ones reported in welding literature ($10^{-4} - 10^{-2} \text{ s}^{-1}$) [7,89]. Thus until now, there are no experimental studies that report the strain rates identified during the L-PBF process.

In addition, the strain rate can be significantly affected by the microstructure (the grain size), as pointed out by Coniglio *et al.* [90]. It is the only parameters in the RDG model, which can have a direct correlation with the grain size since strain partitioning is likely possible in the mushy zone. Increasing the number of interfaces (refining the grain size) to re-distribute the strains can be thought of as a way to increase the strain bearing capacity of the mushy zone. Investigating this link would require running mechanical tests in the mushy zone for microstructures having different grain sizes to establish the link between the strain rate and the grain size.

6.4.3. Viscosity (μ)

Another parameter that we have not discussed yet is the viscosity of the liquid. It is known that the permeability of the liquid depends on the shape of the solid skeleton and fraction of the solid, according to the Carman-Kozeny equation used in the RDG criterion. According to Darcy's law [161], the velocity of liquid feeding (L_v) is described according to **equation 6.4**.

$$L_v = \frac{K_s}{\mu} \frac{dP}{dx} \quad (\text{equation 6.4})$$

Where K_s is the specific permeability, μ is the viscosity and $\frac{dP}{dx}$ is the pressure gradient along the liquid flow direction. Thus, the lower the viscosity of the liquid, the higher will be liquid feeding flow velocity into the dendrites. The liquid flow also depends on the permeability factor, which in turn depends on the morphology of dendrites, see **section 6.4.1**. This current section focuses on the effect of variation in viscosity on the total pressure drop.

In our analysis of the RDG criterion, the viscosity was assumed to be constant ($\mu = 0.0014 \text{ Pa.s}$) [157] and taken as the one for pure Al, as mentioned in **Table 5-4**. However, in reality, viscosity is dependent on temperature and can strongly fluctuate due to solute content. **Figure 6-10**, shows the sensitivity analysis of viscosity in determining the pressure drop. Viscosity seems to have a strong dependence on pressure drop based on **equation 5.1**. The total pressure drop is directly proportional to μ . Thus, a slight variation in μ can significantly increase or decrease the cracking sensitivity.

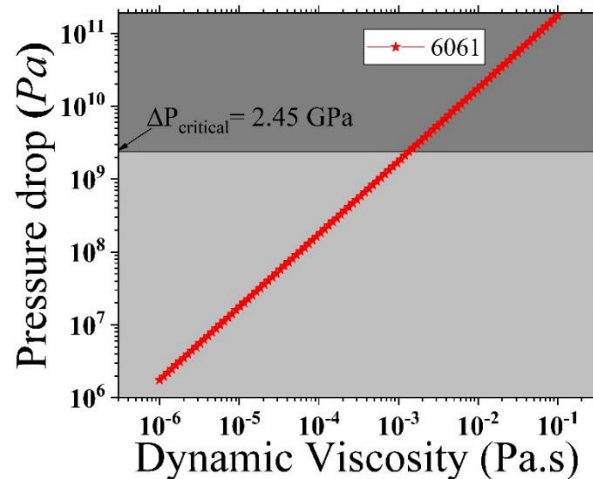


Figure 6-10 Shows the effect of viscosity on variation in total pressure drop calculated for $G=2.8 \times 10^6$ K/m, $v=0.3$ m/s, and $\theta=15^\circ$.

A similar exercise was done by generating the hot cracking sensitivity maps in L-PBF processing conditions for various viscosities, as shown in **Figure 6-11**. From **a)** to **e)** in **Figure 6-11**, the viscosity is decreased to see its eventual effect on the HCS maps. A large variation of the viscosities was deliberately performed to identify values that lower the pressure drops. The realistic feasibility of these viscosities will be discussed later.

For the case of viscosity value ($\mu = 0.0014$ Pa.s), which is used in the current study corresponding to pure Al alloy (i.e. **Figure 6-11b**), the crack-free region can be achieved for $v < 0.2$ m/s. Decreasing the viscosity by an order of magnitude ($\mu = 0.00014$ Pa.s), as shown in the HCS map of **Figure 6-11e**), a less crack sensitive region can be predicted for the L-PBF conditions. **This suggests that, viscosity of the melt can be an important factor to be considered while designing crack-resistant alloys for L-PBF. In other words, it should be looked as a parameter for alloy design.**

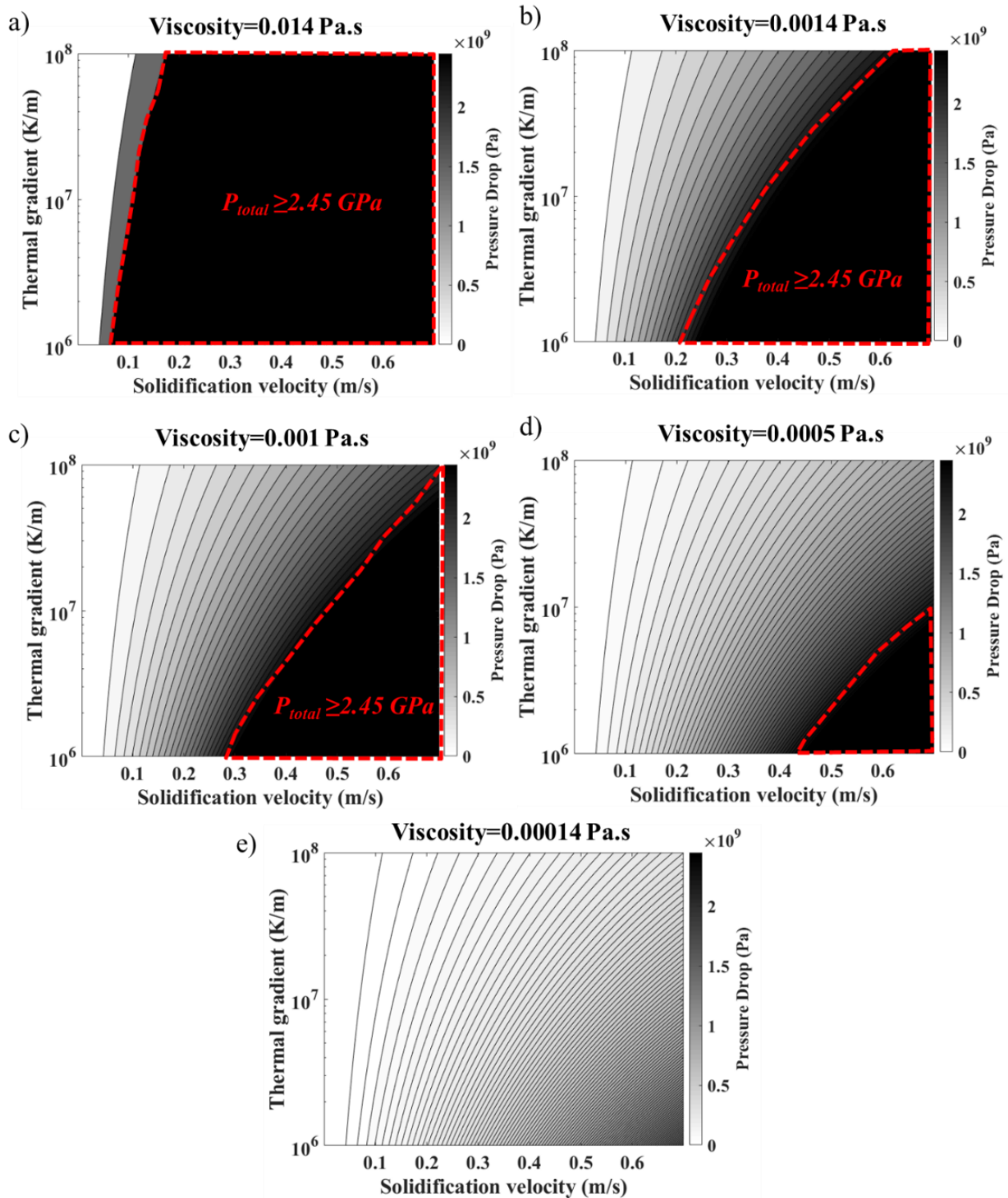


Figure 6-11 a) – e) Hot cracking sensitivity maps in L-PBF processing conditions as a function of viscosity.

It is known that viscosity can be affected by temperature and also by the presence of solutes. Investigating effect of solutes on the viscosity of the alloy is a difficult task. Considering the temperature aspect, a way to estimate viscosity dependence on temperature is using the Arrhenius form as reported in ref [157].

Many other parametric based models and empirical formulas have been proposed in literature but the Arrhenius based viscosity seems to fit most of the metal viscosities, according to ref [164]. Thus to understand the variation of viscosity in the range of solidification temperatures, **equation 6.5** was used.

$$\mu(T) = \mu_o e^{\frac{E}{RT}} \quad (\text{equation 6.5})$$

Where, μ_o is pre-exponential viscosity, E is the activation energy for the viscous flow, R is the gas constant ($8.314 \text{ Jmol}^{-1} \text{ K}^{-1}$) and T is the temperature (K). **Table 6-2**, provides the data needed to estimate the temperature dependent viscosity for pure Aluminum.

Table 6-2 Viscosity data for pure Aluminum at melting temperatures, adapted from [157] [164].

Solute elements	$T_L (^{\circ}\text{C})$	$\mu_o (\text{Pa.s})$	$E (\text{KJ/mol})$	$\mu(T_L) \text{ in mPa.s}$
<i>Al</i>	660	0.000257	13.08	1.4

Using the data of **Table 6-2** for pure Al, the evolution of viscosity in the temperature range (Liquidus to grain coalescence temperature considered at $\theta=15^{\circ}$) is shown in **Figure 6-12a**). In the current study, $\mu(T_L)$ for pure Al was assumed to be constant (1.4 mPa.s), for the entire solidification range. However, as seen in **Figure 6-12a**), the viscosity can vary with the temperature based on the Arrhenius law. As the solidification progresses (temperature approaching solidus), the viscosity continuous to increase and reaches a high point of about 0.003 Pa.s, indicating that at the end of solidification the liquid feeding will be difficult. It should be noted that, for $T=T_L=652^{\circ}\text{C}$ for 6061-grade, the calculated viscosity is around 0.0014 Pa.s and around $T=T_{gc}(\theta=5^{\circ})=558^{\circ}\text{C}$, the $\mu \sim 0.0017$ Pa.s. This difference is not so much; however, it can still affect liquid feeding. To take this temperature dependent viscosity into account and estimating the cracking sensitivity based on pressure drop, the **equation 5.1** must be updated to **equation 6.6**, to include the $\mu(T)$ inside the integrand function. In such a way, while computing the integrand function in a range from T_L to T_{gc} , the μ corresponding to different temperatures will be taken into account. This modification allows us to compute the pressure drop and also develop the HCS maps, taking into account the $\mu(T)$. Thus, the HCS map of **Figure 6-1b**) (for constant μ and $\theta=15^{\circ}$) can be updated to **Figure 6-12b**) (considering $\mu(T)$ and $\theta=15^{\circ}$). In comparison to the **Figure 6-1b**), the **Figure 6-12b**) shows a slight increase in the cracking sensitive area. By taking into account $\mu(T)$, the solidification velocity needed to achieve the crack free regions tends to occur around $v < 0.15$ m/s, compared to previously predicted $v < 0.2$ m/s. Thus, in reality, it indicates that we might need to even further decrease the v since viscosity is temperature dependent. This inference is just by considering the pure aluminum case as a function of temperature, practically, the viscosity can also deviate due to the presence of other solute elements present in the 6061 Al alloy.

$$\begin{aligned} \Delta P_{total} &= \frac{180(1+\beta)}{\lambda^2 G} \int_{T_{gc}}^{T_l} \frac{\mu(T)E(T)f_s(T)^2}{(1-f_s(T))^3} dT \\ &+ \frac{180v\beta}{\lambda^2 G} \int_{T_{gc}}^{T_l} \frac{\mu(T)f_s(T)^2}{(1-f_s(T))^2} dT \end{aligned} \quad (\text{equation 6.6})$$

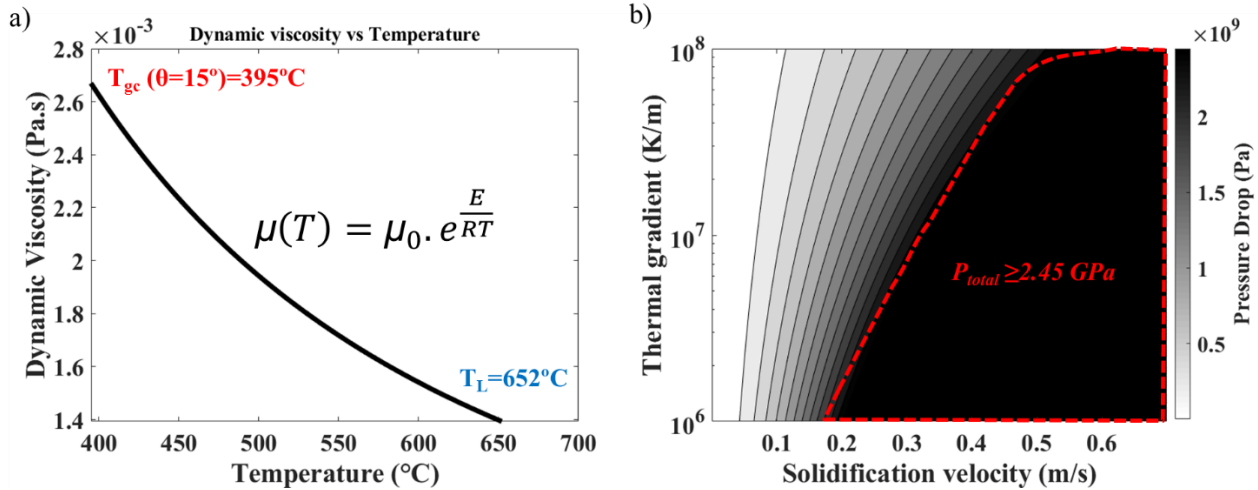


Figure 6-12 a) Dynamic viscosity of pure Aluminum as a function of temperature in the solidification range (T_L to $T_{gc}(\theta=15^\circ)$). b) HCS map of 6061 Al alloy for L-PBF, taking into account the $\mu(T)$ for pure Aluminum.

To take into account the effect of solute contents on the net viscosity of the 6061 Al alloy is a difficult task. However, various models have been already published to evaluate the viscosities of the binary and ternary alloy systems. Analyzing the net viscosity of an alloy, will need further experimental studies like the ‘oscillating vessel method’ or capillary rheometry experiments, as reported in ref [157]. The viscosity range of some of the Al-alloys is listed in **Table 6-3** for a temperature range of 900-1073K. According to Valencia *et al.* [17], the viscosity of the Al-alloys varies from 1-1.4 mPa.s and there is not much of a difference when comparing alloys from different series. However, the viscosity of the individual Al-alloys can be altered by changing the solute composition but there are very few published studies that evaluate this effect.

According to ref [157], Si and Zn tend to decrease the net viscosity of the binary Al alloys, however, till now, their effect on alloys like 6061, is not yet reported. The reduction of cracking observed in 7075 Al-alloy by addition of Si, is attributed to the reduction of melt viscosity by Si addition, according to Sistiaga *et al.* [5]. Similarly, according to ref [157], elements like Mg, Cr, Mn, Ti, Ni tend to increase the net viscosity of the binary Al-alloys, but the literature lacks information concerning the effect on alloys having many solute elements. Thus, it is very difficult to predict the net viscosity of the 6061 Al-alloy based on solute content modification and it is highly unlikely that the modification can lower the viscosity by at least an order of magnitude (see **Figure 6-11e**) to be less cracking sensitive.

Table 6-3 Dynamic viscosities of Al-alloys (adapted from ref. [17])

Al-alloys (wt%)	Dynamic viscosity (mPa.s)
7075 (6.1Zn-2Cu)	1.1-1.3
6061 (1.2Mg-0.8Si)	1.15-1.4
2024 (4.4Cu-1.5Mg)	1.1-1.3
3004 (1Mg-1Mn-0.4Fe)	1-1.15
A319 (5Si-3Cu-1Zn)	1-1.3

Thus, knowing the present state of the literature with viscosity, a large variation of viscosity is unlikely to be possible. It is highly probable that solute content modification to a greater extent can decrease the viscosity, but changing alloy composition drastically is not always desirable.

6.5. Summary

The chapter focuses on the implementation of the RDG criterion based on a critical pressure drop of 2.45 GPa, developed in **chapter 5** to evaluate the processing conditions of L-PBF. Using the Rosenthal analytical solution, the L-PBF melting parameters namely, power (P) and laser speed (v_{laser}) were linked to corresponding solidification parameters: G, v , which are the direct inputs of the RDG criterion. Using such methodology, hot cracking sensitivity (HCS) maps were developed, which is an original way to identify the hot cracking regions based on solidification parameters. Experimental feedback from the crack density analysis was qualitatively compared with the prediction. The modeling approach was able to predict the crack sensitive zones and further provide guidelines to reduce the cracking density in the 6061 alloy fabricated by L-PBF. Based on the HCS maps, to be in a crack-free region during L-PBF, it is necessary to have a solidification speed of less than 0.2 m/s, this can be done by lowering the laser speeds to around 200-400 mm/s. However, with such low laser speeds, there is an increase of linear energy input causing other technological issues (blocking of powder spreading roller, keyhole porosities, or possible Mg evaporation). Thus, it is very difficult to expect less cracking sensitivity just by modifying the first-order melting parameters of L-PBF.

Another promising way to avoid the cracking, which has been already reported in literature [3], is the preheating of the base plate during fabrication. The reasoning behind the beneficial results with preheating was not clearly highlighted in ref [3]. To explain this effect using the RDG model, estimation of solidification parameters for the preheating of 500°C was done using Rosenthal solution. It was found

that, thermal gradients were significantly reduced and solidification velocity was not affected. In addition to that, the primary dendrite arm spacing (PDAS), was found to significantly increase with the preheating conditions, which was never identified as a parameter affected by preheating. Thus, including this observation of PDAS in the RDG criterion, helps to predict the beneficial effect of the preheating condition during L-PBF. Thus combining slow laser speeds along with preheating of 500°C, can result in crack-free 6061 Al alloy parts, by L-PBF.

Based on our sensitivity analysis, various parameters like the PDAS, the viscosity of the melt, and the strain rate experienced by the mushy zones were found to affect the cracking sensitivity, see **Figure 6-13**. As summarized in **Figure 6-13**, the black curve of PDAS indicates that it is the most sensitive parameter to affect the pressure drop, followed by viscosity and strain rate. In L-PBF framework, large variations of PDAS are possible, since preheating was found to affect the PDAS significantly. Viscosity of the melt liquid is the second most sensitive parameter and its variation to a larger extent is less likely to occur according to ref [17]. In addition, viscosity is the metallurgical parameter that needs some consideration while designing crack-resistant alloys for L-PBF. Similarly, strain rate does influence the cracking sensitivity but measuring and estimating the strain rate in the L-PBF framework is challenging since it can be easily affected by the solidification conditions and the microstructure.

Thus to summarize, future research efforts must concentrate on finding new ways to alter the PDAS (like in the case of preheating) or refine the microstructure to accommodate the strain rates to minimize the cracking in 6061 Al-alloy during L-PBF.

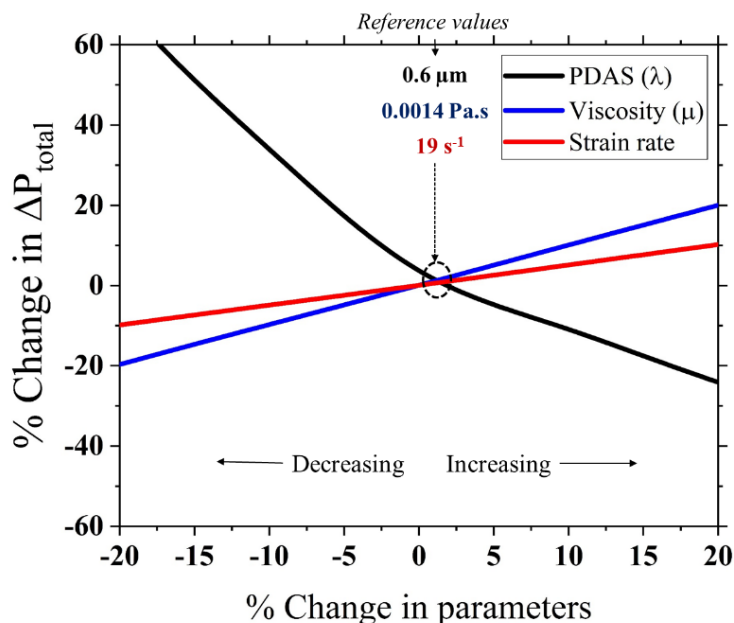


Figure 6-13 Summarized pressure drop sensitivity analysis due to variation in parameters, namely, PDAS, viscosity, and strain rate.

7. Effect of chemical composition modification on the hot cracking sensitivity

This chapter focuses on understanding the effect of solute content modification on predicting cracking sensitivity. It identifies the solute elements in 6061 Al-alloy, which play a major role in driving the cracking issues of the alloy.

It details the key insights needed to be considered during alloying additions, by combining the thermodynamics with the reported experimental observations. The chapter constructs out a methodology to find new alloy compositions, which are not sensitive to cracking during L-PBF, and provides qualitative inputs to incorporate the effect of nucleating agents in predicting the cracking sensitivity.

7.1. Introduction

As mentioned in the literature, several Al-alloys have been tested with L-PBF. For example, the AlSi10Mg and AlSi7Mg have been reported in numerous literature to be easily fabricated (crack-free, less porosity) by L-PBF, compared to structural Al alloys (6xxx and 7xxx series). This feasibility of fabrication to produce crack-free parts can be attributed to the solute content and the nature of solutes present in the alloys. **Table 7-1** shows the solute content of selected Al-alloys tested using L-PBF. The Al-Si-Mg family contains a lot of Silicon compared to other structural Al –alloys. For the 7075 Al alloy, which is also frequently reported to be cracking sensitive, high levels of Zn and Cu are present, compared to the 6061 Al-alloy. Thus, variations in alloying elements can directly affect the solidification path of the respective alloys and affect their processability.

Table 7-1 Standard solute content in different Aluminum alloys (wt%) [67]

	Si	Mg	Fe	Cu	Cr	Mn	Zn	Ti	Al
6061	0.8	1.2	0.7	0.4	0.35	0.15	0.25	0.15	Bal.
AlSi10Mg	10	0.45	0.55	0.05	-	0.45	0.1	0.15	Bal.
AlSi7Mg	7	0.65	0.55	0.2	-	0.35	0.15	0.25	Bal.
7075	0.4	2.9	0.5	2	0.28	0.3	6.1	0.2	Bal.

According to the RDG criterion mentioned in **section 5.1**, the cracking sensitivity of an alloy is affected by its solidification path. Thus to correlate the alloys for their cracking sensitivity, their solidification paths can be used as an input to run the RDG criterion. In this way, we can focus our attention on the effect of chemical composition. This chapter will focus on understanding the effect of solute content on the cracking sensitivity of 6061 Al-alloy, and help us suggest guidelines to predict compositions that could be processed more easily during L-PBF.

7.2. Effect of Solute content modification

For several decades, the work on variation of composition in welding metallurgy has been carried out to study the resulting cracking sensitivity. The work reported on binary Al-alloys by Sindo Kou *et al* [81], showed the cracking sensitivity is based on the solute element concentration, as summarized in **Figure 7-1**. A lambda-shaped curve can be observed for the cracking sensitivity as a function of solute content. For the binary alloys, with Si and Mg addition, the cracking sensitivity is at its peak for ~1 wt% additions; whereas for Cu, the sensitivity shifts towards higher values, ~2 wt% addition of Cu. This is the general

trend observed during welding of the classic binary alloys, however, when it comes to alloys with the presence of various solutes, the solidification paths of the resultant alloys can be significantly affected.

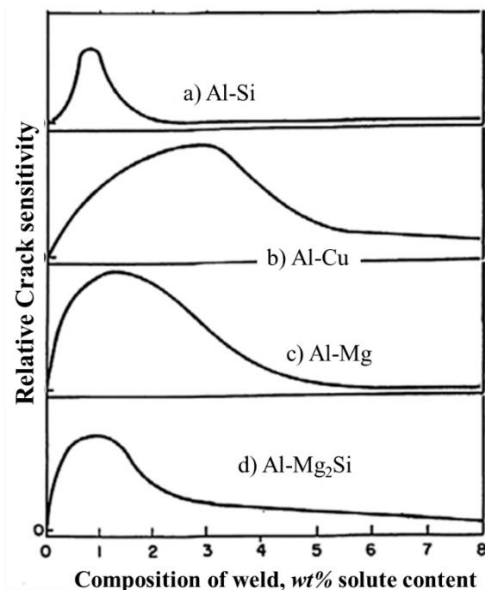


Figure 7-1 Shows the cracking sensitivity during welding of the binary Al-alloys for different solute elements a) Si, b) Cu, c) Mg, and d) phase Mg₂Si, adapted from ref. [81].

As mentioned in the literature that ZrH₂ addition on the powder surface was able to produce crack-free Al 6061 [4]. It is known that this solution exists, however, the addition of Zr, can be considered as an external element in the standard composition of the 6061 alloy. Thus, it is worth having a first look, whether the solute elements present in the standard 6061 alloy are themselves prone to inducing cracking or not. Solute content effect on cracking sensitivity of the Al-alloys is well documented for welding literature[33,165], but not for the L-PBF solidification conditions.

To study the effect of variation of solute contents on the hot cracking sensitivity, the first step is to understand the change in the solidification path. To do so, all the solute elements present in the standard 6061 alloys, were varied and their resultant solidification paths were estimated using the Scheil-Gulliver model as in **Figure 7-2 a) to f)** reports the $f_s(T)$ for the variation in Cr, Fe, Zn, Cu, Si, and Mg, respectively in the standard 6061 Al-alloy. Apart from the major solutes (Si and Mg), other minor solutes like Cr, Fe, Zn, and Cu were also examined since minor elements can also play a major role in depicting the $f_s(T)$. The composition was randomly varied to get an idea about the variation in the $f_s(T)$, the idea being to obtain a qualitative understanding of the role of each solute in affecting the $f_s(T)$. From the studied solute content modification, Cr, Fe and Zn are found to not drastically affect the $f_s(T)$, as shown in **Figure 7-2 a), b) and c)**, respectively. The Cr and Fe solute modification up to 4.65 wt% and 3.3 wt%, respectively, traces an exact $f_s(T)$, as for the case of standard 6061 alloy. There is a slight variation with Zn additions up to 1.75 wt%. On the contrary, Cu, Si, and Mg significantly affect the $f_s(T)$ for $f_s \geq 0.8$, as shown in **Figure 7-2 d), e) and f)**, respectively. To understand better the effect of solutes, the major solutes in 6061 Al-alloy, i.e. Si and Mg were selected for further analysis.

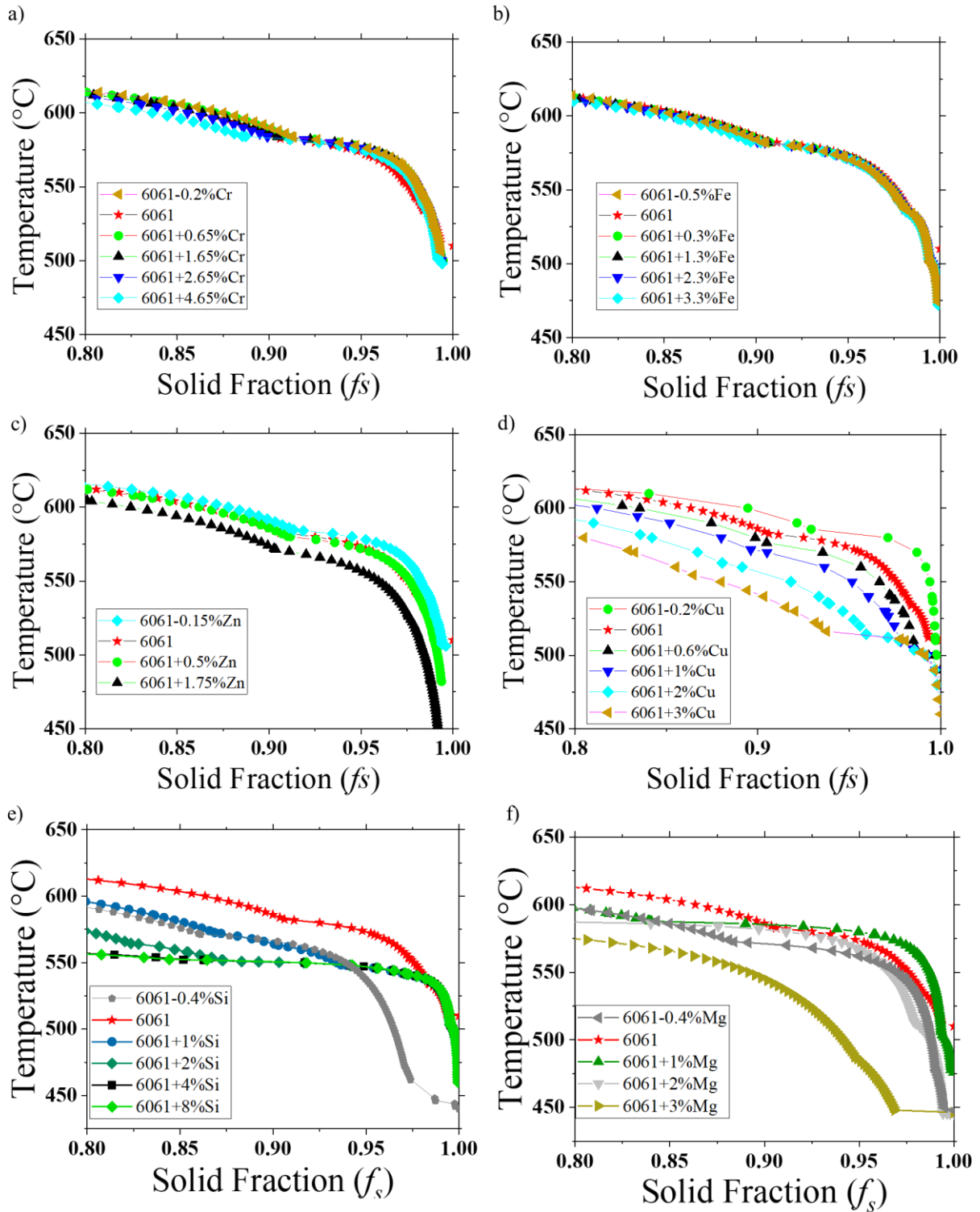


Figure 7-2 Solidification paths calculated using Scheil Gulliver assumptions for 6061 Al-alloy, subjected to different solute content variation: a) Cr, b) Fe, c) Zn, d) Cu, e) Si and d) Mg.

7.2.1. Effect of Silicon and Magnesium additions

The standard composition of the 6061 Al-alloy shown in **Table 7-1**, comprises mainly of Silicon (0.8 wt%) and Magnesium (1.2 wt%) as its principal alloying additions. The cracking sensitivity and weldability of the Al-Si-Mg system as reported in ref [26], shows high cracking sensitivity of around 1% for Si/Mg additions. This suggests that Si and Mg contents in the 6061 alloy, can influence the cracking sensitivity under L-PBF conditions.

The key inputs needed to apply the RDG criterion, which will be affected by compositional variations are: (i) the solidification path $f_s(T)$, and, (ii) the dendrite coalescence temperature T_{gc} . All the other inputs mentioned in **Table 5-2**, **Table 5-3**, and **Table 5-4**, including G and v typical of L-PBF, are considered to be independent of the alloying additions.

A similar effort of applying the RDG criterion to assess the effect of chemical composition has been reported by Drezet *et al.*[96]. They compared the sensitivity of Al-alloys belonging to different series, namely 2XXX and 6XXX series [96]. They used the solidification paths $f_s(T)$ for the different alloys as an input to apply the RDG criterion and compared their pressure drop (ΔP_{total}). Here, we rather investigate the consequence of variations of the Si or Mg contents in the standard 6061 Al-alloy on the pressure drop. **Figure 7-2 e) and f)** show the solidification paths during the last stage of solidification as a function of alloying variations of Si and Mg. With Si variations, the solidification path is affected for $0.8 \leq f_s \leq 0.97$ compared to the standard 6061 Al-alloy (red curve with stars). For $f_s \geq 0.97$, all Si additions follow the same path that of standard 6061 (except for 6061- 0.4 wt % Si). This indicates that addition of Si does not affect the solidification path during the very last stage of solidification ($f_s \geq 0.97$) in comparison to the standard 6061 Al-alloy (red curve with stars), see **Figure 7-2e)**. On the contrary, in **Figure 7-2f)**, with increasing Mg content compared to the standard 6061 Al-alloy, the $f_s(T)$ curve tends to become less steep in the entire range when $f_s \geq 0.8$. Such a comparison between solidification paths of Si and Mg, suggests that the cracking sensitivity can be affected by Si/Mg content modifications.

As already seen in **chapter 5**, the work done by E. Giraud *et al.* [73] was useful in determining the coalescence temperature for the 6061 Al-alloy. As mentioned in **section 2.3.1**, E. Giraud *et al.* [73] studied experimentally the mushy zone of the 6061 Al-alloy using the constrained solidification at 80 K/s. According to **Figure 2-15b)**, it was found that the ductility of the 6061 alloy is minimum in the solid fraction range of 0.94 to 0.97.

E. Giraud *et al.* [73] also examined the variation in coalescence f_s by Si and Mg solute content modification. They used filler wires of 4043 (Al-5Si) and 5356 (Al-5Mg) to modify the Si and Mg content, respectively, in the base 6061 Al-alloy. These various compositions were examined for the development of stress inside their respective mushy zones. According to **Figure 7-3**, irrespective of the composition, the stress level starts to increase at $f_s=0.6$ (indicating the coherency point, where the dendrite starts to be in contact). Similarly, for the 6061 base alloy, a rapid increase in the stress is observed at $f_s=0.97$ (indicating the coalescence point, after which the continuous liquid films start to be in the form of droplets).

As shown in **Figure 7-3a)**, the stress development in the mushy zone of Si-modified alloys starts exactly at $f_s=0.97$ for all the Si contents investigated up to 5 wt%. Thus, for Si contents up to 5 wt%, the fraction of coalescence did not vary and was equal to $f_s=0.97$. This indicates that, after $f_s=0.97$, the grains for Si additions can transmit the deformation to its neighboring grains. In other words, coalescence takes place at $f_s=0.97$. Whereas for Mg contents up to 4 wt%, the coalescence fraction decreases, i.e. stress developing at an earlier stage with Mg additions, as shown in **Figure 7-3b)**. **To summarize for all the variation of Si/Mg content, the coalescence solid fraction values were adapted from the E. Giraud *et al.* [73] as mentioned in Table 7-2.**

Even though L-PBF encounters a higher cooling rate ($\sim 10^6$ K/s), compared to the solidification process studied by E. Giraud *et al.* [73], we assumed that the coalescence temperatures (T_{gc}) determined experimentally for alloying additions of Si or Mg would not be affected. Therefore, the observations made by E. Giraud *et al.* [73], are further incorporated in our work as inputs (lower bound of the integrals in **equation 5.1**) to rationalize the use of different coalescence temperature T_{gc} depending on the content of Si or Mg. The coalescence fractions were systematically adapted from **Table 7-2**. Due to the unavailability of data, the coalescence fraction for decreasing Si or Mg contents by 0.4wt% in the standard 6061 Al-alloy was also assumed to coalesce at $f_s=0.97$.

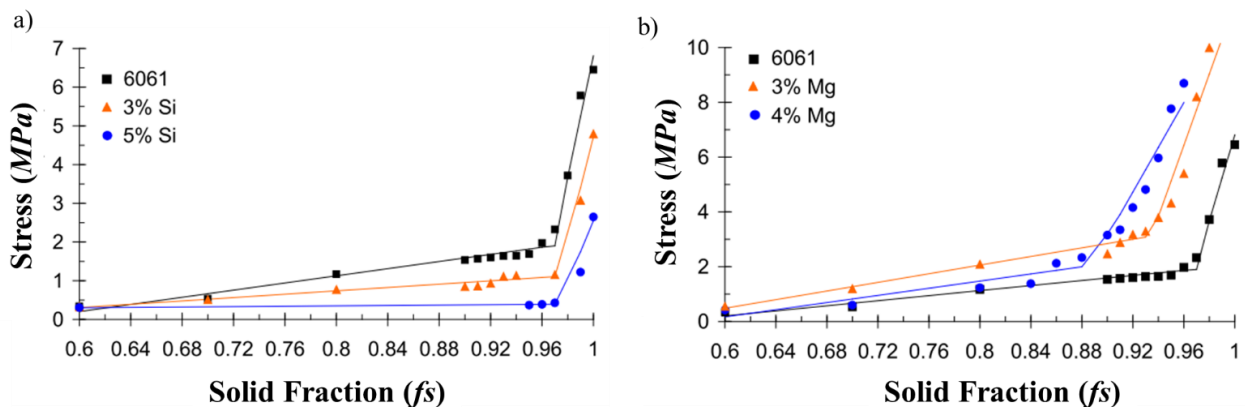


Figure 7-3 Constrained solidification studies, showing the development of stress in the mushy zone during solidification of modified 6061 Al alloy, a) Si content variation and b)Mg content variation, adapted from E. Giraud *et al.* [73].

Table 7-2 Coalescence solid fraction (f_s) for different Si/Mg content in the 6061 Al-alloy, adapted from [73].

Content (wt%) →	6061 standard	2	3	4
Silicon	$f_s=0.97$			
Magnesium	$f_s=0.97$	$f_s=0.97$	$f_s=0.92$	$f_s=0.88$

For the sake of clarity, the coalescence temperatures for each Si/Mg addition are mentioned onto their solidification paths as shown in **Figure 7-4 a) and b)**, respectively. It must also be highlighted that the adapted coalescence temperature T_{gc} (shown in **Figure 7-4 a) and b)**) for various alloying contents does not include the undercooling effect due to misorientation observed for standard 6061 alloy. Thus, to predict the total pressure drop (ΔP_{total}) for compositional variations of Si and Mg and compare it with the critical pressure drop $\Delta P_{critical}(\theta=15^\circ, f_s = 0.97) = 2.45 \text{ GPa}$ established for the standard 6061 Al-alloy, it is required to update the coalescence temperature $T_{gc}(\theta=15^\circ)$ for the respective variations of Si or Mg contents. Assuming that the grain boundary energy $\gamma_{gb}(\theta)$ is independent of compositional variations in the standard 6061 Al-alloy, the total pressure drop $\Delta P_{total}(\theta=15^\circ)$ can be estimated for all the alloying variations of Si and Mg considering the coalescence undercooling. This allows us to estimate the $\Delta P_{total}(\theta=15^\circ)$ for different alloying contents as shown in **Figure 7-4c)**.

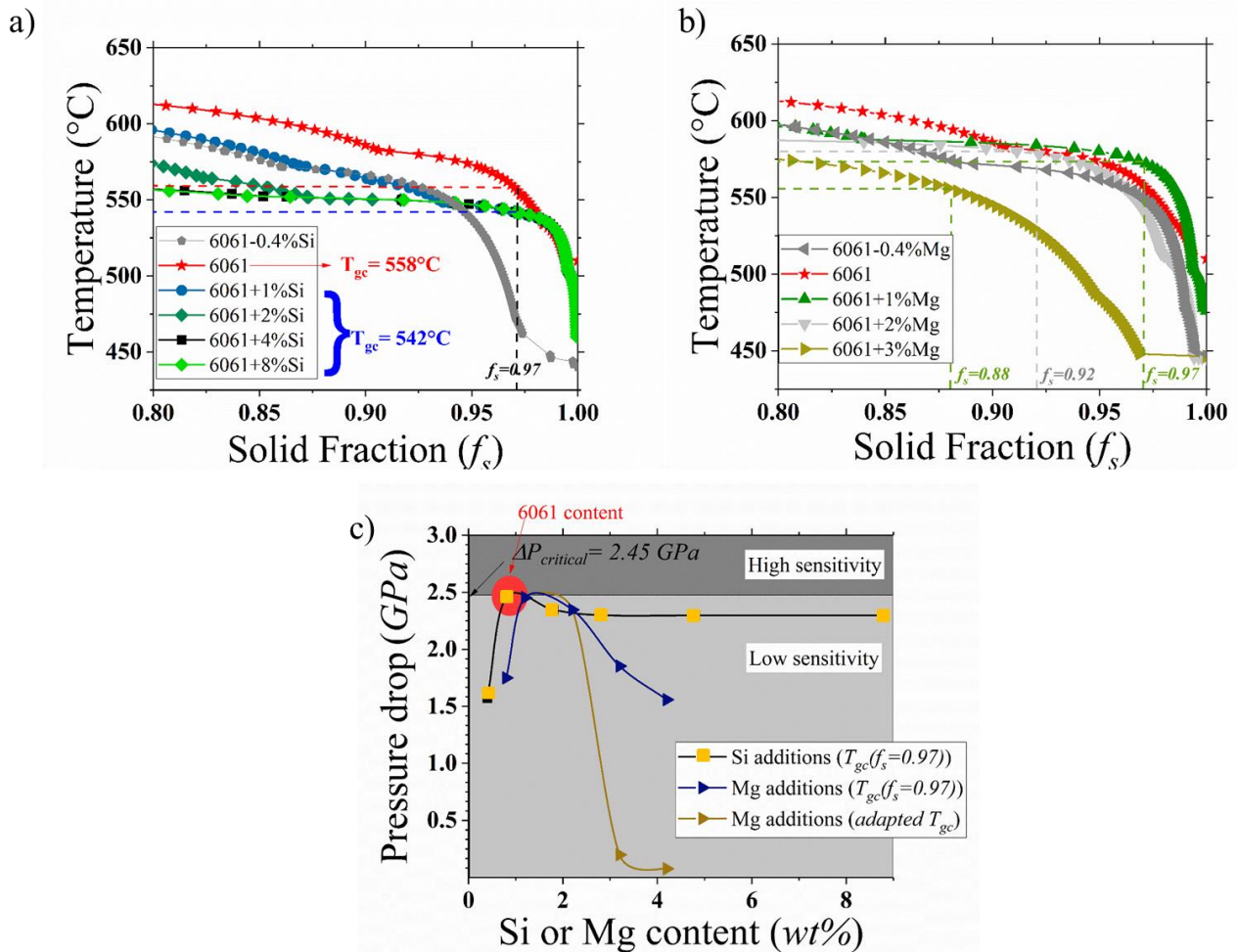


Figure 7-4 a) & b) Solidification paths in the final stage of the solidification process for varying Si and Mg additions to the 6061 Al-alloy respectively. c) Pressure drop calculated using the RDG criterion for various Si and Mg contents to the base 6061 Al-alloy (for $G = 2.8 \cdot 10^6 \text{ K/m}$, $v = 0.3 \text{ m/s}$, coalescence fraction estimated from **Table 7-2** and considering the coalescence undercooling for $\theta = 15^\circ$).

Three curves are shown in **Figure 7-4c**), the first one for the Si content and two others for the Mg content, considering on one side adapted fractions of coalescence from **Table 7-2**, and on the other side a constant fraction of coalescence, $f_s=0.97$. These modifications will allow us to determine the impact of the coalescence fraction to estimate the total pressure drop. The pressure drop sensitivity curve with Si or Mg contents exhibits a typical λ -shape, similar to what has been reported in [26,73] and also mentioned in **Figure 7-1**. For Si, the peak sensitivity is found to be around 0.8wt%, while for Mg additions the peak is at around 1.2% (the content of Mg in the 6061 base alloy). The work reported by J. Liu *et al.* [33] using a different cracking sensitivity criterion [93], predicts a similar peak sensitivity at Si and Mg contents of standard 6061 Al-alloy, for the Al-Si-Mg ternary alloy system. For all other Mg contents (irrespective of the fraction of coalescence) to the standard 6061 Al-alloy, the $\Delta P_{\text{total}}(\text{Mg}) \leq \Delta P_{\text{critical}} = 2.45 \text{ GPa}$, suggesting that Mg addition would make the 6061 Al-alloy less sensitive to cracking (for given processing conditions $G=2.8 \times 10^6 \text{ K/m}$ and $v=0.3 \text{ m/s}$). This indicates that even when considering a constant fraction of coalescence taken as $f_s=0.97$, whatever the Mg content, the general trend is still there (beneficial effect of Mg addition to the pressure drop). **This suggests that the general trend is governed by the $f_s(T)$ curve and modifying (decreasing) the fraction of coalescence, will further benefit to lower the ΔP_{total} .** On the contrary, the ΔP_{total} for Si additions is comparatively higher than for Mg additions, i.e. $\Delta P_{\text{total}}(\text{Si}) > \Delta P_{\text{total}}(\text{Mg})$, except for decreasing Si content. This result of higher sensitivity with Si addition is similar to the conclusion reported by E. Giraud *et al.* [73]. Even the experimental studies reported in ref [71] for cracking density as a function of Si/Mg additions show that for Mg additions, the crack density is less than the Si addition (see **Figure 7-5**). Shimizu *et al.* [166] reported a similar beneficial effect of Mg addition in their electron beam welding studies on 6061 Al-alloy.

To summarize, by increasing the Mg content in the 6061 Al-alloy, the coalescence of grains happen at an early stage (lower f_s), suggesting that the grain coalescence in the mushy zone makes the Al-matrix more resistant to the deformation and shrinkage effects. Therefore, predicting less ΔP_{total} for Mg additions compared to Si additions.

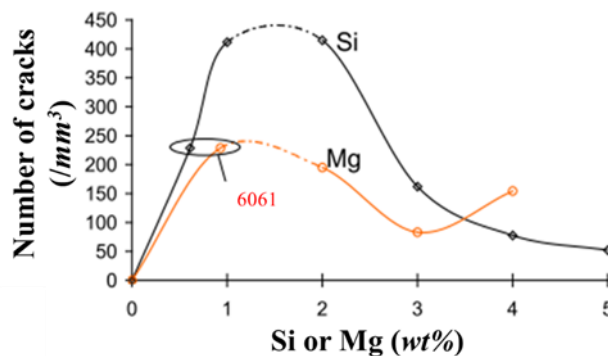


Figure 7-5 Crack density reported for 6061 Al-alloy as a function of Si/Mg content, during welding, adapted from ref [71].

Another observation from **Figure 7-4c)** is that by increasing Si content in the standard 6061 Al-alloy, $\Delta P_{\text{total}}(Si)$ tends to be slightly less than the 2.45 GPa, i.e. $\Delta P_{\text{critical}} > \Delta P_{\text{total}}(Si)$, but still it is close to the critical pressure drop. Adding a large amount of alloying elements might drastically change the standard composition of the initial alloy and lead to deviation from the desired mechanical properties of the fabricated specimens. Assessing the mechanical properties of modified alloys with the addition of Si or Mg is considered out of the scope of the present work. Similarly, adding a high amount of Si will also affect the melt viscosity [5]. However, considering the rheological behavior of the liquid due to solute elements in this analysis is considered out of the scope of the current work. The study only takes into account the effect of solute content on the solidification path and the resulting coalescence behavior to predict the cracking sensitivity of alloys.

So far, we have been analyzing the pressure drop as a function of Si/Mg solute variation for a constant solidification parameter ($G=2.8 \cdot 10^6$ K/m and $v=0.3$ m/s). It is also important to verify whether the combination of alloying additions and processing parameter optimization can lead to a reduction of the cracking sensitivity. The HCS maps shown in **Figure 7-6** illustrate the combined effect of processing parameters and alloying additions. To evaluate this combined effect as shown in **Figure 7-6 a) and b)**, we take as examples alloys with a 2wt% addition of Si and Mg, respectively. It is evident to point out that, with 2wt% Mg addition, the region of cracking-sensitive material ($\Delta P_{\text{total}} \geq 2.45$ GPa) is eliminated in comparison to 2wt% Si content. Moreover, with the Mg additions of 2wt%, the $\Delta P_{\text{critical}}$ is not reached for the studied range of solidification velocity, as compared to the standard 6061 Al-alloy (refer to **Figure 6-1b)**). This suggests that in addition to decreasing the solidification velocity to avoid cracking; it could be even more beneficial to increase the Mg content in the standard 6061 Al-alloy by 2 wt%. **Therefore, to summarize, Mg additions of (≥ 2 wt%) will be more efficient than Si additions to reduce cracking sensitivity in 6061 Al-alloy fabricated by L-PBF.**

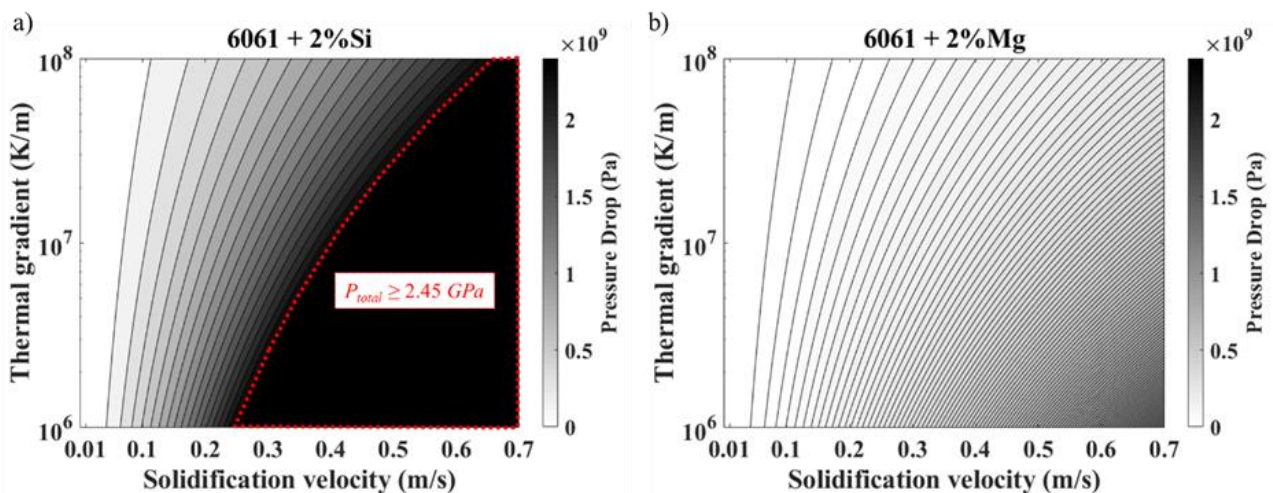


Figure 7-6 HCS maps to illustrate the effect of chemical composition and process parameters. a) and b) HCS map for 2wt% Si and 2wt% Mg addition to the 6061 Al-alloy, respectively.

7.2.2. Summary

Major solute elements of 6061 Al-alloy (Si and Mg) were evaluated for their role in affecting the cracking sensitivity. A typical λ -shaped cracking sensitivity for L-PBF processing conditions is predicted for the increasing content of Si/Mg contents. With increasing Mg content, the coalescence solid fraction of the alloy is shifted to lower values, making the alloy more resistant to solidification cracking, in comparison to the Si additions. Moreover, the HCS maps developed with the 2 wt% addition of Mg to 6061 Al-alloy, tends to eliminate the cracking susceptible zones during L-PBF.

Finally, one should note that the cracking sensitivity as summarized in this section is found to be coherent in the lines of welding literature [81]. In the framework of L-PBF, it is yet to be experimentally proven. However, based on the present work on predicting the cracking sensitivity using the RDG model, the trends reported in welding literature are certainly valid for L-PBF.

7.3. Effect of Zirconium (Zr) addition

For now, we have considered modifying the main solute elements in the standard composition of 6061 Al-alloy, namely Si and Mg. We studied their effect on the hot cracking sensitivity in **section 7.2**. This section deals with understanding the effect of an element that induces grain refinement.

As described in the literature section, refining grain size is also a proven methodology to mitigate cracking. A frequently reported element to avoid cracking in the Al-alloys during L-PBF is Zirconium (Zr). Martin *et al.* [4] proposed to add ZrH_2 particles on the powder surface to increase the grain nucleation of the matrix by the formation of the metastable Al_3Zr phase that lead to grain refinement to mitigate cracking. A similar approach has been implemented for aluminum alloys with Sc/Zr or Yttrium stabilized zirconia (YSZ) additions [51,110][104].

To start with, the solidification paths $f_s(T)$ of the Zr-additions to 6061 Al-alloy are generated as shown in **Figure 7-7**, since it is an input to run the RDG criterion (see **section 5.1**). Zr content is varied up to 5wt% in the standard 6061 Al-alloy, to visualize its effect on the $f_s(T)$. Compared to the standard 6061 solidification path, the liquidus is at elevated temperatures for the Zr additions. The liquidus temperature of the modified alloy increases as the quantity of Zr increases. For example at 2 wt% Zr addition, the liquidus is at 1000°C and for 4wt% Zr it is at 1100°C. Interestingly, for the Zr additions, the phase Al_3Zr precipitates out of the liquid prior to the α -Al matrix (see the magnified region of **Figure 7-7**). In literature, usually, the metastable Al_3Zr phase is reported to be responsible for heterogeneous nucleation of the equiaxed grains, see ref [51,110][104]. Thus, it makes sense that, once the Al_3Zr forms from the liquid, it acts as nucleating sites for the primary-Al grains.

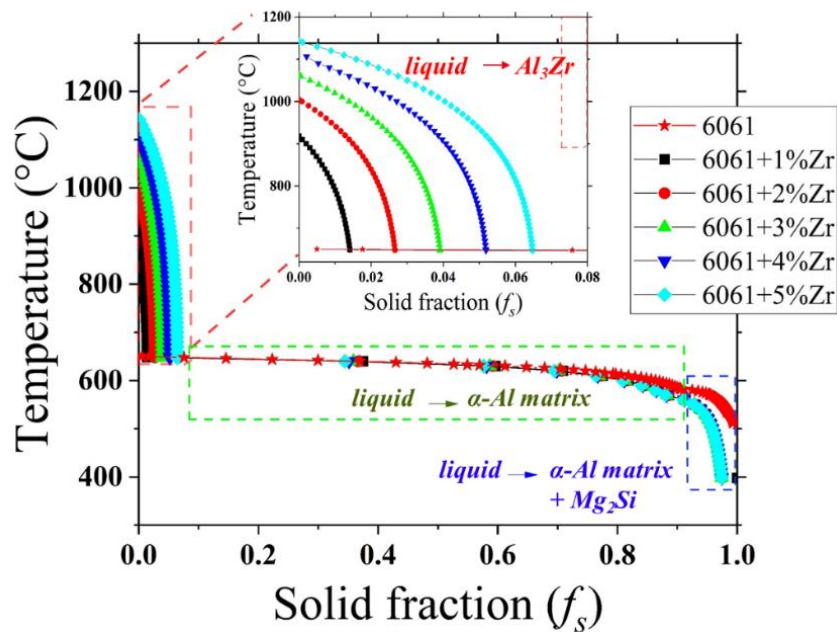


Figure 7-7 Solidification paths for various Zr additions to the standard 6061 Al-alloy, calculated using Scheil-Gulliver model.

The solidification path in **Figure 7-7**, allowed us to run the RDG criterion for Zr-modified alloys. As shown in **Figure 7-8**, the pressure drop is calculated (using **equation 5.1**) for various Zr additions and for the standard 6061 Al-alloy under processing condition typical of L-PBF. All the parameters mentioned in **Table 5-2** and **Table 5-4** were assumed constant. The coalescence was assumed to occur at a temperature $T_{gc}(f_s = 0.97) - \Delta T_{undercooling}(\theta = 15^\circ)$ for the respective modified alloys (using **equation 5.5** and similar to **Figure 5-5b**).

Firstly, in **Figure 7-8**, the pressure drop was estimated using the standard empirical strain rate equation. A crude estimation of strain rate was done corresponding to the solidification parameters of $G = 2.8 \cdot 10^6$ K/m, $v = 0.3$ m/s ($P=242$ W, $v_{laser}=600$ mm/s) with the empirical relation mentioned in **Table 5-4**. The pressure drops tend to increase for the increasing Zr content in the alloy. For all the Zr additions, the pressure drop is much higher than the critical pressure predicted for the standard 6061 Al-alloy. This is majorly due to the high solidification temperature range ($T_{liquidus} - T_{gc}$) compared to the standard 6061 Al-alloy. With Zr additions, the liquidus temperature increases, and so does the integration limits of **equation 5.1** in the RDG criterion. This indicates that the addition of Zr increases the cracking sensitivity of the alloys, which is not consistent with the beneficial effect of Zr reported in the literature [51,110][104]. **This exercise demonstrates that the RDG criterion cannot capture the beneficial effect of Zr additions, and thus it suggests that the model is missing key metallurgical factors. A possible reason for this discrepancy could be the assumption of coalescence happening at $f_s=0.97$ at an undercooling with 15° of misorientation for the Zr-modified alloys. Another reason could be the grain refinement aspect induced by Zr-additions, which the RDG model does not consider.**

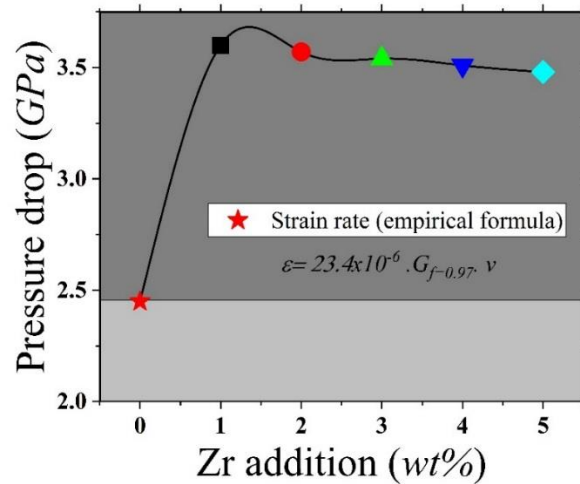


Figure 7-8 Pressure drop as a function of Zr content in the 6061 Al-alloy (using empirical strain rate relation).

7.3.1. Microstructure of Zr-modified 6061 Al-alloy.

To better understand the missing details which make the RDG criterion predict higher pressure drops with Zr additions, even though it is known to mitigate cracking, we tried to look into the consequences of Zr addition on the microstructure, in particular the grain size. To start with, the work of Opprecht *et al.* [104] was considered, since they added ZrO₂ onto the powder surface of the same 6061 Al-alloy used in this current study. They observed significant grain refinement by varying the quantity of Zr on the powder surface and obtained crack-free parts by L-PBF. They showed that, by the addition of 2wt% Zr to 6061 Al-alloy, columnar grain growth can be hindered by the new equiaxed grains in the melt pools, as shown in **Figure 7-9**. A duplex microstructure was observed, as shown in **Figure 7-9**, which includes equiaxed grain near the melt pool boundaries and fine columnar grains within the melt pools. Moreover, as reported by Opprecht *et al.* [104], the density of the Al₃Zr phase makes its formation localized near the melt pool boundaries, and as a result, a duplex microstructure is generated (see **Figure 7-9**). Cracking was found to be eliminated for a range of 2-4 wt% Zr addition in the 6061 Al-alloy [104].

The addition of Zr modifies the microstructure, but columnar grains can still be observed. By Zr addition to the standard alloy, grain refinement can be achieved but does it also lower the GB misorientation to mitigate cracking? To understand the misorientation nature of the columnar GB's in the modified microstructure of 6061 + 2 wt% Zr, consider **Figure 7-10**. Due to the availability of data from Opprecht *et al.* [104], the GB misorientation analysis was performed on the Zr modified microstructures.

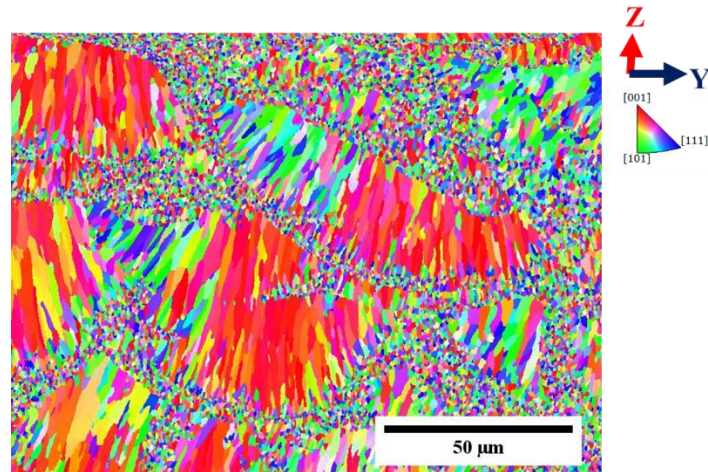


Figure 7-9 As-built building direction IPF-EBSD map normal to the build direction for the 6061 Al-alloy with 2% of Zirconium, adapted from ref [104].

The standard 6061 alloy and Zr addition misorientation data is shown in **Figure 7-10**. The probabilistic misorientation distribution of the GB for various addition of Zr is reported. In total, ~ 300 GB (in the columnar region) were analyzed for all the compositions from their respective EBSD microstructure. **It should be pointed out that, for the modified Zr microstructure, the GB misorientations were also along high angles ($>15^\circ$).** As shown in **Figure 7-10**, the GB misorientation statistics for various Zr additions demonstrate that, for all the Zr additions, the GB misorientation is not restricted to the LAGB. There are GB having high misorientation as well. This suggests the mechanism that mitigates cracking in Zr modified alloys has no correlation to the GB misorientations. **Thus, cracking mitigation with Zr additions is by the virtue of significant grain refinement by the formation of Al_3Zr and not by the absence of HAGB (interfaces identified as sensitive to cracking in this work).**

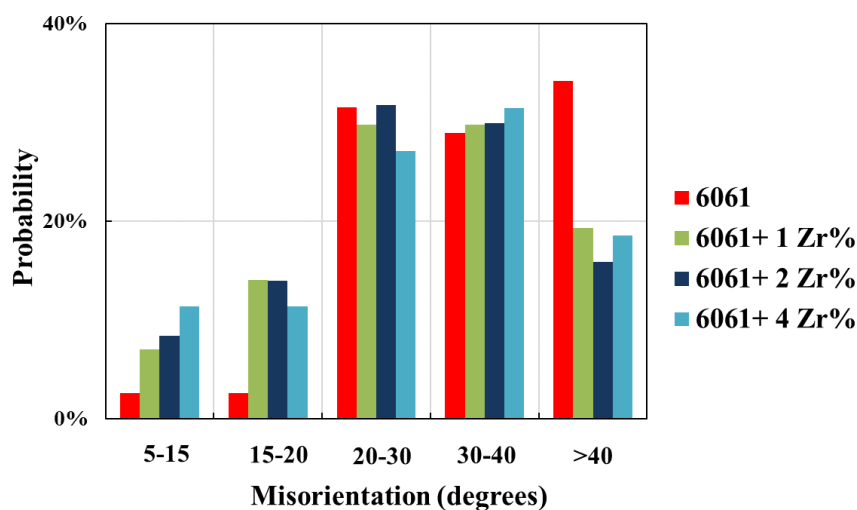


Figure 7-10 Statistics of the misorientation distribution for various Zr additions.

Figure 7-11a) & b), shows the standard 6061 microstructure and the Zr modified 6061 microstructure, respectively. Due to the fine nature of the columnar grains in the Zr modified 6061 (**Figure 7-11b**), the EBSD image was processed to observe properly the grain boundaries, as shown in **Figure 7-11c**. The processed image was useful to estimate the columnar width. At first sight, the columnar grains of the 6061 as-built sample (**Figure 7-11a**) appears to be wider than the fine columnar grain of the Zr-modified 6061 (**Figure 7-11b**). The standard cracking microstructure of **Figure 7-11a** has a columnar width of $66 \pm 4 \mu\text{m}$ (determined with the intercept method). On the other hand, the non-cracking modified 6061 (+ 2 wt% Zr) microstructure shown in **Figure 7-11b** exhibits a columnar width of $1.5 \pm 0.4 \mu\text{m}$. This indicates that the columnar grains that induce cracking in the standard 6061 Al-alloy have a much larger columnar width than the ones observed in the non-cracking version (6061+2wt%Zr).

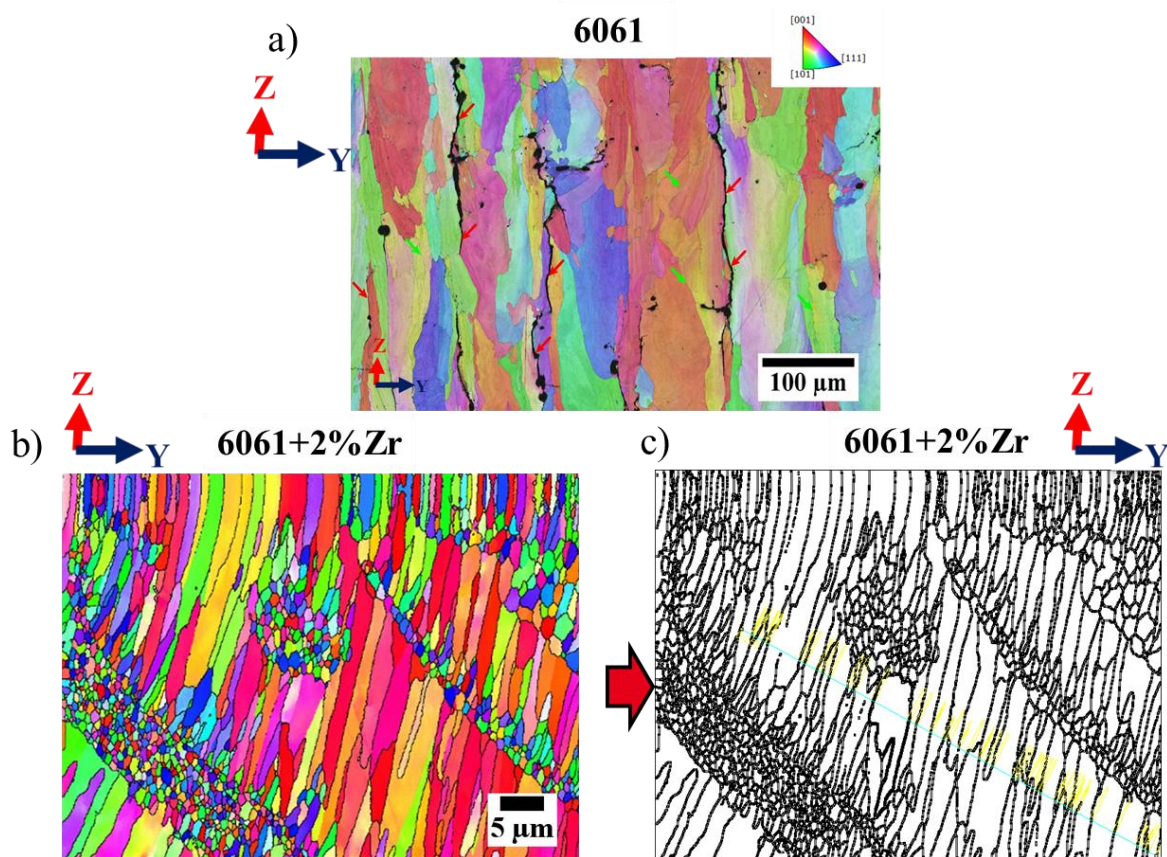


Figure 7-11 a) IPF EBSD image of the standard 6061 Al-alloy normal to the build direction (present study). b) Grain map of the 6061+2wt% Zr alloy in the as-built conditions (adapted from ref [104]). c) Grain boundaries map of the 6061+2wt% Zr alloy.

7.3.2. Summary

- The addition of Zirconium to the standard 6061 Al-alloy is reported to refine the microstructure and mitigate cracking [51,110][104]. Zirconium addition to 6061 Al-alloy gives a duplex kind of microstructure (thin columnar grains and equiaxed regions inside the melt pools). Grain refinement happens because of the nucleating Al_3Zr phase, which precipitates prior to the primary-Al phase during the solidification.
- Taking into account just the solidification path of Zr modified 6061, the pressure drops are comparatively higher than standard 6061. The microstructure of the Zr modified 6061 Al-alloy, has fine columnar grains compared to the standard 6061 microstructure. Despite the HAGB's in the microstructure, the 6061+ 2wt%Zr alloy does not show any evidence of cracking.
- RDG model is based on growing columnar grains. It does not take into account the effect due to external nucleating agents. One take away message is that, alloys can be compared for their cracking sensitivity with the RDG criterion, if they have more or less similar microstructures. Thus, whenever the RDG model is applied to an alloy, experimental parameters like columnar widths and primary dendrite spacing are needed to be updated in the calculation to get a reliable cracking sensitivity estimation.

8. Conclusions and recommendation for future work

Conclusions and Perspectives.



8.1. Conclusions

Processing Aluminum alloys using L-PBF has always been challenging due to their low absorptivity towards laser, high thermal conductivity and high latent heat of fusion. Al-alloys are also sensitive to H₂ induced porosities due to the increased solubility of H₂ in the molten Al-alloys. In addition to these issues, structural Al-alloys from 6xxx series suffer from severe hot cracking issues in the as-built parts, similarly as reported for welding.

The objectives of this PhD thesis were as follows:

1. **To investigate whether a crack-free 6061 Al-alloy can be produced by L-PBF using process optimizations.**
2. **To clarify the cracking mechanism occurring in the framework of L-PBF and investigate its sensitivity to processing conditions.**
3. **To evaluate with the help of a hot tearing criterion the impact of different cracking mitigation strategies (process and composition based) reported in the literature and consequently identify the key metallurgical/process parameters that need to be considered to have better control on the cracking tendency.**

Following are the major outcomes of the Ph.D. thesis:

- i. A process parameter optimization was performed to identify stable melting conditions with an objective to minimize lack-of fusion defects and to achieve high build density (>98%). With the bottom-up strategy employed in this work (as summarized in **Figure 8-1**), melting modes (conduction or keyhole), parameters causing instabilities like balling/humping were identified. **Thus, such kind of investigation at different intermediate levels helped us to identify stable processing parameters.** In this work, a processing window was identified leading to the lowest lack-of-fusion porosity and thus the highest relative density of 98.5%. However, no melting conditions were found to produce crack-free parts.

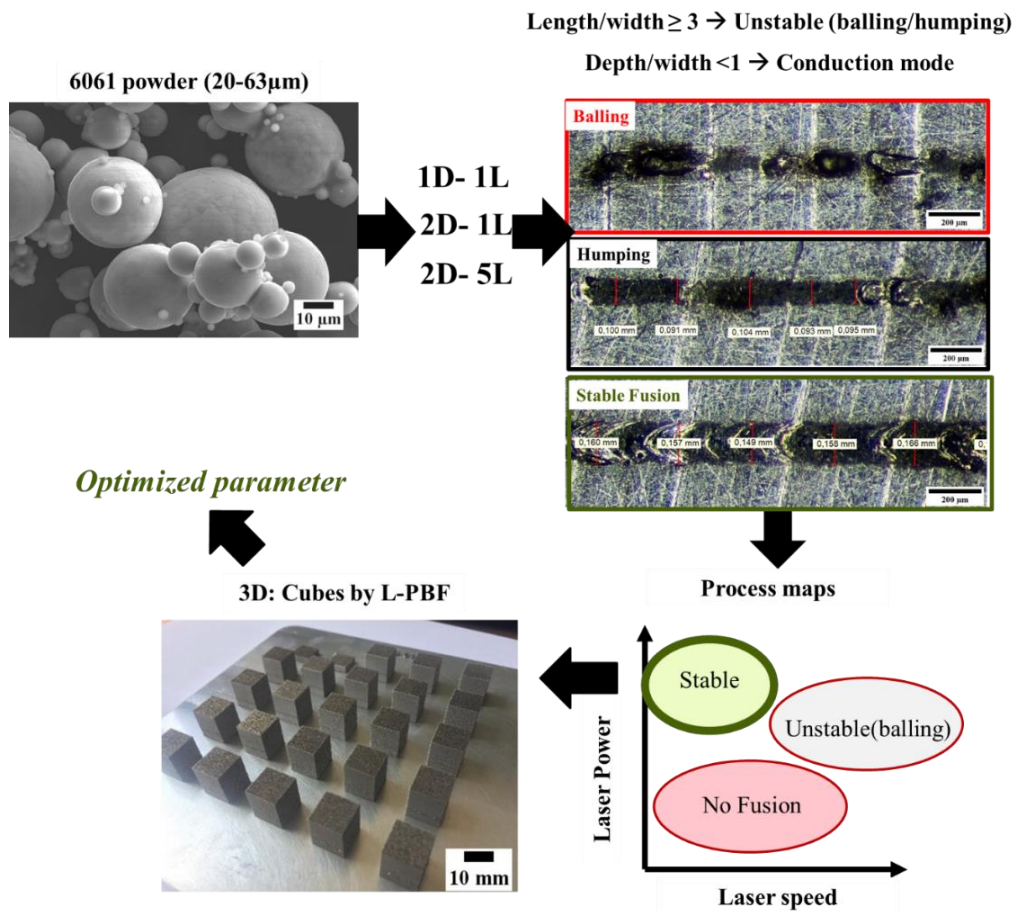


Figure 8-1 Bottom-up strategy employed to identify the optimized parameters.

- ii. Based on microstructural observations, cracks develop during the last stage of solidification, qualifying the mechanism as solidification cracking (see Figure 8-2). Solidification cracks were found to propagate along HAGBs while LAGBs were systematically found to be crack-free showing striking similarities with other cubic systems, see e.g. [89,134]. However, not all HAGBs were cracked, suggesting that other factors are involved in the cracking mechanism. In particular, the position of the HAGB within the melt pool was identified as a key parameter. To summarize, two conditions are required for a grain boundary to be cracked: (i) being a HAGB, and, (ii) being located at the central position of the melt pools (see Figure 8-2). Those conditions show similarities to the welding literature [97][135][136] and prior to this work were rarely emphasized in the framework of 6061 Al-alloy processed by L-PBF. Those conditions were then discussed using the Rappaz Drezet and Gremaud (RDG) hot cracking criterion [7].

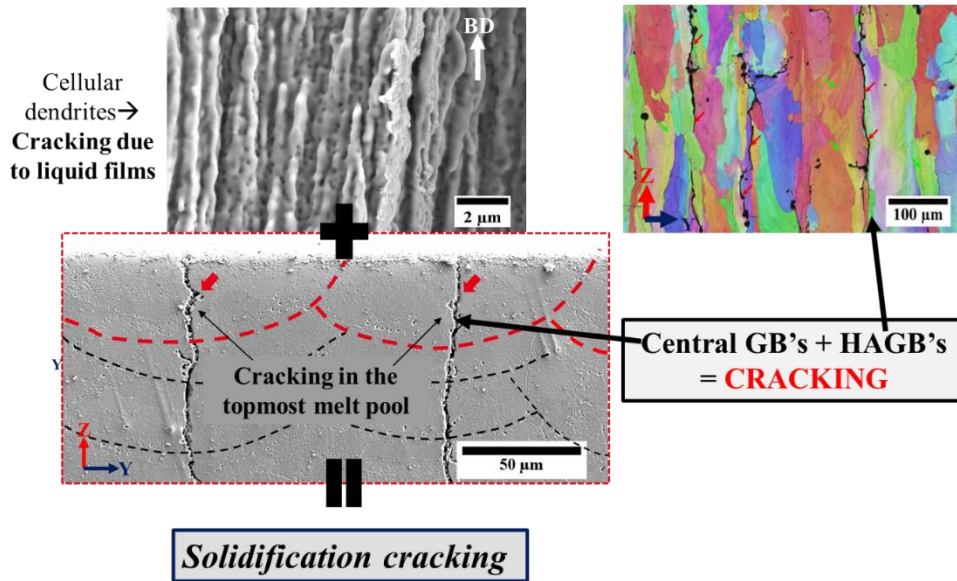


Figure 8-2 Cracking mechanism and its characteristics identified for the 6061 Al-alloy fabricated by L-PBF.

- iii. A multi-scale microstructural study was performed on the as-built optimized sample, as summarized in **Figure 8-3**. Two types of second-phase particles were observed in the as-built microstructure. Based on the STEM-EDX analysis, the first population of second-phase particles was found to be enriched in Si/Mg/Fe and were detected within the grains. The second population was enriched in the same elements (Si/Mg/Fe) including Cu and decorate the two investigated high angle grain boundaries.

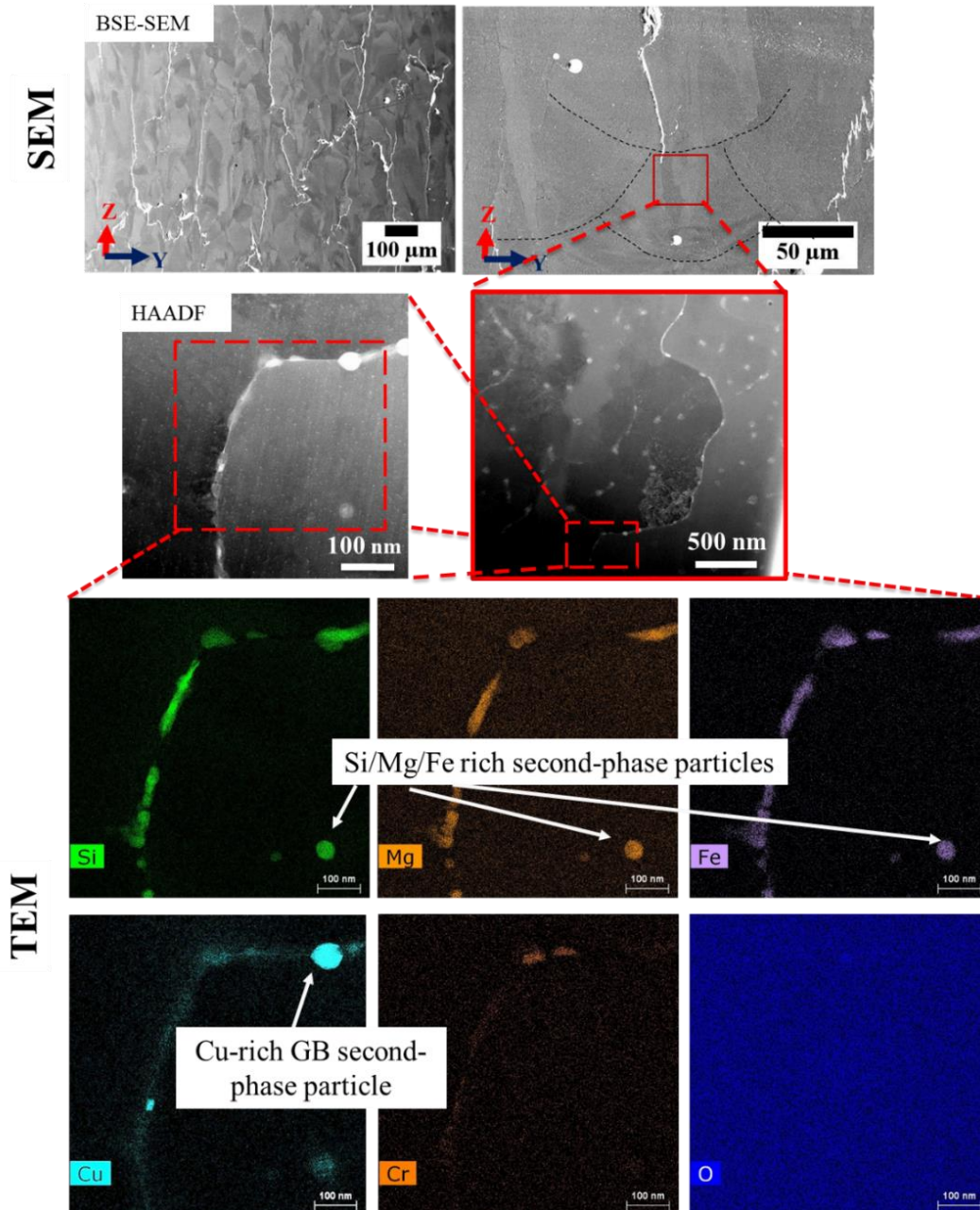


Figure 8-3 Multi-scale characterization performed on the as-built 6061 Al-alloy.

- iv. In our work, we employed the RDG criterion on the 6061 Al-alloy while including the typical inputs from the L-PBF process, namely the thermal gradient (G) and the solidification velocity (v) estimated using the Rosenthal analytical model. We used the Scheil-Gulliver model to obtain the solidification path $f(T)$ of the alloy. For inputs like the primary dendrite arm spacing, we relied on the fracture surface observations of the as-built samples. **Moreover, we also included our experimental observation of HAGB cracking in the RDG criterion by using the grain coalescence undercooling to rationalize the effect of misorientation: liquid films being stable down to lower temperatures along HAGBs compared to LAGBs.**

Besides, there were other inputs that were difficult to estimate experimentally, for instance, strain rates in the mushy zone, the melt viscosity of the alloy, the coalescence solid fraction and the solid-liquid interface energy. To provide estimates of those inputs, we relied on the empirical relations for the strain rates and literature for the others (viscosity, coalescence solid fraction and solid-liquid interface energy). A sensitivity analysis of those peculiar inputs was conducted being aware that the variations predicted by the empirical relations can be physically questionable. However, it roughly gave us the main trends in predicting the cracking sensitivity. Thus, the RDG criterion was best utilized by the use of experimental feedback as well as estimations of other input parameters that were more challenging to measure experimentally.

- **Our sensitivity analysis of the effect of the fraction of coalescence on the pressure drop demonstrates that this is an important metallurgical factor controlling the hot tearing sensitivity. A small change in the coalescence solid fraction from 0.97 to 0.9 can decrease the pressure drop by an order of magnitude, see Figure 8-4. Thus, decreasing the coalescence fraction turns out to be an efficient way to make the alloy more resistant to cracking.**

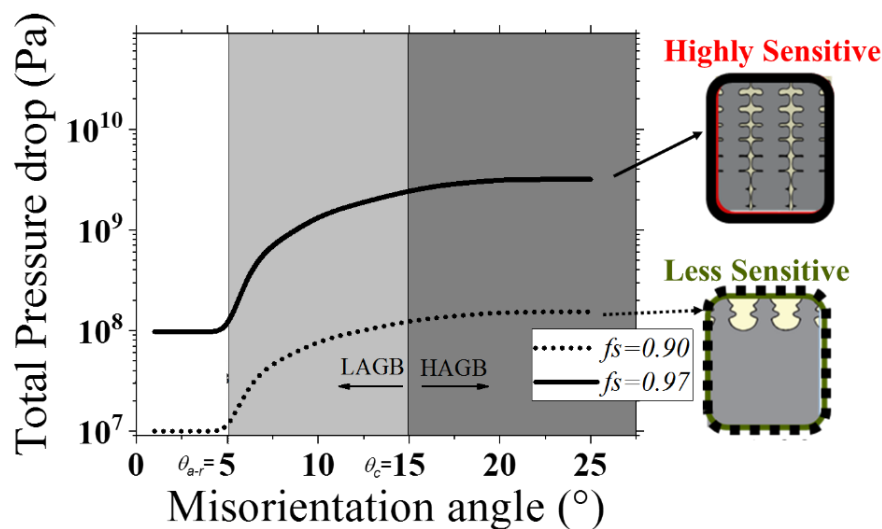


Figure 8-4 Cracking sensitivity analysis for coalescence solid fraction ($f_s=0.97$ and $f_s=0.9$), based on total pressure drop estimated using the RDG criterion.

- Similarly, the characteristic length of the microstructure, i.e. the PDAS (λ) was also found to significantly impact the cracking sensitivity: larger PDAS increases the alloy resistance to solidification cracking. With our investigation, we found that, preheating the powder bed results in a crack-free microstructure having higher PDAS ($\lambda = 15 \mu\text{m}$ compared to $\lambda = 0.6 \mu\text{m}$ for not preheated cracked microstructure). Although it must be highlighted that, there are technological/safety concerns by the use of powder bed heating system, since it can cause self-ignition and is difficult to implement industrially [3].

- The same RDG criterion coupled with thermal simulations using the Rosenthal analytical allowed the effect of the first order processing parameters, namely the laser power and speed on the hot cracking sensitivity to be studied. **An original way to present the results was proposed through the development of Hot Cracking Sensitivity (HCS) maps, as exemplified in Figure 8-5.** The HCS maps suggested that lowering the laser scanning speed to reduce hot cracking. These predictions were in qualitative agreement with previous experimental observations, that crack density can be reduced by increasing the laser energy density.

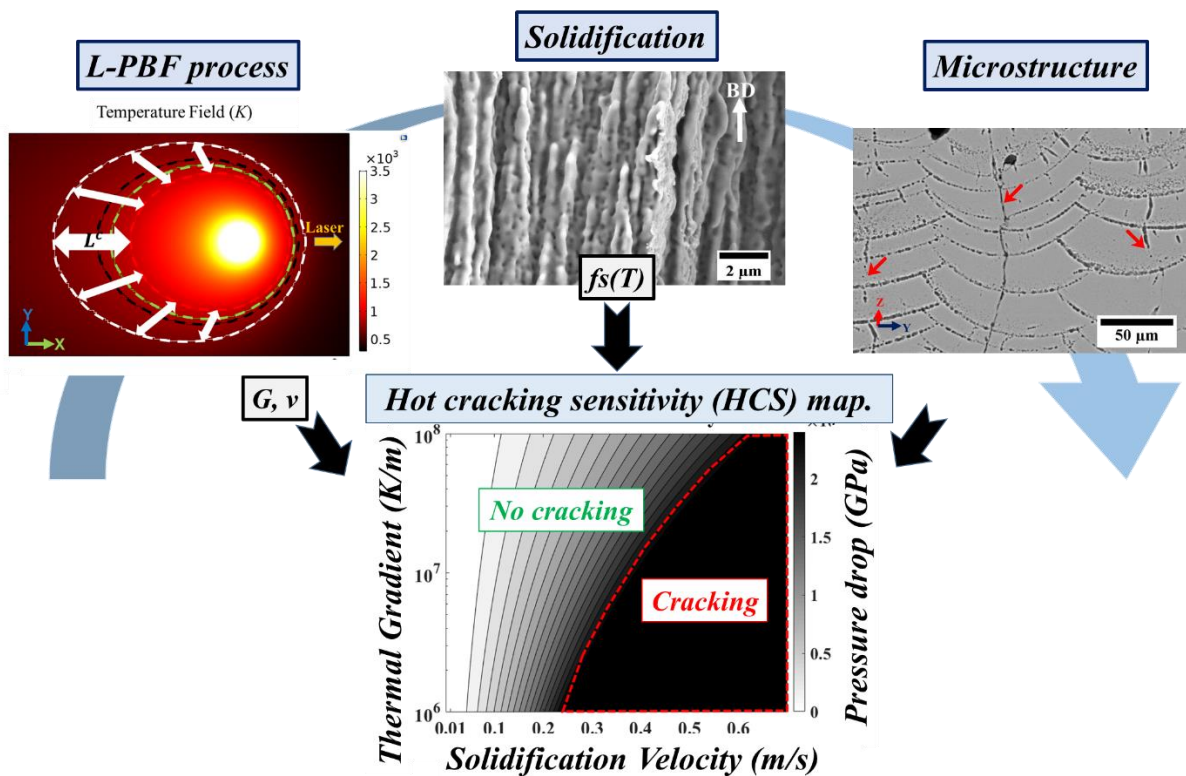


Figure 8-5 Development of hot cracking sensitivity map based on process parameters and microstructure.

Nevertheless, one of the conclusions drawn from this work is that it is highly challenging to fully prevent hot cracking by tuning only the process parameters since the L-PBF process is constrained by other technological/safety issues. For instance, reducing laser speeds ($< 200\text{mm/s}$) can lead to a change of melting mode, giving rise to process instabilities, which are not desirable. This suggests that the adjustment of the nominal composition is likely a more efficient way to produce crack-free samples. Our work on predicting the effect of the major alloying elements on the cracking sensitivity of 6061 Al-alloy points out that Mg addition (2 wt%) will be beneficial. This was in agreement with the experimental results published by Giraud *et al.* [73]. While this appears as a promising strategy to prevent

cracks, this might lead to non-optimized mechanical properties and cause issues concerning Mg evaporation during L-PBF.

8.2. Perspectives

The perspectives of this work can be visualized into three different ways, based on their need of immediate effect:

(1) Alloy designing parameters

The methodology employed in the present work, allowed us to identify key factors that play a role in determining the hot cracking sensitivity namely, **the characteristic length of the microstructure, the fraction of coalescence, the solid-liquid interface energy and the viscosity**. Future research efforts must be oriented towards having better control over these parameters since it can be considered as the most effective method to mitigate cracking. Playing with those factors can lead to improvements of the alloy design strategies to produce crack-sensitive materials during L-PBF. As summarized in **Figure 8-6**, those parameters are classified depending on how easy it is to control them and whether an increase or decrease in their magnitude is needed to design crack-resistant alloys. Based on their feasibility to control these parameters, the parameters can be ranked as follows:

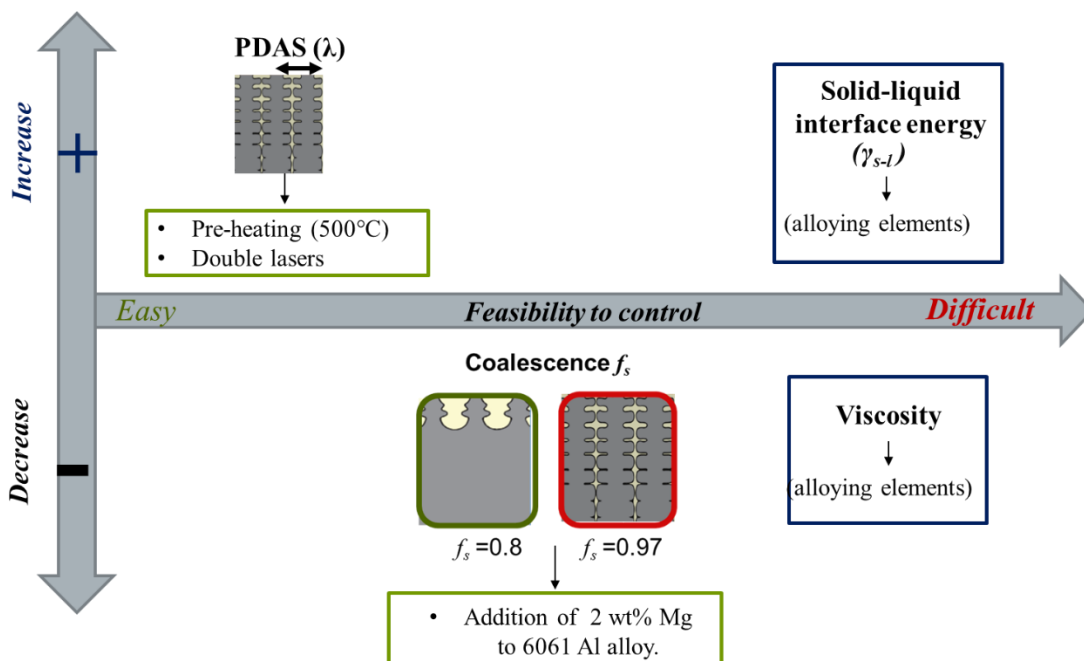


Figure 8-6 Metallurgical parameters needed to be considered to improve alloy design strategies.

-
- i. **The characteristic length of microstructure:** Increasing PDAS will result in better liquid feeding, better development of secondary arms and hence better coalescence of dendrites. However, it is highly possible that high PDAS can affect the columnar grain width, but this link is not straightforward. Refining columnar grain width is known to mitigate cracking. Thus, the correlation between PDAS and columnar grain width will need investigation. To control PDAS, it can be linked to cooling rates and thus by modifying the cooling rate characteristics, the PDAS can be manipulated. To have a crack-resistant microstructure, a general guideline can be that the PDAS should be $\sim 15 \mu\text{m}$ (as observed in the crack-free preheated 6061 Al-alloy, [74]). However, this does not guarantee total mitigation of cracking, since several other factors (coalescence behavior, strain rate, viscosity etc) are also responsible. Controlling PDAS in the L-PBF framework will require techniques similar to preheating to be employed, like investigating the effect of double lasers will be fruitful.
- ii. **The coalescence solid fraction: The coalescence solid-fraction must be low enough (typically $f_s < 0.9$) to induce coalescence at an early stage of solidification.** The underlying scientific question is how one can control this grain coalescence fraction. This can be achieved by having a better control on the dendrite morphology, promoting the development of secondary dendrite arms to make easier the dendrite coalescence. A possible way to promote coalescence is by identifying elements like Mg that can back-diffuse, as shown in ref [167,168]. On the other hand, back diffusion can be promoted if the solid-state diffusion coefficient or partition coefficient of the element increases. Thus, identifying such elements will require further thermodynamic simulations, similar to the phase field simulations done by Geng *et al.* [167]. Similarly, coalescence can occur at lower solid fractions by controlling the solid-liquid interface energy since it plays a major role in affecting the coalescence undercooling. This can be done by adding elements that are known to affect the solid-liquid interface energy, such as adding surface active elements.
- iii. **Solid-liquid interface energy (γ_{s-l}):** It is the key metallurgical factor controlling the coalescence undercooling. **The solid-liquid interface energy should reach a high value of $\left(\frac{\gamma_{gb}(\theta)_{max}}{2} \approx 0.25 \text{ J/m}^2\right)$ to avoid any coalescence undercooling, in comparison to the $\gamma_{s-l} = 0.12 \text{ J/m}^2$ for pure Aluminum. Tailoring γ_{s-l} by modifying solute content will also result in having better control over the Al-dendrite growth direction.** Although the experimental determination of the solid-liquid interface energy is a difficult task, our work shows that research efforts are needed to evaluate the effect of alloying elements on this solid-liquid interface energy. According to Rappaz *et al.* [169], the solid-liquid interface energy can be manipulated to change the dendrite growth direction. This can be achieved through solute content modification. Such transition of dendrite orientation by addition of solute content was first observed in Al-Zn alloys by varying Zn content from 25 wt % to 60 wt% [170]. Thus, for the 6061 Al-alloy, the anisotropic behavior of the γ_{s-l} must be investigated to identify solutes that can result in such anisotropy to control the coalescence behavior of the alloy.

- iv. **The Viscosity** of the liquid is a parameter that can highly affect the liquid feeding rates to avoid cracking. Research efforts must focus on identifying solutes that lower the net viscosity of the alloy below 1.4 mPa.s (viscosity of 6061 Al-alloy). Further work is also required to clarify the effect of alloying elements on the melt viscosity. For example, the variation of solute content modification on the net viscosity needs to be understood. In literature [157], elements like Ti, Cr, Cu, Mn, Ni are found to increase the viscosity of the alloy by increasing the solute content in the alloy. Similarly, elements like Si and Zn tend to decrease the melt viscosity of the selected Al-alloy. Thus, it is necessary to investigate further the liquid viscosity of pure Aluminum, binary/ternary systems and the 6061 Al-alloy. This will give an idea about the variation in viscosity depending on the nature of alloying elements.

(2) Improving hot cracking criterion.

- The recent progress made regarding the development of Al-alloys for L-PBF, see e.g. [4,104] shows that refining the grain size is an efficient way to mitigate cracking in L-PBF parts. Compositional variations have proven to be efficient in inducing grain refinement to mitigate cracking. For example, refining the grain size is usually made possible through the use of the addition of nucleating agents such as TiB_2 [106], $\text{ZrH}_2/\text{ZrO}_2$ particles on powder surface [104][4], or the adjustment of the nominal composition to precipitate a primary phase that will further act as nucleation site (e.g. Sc and Zr addition that induce precipitation of the primary phase such as $\text{Al}_3(\text{Zr,Sc})$).
- Evaluating the effect of grain size or the presence of a higher density of grain boundaries on the hot tearing sensitivity using the RDG criterion is not an easy task since the model does not explicitly take into account the grain size. Taking into account the effect of the microstructure in the RDG model would be interesting to evaluate the consequences on the pressure drop and thus on the hot tearing sensitivity. So far only Sun *et al.* [163] have claimed to have included the grain size aspect into the RDG criterion in the L-PBF framework, however, the mathematical demonstration was missing. One possibility is to qualitatively link the grain size and the cracking sensitivity by relying on the fact that, **fine grains are thought to help to distribute thermal strains over more interfaces**. An indirect way to include such an effect in the RDG criterion would be through the strain rate.

To remind, we used the solidification parameters namely (G, v) to make a crude estimate of strain rate (refer to **Table 5-4**) but investigating more thoroughly the link between the strain rate and the grain size would be useful to move a step further in the predictions of hot cracking in the framework of L-PBF. Experimentally assessing this relationship would require conducting tensile tests with different grain sizes while imposing different strain rates, ideally at temperatures close

to the coalescence temperature for microstructures exhibiting different grain sizes and to further evaluate the cracking sensitivity. In this way, the actual strain rate could be linked to grain size and should allow us to evaluate the effect of grain refinement on the hot cracking sensitivity. However, one should note that important research efforts would be required to run such tests.

However, qualitatively we can compare the relative behavior of the strain rates beared by the cracking standard 6061 alloy and the non-cracking Zr-modified alloy. This means fine microstructure of Zr-modified 6061 alloy will be able to distribute the deformation over several interfaces compared to the coarse microstructure of the standard 6061 Al-alloy. The ratio of columnar widths of the cracked microstructure to the non-cracked microstructure can give us a relative comparison of the strain rates. For instance, a single columnar grain of the standard 6061 can accommodate ~ 50 fine columnar grain of the Zr-modified alloy (refer to **Figure 7-11**). According to the schematic of **Figure 8-7a) & b)**, a single columnar grain of 6061 alloy can undergo a strain rate ($\dot{\epsilon}$). Whereas, when a refined Zr modified microstructure is concerned within a fixed columnar width of 6061 Al-alloy, the total strain rate will have a contribution from N number of grains, with each grain concerned with a strain rate ($\dot{\epsilon}_G$). The grain boundaries can as well contribute to the strain rate, however their contribution is neglected. Thus, the strain rate beared by a single columnar grain of the Zr-modified alloy, is $\sim N$ times smaller than the strain rate felt by the standard 6061 columnar grain. Such microstructural observations can be best used to qualitatively incorporate the aspect of grain size in the RDG criterion. A similar methodology was used by Coniglio *et al.* [90], where they used a strain partitioning model in the mushy zone. They estimated the total displacement rate ($\dot{\delta}$) of the mushy zone, to show that grain refinement (increasing number of grains, N) is beneficial in reducing cracking susceptibility.

Figure 8-7c), incorporates the relative strain rates (based on microstructure) into the RDG criterion. Using this microstructural based inputs from **Figure 7-11**, the predicted pressure drops of **Figure 8-7c)** are no longer in the critical zone. The decrease in pressure drop is proportional to the grain refinement, i.e. the number of grains N . In fact, for all the Zr additions, the pressure drops are lower than the standard 6061 Al-alloy. Thus by varying the strain rate in the same manner as the grain size, beneficial effect of Zr can be captured using the strain partitioning concept in the RDG criterion. Without such link of strain rates to the grain size/columnar width, the RDG criterion cannot predict accurately the cracking sensitivity and thus needs improvements to take grain size in predicting the cracking sensitivity.

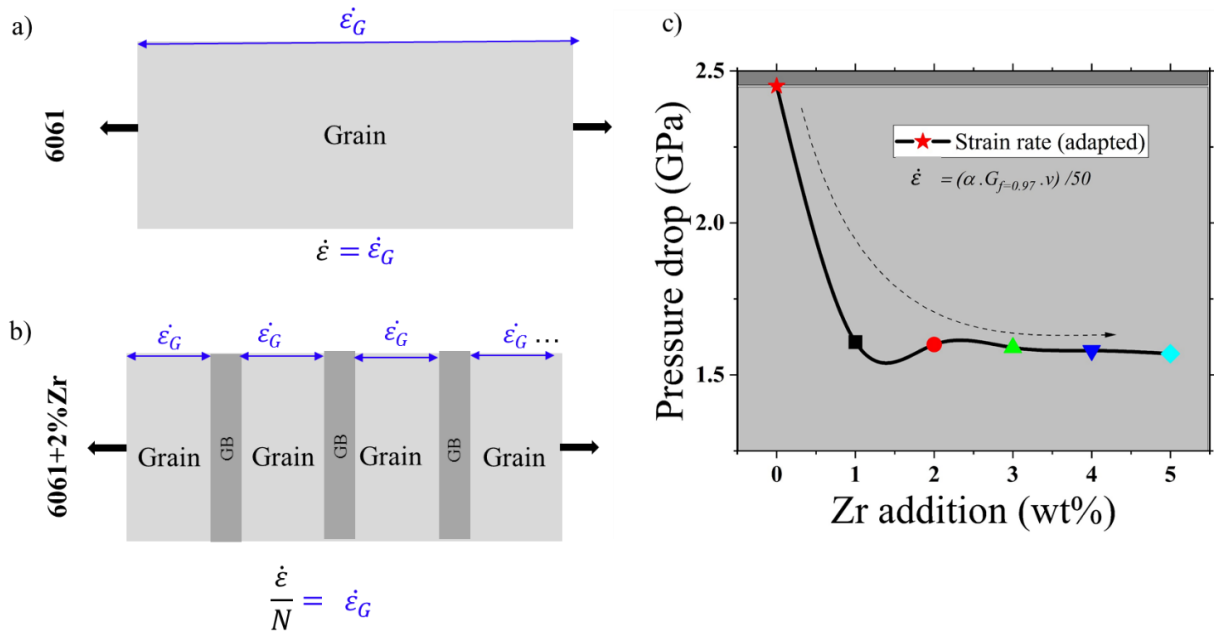


Figure 8-7 a) & b) Strain rate schematic for a single columnar grain of 6061 Al-alloy and N number of columnar grains of Zr modified 6061 alloy. c) Pressure drop as a function of Zr content in the 6061 Al-alloy (taking into account the relative strain rates, thanks to variation in columnar grain width).

- Another strategy could be by coupling the RDG criterion with other fluid-flow models using a cellular automaton, as in ref [171]. Such approaches would certainly help to further improve our current understanding of the hot cracking resistance of the sensitive Al-alloys fabricated by L-PBF.
- In our modelling approach, we used the Scheil-Gulliver model to estimate the solidification path, without taking into account the cooling rates associated with L-PBF. However, with high solidification velocities typical of L-PBF, loss of equilibrium conditions due to rapidly moving dendrites can occur. This can eventually decrease the rise in the solute concentration at the dendrite tip, and thus solute trapping can occur [147,172,173]. To include the aspect of solute trapping, the partition coefficient as a function of solidification velocity $k(v)$, can be estimated by the model proposed by Aziz [174]. Similarly, it will be desirable to perform critical experiments to investigate solute trapping quantitatively, for example, accurate measurement of solute content in the solid dendrites for various conditions (v, T) can give information related to $k(v, T)$.

Thus improving the hot cracking criterion can be considered as a reliable methodology to predict crack-resistant compositions suitable for L-PBF applications.

(3) Advanced characterizations

- Another strategy for future investigation can be concentrated towards grain boundary engineering [175]. It is true that in our TEM analysis of grain boundaries, we did not observe huge differences in the solutes decorating the cracked and non-cracked grain boundaries. It is because our sample set of GBs was small. Investigation of misorientation based segregation along the GBs can be helpful in providing insights about the solute enrichment. With such information about the concentration of the solutes facilitating the liquid film formation can be controlled. The methodology have already proved beneficial in mitigating cracking in Ni-based alloys [134,176]. Thus, quantitative investigation of GB segregation for the crack-sensitive Al-alloys, by atom probe tomography (APT) analysis can be fruitful.
- In our study we observed the interconnection between the metallurgical pores and the solidification cracking. This was also recently reported by the ref [123] in their dynamic X-ray visualization, which suggested that pores are the favorable location for crack nucleation. Thus, future research efforts can also be concentrated on factors that promote porosity formation. Advance *in situ* characterizations with synchrotron X-ray imaging will further enhance our knowledge and help us improve the numerical modelling of the defect formation in L-PBF.

Appendix

Laser tracks on 6061 Al-alloy (bulk substrates)

Before starting experiments using 6061 alloy powders, bulk substrates of the 6061 alloy were laser scanned. The substrate chemical composition of the bulk substrate is given in **Table A-1**. The standard chemical composition of the 6061 Al-alloy is also provided for comparison. The bulk substrate is well within the norm of the standard 6061 Al-alloy composition.

Table A-1 Composition of the 6061 bulk substrate (wt%).

	Al	Si	Mg	Fe	Cu	Cr	Ti	Mn	Zn
Standard [67]	Bal.	0.4- 0.8	0.8- 1.2	<0.2	0.15- 0.4	0.04- 0.35	<0.15	<0.15	<0.25
Bulk substrate.	Bal.	0.78	1.02	0.17	0.32	0.09	0.019	0.13	0.008

Bulk substrate experiments dealing with two different surface roughness ($R_a=1.2\mu\text{m}$ and $6\mu\text{m}$) were tested, one with the as-machined state (for single tracks- 1D) and the other rough sand-blasted sample (for multiple tracks- 2D). Throughout the experiments, the laser spot size was fixed at $70\mu\text{m}$. Two hatch spacing were used ($50\mu\text{m}$ and $100\mu\text{m}$) for the multiple adjacent track experiments to create a 2D region of $5\times 3\text{mm}^2$. The laser speed (v_{laser}) was varied between 200mm/s to 1400mm/s , whereas the Power (P) was varied between 180W to 274W .

- **A.1. 1D experiments: Single tracks**

Preliminary experiments dealing with (as-machined) bulk 6061 substrate were laser scanned with a single track. The cross-section of these single tracks was analyzed to evaluate the morphology of the melt pools, as shown in **Figure A-1**. According to **Figure A-1**, for a fixed $P=274\text{W}$ and variation of laser speeds from $200\text{--}800\text{mm/s}$, the melt pool morphology appears to be hemispherical. Similar hemispherical behavior is observed for $P=250\text{W}$ and $v_{laser}=200\text{mm/s}$ (in **Figure A-1b**).

According to Nie *et al.* [177], the variation of power and laser speed has a great influence on the morphology of the melt pools. The melting mode in literature can be classified as conductive (depth(d)/width(w) ratio is typically <1), and keyhole mode (d/w ratio is typically >1) [177]. Having said that, according to the analysis of melt pool dimensions done in **Figure A-2**, the depth (**Figure A-2b**) of the observed melt pools is significantly smaller than the width (**Figure A-2a**) of the melt pools. For the linear

energy density varying from 300-1400 J/m, the depth/width ratio varies from 0.14-0.19. This indicates that a conductive mode of melting exists for the studied process parameters. Even though the melt pool width and depth increases with the linear energy density (E_L) as seen in **Figure A-2**, in agreement with the literature [178], the melt pool depths only varied from 13 to 24 μm . These depths are comparatively 4-5 times smaller than the ones observed in single tracks experiments performed on 7xxx alloys substrates [178]. This was probably due to the high energy density of the laser, since they used powers up to 500W in comparison to maximum power of 274W in the present study. Another possible reason for this can be the high reflectivity of the (as-machined) bulk substrate of around $\sim 80\%$ for a laser wavelength of 1064nm (see **section 4.1.2**).

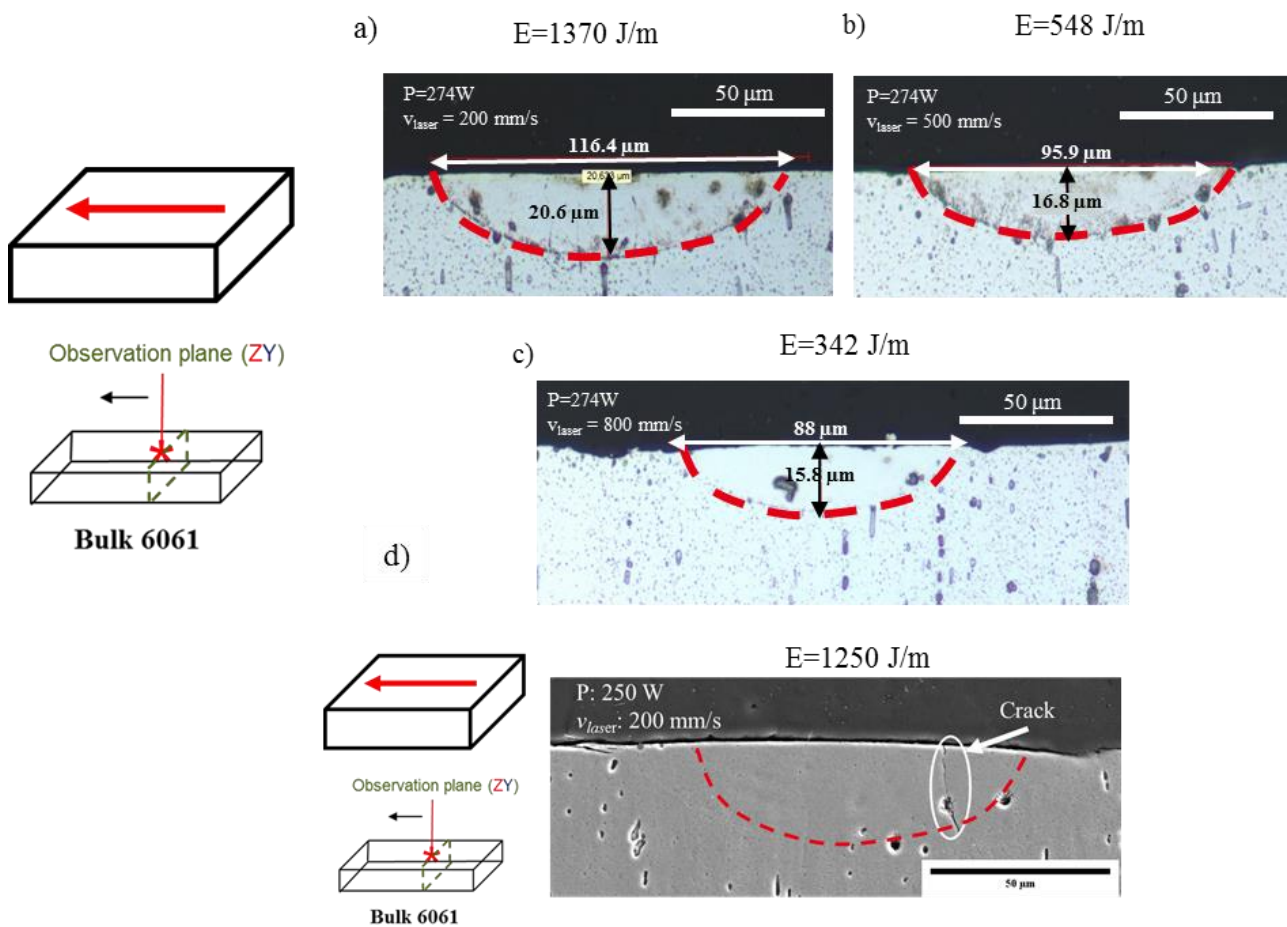


Figure A-1 a)-c) Cross-section view of the single tracks made on the bulk substrate (after Keller's etching) as a function of increasing laser speed. d) Cross-section melt pool morphology showing evidence of cracking.

Several defects like pores and cracks were also detected in the melt pool cross-sections of **Figure A-1**. Pores with a size range of $\sim 7-8\ \mu\text{m}$ were found to be entrapped within the melt pool cross-sections. Since keyhole melting mode was not identified within the studied parameters, these identified pores cannot be classified as keyhole pores. However, in literature, it is known that Al-alloys are very susceptible to H_2 porosities [1]. These pores occur due to the high solubility of H_2 in the molten pool. So probably, the

identified pores are due to the influence of H_2 during the melting process. In addition to the pores, the first evidence of cracking was also observed. For example in **Figure A-1d)**, the only cracking observed was for the parameter $P=250W$ and $v_{laser}=200mm/s$. The crack position is located inside the melt pool and it appears to be originating from the pore beneath. Apart from this evidence of cracking, no other process parameter yielded cracking, probable due to the smaller melt pools arising due to insufficient local melting.

Thus, the single-track experiment on the bulk substrate allowed us to identify the conduction mode of melting for the studied parameters. A very small depth/width ratio (0.14-0.19) was obtained, which was attributed to the high reflectivity of the bulk 6061 substrates. This allowed us to focus our attention to improve the surface state of the substrate by sand-blasting it and performing multiple adjacent laser tracks for further process parameters optimization.

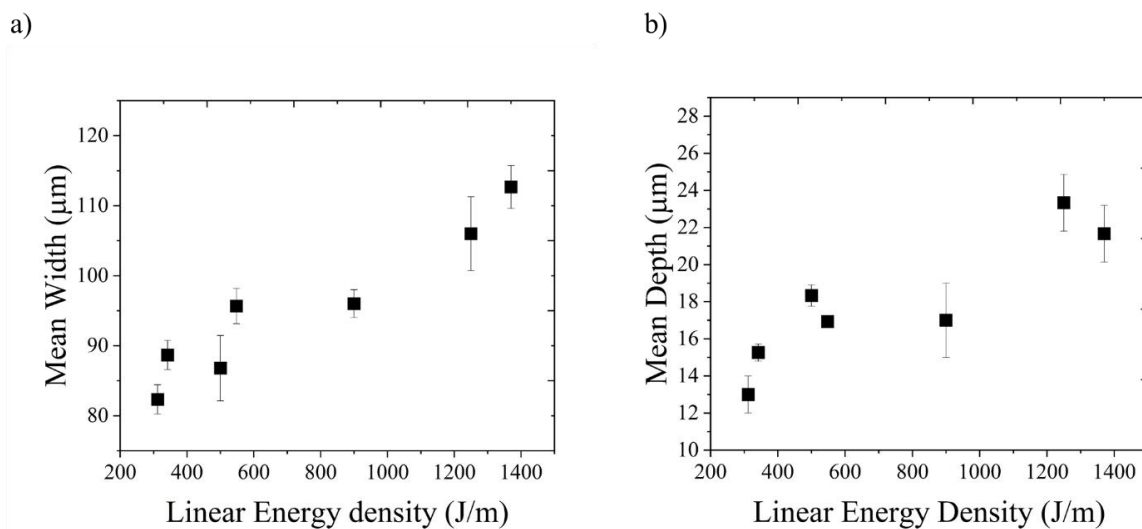


Figure A-2 a) Variation of melt pool width and b) melt pool depth with the linear energy density (1D-bulk substrate)

- **A.2. 2D experiments: Multiple adjacent tracks**

To increase the absorptivity of the bulk substrate, the surface roughness was increased by using sand-blasting (see **section 4.1.2** for details). Just by increasing the surface roughness from $Ra=1.3\mu m$ to $Ra=6.3\mu m$, the laser reflectivity was reduced from 80% to around 40% by the sand-blasting process. These rough ($Ra=6.3\mu m$) substrates were then treated with 2D multiple adjacent laser tracks. As mentioned previously, throughout the experiments, the laser spot size was fixed at $70\mu m$. Whereas, two hatch spacing were used ($50\mu m$ and $100\mu m$) for the multiple adjacent track experiments to melt a surface of $5 \times 3\text{ mm}^2$. The two hatch spacings were selected since through literature of Al-alloys in L-PBF [30], it was

recommended to use a smaller hatch spacing to improve the inter-intra overlap between the layers. Moreover, according to Louvis *et al.* [55] the hatch spacing greater than 300μ leads to delamination, and a hatch less than 50μ leads to low build density of the L-PBF parts of the 6061 Al-alloy.

Figure A-3 shows the top surface view of the 2D scanned region for the two hatch spacing ($50/100\mu$). For the case of 50μ hatch spacing, at a lower speed of 200mm/s and $P=240\text{W}$, instability due to high energy was observed. A similar high energy instability was observed by Nie *et al.* [177], during the multiple scans performed on the Al-Cu-Mg alloy. On the contrary, a stable continuous region with clear evidence of the melt pool adjacent tracks was observed for $P=240\text{W}$ and $v_{laser}=1400\text{ mm/s}$. This continuous laser track formation can therefore be classified as a ‘stable region’.

When considering a higher hatch spacing (100μ) in **Figure A-3**, the top view of the 2D region indicates continuous laser tracks for $P=240\text{W}$ for a $v_{laser}=200\text{ mm/s}$. However, as laser speed is increased to 1400 mm/s , the continuous laser tracks start to become discontinuous and can therefore be qualified as unstable, probably due to melt pool instability due to high laser speeds like balling/humping. At lower speeds (200mm/s), the 2D region appears to be unstable (high energy), whereas at higher speeds (1400 mm/s) the 2D region becomes unstable (high laser speed). This unstable nature of the 2D region (based on top view images of the tracks) is similar to what has been reported by Nie *et al.* [177] for higher laser speeds.

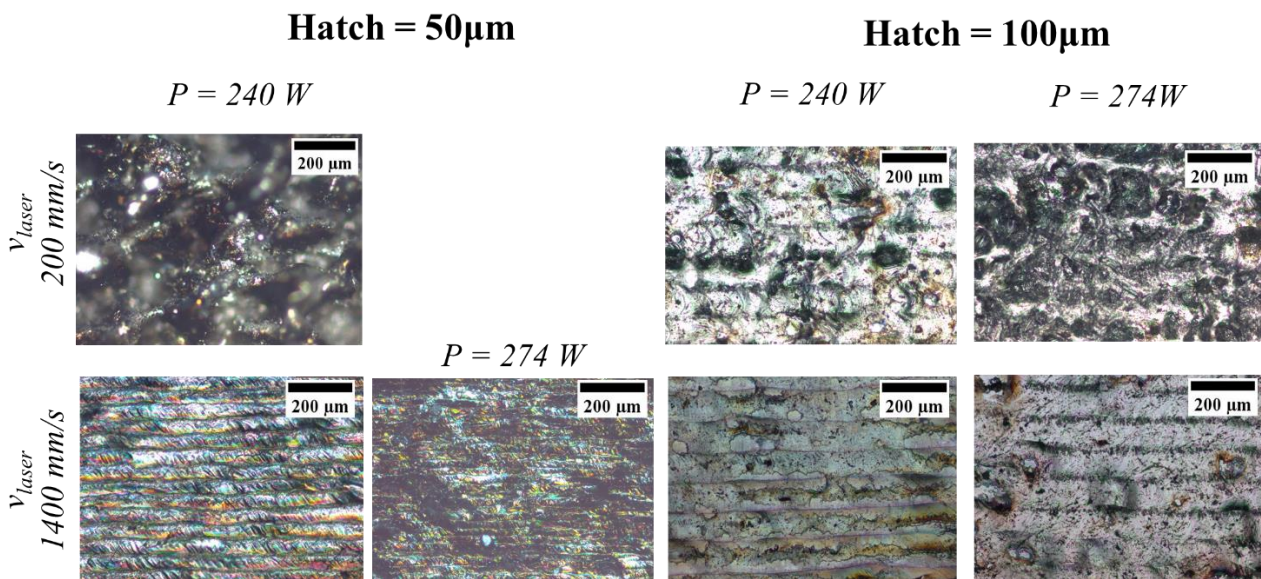


Figure A-3 Top view images of the 2D region scanned with multiple adjacent tracks on the bulk substrate.

Based on the observation of the 2D region of multiple tracks, a preliminary processing map illustrating different regimes can be established, as shown in **Figure A-4**. According to **Figure A-4a**), two regions can be identified when applying a 50μ hatch spacing: the unstable (high energy) region and the stable region. The unstable region corresponds to most of the studied process parameters (typically for

$v_{laser} < 600 \text{ mm/s}$). At higher speeds ($> 1000 \text{ mm/s}$) and low power ($< 240 \text{ W}$), stable conditions are observed in the form of continuous molten tracks.

For a $100 \mu\text{m}$ hatch spacing, three regimes were identified. A stable regime (continuous tracks), unstable (high energy) and unstable (high laser speed) regimes. It must be noted that, when hatch spacing is increased to $100 \mu\text{m}$, the volumetric energy density is reduced and this caused the stable region which was identified when applying a $50 \mu\text{m}$ hatch spacing to be converted into an unstable regime. The stable regime for a $100 \mu\text{m}$ hatch spacing was widened in comparison to the case where a hatch spacing of $50 \mu\text{m}$ was employed, see the comparison between **Figure A-4a)** and **Figure A-4b)**.

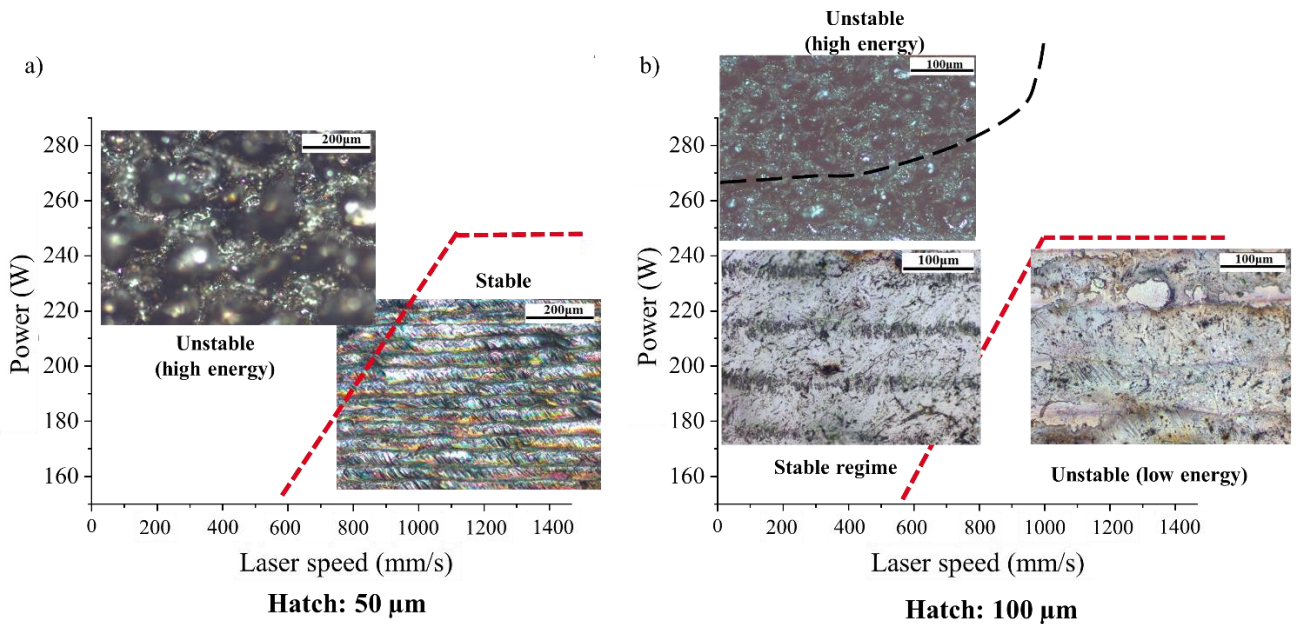


Figure A-4 Identification of the different regimes of stability with the 2D experiments performed on the bulk substrates for respectively a) a $50 \mu\text{m}$ hatch spacing and b) a $100 \mu\text{m}$ hatch spacing.

Figure A-5 shows the melt pools of the scanned bulk substrate with few selected laser processing parameters. The cross-section of the bulk substrate was etched with Keller's reagent to be able to observe the melt pool boundaries. The melt pool boundaries are highlighted in 'red dashed' lines. **Figure A-5a)** and **b)** shows the cross-section of the selected parameters for two hatch spacing (50 and $100 \mu\text{m}$).

Observing the melt pool shape in **Figure A-5** and comparing it with the ones reported in the literature [76], all the studied parameters yielded a hemispherical melt pool shape, suggesting that the experiments were all conducted in the conduction mode of fusion. In addition, for all the studied parameters the depth/width ratio was always less than 1, again pointing towards conduction melting mode, see **Figure A-6c)**). This is probably because the used laser energy density is not enough to induce the keyhole mode of fusion. High energy laser parameters often cause keyhole mode of melt pool causing keyhole porosities [76]. For a given power of 274 W (see **Figure A-5a)** & **b)**), the variation in laser speeds (200 - 1400 mm/s) caused the hemispherical melt pool depth to decrease since the linear energy density is decreased.

For the studied process parameter range in the case of both 50 and 100 μm hatch spacing, the depth and width of the melt pools both increased as a function of linear energy density as expected (see **Figure A-6 a) & b)**), similar to the 1D single tracks. The depth of the 2D tracks was comparatively higher than the single tracks. The d/w ratio for the melt pools originating from the 2D multiple tracks experiments was in the range of $0.2 < d/w < 0.7$, comparatively higher than the one's observed for the 1D single tracks ($0.14 < d/w < 0.19$). This suggests that melting conditions improved with the rough bulk 6061 substrates. This indicates that the energy transferred to the substrate was better in the case of the sand-blasted substrate in comparison with the high reflective as-machined bulk substrate.

Speaking about the difference in the melt pool morphology for the two hatch spacing studied as a function of linear energy density, there was not much of a difference. Both morphologies resulted in sufficient overlap that leads to a proper fusion between adjacent laser tracks. We did not observe any gaps/lack of fusion defects in the inter-track regions. For both the hatch spacing (50 and 100 μm), the variation in depths as a function of linear energy density did not show any significant difference (see **Figure A-6b)**). However, in the case of the width of the melt pools, a 100 μm hatch spacing leads to comparatively smaller widths at high linear energy density ($>1000\text{J/m}$) than the width's when a 50 μm hatch spacing is used (see **Figure A-6a)**). This is probably due to a decrease in overlapping distance between the two adjacent tracks for a higher hatch spacing of 100 μm in comparison with the 50 μm one. This decreases the effect of melting on the neighboring adjacent track.

As shown in **Figure A-5a)** for the 50 μm hatch spacing cases, even without the typical melt pool shape of keyhole melt pools, an increase in porosities was observed for higher energy density process parameters. In the current situation, the observed melt pools result from a conduction mode (since $d/w < 1$). This suggests that the observed pores are due to H_2 entrapment in the molten liquid since Al-alloys are quite susceptible to H_2 induced porosities. According to Aboulkhair *et al.* [30], metallurgical pores also known as Hydrogen pores are less than 100 μm in size, whereas, keyhole pores are comparatively larger ($>100\mu\text{m}$). As observed in **Figure A-5a)**, by decreasing the laser speeds from 1400 mm/s to 200/400 mm/s (i.e increasing laser energy density), porosities were found to be trapped inside the melt pool (see **Figure A-5a)**). Higher energy densities mean, higher molten pool volume and therefore longer time to solidify, thus giving enough time for the H_2 to dissolve in the melt pool. This hypothesis is also verified by the optical microscopy analysis for the %porosity as a function of linear energy density. According to **Figure A-7a)**, porosity % increases as a function of linear energy density. For the sample with the highest linear energy density (1370 J/m, i.e $P=274\text{W}$, $v_{laser}=200\text{mm/s}$), the porosity% is $\sim 8.2\%$, whereas for the sample with lowest energy density (195.7 J/m, i.e $P=274\text{W}$, $v_{laser}=1400\text{mm/s}$) the porosity% is $\sim 0.36\%$. The trend is also visually observed in the cross-section images of **Figure A-5a)**. These results of increased metallurgical porosities at lower scanning speeds (or higher E_L) are consistent with the experimental studies reported by Aboulkhair *et al.* [30] on the L-PBF of AlSi10Mg alloy.

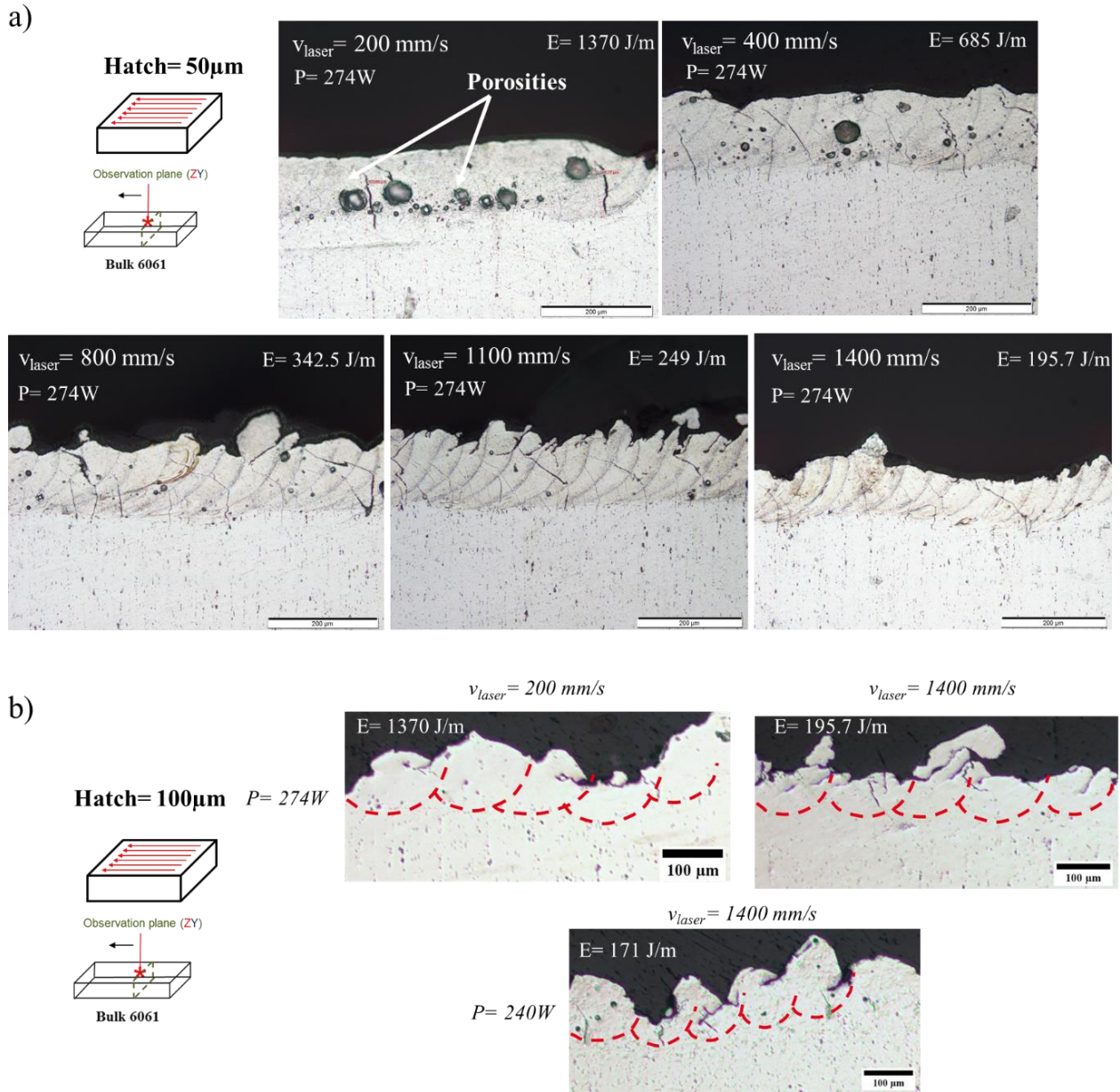


Figure A-5 Cross section view of the melt pools formed by the 2D multiple tracks on the bulk substrates. a) 50 μ m hatch spacing and b) 100 μ m hatch spacing.

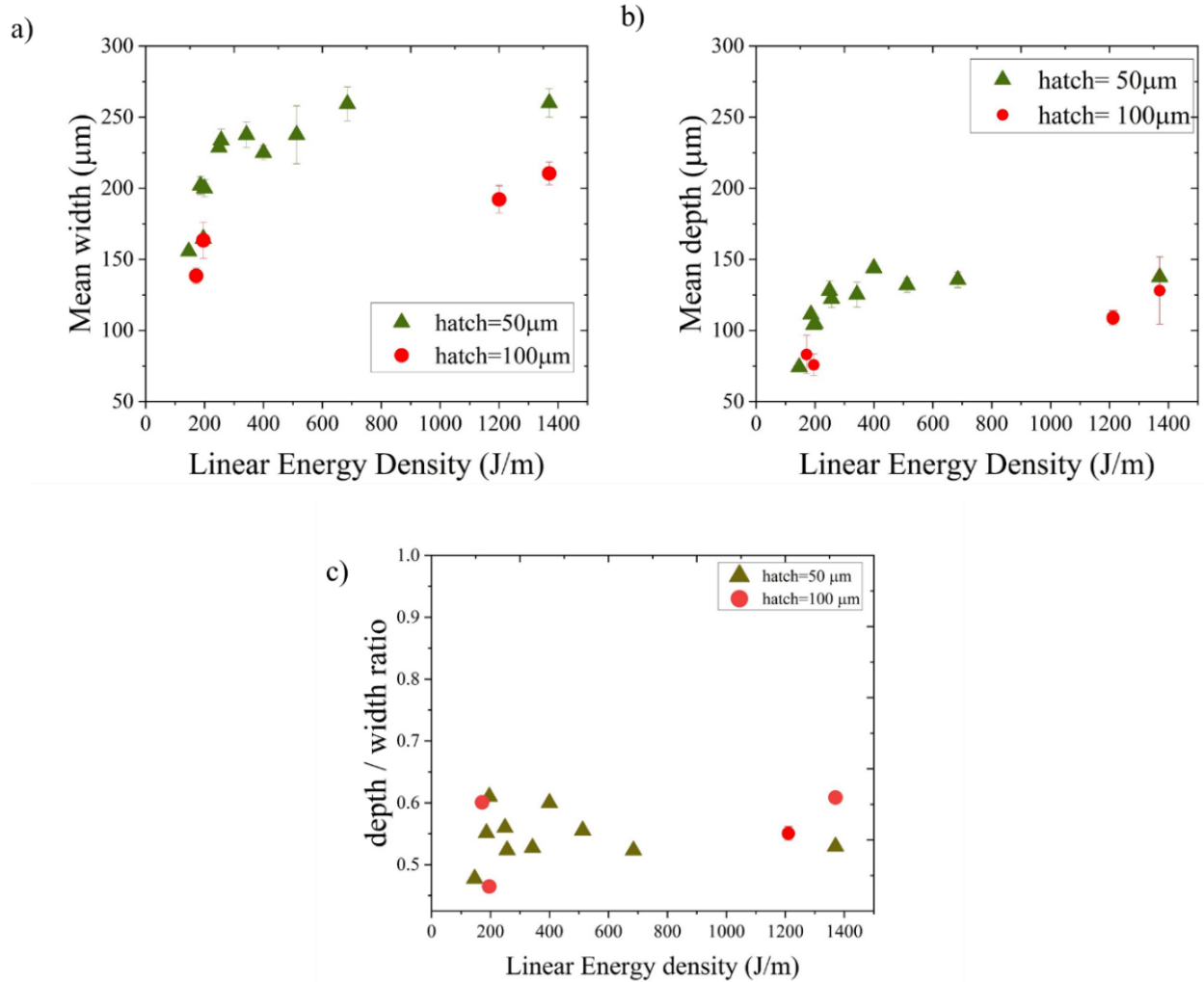


Figure A-6 Melt pool dimensions a) width, b) depth and c) depth/width ratio for the two hatch spacing used (50 and 100 μm).

Another important feature of the pores observed in **Figure A-5a)** for the case of 50μm hatch spacing is the size of those pores. For the higher density samples ($E_L=1370/685$ J/m), the porosity appears to be bigger compared to the low energy density samples ($E_L=342/249/195.7$ J/m). The largest pore size of $\sim 43\mu\text{m}$ corresponds to the $E_L=1370$ J/m. Similarly, as the E_L decreases, the pore size becomes smaller $<20\mu\text{m}$. This analysis of **Figure A-7a)** confirms the sensitivity of porosity and its size to the increasing linear energy density. A similar explanation that, high energy density creates bigger melt pools that can entrap high amount of H_2 is probably true for the formation of larger metallurgical pores for the high linear energy density samples.

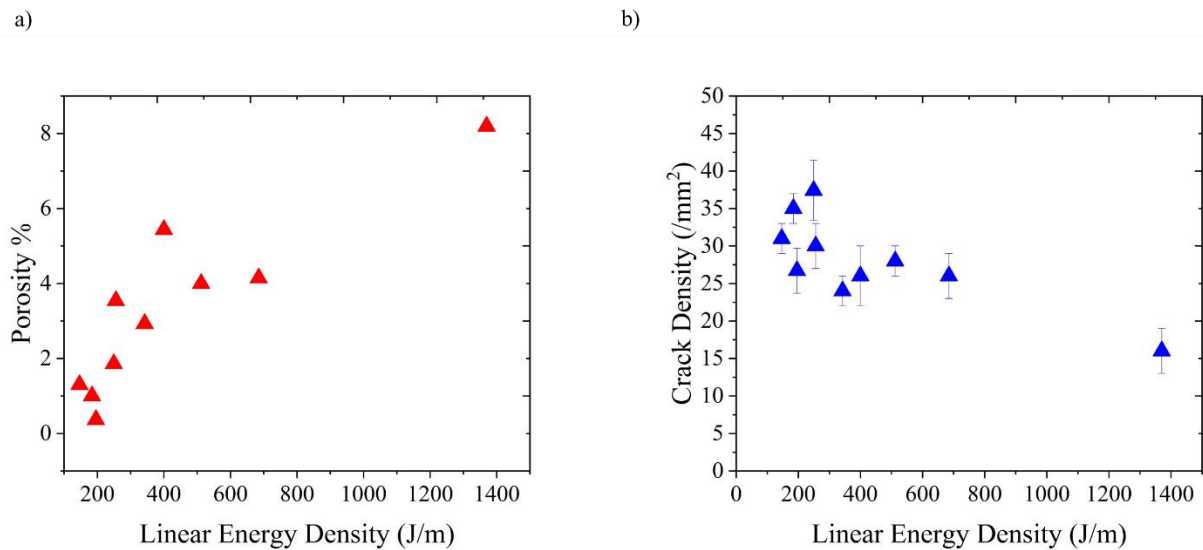


Figure A-7 a) Porosity % as a function of linear energy density. b) Crack density as a function of linear energy density.

In addition to pores, cracks were also observed in the cross-sections as shown in **Figure A-5a) & b)**. In all the studied parameters, cracking was observed. More importantly, for the case of the 50 μm hatching, tilted cracks were observed propagating to the neighboring melt pools caused by the adjacent laser tracks (see **Figure A-5a)**). On the other hand, for the 100 μm hatching, cracks were comparatively less tilted and rather positioned in the center of the melt pools, as illustrated in **Figure A-5b)**. This observation can be attributed to the fact that, by increasing the hatch spacing, the overlapping of the neighboring melt pool decreases, and thus the remelting zone decreases, making the crack form in its respective melt pools, i.e. closer to the center of the melt pool.

The cracking density for the samples melted using a hatch spacing of 50 μm was estimated as a function of the linear energy density, see **Figure A-7b)**. The crack density was estimated in an area of 700x550 μm^2 that fluctuated between 15-37 cracks per mm^2 . According to **Figure A-7b)**, the crack density was found to decrease while increasing linear energy. This observation followed an opposite trend compared to the relation between pore formation and the linear energy (an increase of pore density with the linear energy density, see **Figure A-7a)**). A similar inverse relationship between the pores and the cracks was reported by Stopyra *et al.* [178], where they concluded that cracks cannot be avoided during the 1D/2D process optimizations in laser scanning of 7075 Al-alloy. They attributed the increase in porosity % to compensate for the shrinkage associated with the Al-alloys. Thus, despite the fluctuation in cracking density, cracks were present in all the samples. This made us focus on identifying the optimum process parameters for achieving stable continuous melt pool tracks while reducing the pore content.

To understand further the tilted cracks observed in bulk substrate melt pools, the melt pool cross-section was characterized using EBSD. **Figure A-8a)** shows the pattern quality image of the cross-section of the melt pool formed using the laser parameters ($P=240\text{W}$, $v_{laser}=600\text{ mm/s}$, 50 μm hatch spacing, 70 μm spot size). Columnar grains can be observed inside the melt pool. Cracks are systematically found along

the grain boundaries. Due to the curved nature of the columnar grains, cracks are observed to follow the curved nature of the grain boundaries. This is probably because of the direction of laser tracks and their effect on the direction of the thermal gradients inside the melt pools.

To explain these curved grain boundaries, consider **Figure A-8c) & d)**. The first **Figure A-8c)** illustrates a schematic of the thermal gradient contours ($\vec{G} = \vec{G}_Y + \vec{G}_Z$) in the cross section of melt pool (ZY plane), considering a single track of laser moving inside the plane (along X-axis). \vec{G}_Y and \vec{G}_Z refers to thermal gradient along Y and Z-directions, respectively. When only a single laser is moving inside the plane, the net thermal gradient contour in the ZY-plane cross-section will be always pointed perpendicular to the melt pool boundaries. According to the classical literature [81], the direction of thermal gradients dictates the direction of columnar grain growth, the grains will be aligned towards the Z-direction. Now, consider **Figure A-8d)**, where multiple laser tracks (n, (n+1)th and (n+2)th) moving inside the plane ZY and assuming the net movement of the laser is along the Y-direction. The thermal gradients inside the ZY plane at each location will point towards the net laser direction (i.e. along the Y-direction), making a curved \vec{G} . This will result in a curved grain boundary, as we observe in the case of multiple adjacent laser tracks in **Figure A-8a)**. To remind you, this is the case for a smaller hatch spacing of 50 μ m. When increasing the hatch spacing, the overlap region would decrease, and the net \vec{G} in that case, will result in less curved behavior.

Similarly according to the classification of GB's based on their misorientation angle (see **Figure A-8b)**), the grain boundaries that were cracked did not belong to low angle grain boundaries (5-15°: marked in white), they rather had (15-30°: marked in black) of misorientation. However, to conclude this misorientation based cracking behavior, further statistics would be required.

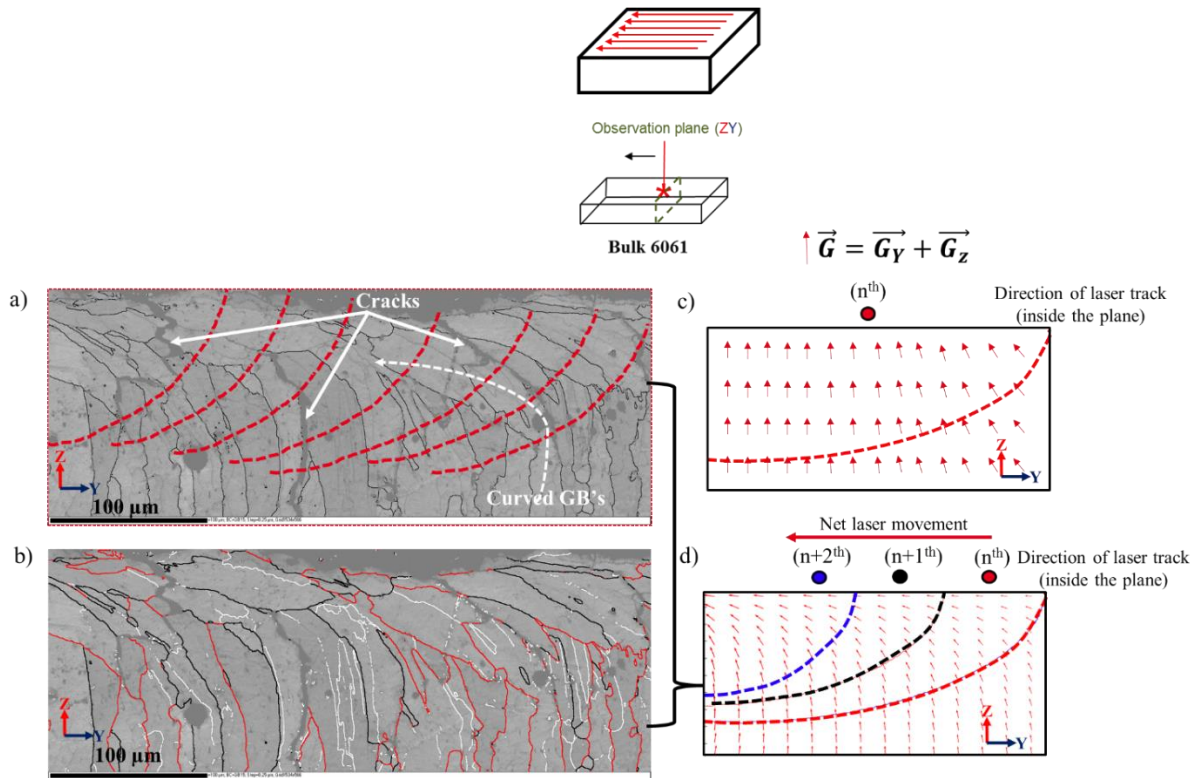


Figure A-8 a) Pattern quality image of the observed bulk substrate melt pool with $P=240\text{W}$ and $v_{laser}=600$ mm/s, hatch spacing = $50\mu\text{m}$ (melt pool boundaries in red dashed lines). b) Pattern quality showing grain boundaries: LAGBs in white (5-15°) and HAGBs in black (15-30°) and red (>30°). c) Schematic of the melt pool cross-section indicating the net thermal gradient direction due to a single laser track. d) Schematic of the melt pool cross-section indicating the net thermal gradient direction due to multiple adjacent laser tracks.

Figure A-9 shows the Inverse pole figure (IPF) of the observed bulk laser-scanned melt pool. The microstructure contains tilted columnar grains with an average width of about $35\pm 5\mu\text{m}$, estimated based on the intercept method. Since columnar grains cross several neighboring melt pools, the cracks also tend to follow this path since they propagate along the grain boundaries.

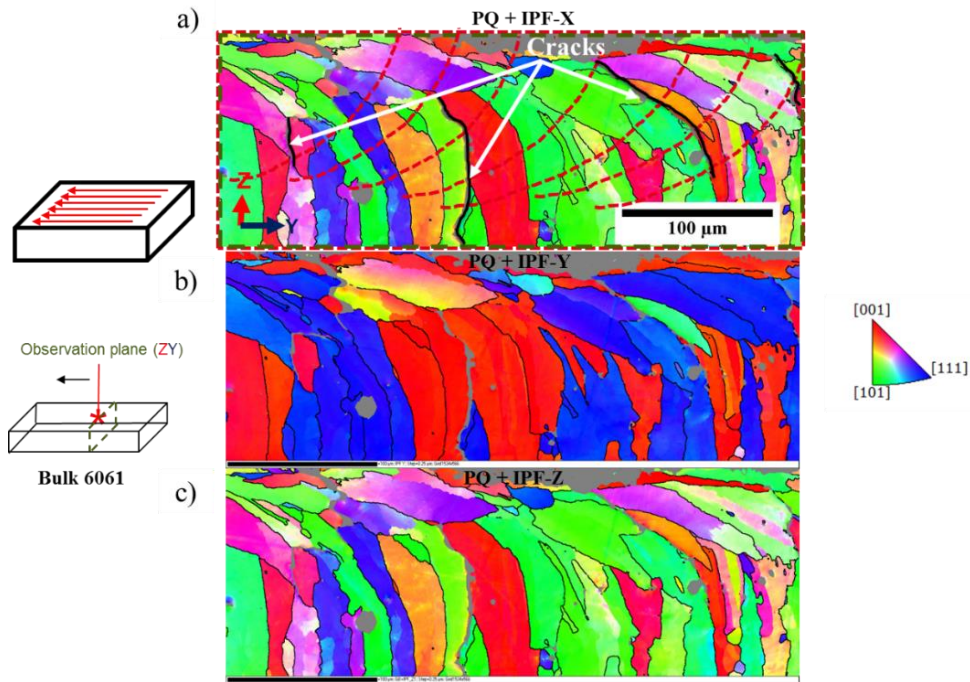


Figure A-9 a), b) &c) Shows the IPF-X, IPF-Y, IPF-Z of the bulk 6061 Al-alloy laser scanned with multiple adjacent tracks ($P=240\text{W}$ and $v_{laser}=600\text{ mm/s}$, hatch= 50μ).

Summary:

Single-tracks (1D) and the multiple tracks (2D) allowed us to get a preliminary idea about the stability regimes of the laser tracks. As the laser speed increased, the unstable (discontinuous) laser tracks became predominant. Within the studied parameters, based on the melt pool morphology it was concluded that conduction mode of melting occurred and no keyhole melt pools were observed since the d/w ratio was always found to be less than 1. Also because the typical powers used to generate the keyhole melt pool in 6061 Al-alloy were $\sim 500\text{W}$ according to ref [124], way higher than the ones used in the present study (max 274W). Speaking in terms of the defects observed, metallurgical pores (due to trapped gas) were identified to be trapped inside the melt pool cross-sections. Similarly, the first evidence of cracking was also observed throughout the samples with various processing conditions. Moreover, cracking was found to be intergranular and depending on the hatch spacing, the location of cracks varied within the melt pools. These preliminary results on the bulk-substrate gave an interesting overview of the processing issues encountered while laser scanning the 6061-Al alloy. Using the understanding gained from these experiments, we focused on the powder layer experiments (**section 4.1.3**) to perform process optimization, since it was thought to be a better representative of the L-PBF process.

List of Figures

Figure 1-1 a) Principle of laser powder bed fusion (L-PBF), adapted from [9] b) Steps involved in L-PBF fabrication, adapted from [10].....	4
Figure 1-2 a) Process parameters for L-PBF process and b) schematic of a scan strategy depicting the hatch spacing, adapted from [1].....	5
Figure 1-3 Classification of Al-alloys based on the alloying elements, adapted from [12][1].	6
Figure 1-4 a) Schematic of L-PBF process. b) Typical length scale in which solidification happens and different modes of solid-liquid modes. c) Typical as-built microstructure of an alloy from 6XXX fabricated by L-PBF, adapted from [4].	7
Figure 1-5 Schematic of the thesis methodology in understanding the cracking in 6061 Al-alloy fabricated during L-PBF.....	8
Figure 1-6 Overview of the thesis chapters and their mutual link.	10
Figure 2-1 a) Al-Si binary phase diagram. b) Building direction EBSD map of the as-built AlSi10Mg alloy. c), d)&f) High magnification microstructure images and e) EDX mapping with Al in blue and Si in red, adapted from [1].	15
Figure 2-2 Optical microstructure of 2024 Al-alloy fabricated via L-PBF a) vertical section/building direction, b) zoomed image of a, c) horizontal section, d) magnified image of figure c) [34].....	16
Figure 2-3 Cracking observed in the as-built 7075 samples along the building direction, adapted from [36].....	17
Figure 2-4 a)-b) Showing the as-built microstructure of 6061 Al-alloy along the building direction (non-etched). c)-d) Etched microstructure showing the location of cracks and porosities with respect to the melt pool boundaries [2][61].....	21
Figure 2-5 a)-c) A typical microstructure of the 6061 Al-alloy during casting using spray forming, adapted from ref. [68]. d)-e) High resolution TEM bright-field image and its corresponding phase map, showing red zone as Aluminum and green zone as the cubic α -Al ₁₅ (Fe,Mn) ₃ Si ₂ phase, adapted from ref [68].	25
Figure 2-6 Typical microstructure of 6061 Al-alloy during laser beam welding, adapted from ref [72].....	26
Figure 2-7 a) Optical microstructure of the as-built 6061 Al-alloy along the building direction and b) Magnified SEM image of the dispersoids.....	26
Figure 2-8 a)Metallurgical pores and b)-d) keyhole pores in as-built AlSi10Mg samples [1]. e) Schematic of the occurrence of metallurgical pores due to Hydrogen entrapment [75]. f) Schematic mechanism of keyhole melt pool formation, adapted from [76]. g) Schematic mechanism of keyhole porosity formation, adapted from [77].	28
Figure 2-9 a)-f) Effect of laser scanning speed on melting mode transition in 7050 Al-alloy during L-PBF. i)-j) Typical microstructure in keyhole melting mode. k)-l) Microstructure in conduction melting mode, adapted from [76].	30
Figure 2-10 Absorptivity of metals as a function of laser wavelength [79].	31
Figure 2-11 Schematic of the mechanism of oxide film formation between layers of Al-alloys fabricated by L-PBF, adapted from [55].	32
Figure 2-12 Different growth morphologies possible depending on the solidification parameters, adapted from [81].	33

Figure 2-13 Solidification cracking in gas metal arc weld of 6061 Al-alloy, adapted from [81]	34
Figure 2-14 Schematic of events happening in the mushy zone during dendritic solidification of Al-alloys, adapted from [85].....	35
Figure 2-15 Constrained solidification studies on 6061 Al-alloy, adapted from [71]. a) Stress vs displacement curve. b) Measure ductility (mm) as a function of solid fraction. c) & d) Reveal the fracture morphology for $f_s=0.95$ and $f_s=0.99$, respectively. e) Variation of stress vs solid fraction for the 6061 Al-alloy.	36
Figure 2-16 Schematic showing the effect of grain boundary liquid surface tension on solidification cracking, adapted from [81].....	38
Figure 2-17 a) Gas-metal arc weld region of 6061 Al-alloy and b) shows the magnified regions. c) Schematic of the liquation cracking mechanism in the PMZ. d) adapted from [81]	39
Figure 2-18 Solidification path of 6061 Al-alloy in comparison with 7075 Al-alloy and AlSi ₁₀ Mg [4].	41
Figure 2-19 a)-b) Schematic of temperature vs $f_s^{1/2}$ curves for the example alloys, adapted from [19]. c) Comparison of actual cracking sensitivity observed for different Al-alloys with the freezing temperature range and with S. Kou cracking index (data adapted from [19]).....	42
Figure 2-20 Schematic of hot crack formation due to localized strains and decrease in metallographic pressure along the mushy zone, adapted from RDG criterion [7].....	44
Figure 2-21 a) Optical micrograph of as-built 6061 Al-alloy and b) after preheating the powder bed at 500°C, adapted from [3].....	47
Figure 2-22 Effect of twin lasers in welding a 6XXX Al-alloy, adapted from [97].....	48
Figure 2-23 Effect of high-intensity ultrasound employed in laser powder deposition for the Ti-6Al-4V alloy, adapted from [102].....	49
Figure 2-24 Effect of ZrH ₂ nanoparticles addition on the powder surface to mitigate cracking in 6061/7075 Al-alloys, adapted from [4].....	50
Figure 2-25 Effect of TiBor and Sc addition in the laser melted 6061 Al-alloy. a) EBSD of laser melted 6061 Al-alloy melt pool, b) with 0.33 wt% TiBor addition and c) 0.4 wt% Sc addition, adapted from [106].	51
Figure 2-26 Building direction microstructure of Si modified 7075 Al-alloy. a)-e) Si content added 0, 1, 2, 3, 4 wt%, respectively, adapted from [5].	52
Figure 2-27 a) Welded microstructure of standard 6061 Al-alloy showing fusion zone and PMZ, b) Welded microstructure of 6061 with a filler of 4043 alloy. c) Temperature vs solid fraction curves for standard 6061 alloy, with 4043 filler and with 5356 filler alloy, adapted from [94].....	53
Figure 3-1 Powder size distribution determined using Mastersizer 2000 (laser particle size analyzer). a) TLS Technik powder batch and b) Powder-2 batch.....	59
Figure 3-2 Morpho-granulometry of the a) TLS Technik powder batch and b) Powder-2 batch, determined using a Morphologi G3S morpo-granulometer.....	60
Figure 3-3 TLS Technik powder: a) & b) Powder morphology at different magnification observed using SEM-SE micrographs. c) Cross-section of the powder showing different grains (SEM-BSE contrast). d) Grain map of the powder cross-section measured using EBSD. Powder-2 batch: e) & f) Powder morphology at different magnification, respectively.....	61
Figure 3-4 Schematic of the rotating drum used for avalanche angle measurement [114].....	62
Figure 4-1 Experimental strategy employed to identify stable melting conditions.	68
Figure 4-2 Reflectivity measured on the 6061 bulk substrates and the 6061 powder (TLS Technik) using the laser spectrophotometer. The reflectivity of pure Al is also shown for reference.....	70

Figure 4-3 Profilometry analysis to measure the mean roughness of the a) as-machined bulk substrate and b) sand-blasted bulk substrate.	71
Figure 4-4 ProX 200 L-PBF machine from 3D systems [119].	72
Figure 4-5 Single tracks for various processing parameters carried out on a single powder layer.	73
Figure 4-6 Single tracks showing the typical signature of humping and balling, adapted from [12,121].	74
Figure 4-7 Analysis of single tracks to identify the criterion for humping/balling. a) Melt pool width, b) Melt pool length, c) Length/Width ratio, and d) Top view of the single tracks for the parameters marked in figure c).	76
Figure 4-8 a) Processing map for the single tracks experiments performed on a single powder layer. b) Observation of typical regimes identified in the processing map.	77
Figure 4-9 Comparison of mean width's for different lasing conditions: powder, rough bulk substrate (sandblast, Ra = 6.3µm), and bulk substrate (as-machined, Ra = 1.2 µm).	78
Figure 4-10 Top views of the 2D region scanned with multiple adjacent tracks on a single powder layer.	79
Figure 4-11 a) Processing map for the 2D multiple tracks on a single powder layer. b) Observation of typical regimes identified in the processing map.	81
Figure 4-12 a) Processing map for the 2D multiple tracks on five successive powder layers. b) Observation of typical regimes identified in the processing map.	82
Figure 4-13 Cracking observation in a) 1D-bulk substrate, b) 2D-bulk substrate, c) Single tracks on a single powder layer, d) multiple tracks on a powder layer.	83
Figure 4-14 Parallel scanning strategy without rotation between layers used to fabricate L-PBF cubes.	84
Figure 4-15 a) 6061 Al-alloy cubes made using L-PBF. b) Surface state of unfinished cube due to blocking of powder spreader, when excessive energy input is used ($E_L > 400$ J/m)	86
Figure 4-16 a) Relative density and porosity as a function of laser energy density for cubes fabricated using TLS powder. b) Variation of crack density with laser energy density. c) and d) Optical micrographs of the samples with $E_L = 400$ J/m and $E_L = 117$ J/m, respectively. e) Optical micrograph showing porosity enhanced cracking. f) Variation of porosity enhanced crack density with linear energy density.	87
Figure 4-17 a) Low magnification optical micrograph along the build direction (etched with Keller's reagent) taken from a cube fabricated with optimized parameters ($E_L = 400$ J/m). b) Pattern quality image measured using EBSD. c) IPF-EBSD map of the 6061 cube sample normal to the X-direction of the cube sample. d) (100), (111) and (110) Pole figures determined over the map shown in c).	92
Figure 4-18 a) IPF-EBSD map normal to the X-direction of 6061 cube sample, showing intergranular cracking. b) IPF-EBSD map showing non-cracked low angle grain boundaries ($5^\circ < \text{LAGB} < 15^\circ$) marked in white and high angle grain boundaries ($\text{HAGB} > 15^\circ$) marked in black. c) Distribution of misorientation angle for cracked and non-cracked grain boundaries.	94
Figure 4-19 a) & b) BSE-SEM contrast micrographs of the as-built 6061-alloy using the optimized processing conditions ($P = 240$ W and $v_{laser} = 600$ mm/s). b) IPF-EBSD map of 6061 cube sample in XY plane.	95
Figure 4-20 a) & b) Grain average misorientation map of the XY and ZY plane, respectively.	96
Figure 4-21 a) Schematic showing how the tensile coupons were extracted from cube samples. b) Micrograph of fracture surface demonstrating Marangoni convection inside the melt pool c) Low magnification SE-SEM contrast micrograph of the melt pool. d) & e) High magnification SE-SEM contrast micrograph at the surface of cracks.	97
Figure 4-22 Optical micrograph of the topmost layer of L-PBF cube sample along the building direction. The cracks are denoted by the red arrows, and the topmost melt pools by red dashed lines.	98

Figure 4-23 a)-d) Typical 6061 Al-alloy L-PBF as-built microstructure revealed by chemical etching (BSE-SEM contrast) at various magnifications extracted in the plane containing the build direction.	100
Figure 4-24 X-ray diffraction analysis on the as-built cube (XY plane)-top and the gas atomized TLS powder – bottom.	101
Figure 4-25 a)-b) SEM-BSE micrographs (not chemically etched) taken along building direction with increasing order of magnification. The FIB sample was extracted in the location indicated by the ‘black square’ in b).102	102
Figure 4-26 a) & b) SEM-SE micrographs (not chemically etched) showing the location of FIB sample with cracked GB (marked in red) and non-cracked GB (marked in green). c) FIB lamellas having a cracked GB and non-cracked GB.....	103
Figure 4-27 a) FIB lamella with cracked (red) and non-cracked GB (green). b) & c) HAADF (left) image and BF (right) image taken from a region including the non-cracked GB and cracked GB, respectively.....	104
Figure 4-28 a) HAADF (left) image and BF (right) image of the cracked GB. b) HAADF image of the top region of the cracked GB. c) HAADF (left) image and BF (right) image of the bottom region of the cracked GB.	105
Figure 4-29 HAADF image of the top region of the cracked GB and the corresponding STEM-EDX maps showing various solute elements.	106
Figure 4-30 BF image of the bottom region of cracked GB and the corresponding STEM-EDX maps showing various solute elements.	107
Figure 4-31 a) HAADF (left) image and BF (right) image of the non-cracked GB. b) High magnification region of the non-cracked GB, HAADF (left), and BF (right).....	108
Figure 4-32 HAADF image of the non-cracked GB and the corresponding EDX maps showing various solute elements.	109
Figure 5-1. Solidification path of the 6061 Al-alloy, showing the solidification path $T(f)$ using Scheil-Gulliver assumptions (no diffusion in solid and infinite diffusion in liquid).....	118
Figure 5-2. Atomistic view of liquid film thickness diminishing between the two neighboring grains ($\theta \neq 0$) during coalescence and schematic of excess free Gibb’s energy as a function of location, adapted from [85].	119
Figure 5-3 a)Schematic of grain boundary energy as a function of misorientation angle (θ) [85]. b) illustration showing the columnar dendrites growing with different misorientation, adapted from ref.....	120
Figure 5-4 Grain boundary energy as a function of misorientation angle (based on estimation using the Read-Shockley model)	122
Figure 5-5. a) Grain boundary energy of pure Aluminum for different tilt boundaries as a function of misorientation angle [150][151]. b) Effect of misorientation on the dendrite coalescence temperature.....	123
Figure 5-6 Geometrical relation between the solidification velocity and the laser scanning speed, on a melt pool schematic, adapted from [120].	125
Figure 5-7 (Top) Estimated melt pool depths using Rosenthal simulation and experimentally verified melt pool depths on the bulk substrate (middle) for different laser speeds (v_{laser}). The bottom graph shows the variation in melt pool depth as a function of v_{laser} for different absorptivity coefficients (η): 0.8 and 0.6.	127
Figure 5-8 Thermal Gradient (G) contours for P=240 W and v_{laser} =600 mm/s in different plane (a) ZX-plane, b) XY-plane and c)-f) ZY-plane at different cross sections of ZX-plane.....	129
Figure 5-9 Solidification velocity (v) contours for P=240 W and v_{laser} _r =600 mm/s in different plane (a) ZX-plane, b) XY-plane and c)-e) ZY-plane at different cross-sections of ZX-plane.	130

Figure 5-10 a) and b) Thermal gradients inside the melt pool (XZ-plane and YZ-plane) computed using Rosenthal analytical solution when a bulk 6061 Al alloy substrate is subjected to laser power of 240W and laser speed of 600 mm/s (optimized conditions suppressing lack-of-fusion defects). c) Variation of thermal gradients (G) and solidification velocity (v) along the melt pool depth.....	131
Figure 5-11 a) Temperature field inside the melt pool computed using Rosenthal simulation in the XZ-plane. b) Evolution of length of the mushy zone along the laser scanning direction (X-axis) using the T_{gc} ($f_s=0.97$): black curve and another using the coalescence temperature of T_{gc} ($f_s=0.97$ and $\theta=15^\circ$): red curve.....	132
Figure 5-12 a), b) and c) Temperature field inside the melt pool (XY, ZX plane, and ZY plane) computed using Rosenthal analytical solution when a bulk 6061 Al alloy substrate is subjected to laser power of 240W and laser speed of 600 mm/s (optimized conditions suppressing lack-of-fusion defects). d) Variation of the length of the mushy zone (L^c) in the ZX-plane, inside the melt pool, as a function of laser scanning direction for different Y-coordinate values to rationalize the central location of cracking.....	134
Figure 5-13 a)-c) Calculation of the different integrand functions used to define the shrinkage and deformation part of RDG criterion as a function of the temperature bounds ($T_{liquidus}$ to $T_{gc}(f_s=0.97)$), for the case of attractive boundaries (since $\theta \leq \theta_{a-r}=5^\circ$). d)-f) For the case of repulsive boundaries those are HAGB at $\theta=15^\circ$	137
Figure 5-14 a) Pressure drop due to deformation, b) Pressure drop due to shrinkage and c) Total pressure drop for a given $G= 2.8 \times 10^6$ K/m and $v= 0.3$ m/s, typical values extracted from our Rosenthal simulations for $P = 240$ W and $v = 600$ mm/s.....	140
Figure 5-15 Effective contribution of deformation and shrinkage terms as a function of misorientation angle for different coalescence solid fraction: a) $f_s=0.92$, b) $f_s=0.97$ and c) $f_s=0.99$	141
Figure 5-16 Effective contributions of deformation and shrinkage terms as a function of solid fraction for different misorientation angles: a) $\theta=5^\circ$, b) $\theta=10^\circ$ and c) $\theta=15^\circ$	142
Figure 5-17 a) Shows the pressure drop map inside the XY plane melt pool. b) Evolution of pressure drop along the X-axis for different Y-coordinates. c) Pressure drop variation as a function of the Y-axis for different temperature contours inside the XY-plane melt pool.....	143
Figure 6-1 a) b) & c) Hot cracking sensitivity (HCS) map for $\theta = 5^\circ$, $\theta = 15^\circ$ & $\theta = 25^\circ$ respectively. Mean crack density (measured experimentally) is also superimposed on the HCS map of figure c).....	150
Figure 6-2 Shows the total pressure drop as a function of melting parameters (linear energy density). Mean crack density (found experimentally) is also superimposed to qualitatively compare the predictions and experimental observations.	151
Figure 6-3 Effect of laser scanning speed (v_{laser} : 200, 600, 1000 mm/s) on the spatial distribution of pressure drop inside the melt pool in the XY-plane. The first two rows show the thermal gradients and solidification velocity inside the melt pool corresponding to a constant laser power of 240 W. Pressure drop is estimated inside the melt pool by implementing RDG criterion based on the location specific solidification parameters (G, v).....	153
Figure 6-4 Maximum length of mushy zone (L^c) as a function of laser linear energy density. The maximum length of mushy zone was estimated using the concept of coalescence undercooling at $\theta=15^\circ$ for a the studied process parameters (P, v_{laser}).....	155
Figure 6-5 a) Effect of the preheating temperature on thermal gradients along the $f_s=0.97$ contour of the respective melt pools (for $P = 240$ W and $v_{laser} = 600$ mm/s). b) Effect of the preheating temperature on solidification velocities along the $f_s=0.97$ contour. c) Typical melt pools in ZX-plane for different preheating temperatures ($T_0=23^\circ\text{C}$ and $T_0=500^\circ\text{C}$). d) HCS map ($T_0 = 500^\circ\text{C}$) estimated using the updated G and v of the preheated melt pools and updated PDAS using the empirical formula ($\lambda = 43.2 (G.v)^{0.324}$).....	156
Figure 6-6 a)- b) SEM micrograph and corresponding HCS map, respectively, of 6061 Al alloy fabricated under L-PBF ($P: 240$ W, $v_{laser}: 600$ mm/s) with ‘no preheating’. c)-d) Optical micrograph (adapted from ref. [3])	

and corresponding HCS map, respectively, of 6061 Al alloy fabricated under L-PBF with 'preheating $T_0=500^\circ\text{C}$ '.....	157
Figure 6-7 a) Evolution of PDAS as a function of thermal gradient and solidification velocity (according to $(\lambda = 43.2 (G.v)^{-0.324})$. b) Sensitivity analysis for variation in primary dendrite arm spacing (PDAS). The effect of PDAS variation on pressure drop is shown assuming all other input parameters to be not affected ($G=2.8 \times 10^6$ K/m and $v=0.3$ m/s, for $\theta=15^\circ$).	161
Figure 6-8 Hot cracking sensitivity map showing three different process regimes: casting, welding, and L-PBF marked in 'colored dashed squares'. The pressure drop was calculated assuming inputs from Table 5-4 and at coalescence undercooling of 15°	163
Figure 6-9 a) Shows the effect of strain rate sensitivity on total pressure drop estimated for $G=2.8 \times 10^6$ K/s and $v=0.3$ m/s & $\theta=15^\circ$. b) Effect of solidification velocity on the critical strain rate (beyond which cracking is highly probable), considering the $\Delta P_{critical}=2.45$ GPa.....	164
Figure 6-10 Shows the effect of viscosity on variation in total pressure drop calculated for $G=2.8 \times 10^6$ K/m, $v=0.3$ m/s, and $\theta=15^\circ$	167
Figure 6-11 a) – e) Hot cracking sensitivity maps in L-PBF processing conditions as a function of viscosity.....	168
Figure 6-12 a) Dynamic viscosity of pure Aluminum as a function of temperature in the solidification range (T_L to $T_{gc}(\theta=15^\circ)$). b) HCS map of 6061 Al alloy for L-PBF, taking into account the $\mu(T)$ for pure Aluminum. ..	170
Figure 6-13 Summarized pressure drop sensitivity analysis due to variation in parameters, namely, PDAS, viscosity, and strain rate.....	172
Figure 7-1 Shows the cracking sensitivity during welding of the binary Al-alloys for different solute elements a) Si, b)Cu, c)Mg, and d) phase Mg_2Si , adapted from ref. [81].	176
Figure 7-2 Solidification paths calculated using Scheil Gulliver assumptions for 6061 Al-alloy, subjected to different solute content variation: a) Cr, b) Fe, c) Zn, d) Cu, e) Si and d) Mg.....	177
Figure 7-3 Constrained solidification studies, showing the development of stress in the mushy zone during solidification of modified 6061 Al alloy, a) Si content variation and b)Mg content variation, adapted from E. Giraud <i>et al.</i> [73]......	179
Figure 7-4 a) & b) Solidification paths in the final stage of the solidification process for varying Si and Mg additions to the 6061 Al-alloy respectively. c) Pressure drop calculated using the RDG criterion for various Si and Mg contents to the base 6061 Al-alloy (for $G = 2.8 \cdot 10^6$ K/m, $v = 0.3$ m/s, coalescence fraction estimated from Table 7-2 and considering the coalescence undercooling for $\theta = 15^\circ$).....	180
Figure 7-5 Crack density reported for 6061 Al-alloy as a function of Si/Mg content, during welding, adapted from ref [71]......	181
Figure 7-6 HCS maps to illustrate the effect of chemical composition and process parameters. a) and b) HCS map for 2wt% Si and 2wt% Mg addition to the 6061 Al-alloy, respectively.....	182
Figure 7-7 Solidification paths for various Zr additions to the standard 6061 Al-alloy, calculated using Scheil-Gulliver model.....	184
Figure 7-8 Pressure drop as a function of Zr content in the 6061 Al-alloy (using empirical strain rate relation). 185	
Figure 7-9 As-built building direction IPF-EBSD map normal to the build direction for the 6061 Al-alloy with 2% of Zirconium, adapted from ref [104]......	186
Figure 7-10 Statistics of the misorientation distribution for various Zr additions.	186
Figure 7-11 a) IPF EBSD image of the standard 6061 Al-alloy normal to the build direction (present study). b) Grain map of the 6061+2wt% Zr alloy in the as-built conditions (adapted from ref [104]). c) Grain boundaries map of the 6061+2wt% Zr alloy.	187

Figure 8-1 Bottom-up strategy employed to identify the optimized parameters.....	192
Figure 8-2 Cracking mechanism and its characteristics identified for the 6061 Al-alloy fabricated by L-PBF.....	193
Figure 8-3 Multi-scale characterization performed on the as-built 6061 Al-alloy.....	194
Figure 8-4 Cracking sensitivity analysis for coalescence solid fraction ($f_s=0.97$ and $f_s=0.9$), based on total pressure drop estimated using the RDG criterion.....	195
Figure 8-5 Development of hot cracking sensitivity map based on process parameters and microstructure.....	196
Figure 8-6 Metallurgical parameters needed to be considered to improve alloy design strategies.....	197
Figure 8-7 a) & b) Strain rate schematic for a single columnar grain of 6061 Al-alloy and N number of columnar grains of Zr modified 6061 alloy. c) Pressure drop as a function of Zr content in the 6061 Al-alloy (taking into account the relative strain rates, thanks to variation in columnar grain width).....	201
Figure A-1 a)-c) Cross-section view of the single tracks made on the bulk substrate (after Keller's etching) as a function of increasing laser speed. d) Cross-section melt pool morphology showing evidence of cracking.	204
Figure A-2 a) Variation of melt pool width and b) melt pool depth with the linear energy density (1D-bulk substrate).....	205
Figure A-3 Top view images of the 2D region scanned with multiple adjacent tracks on the bulk substrate.....	206
Figure A-4 Identification of the different regimes of stability with the 2D experiments performed on the bulk substrates for respectively a) a 50 μ m hatch spacing and b) a 100 μ m hatch spacing.....	207
Figure A-5 Cross section view of the melt pools formed by the 2D multiple tracks on the bulk substrates. a) 50 μ m hatch spacing and b) 100 μ hatch spacing.....	209
Figure A-6 Melt pool dimensions a) width, b) depth and c) depth/width ratio for the two hatch spacing used (50 and 100 μ m).....	210
Figure A-7 a) Porosity % as a function of linear energy density. b) Crack density as a function of linear energy density.....	211
Figure A-8 a) Pattern quality image of the observed bulk substrate melt pool with P=240W and $v_{laser}= 600$ mm/s, hatch spacing =50 μ m (melt pool boundaries in red dashed lines). b) Pattern quality showing grain boundaries: LAGBs in white (5-15 $^\circ$) and HAGBs in black (15-30 $^\circ$) and red (>30 $^\circ$). c) Schematic of the melt pool cross-section indicating the net thermal gradient direction due to a single laser track. d) Schematic of the melt pool cross-section indicating the net thermal gradient direction due to multiple adjacent laser tracks.	213
Figure A-9 a), b) &c) Shows the IPF-X, IPF-Y, IPF-Z of the bulk 6061 Al-alloy laser scanned with multiple adjacent tracks (P=240W and $v_{laser}= 600$ mm/s, hatch=50 μ)......	214

List of Tables

Table 2-1 Review of Al-alloys tested in L-PBF for hot cracking sensitivity/build density [38].	18
Table 2-2 Comparison of mechanical properties of some of the Al-alloys tested in L-PBF.	20
Table 2-3 Review on as-built 6061 Al-alloy (L-PBF fabricated).	22
Table 2-4 Standard composition of 6061 Al-alloy [67].	23
Table 2-5 Summary of the role of solute elements in 6xxx Al-alloys [66][12].	23
Table 2-6 Solidification parameters for different processes.	33
Table 2-7 Composition of 4043 filler used in the welding of 6061 alloy, adapted from [94].	54
Table 3-1 Chemical composition of the 6061 Al-alloy powder used in the present study in (wt %). The standard is also given for comparison.	57
Table 3-2 Powder size distribution of the two 6061 Al-alloy powders.	58
Table 3-3 Powder morphology (aspect ratio) of the two 6061 Al-alloy powders.	60
Table 3-4 Powder flowability of the two 6061 Al-alloy powders.	62
Table 4-1 Constants used to estimate the normalized enthalpy for the two melting modes observed in 6061 Al-alloy.	89
Table 5-1 Constants for pure Al used to estimate grain boundary energy (Read-Shockley model [148]).	121
Table 5-2 Constants used to estimate coalescence undercooling.	123
Table 5-3 Constants used for Rosenthal analytical simulations.	126
Table 5-4 Constants used as inputs for RDG criterion.	136
Table 6-1 Estimated PDAS for various processes based on solidification parameters.	160
Table 6-2 Viscosity data for pure Aluminum at melting temperatures, adapted from [157] [164].	169
Table 6-3 Dynamic viscosities of Al-alloys (adapted from ref. [17]).	171
Table 7-1 Standard solute content in different Aluminum alloys (wt%) [67].	175
Table 7-2 Coalescence solid fraction (f_i) for different Si/Mg content in the 6061 Al-alloy, adapted from [73].	179
Table A-1 Composition of the 6061 bulk substrate (wt%).	203

References

- [1] N.T. Aboulkhair, M. Simonelli, L. Parry, I. Ashcroft, C. Tuck, R. Hague, 3D printing of Aluminium alloys: Additive Manufacturing of Aluminium alloys using selective laser melting, *Prog. Mater. Sci.* 106 (2019) 100578. <https://doi.org/10.1016/j.pmatsci.2019.100578>.
- [2] B.A. Fulcher, D.K. Leigh, T.J. Watt, Comparison of AlSi10Mg and Al 6061 Processed Through DMLS, *Proc. 25th Solid Free. Fabr. Symp.* (2014) 404–419. <http://sffsymposium.engr.utexas.edu/2014TOC>.
- [3] S.Z. Uddin, L.E. Murr, C.A. Terrazas, P. Morton, D.A. Roberson, R.B. Wicker, Processing and characterization of crack-free aluminum 6061 using high-temperature heating in laser powder bed fusion additive manufacturing, *Addit. Manuf.* 22 (2018) 405–415. <https://doi.org/10.1016/j.addma.2018.05.047>.
- [4] J.H. Martin, B.D. Yahata, J.M. Hundley, J.A. Mayer, T.A. Schaedler, T.M. Pollock, 3D printing of high-strength aluminium alloys, *Nature*. 549 (2017) 365–369. <https://doi.org/10.1038/nature23894>.
- [5] M.L. Montero Sistiaga, R. Mertens, B. Vrancken, X. Wang, B. Van Hooreweder, J.P. Kruth, J. Van Humbeek, Changing the alloy composition of Al7075 for better processability by selective laser melting, *J. Mater. Process. Technol.* 238 (2016) 437–445. <https://doi.org/10.1016/j.jmatprotec.2016.08.003>.
- [6] M. Rappaz, A. Jacot, W.J. Boettinger, Last-stage solidification of alloys: Theoretical model of dendrite-arm and grain coalescence, *Metall. Mater. Trans. A.* 34 A (2003) 467–479. <https://doi.org/10.1007/s11661-003-0083-3>.
- [7] M. Rappaz, J.M. Drezet, M. Gremaud, A new hot-tearing criterion, *Metall. Mater. Trans. A.* 30 (1999) 449–455. <https://doi.org/10.1007/s11661-999-0334-z>.
- [8] ASTM, F2792 – 12a, *Stand. Terminol. Addit. Manuf. Technol.* 10.04 (2013). <https://doi.org/10.1520/F2792-12A>.
- [9] Rapid Prototyping - Three Dimensional Printing, (n.d.). <http://www.custompartnet.com/wu/3d-printing> (accessed December 26, 2020).
- [10] Additive Manufacturing solutions & industrial 3D printer by EOS, (n.d.). <https://www.eos.info/en> (accessed December 26, 2020).
- [11] A. Aversa, G. Marchese, A. Saboori, E. Bassini, D. Manfredi, S. Biamino, D. Ugues, P. Fino, M. Lombardi, New aluminum alloys specifically designed for laser powder bed fusion: A review, *Materials (Basel)*. 12 (2019). <https://doi.org/10.3390/ma12071007>.
- [12] N.T. Aboulkhair, *Additive Manufacture of an Aluminium alloy: processing, microstructure, and mechanical properties.*, 2015.
- [13] K. Kempen, L. Thijs, J. Van Humbeek, J.P. Kruth, Mechanical Properties of AlSi10Mg Produced by Selective Laser Melting, *Phys. Procedia*. 39 (2012) 439–446. <https://doi.org/10.1016/j.phpro.2012.10.059>.
- [14] F. Trevisan, F. Calignano, M. Lorusso, J. Pakkanen, A. Aversa, E.P. Ambrosio, M. Lombardi, P. Fino, D. Manfredi, On the selective laser melting (SLM) of the AlSi10Mg alloy: Process, microstructure, and mechanical properties, *Materials (Basel)*. 10 (2017). <https://doi.org/10.3390/ma10010076>.
- [15] M. Tang, P.C. Pistorius, S. Narra, J.L. Beuth, Rapid Solidification: Selective Laser Melting of AlSi10Mg, *JOM J. Miner. Met. Mater. Soc.* 68 (2016) 960–966. <https://doi.org/10.1007/s11837-015-1763-3>.
- [16] F. Ozturk, A. Sisman, S. Toros, S. Kilic, R.C. Picu, Influence of aging treatment on mechanical properties of 6061 aluminum alloy, *Mater. Des.* 31 (2010) 972–975. <https://doi.org/10.1016/j.matdes.2009.08.017>.
- [17] J.J. Valencia, P.N. Quested, *Thermophysical Properties*, *ASM Handbook*, Asm. 15 (2008) 468–481. <https://doi.org/10.1361/asmhba0005240>.
- [18] S. Kou, Solidification and liquation cracking issues in welding, *JOM J. Miner. Met. Mater. Soc.* 55 (2003) 37–42. <https://doi.org/10.1007/s11837-003-0137-4>.

- [19] S. Kou, A simple index for predicting the susceptibility to solidification cracking, *Weld. J.* 94 (2015) 374s-388s.
- [20] E. Cicală, G. Duffet, H. Andrzejewski, D. Grevey, S. Ignat, Hot cracking in Al-Mg-Si alloy laser welding - Operating parameters and their effects, *Mater. Sci. Eng. A.* 395 (2005) 1–9. <https://doi.org/10.1016/j.msea.2004.11.026>.
- [21] C.E. Roberts, D. Bourell, T. Watt, J. Cohen, A novel processing approach for additive manufacturing of commercial aluminum alloys, *Phys. Procedia.* 83 (2016) 909–917. <https://doi.org/10.1016/j.phpro.2016.08.095>.
- [22] T. Böllinghaus, H. Herold, C.E. Cross, J.C. Lippold, Hot cracking phenomena in welds II, *Hot Crack. Phenom. Welds II.* (2008) 1–467. <https://doi.org/10.1007/978-3-540-78628-3>.
- [23] J.C. Lippold, *Welding Metallurgy and Weldability*, Wiley Blackwell, 2014. <https://doi.org/10.1002/9781118960332>.
- [24] M. Miyazaki, K. Nishio, M. Katoh, S. Mukae, H.W. Kerr, Quantitative investigation of heat affected zone cracking of aluminium alloy 6061, *Weld. Int.* 4 (1990) 600–609. <https://doi.org/10.1080/09507119009447787>.
- [25] M. Katoh, H.W. Kerr, Investigation of heat-affected zone cracking of GTA welds of Al-Mg-Si alloys using the vareststraint test., *Weld. J.* 66 (1987) 360–368.
- [26] A. Mauduit, S. Pillot, H. Gransac, Study of the suitability of aluminum alloys for additive manufacturing by laser powder-bed fusion, *UPB Sci. Bull. Ser. B Chem. Mater. Sci.* 79 (2017) 219–238.
- [27] D. Grange, J. Bartout, B. Macquaire, C. Colin, Processing a non-weldable Nickel-base superalloy by Selective Laser Melting : role of the shape and size of the melt pools on solidification cracking, *Materialia.* (2020) 100686. <https://doi.org/10.1016/j.mtla.2020.100686>.
- [28] ROSENTHAL, D., The Theory of Moving Sources of Heat and Its Application of Metal Treatments, *Trans. ASME.* 68 (1946) 849–866.
- [29] R.S. Rana, R. Purohit, S. Das, Influences of alloying elements on the microstructure and properties of Mg-Li alloys, *Int. J. Sci. Res. Publ.* 2 (2012).
- [30] N.T. Aboulkhair, N.M. Everitt, I. Ashcroft, C. Tuck, Reducing porosity in AlSi10Mg parts processed by selective laser melting, *Addit. Manuf.* 1 (2014) 77–86. <https://doi.org/10.1016/j.addma.2014.08.001>.
- [31] D. Buchbinder, H. Schleifenbaum, S. Heidrich, W. Meiners, J. Bültmann, High power Selective Laser Melting (HP SLM) of aluminum parts, *Phys. Procedia.* 12 (2011) 271–278. <https://doi.org/10.1016/j.phpro.2011.03.035>.
- [32] L. Thijs, K. Kempen, J.P. Kruth, J. Van Humbeeck, Fine-structured aluminium products with controllable texture by selective laser melting of pre-alloyed AlSi10Mg powder, *Acta Mater.* 61 (2013) 1809–1819. <https://doi.org/10.1016/j.actamat.2012.11.052>.
- [33] J. Liu, S. Kou, Susceptibility of ternary aluminum alloys to cracking during solidification, *Acta Mater.* 125 (2017) 513–523. <https://doi.org/10.1016/j.actamat.2016.12.028>.
- [34] H. Zhang, H. Zhu, T. Qi, Z. Hu, X. Zeng, Selective laser melting of high strength Al-Cu-Mg alloys: Processing, microstructure and mechanical properties, *Mater. Sci. Eng. A.* 656 (2016) 47–54. <https://doi.org/10.1016/j.msea.2015.12.101>.
- [35] M.C.H. Karg, B. Ahuja, S. Wiesenmayer, S.V. Kuryntsev, M. Schmidt, Effects of process conditions on the mechanical behavior of aluminium wrought alloy EN AW-2219 (AlCu6Mn) additively manufactured by laser beam melting in powder bed, *Micromachines.* 8 (2017) 1–11. <https://doi.org/10.3390/mi8010023>.
- [36] W. Reschetnik, J.P. Brüggemann, M.E. Aydinöz, O. Grydin, K.P. Hoyer, G. Kullmer, H.A. Richard, Fatigue crack growth behavior and mechanical properties of additively processed en AW-7075 aluminium alloy, in: *Procedia Struct. Integr.*, Elsevier B.V., 2016: pp. 3040–3048. <https://doi.org/10.1016/j.prostr.2016.06.380>.

- [37] W. Stopyra, K. Gruber, I. Smolina, T. Kurzynowski, B. Kuźnicka, Laser powder bed fusion of AA7075 alloy: Influence of process parameters on porosity and hot cracking, *Addit. Manuf.* 35 (2020). <https://doi.org/10.1016/j.addma.2020.101270>.
- [38] C. Galy, E. Le Guen, E. Lacoste, C. Arvieu, Main defects observed in aluminum alloy parts produced by SLM: From causes to consequences, *Addit. Manuf.* 22 (2018) 165–175. <https://doi.org/10.1016/j.addma.2018.05.005>.
- [39] E.O. Olakanmi, R.F. Cochrane, K.W. Dalgarno, A review on selective laser sintering/melting (SLS/SLM) of aluminium alloy powders: Processing, microstructure, and properties, *Prog. Mater. Sci.* 74 (2015) 401–477. <https://doi.org/10.1016/j.pmatsci.2015.03.002>.
- [40] K. Bartkowiak, S. Ullrich, T. Frick, M. Schmidt, New developments of laser processing aluminium alloys via additive manufacturing technique, in: *Phys. Procedia*, Elsevier B.V., 2011: pp. 393–401. <https://doi.org/10.1016/j.phpro.2011.03.050>.
- [41] X.P. Li, X.J. Wang, M. Saunders, A. Suvorova, L.C. Zhang, Y.J. Liu, M.H. Fang, Z.H. Huang, T.B. Sercombe, A selective laser melting and solution heat treatment refined Al-12Si alloy with a controllable ultrafine eutectic microstructure and 25% tensile ductility, *Acta Mater.* 95 (2015) 74–82. <https://doi.org/10.1016/j.actamat.2015.05.017>.
- [42] K.G. Prashanth, S. Scudino, H.J. Klauss, K.B. Surreddi, L. Löber, Z. Wang, A.K. Chaubey, U. Kühn, J. Eckert, Microstructure and mechanical properties of Al-12Si produced by selective laser melting: Effect of heat treatment, *Mater. Sci. Eng. A.* 590 (2014) 153–160. <https://doi.org/10.1016/j.msea.2013.10.023>.
- [43] W. Li, S. Li, J. Liu, A. Zhang, Y. Zhou, Q. Wei, C. Yan, Y. Shi, Effect of heat treatment on AlSi10Mg alloy fabricated by selective laser melting: Microstructure evolution, mechanical properties and fracture mechanism, *Mater. Sci. Eng. A.* 663 (2016) 116–125. <https://doi.org/10.1016/j.msea.2016.03.088>.
- [44] T. Kimura, T. Nakamoto, Microstructures and mechanical properties of A356 (AlSi7Mg0.3) aluminum alloy fabricated by selective laser melting, *Mater. Des.* 89 (2016) 1294–1301. <https://doi.org/10.1016/j.matdes.2015.10.065>.
- [45] T. Kimura, T. Nakamoto, M. Mizuno, H. Araki, Effect of silicon content on densification, mechanical and thermal properties of Al-xSi binary alloys fabricated using selective laser melting, *Mater. Sci. Eng. A.* 682 (2017) 593–602. <https://doi.org/10.1016/j.msea.2016.11.059>.
- [46] P. Ma, K. Prashanth, S. Scudino, Y. Jia, H. Wang, C. Zou, Z. Wei, J. Eckert, Influence of Annealing on Mechanical Properties of Al-20Si Processed by Selective Laser Melting, *Metals (Basel)*. 4 (2014) 28–36. <https://doi.org/10.3390/met4010028>.
- [47] N. Read, W. Wang, K. Essa, M.M. Attallah, Selective laser melting of AlSi10Mg alloy: Process optimisation and mechanical properties development, *Mater. Des.* 65 (2015) 417–424. <https://doi.org/10.1016/j.matdes.2014.09.044>.
- [48] R. Chou, J. Milligan, M. Paliwal, M. Brochu, Additive Manufacturing of Al-12Si Alloy Via Pulsed Selective Laser Melting, *JOM*. 67 (2015) 590–596. <https://doi.org/10.1007/s11837-014-1272-9>.
- [49] D.K. Kim, W. Woo, J.H. Hwang, K. An, S.H. Choi, Stress partitioning behavior of an AlSi10Mg alloy produced by selective laser melting during tensile deformation using in situ neutron diffraction, *J. Alloys Compd.* 686 (2016) 281–286. <https://doi.org/10.1016/j.jallcom.2016.06.011>.
- [50] Y.D. Jia, P. Ma, K.G. Prashanth, G. Wang, J. Yi, S. Scudino, F.Y. Cao, J.F. Sun, J. Eckert, Microstructure and thermal expansion behavior of Al-50Si synthesized by selective laser melting, *J. Alloys Compd.* 699 (2017) 548–553. <https://doi.org/10.1016/j.jallcom.2016.12.429>.
- [51] A.B. Spierings, K. Dawson, T. Heeling, P.J. Uggowitzer, R. Schäublin, F. Palm, K. Wegener, Microstructural features of Sc- and Zr-modified Al-Mg alloys processed by selective laser melting, *Mater. Des.* 115 (2017) 52–63. <https://doi.org/10.1016/j.matdes.2016.11.040>.
- [52] A.B. Spierings, K. Dawson, M. Voegtlin, F. Palm, P.J. Uggowitzer, Microstructure and mechanical properties of as-processed scandium-modified aluminium using selective laser melting, *CIRP Ann. - Manuf. Technol.* 65 (2016) 213–216. <https://doi.org/10.1016/j.cirp.2016.04.057>.

- [53] A.B. Spierings, K. Dawson, P.J. Uggowitzer, K. Wegener, Influence of SLM scan-speed on microstructure, precipitation of Al₃Sc particles and mechanical properties in Sc- and Zr-modified Al-Mg alloys, *Mater. Des.* 140 (2018) 134–143. <https://doi.org/10.1016/j.matdes.2017.11.053>.
- [54] K. Schmidtke, F. Palm, A. Hawkins, C. Emmelmann, Process and mechanical properties: Applicability of a scandium modified Al-alloy for laser additive manufacturing, in: *Phys. Procedia*, Elsevier B.V., 2011: pp. 369–374. <https://doi.org/10.1016/j.phpro.2011.03.047>.
- [55] E. Louvis, P. Fox, C.J. Sutcliffe, Selective laser melting of aluminium components, *J. Mater. Process. Technol.* 211 (2011) 275–284. <https://doi.org/10.1016/j.jmatprotec.2010.09.019>.
- [56] A. SONAWANE, G. ROUX, J.-J. BLANDIN, A. DESPRES, G. MARTIN, Cracking mechanism and its sensitivity to processing conditions during laser powder bed fusion of a structural Aluminum alloy., *Materialia*. 15 (2020) 100976. <https://doi.org/10.1016/j.mtla.2020.100976>.
- [57] P. Wang, H.C. Li, K.G. Prashanth, J. Eckert, S. Scudino, Selective laser melting of Al-Zn-Mg-Cu: Heat treatment, microstructure and mechanical properties, *J. Alloys Compd.* 707 (2017) 287–290. <https://doi.org/10.1016/j.jallcom.2016.11.210>.
- [58] S. Sun, L. Zheng, Y. Liu, J. Liu, H. Zhang, Characterization of Al-Fe-V-Si heat-resistant aluminum alloy components fabricated by selective laser melting, *J. Mater. Res.* (2015) 1–9. <https://doi.org/10.1557/jmr.2015.110>.
- [59] S. Sun, L. Zheng, H. Peng, H. Zhang, Microstructure and mechanical properties of Al-Fe-V-Si aluminum alloy produced by electron beam melting, *Mater. Sci. Eng. A.* 659 (2016) 207–214. <https://doi.org/10.1016/j.msea.2016.02.053>.
- [60] L. Zheng, Y. Liu, S. Sun, H. Zhang, Selective laser melting of Al-8.5Fe-1.3V-1.7Si alloy: Investigation on the resultant microstructure and hardness, *Chinese J. Aeronaut.* 28 (2015) 564–569. <https://doi.org/10.1016/j.cja.2015.01.013>.
- [61] A.H. Maamoun, Y.F. Xue, M.A. Elbestawi, S.C. Veldhuis, The effect of selective laser melting process parameters on the microstructure and mechanical properties of Al6061 and AlSi10Mg alloys, *Materials (Basel)*. 12 (2018). <https://doi.org/10.3390/ma12010012>.
- [62] M. Karg, B. Ahuja, S. Wiesenmayer, S. Kuryntsev, M. Schmidt, Effects of Process Conditions on the Mechanical Behavior of Aluminium Wrought Alloy EN AW-2219 (AlCu6Mn) Additively Manufactured by Laser Beam Melting in Powder Bed, *Micromachines*. 8 (2017) 23. <https://doi.org/10.3390/mi8010023>.
- [63] M.C. Flemings, Solidification processing, *Metall. Trans.* 5 (1974) 2121–2134. <https://doi.org/10.1007/BF02643923>.
- [64] M. Wong, I. Owen, C.J. Sutcliffe, A. Puri, Convective heat transfer and pressure losses across novel heat sinks fabricated by Selective Laser Melting, *Int. J. Heat Mass Transf.* 52 (2009) 281–288. <https://doi.org/10.1016/j.ijheatmasstransfer.2008.06.002>.
- [65] P.G.E. Jerrard, L. Hao, S. Dadbakhsh, K.E. Evans, Consolidation behaviour and microstructure characteristics of pure aluminium and alloy powders following Selective Laser Melting processing, in: *Proc. 36th Int. MATADOR Conf.*, Springer London, 2010: pp. 487–490. https://doi.org/10.1007/978-1-84996-432-6_108.
- [66] P. Mukhopadhyay, Alloy Designation, Processing, and Use of AA6XXX Series Aluminium Alloys, *ISRN Metall.* 2012 (2012) 1–15. <https://doi.org/10.5402/2012/165082>.
- [67] International Alloy Designations and Chemical Composition Limits for Wrought Aluminum and Wrought Aluminum Alloys With Support for On-line Access From: Aluminum Extruders Council Use of the Information, 2015. www.aluminum.org (accessed May 3, 2020).
- [68] L.H. Pereira, G.H. Asato, L.B. Otani, A.M. Jorge, C.S. Kiminami, C. Bolfarini, W.J. Botta, Changing the solidification sequence and the morphology of iron-containing intermetallic phases in AA6061 aluminum alloy processed by spray forming, *Mater. Charact.* 145 (2018) 507–515. <https://doi.org/10.1016/j.matchar.2018.09.006>.
- [69] C.M. Dinnis, J.A. Taylor, A.K. Dahle, As-cast morphology of iron-intermetallics in Al-Si foundry alloys,

- Scr. Mater. 53 (2005) 955–958. <https://doi.org/10.1016/j.scriptamat.2005.06.028>.
- [70] H.Q. Wang, W.L. Sun, Y.Q. Xing, Microstructure analysis on 6061 aluminum alloy after casting and diffuses annealing process, *Phys. Procedia*. 50 (2013) 68–75. <https://doi.org/10.1016/j.phpro.2013.11.013>.
- [71] E. Giraud, Etude expérimentale et modélisation du comportement mécanique d'une alliage d'aluminium 6061 à l'état pâteux : application à la fissuration à chaud lors du soudage TIG et FE, 2010.
- [72] Q. Chu, R. Bai, H. Jian, Z. Lei, N. Hu, C. Yan, Microstructure, texture and mechanical properties of 6061 aluminum laser beam welded joints, *Mater. Charact.* 137 (2018) 269–276. <https://doi.org/10.1016/j.matchar.2018.01.030>.
- [73] E. Giraud, M. Suéry, J. Adrien, E. Maire, M. Coret, Hot tearing sensitivity of al-mg-si alloys evaluated by x-ray microtomography after constrained solidification at high cooling rate, *Hot Crack. Phenom. Welds III*. (2011) 87–99. <https://doi.org/10.1007/978-3-642-16864-2-6>.
- [74] S.Z. Uddin, L.E. Murr, C.A. Terrazas, P. Morton, D.A. Roberson, R.B. Wicker, Processing and characterization of crack-free aluminum 6061 using high-temperature heating in laser powder bed fusion additive manufacturing, *Addit. Manuf.* 22 (2018) 405–415. <https://doi.org/10.1016/j.addma.2018.05.047>.
- [75] C. Weingarten, D. Buchbinder, N. Pirch, W. Meiners, K. Wissenbach, R. Poprawe, Formation and reduction of hydrogen porosity during selective laser melting of AlSi10Mg, *J. Mater. Process. Technol.* 221 (2015) 112–120. <https://doi.org/10.1016/j.jmatprotec.2015.02.013>.
- [76] T. Qi, H. Zhu, H. Zhang, J. Yin, L. Ke, X. Zeng, Selective laser melting of Al7050 powder: Melting mode transition and comparison of the characteristics between the keyhole and conduction mode, *Mater. Des.* 135 (2017) 257–266. <https://doi.org/10.1016/j.matdes.2017.09.014>.
- [77] Y. Chen, S.J. Clark, C.L.A. Leung, L. Sinclair, S. Marussi, M.P. Olbinado, E. Boller, A. Rack, I. Todd, P.D. Lee, In-situ Synchrotron imaging of keyhole mode multi-layer laser powder bed fusion additive manufacturing, *Appl. Mater. Today*. 20 (2020) 100650. <https://doi.org/10.1016/j.apmt.2020.100650>.
- [78] S.Z. Uddin, D. Espalin, J. Mireles, P. Morton, C. Terrazas, S. Collins, L.E. Murr, R. Wicker, Laser powder bed fusion fabrication and characterization of crack-free aluminum alloy 6061 using in-process powder bed induction heating, *Solid Free. Fabr. 2017 Proc. 28th Annu. Int. Solid Free. Fabr. Symp. - An Addit. Manuf. Conf. SFF 2017*. (2020) 214–227.
- [79] Laser Welding Copper with Blue Diode Lasers | LASERLINE, (n.d.). <https://www.laserline.com/en-int/laser-welding-copper/> (accessed March 15, 2021).
- [80] S. Patel, M. Vlasea, Melting modes in laser powder bed fusion, *Materialia*. 9 (2020). <https://doi.org/10.1016/j.mta.2020.100591>.
- [81] S. Kou, *Welding Metallurgy*, John Wiley & Sons, Inc., 2003. [https://doi.org/10.1016/S0016-7878\(62\)80017-0](https://doi.org/10.1016/S0016-7878(62)80017-0).
- [82] S.N. Lekakh, R.O. Malley, M. Emmendorfer, B. Hrebec, Control of Columnar to Equiaxed Transition in Solidification Macrostructure of Austenitic Stainless Steel Castings, (2017). <https://doi.org/10.2355/isijinternational.ISIJINT-2016-684>.
- [83] Chapter 1: Weld Solidification, 1997. www.asminternational.org (accessed May 15, 2020).
- [84] M. Lalpoor, D.G. Eskin, G. ten Brink, L. Katgerman, Microstructural features of intergranular brittle fracture and cold cracking in high strength aluminum alloys, *Mater. Sci. Eng. A*. 527 (2010) 1828–1834. <https://doi.org/10.1016/j.msea.2009.11.003>.
- [85] M. Rappaz, P.D. Grasso, V. Mathier, J.M. Drezet, A. Jacot, How does coalescence of dendrite arms or grains influence hot tearing?, *Solidif. Alum. Alloy*. (2004) 179–190.
- [86] D.G. Eskin, Suyitno, L. Katgerman, Mechanical properties in the semi-solid state and hot tearing of aluminium alloys, *Prog. Mater. Sci.* 49 (2004) 629–711. [https://doi.org/10.1016/S0079-6425\(03\)00037-9](https://doi.org/10.1016/S0079-6425(03)00037-9).
- [87] D. Fabregue, Microstructure et fissuration à chaud lors du soudage laser d'alliages d'aluminium 6000, (2004).
- [88] S. Griffiths, H. Ghasemi Tabasi, T. Ivas, X. Maeder, A. De Luca, K. Zwiack, R. Wróbel, J. Jhabvala,

- R.E. Logé, C. Leinenbach, Combining alloy and process modification for micro-crack mitigation in an additively manufactured Ni-base superalloy, *Addit. Manuf.* 36 (2020). <https://doi.org/10.1016/j.addma.2020.101443>.
- [89] N. Wang, S. Mokadem, M. Rappaz, W. Kurz, Solidification cracking of superalloy single- and bi-crystals, *Acta Mater.* 52 (2004) 3173–3182. <https://doi.org/10.1016/j.actamat.2004.03.047>.
- [90] N. Coniglio, C.E. Cross, Mechanisms for solidification crack initiation and growth in aluminum welding, *Metall. Mater. Trans. A Phys. Metall. Mater. Sci.* 40 (2009) 2718–2728. <https://doi.org/10.1007/s11661-009-9964-4>.
- [91] Prokhorov, Resistance to hot tearing of cast metals during solidification, *Russ. Cast. Prod.* 2 (1962) 172–175.
- [92] V. FEVRER, F. V, Mathematisches modell der warmrissneigung von binaeren Aluminiumlegierungen., (1976).
- [93] S. Kou, A criterion for cracking during solidification, *Acta Mater.* 88 (2015) 366–374. <https://doi.org/10.1016/j.actamat.2015.01.034>.
- [94] C. Huang, S. Kou, Liquation Cracking in Full-Penetration Al-Mg-Si Welds A higher fraction solid in the weld metal than in the partially melted zone during terminal solidification is a necessary condition for cracking to occur, *Weld. J.* (2004) 111–122.
- [95] T. Soysal, S. Kou, Effect of filler metals on solidification cracking susceptibility of Al alloys 2024 and 6061, *J. Mater. Process. Technol.* 266 (2019) 421–428. <https://doi.org/10.1016/j.jmatprotec.2018.11.022>.
- [96] J.M. Drezet, D. Allehaux, Application of the rappaz-drezet-gremaud hot tearing criterion to welding of aluminium alloys, *Hot Crack. Phenom. Welds II.* (2008) 19–37. https://doi.org/10.1007/978-3-540-78628-3_2.
- [97] J.M. Drezet, M.S.F. Lima, J.D. Wagnière, M. Rappaz, W. Kurz, Crack-free aluminium alloy welds using a twin laser process, *Weld. World.* 52 (2008) 87–94.
- [98] M. Rappaz, J.M. Dreze, V. Mathier, S. Vernède, Towards a micro-macro model of hot tearing, *Mater. Sci. Forum.* 519–521 (2006) 1665–1674. <https://doi.org/10.4028/www.scientific.net/msf.519-521.1665>.
- [99] S. Vernède, P. Jarry, M. Rappaz, A granular model of equiaxed mushy zones: Formation of a coherent solid and localization of feeding, *Acta Mater.* 54 (2006) 4023–4034. <https://doi.org/10.1016/j.actamat.2006.04.035>.
- [100] S. Vernede, A granular model of solidification as applied to hot tearing., EPFL, Switzerland, 2007.
- [101] J. Zhang, D.C. Weckman, Y. Zhou, Effects of temporal pulse shaping on cracking susceptibility of 6061-T6 aluminum Nd:YAG laser welds, *Weld. J.* 87 (2008) 18s–30s.
- [102] C.J. Todaro, M.A. Easton, D. Qiu, D. Zhang, M.J. Bermingham, E.W. Lui, M. Brandt, D.H. StJohn, M. Qian, Grain structure control during metal 3D printing by high-intensity ultrasound, *Nat. Commun.* 11 (2020) 1–9. <https://doi.org/10.1038/s41467-019-13874-z>.
- [103] J.R. Croteau, S. Griffiths, M.D. Rossell, C. Leinenbach, C. Kenel, V. Jansen, D.N. Seidman, D.C. Dunand, N.Q. Vo, Microstructure and mechanical properties of Al-Mg-Zr alloys processed by selective laser melting, *Acta Mater.* 153 (2018) 35–44. <https://doi.org/10.1016/j.actamat.2018.04.053>.
- [104] M. Opprecht, J.P. Garandet, G. Roux, C. Flament, M. Soulier, A solution to the hot cracking problem for aluminium alloys manufactured by laser beam melting, *Acta Mater.* 197 (2020) 40–53. <https://doi.org/10.1016/j.actamat.2020.07.015>.
- [105] S. Griffiths, M.D. Rossell, J. Croteau, N.Q. Vo, D.C. Dunand, C. Leinenbach, Effect of laser rescanning on the grain microstructure of a selective laser melted Al-Mg-Zr alloy, *Mater. Charact.* 143 (2018) 34–42. <https://doi.org/10.1016/j.matchar.2018.03.033>.
- [106] D. Carluccio, M.J. Bermingham, Y. Zhang, D.H. StJohn, K. Yang, P.A. Rometsch, X. Wu, M.S. Dargusch, Grain refinement of laser remelted Al-7Si and 6061 aluminium alloys with Tibor® and scandium additions, *J. Manuf. Process.* 35 (2018) 715–720. <https://doi.org/10.1016/j.jmapro.2018.08.030>.

- [107] R. Xiao, X. Zhang, Problems and issues in laser beam welding of aluminum-lithium alloys, *J. Manuf. Process.* 16 (2014) 166–175. <https://doi.org/10.1016/j.jmapro.2013.10.005>.
- [108] N. Coniglio, C.E. Cross, T. Michael, M. Lammers, Defining a critical weld dilution to avoid solidification cracking in aluminum, *Weld. J. (Miami, Fla.)*. 87 (2008) 237–247.
- [109] S. Griffiths, M.D. Rossell, J. Croteau, N.Q. Vo, D.C. Dunand, C. Leinenbach, Effect of laser rescanning on the grain microstructure of a selective laser melted Al-Mg-Zr alloy, *Mater. Charact.* 143 (2018) 34–42. <https://doi.org/10.1016/j.matchar.2018.03.033>.
- [110] K. V. Yang, Y. Shi, F. Palm, X. Wu, P. Rometsch, Columnar to equiaxed transition in Al-Mg(Sc)-Zr alloys produced by selective laser melting, *Scr. Mater.* 145 (2018) 113–117. <https://doi.org/10.1016/j.scriptamat.2017.10.021>.
- [111] L. Zhou, H. Hyer, S. Park, H. Pan, Y. Bai, K.P. Rice, Y. Sohn, Microstructure and mechanical properties of Zr-modified aluminum alloy 5083 manufactured by laser powder bed fusion, *Addit. Manuf.* 28 (2019) 485–496. <https://doi.org/10.1016/j.addma.2019.05.027>.
- [112] DIN EN 14242 - Aluminium and aluminium alloys - Chemical analysis - Inductively coupled plasma optical emission spectral analysis | Engineering360, (n.d.). <https://standards.globalspec.com/std/467330/din-en-14242> (accessed July 22, 2020).
- [113] ASTM B822, Standard Test Method for Particle Size Distribution of Refractory Metal Powders and Related Compounds by Light Scattering, ASTM Int. West Conshohocken, PA. (2010) 1–4. <https://doi.org/10.1520/B0822-10>.
- [114] A.B. Spierings, M. Voegtlin, T. Bauer, K. Wegener, Powder flowability characterisation methodology for powder-bed-based metal additive manufacturing, *Prog. Addit. Manuf.* 1 (2016) 9–20. <https://doi.org/10.1007/s40964-015-0001-4>.
- [115] H. Hausner, Friction conditions in a mass of metal powder., *Int. J. Powder Metall.* 3 (1967) 7–13.
- [116] D. Svetlizky, B. Zheng, T. Buta, Y. Zhou, O. Golan, U. Breiman, R. Haj-Ali, J.M. Schoenung, E.J. Lavernia, N. Eliaz, Directed energy deposition of Al 5xxx alloy using Laser Engineered Net Shaping (LENS®), *Mater. Des.* 192 (2020) 108763. <https://doi.org/10.1016/j.matdes.2020.108763>.
- [117] N. Tissot, Amélioration du procédé LBM par nanostructuration de poudres d'aluminium, 2018.
- [118] C.D. Boley, S.C. Mitchell, A.M. Rubenchik, S.S.Q. Wu, Metal powder absorptivity: modeling and experiment, *Appl. Opt.* 55 (2016) 6496. <https://doi.org/10.1364/ao.55.006496>.
- [119] ProX DMP 200 - Metal 3D Printer | 3D Systems, (n.d.). <https://www.3dsystems.com/3d-printers/prox-dmp-200> (accessed March 11, 2021).
- [120] T. DebRoy, H.L. Wei, J.S. Zuback, T. Mukherjee, J.W. Elmer, J.O. Milewski, A.M. Beese, A. Wilson-Heid, A. De, W. Zhang, Additive manufacturing of metallic components – Process, structure and properties, *Prog. Mater. Sci.* 92 (2018) 112–224. <https://doi.org/10.1016/j.pmatsci.2017.10.001>.
- [121] V. GUNENTHIRAM, Compréhension de la formation de porosités en fabrication additive (LBM). Analyse expérimentale de l'interaction laser – lit de poudre – bain liquide, 2018.
- [122] E.O. Olakanmi, Selective laser sintering/melting (SLS/SLM) of pure Al, Al-Mg, and Al-Si powders: Effect of processing conditions and powder properties, *J. Mater. Process. Technol.* 213 (2013) 1387–1405. <https://doi.org/10.1016/j.jmatprotec.2013.03.009>.
- [123] N. Kouraytem, A.D. Rollett, Solidification crack propagation and morphology dependence on processing parameters in AA6061 from ultra-high-speed x-ray visualization, *Addit. Manuf.* (2021). <https://doi.org/10.1016/j.addma.2021.101959>.
- [124] M. Miyagi, H. Wang, R. Yoshida, Y. Kawahito, H. Kawakami, T. Shoubu, Effect of alloy element on weld pool dynamics in laser welding of aluminum alloys, *Sci. Rep.* 8 (2018) 1–10. <https://doi.org/10.1038/s41598-018-31350-4>.
- [125] K. V. Yang, P. Rometsch, T. Jarvis, J. Rao, S. Cao, C. Davies, X. Wu, Porosity formation mechanisms and fatigue response in Al-Si-Mg alloys made by selective laser melting, *Mater. Sci. Eng. A.* 712 (2018) 166–

174. <https://doi.org/10.1016/j.msea.2017.11.078>.
- [126] A.M. Kiss, A.Y. Fong, N.P. Calta, V. Thampy, A.A. Martin, P.J. Depond, J. Wang, M.J. Matthews, R.T. Ott, C.J. Tassone, K.H. Stone, M.J. Kramer, A. van Buuren, M.F. Toney, J. Nelson Weker, Laser-Induced Keyhole Defect Dynamics during Metal Additive Manufacturing, *Adv. Eng. Mater.* 21 (2019) 1–7. <https://doi.org/10.1002/adem.201900455>.
- [127] H. KYOGOKU, T.-T. IKESHOJI, A review of metal additive manufacturing technologies: Mechanism of defects formation and simulation of melting and solidification phenomena in laser powder bed fusion process, *Mech. Eng. Rev.* 7 (2020) 19-00182-19–00182. <https://doi.org/10.1299/mer.19-00182>.
- [128] P. Lhuissier, X. Bataillon, C. Maestre, J. Sijobert, E. Cabrol, P. Bertrand, E. Boller, A. Rack, J.J. Blandin, L. Salvo, G. Martin, In situ 3D X-ray microtomography of laser-based powder-bed fusion (L-PBF)—A feasibility study, *Addit. Manuf.* 34 (2020) 101271. <https://doi.org/10.1016/j.addma.2020.101271>.
- [129] U. Scipioni Bertoli, G. Guss, S. Wu, M.J. Matthews, J.M. Schoenung, In-situ characterization of laser-powder interaction and cooling rates through high-speed imaging of powder bed fusion additive manufacturing, *Mater. Des.* 135 (2017) 385–396. <https://doi.org/10.1016/j.matdes.2017.09.044>.
- [130] P. Lhuissier, X. Bataillon, C. Maestre, J. Sijobert, E. Cabrol, P. Bertrand, E. Boller, A. Rack, J.J. Blandin, L. Salvo, G. Martin, In situ 3D X-ray microtomography of laser-based powder-bed fusion (L-PBF)—A feasibility study, *Addit. Manuf.* 34 (2020) 101271. <https://doi.org/10.1016/j.addma.2020.101271>.
- [131] ASM Material Data Sheet, (n.d.). <http://asm.matweb.com/search/SpecificMaterial.asp?bassnum=MA6061T6> (accessed May 8, 2020).
- [132] D. Buchbinder, H. Schleifenbaum, S. Heidrich, W. Meiners, J. Bültmann, High power Selective Laser Melting (HP SLM) of aluminum parts, *Phys. Procedia.* 12 (2011) 271–278. <https://doi.org/10.1016/j.phpro.2011.03.035>.
- [133] A. Walker, Pulse Laser Powder Bed Fusion of High Strength Aluminum Alloys, (2018).
- [134] E. Chauvet, P. Kontis, E.A. Jäggle, B. Gault, D. Raabe, C. Tassin, J.J. Blandin, R. Dendievel, B. Vayre, S. Abed, G. Martin, Hot cracking mechanism affecting a non-weldable Ni-based superalloy produced by selective electron Beam Melting, *Acta Mater.* 142 (2018) 82–94. <https://doi.org/10.1016/j.actamat.2017.09.047>.
- [135] A. Niel, C. Bordreuil, F. Deschaux-Beaume, G. Frasn, Modelling hot cracking in 6061 aluminium alloy weld metal with microstructure based criterion, *Sci. Technol. Weld. Join.* 18 (2013) 154–160. <https://doi.org/10.1179/1362171812Y.0000000072>.
- [136] C. Hagenlocher, M. Seibold, R. Weber, T. Graf, Modulation of the local grain structure in laser beam welds to inhibit the propagation of centerline hot cracks, *Procedia CIRP.* 74 (2018) 434–437. <https://doi.org/10.1016/j.procir.2018.08.164>.
- [137] J. Drezet, M. Rappaz, Fem Implementation of a New Hot Tearing Criterion, in: 4th Esaform Conf. Univ. Liege, Ed. A.-M Habraken, 2018: pp. 741–744.
- [138] J. Campbell, Castings, Elsevier Ltd, 2003. <https://doi.org/10.1016/B978-0-7506-4790-8.X5016-5>.
- [139] C.L.A. Leung, S. Marussi, R.C. Atwood, M. Towrie, P.J. Withers, P.D. Lee, In situ X-ray imaging of defect and molten pool dynamics in laser additive manufacturing, *Nat. Commun.* 9 (2018) 1–9. <https://doi.org/10.1038/s41467-018-03734-7>.
- [140] C. Huang, S. Kou, Liquation mechanisms in multicomponent aluminum alloys during welding, *Weld. J.* (Miami, Fla). 81 (2002).
- [141] H. Seo, J. Gu, K. Park, Y. Jung, J. Lee, W. Chung, Solidification and segregation behaviors in 6061 aluminum alloy, *Met. Mater. Int.* 19 (2013) 433–438. <https://doi.org/10.1007/s12540-013-3008-8>.
- [142] D.M. Stefanescu, Solidification Structures of Aluminum Alloys Basic Microstructures of Aluminum-Base Alloys, *ASM Int.* (2004). <https://doi.org/10.13140/RG.2.1.2892.0169>.
- [143] E.F. Prados, V.L. Sordi, M. Ferrante, The effect of Al₂Cu precipitates on the microstructural evolution, tensile strength, ductility and work-hardening behaviour of a Al-4 wt.% Cu alloy processed by equal-

- channel angular pressing, *Acta Mater.* 61 (2013) 115–125. <https://doi.org/10.1016/j.actamat.2012.09.038>.
- [144] P. Shower, J.R. Morris, D. Shin, B. Radhakrishnan, L.F. Allard, A. Shyam, Temperature-dependent stability of θ' -Al₂Cu precipitates investigated with phase field simulations and experiments, *Materialia*. 5 (2019) 100185. <https://doi.org/10.1016/j.mtla.2018.100185>.
- [145] FactSage.com, (n.d.). <http://www.factsage.com/> (accessed May 6, 2020).
- [146] E. Giraud, M. Suery, M. Coret, Mechanical behavior of AA6061 aluminum in the semisolid state obtained by partial melting and partial solidification, *Metall. Mater. Trans. A*. 41 (2010) 2257–2268. <https://doi.org/10.1007/s11661-010-0268-5>.
- [147] W. Kurz, B. Giovanola, R. Trivedi, Theory of microstructural development during rapid solidification, *Acta Metall.* 34 (1986) 823–830. [https://doi.org/10.1016/0001-6160\(86\)90056-8](https://doi.org/10.1016/0001-6160(86)90056-8).
- [148] R. T., S. W., Dislocation Models of Crystal Grain Boundaries, *Phys. Rev.* 78 (1950) 275–289.
- [149] W. Zhou, X. Ren, Y. Ren, S. Yuan, N. Ren, X. Yang, S. Adu-Gyamfi, Initial dislocation density effect on strain hardening in FCC aluminium alloy under laser shock peening, *Philos. Mag.* 97 (2017) 917–929. <https://doi.org/10.1080/14786435.2017.1285073>.
- [150] M.A. Tschopp, D.L. McDowell, Asymmetric tilt grain boundary structure and energy in copper and aluminium, *Philos. Mag.* 87 (2007) 3871–3892. <https://doi.org/10.1080/14786430701455321>.
- [151] V. V. Bulatov, B.W. Reed, M. Kumar, Grain boundary energy function for fcc metals, *Acta Mater.* 65 (2014) 161–175. <https://doi.org/10.1016/j.actamat.2013.10.057>.
- [152] Z. Jian, K. Kuribayashi, W. Jie, Solid-liquid interface energy of metals at melting point and undercooled state, *Mater. Trans.* 43 (2002) 721–726. <https://doi.org/10.2320/matertrans.43.721>.
- [153] A.L. Greer, A.M. Bunn, A. Tronche, P. V. Evans, D.J. Bristow, Modelling of inoculation of metallic melts: application to grain refinement of aluminium by Al-Ti-B, *Acta Mater.* 48 (2000) 2823–2835. [https://doi.org/10.1016/S1359-6454\(00\)00094-X](https://doi.org/10.1016/S1359-6454(00)00094-X).
- [154] COMSOL Multiphysics® software, (n.d.). <https://www.comsol.fr/> (accessed May 6, 2020).
- [155] Z. Liu, H. Qi, Effects of substrate crystallographic orientations on crystal growth and microstructure formation in laser powder deposition of nickel-based superalloy, *Acta Mater.* 87 (2015) 248–258. <https://doi.org/10.1016/j.actamat.2014.12.046>.
- [156] J. Liu, A.C. To, Quantitative texture prediction of epitaxial columnar grains in additive manufacturing using selective laser melting, *Addit. Manuf.* 16 (2017) 58–64. <https://doi.org/10.1016/j.addma.2017.05.005>.
- [157] A.T. Dinsdale, P.N. Quested, The viscosity of aluminium and its alloys - A review of data and models, in: *J. Mater. Sci.*, 2004: pp. 7221–7228. <https://doi.org/10.1023/B:JMISC.0000048735.50256.96>.
- [158] T. Soysal, S. Kou, A simple test for assessing solidification cracking susceptibility and checking validity of susceptibility prediction, *Acta Mater.* 143 (2018) 181–197. <https://doi.org/10.1016/j.actamat.2017.09.065>.
- [159] A. Technologies, Chapter 17 Material Expansion Coefficients, *Laser Opt. User's Man.* (2002) 17–1 to 17–12.
- [160] J.J. Hoyt, A.A. Potter, A molecular dynamics simulation study of the cavitation pressure in liquid Al, *Metall. Mater. Trans. A*. 43 (2012) 3972–3977. <https://doi.org/10.1007/s11661-011-0846-1>.
- [161] Q. Han, A.J. Duncan, S. Viswanathan, Permeability measurements of the flow of interdendritic liquid in equiaxed aluminum-silicon alloys, *Metall. Mater. Trans. B Process Metall. Mater. Process. Sci.* 34 (2003) 25–28. <https://doi.org/10.1007/s11663-003-0051-8>.
- [162] D.R. Poirier, Permeability for flow of interdendritic liquid in columnar-dendritic alloys, *Metall. Trans. B*. 18 (1987) 245–255. <https://doi.org/10.1007/BF02658450>.
- [163] Z. Sun, X.P. Tan, M. Descoins, D. Mangelinck, S.B. Tor, C.S. Lim, Revealing hot tearing mechanism for an additively manufactured high-entropy alloy via selective laser melting, *Scr. Mater.* 168 (2019) 129–133. <https://doi.org/10.1016/j.scriptamat.2019.04.036>.

- [164] L. Battezzati, A.L. Greer, The viscosity of liquid metals and alloys, *Acta Metall.* 37 (1989) 1791–1802. [https://doi.org/10.1016/0001-6160\(89\)90064-3](https://doi.org/10.1016/0001-6160(89)90064-3).
- [165] T. Soysal, S. Kou, Effect of filler metals on solidification cracking susceptibility of Al alloys 2024 and 6061, *J. Mater. Process. Technol.* 266 (2019) 421–428. <https://doi.org/10.1016/j.jmatprotec.2018.11.022>.
- [166] S. S, Study on crack prevention in electron beam welding of 6061 aluminum alloy., *J. Light Met. Weld. Constr.* 40:23–30. (2002).
- [167] S. Geng, P. Jiang, X. Shao, G. Mi, H. Wu, Y. Ai, C. Wang, C. Han, R. Chen, W. Liu, Y. Zhang, Effects of back-diffusion on solidification cracking susceptibility of Al-Mg alloys during welding: A phase-field study, *Acta Mater.* 160 (2018) 85–96. <https://doi.org/10.1016/j.actamat.2018.08.057>.
- [168] J. Liu, H.P. Duarte, S. Kou, Evidence of back diffusion reducing cracking during solidification, *Acta Mater.* 122 (2017) 47–59. <https://doi.org/10.1016/j.actamat.2016.09.037>.
- [169] M. Rappaz, P. Jarry, G. Kurtuldu, J. Zollinger, Solidification of Metallic Alloys: Does the Structure of the Liquid Matter?, *Metall. Mater. Trans. A Phys. Metall. Mater. Sci.* 51 (2020) 2651–2664. <https://doi.org/10.1007/s11661-020-05770-9>.
- [170] F. Gonzales, M. Rappaz, Dendrite growth directions in aluminum-zinc alloys, *Metall. Mater. Trans. A Phys. Metall. Mater. Sci.* 37 (2006) 2797–2806. <https://doi.org/10.1007/BF02586112>.
- [171] C. Bordreuil, A. Niel, Modelling of hot cracking in welding with a cellular automaton combined with an intergranular fluid flow model, *Comput. Mater. Sci.* 82 (2014) 442–450. <https://doi.org/10.1016/j.commatsci.2013.09.067>.
- [172] W. Kurz, D.J. Fisher, Dendrite growth in eutectic alloys: the coupled zone, *Int. Mater. Rev.* 24 (2012) 177–204. <https://doi.org/10.1179/095066079790136408>.
- [173] Z. Malekshahi Beiranyvand, F. Malek Ghaini, H. Naffakh Moosavy, M. Sheikhi, M.J. Torkamany, An Analytical Model for Prediction of Solidification Cracking Susceptibility in Aluminum Alloys Taking into Account the Effect of Solidification Rate, *Metall. Mater. Trans. A Phys. Metall. Mater. Sci.* 50 (2019) 2835–2846. <https://doi.org/10.1007/s11661-019-05171-7>.
- [174] M.J. Aziz, Interface attachment kinetics in alloy solidification, *Metall. Mater. Trans. A Phys. Metall. Mater. Sci.* 27 (1996) 671–686. <https://doi.org/10.1007/BF02648954>.
- [175] A. Hariharan, L. Lu, J. Risse, A. Kostka, B. Gault, E.A. Jäggle, D. Raabe, Misorientation-dependent solute enrichment at interfaces and its contribution to defect formation mechanisms during laser additive manufacturing of superalloys, *Phys. Rev. Mater.* 3 (2019) 123602. <https://doi.org/10.1103/PhysRevMaterials.3.123602>.
- [176] P. Kontis, E. Chauvet, Z. Peng, J. He, A.K. da Silva, D. Raabe, C. Tassin, J.J. Blandin, S. Abed, R. Dendievel, B. Gault, G. Martin, Atomic-scale grain boundary engineering to overcome hot-cracking in additively-manufactured superalloys, *Acta Mater.* 177 (2019) 209–221. <https://doi.org/10.1016/j.actamat.2019.07.041>.
- [177] X. Nie, H. Zhang, H. Zhu, Z. Hu, L. Ke, X. Zeng, Analysis of processing parameters and characteristics of selective laser melted high strength Al-Cu-Mg alloys: From single tracks to cubic samples, *J. Mater. Process. Technol.* 256 (2018) 69–77. <https://doi.org/10.1016/j.jmatprotec.2018.01.030>.
- [178] W. Stopyra, K. Gruber, I. Smolina, T. Kurzynowski, B. Kuźnicka, Laser powder bed fusion of AA7075 alloy: Influence of process parameters on porosity and hot cracking, *Addit. Manuf.* 35 (2020). <https://doi.org/10.1016/j.addma.2020.101270>.



Abstract

In this thesis, an analysis of the hot cracking susceptibility as a function of processing parameters and solute content modification is presented for the structural aluminum alloy 6061 (Al-0.8Si-1.2Mg wt%) processed by laser powder bed fusion (L-PBF). The hot cracking mechanism is identified as solidification cracking based on experimental observations in as-built microstructures. In agreement with previous works, cracks are found to occur at high angle grain boundaries and are preferentially located at the center of the melt pools. Using the Rappaz-Drezet-Gremaud (RDG) model combined with thermal calculations using Rosenthal analytical model, the location of hot cracks corresponds to the regions of highest mechanical solicitation during solidification. Hot cracking sensitivity maps are then developed to predict in a simple manner the variations of hot cracking susceptibility as a function of the first-order process parameters, namely the laser power and scanning speed and as well as for the preheating conditions. The predicted trends are qualitatively in agreement with the experimental observation. The results allow the impact of processing conditions on reducing hot cracking to be discussed and the work also identifies key metallurgical parameters that play a key role in hot cracking. In addition to cracking sensitivity to processing conditions, solute content modification is also studied using the modeling aspect of the work, which helps to suggest guidelines to reduce cracking.

Dans cette thèse, une analyse de la sensibilité à la fissuration à chaud en fonction (i) des paramètres de premier ordre (puissance, vitesse) du procédé de fusion laser sur lit de poudres (L-PBF : Laser Powder Bed Fusion) et (ii) de la variation de la teneur en soluté (Si et Mg principalement) est présentée pour l'alliage d'aluminium à durcissement structural 6061 (Al-0.8Si-1.2Mg wt%). Le mécanisme de fissuration à chaud est identifié comme une fissuration par solidification sur la base d'observations expérimentales des microstructures. En accord avec des travaux antérieurs publiés sur d'autres familles d'alliages, les fissures se propagent aux joints de grains de fortes désorientations et sont préférentiellement situées au centre des bains de fusion. En utilisant le critère de Rappaz-Drezet-Gremaud (RDG criterion) combiné à des simulations thermiques utilisant le formalisme de Rosenthal, la localisation des fissures correspond aux régions des bains de fusion où la sollicitation mécanique intergranulaire est la plus élevée lors de la solidification. Des cartes de sensibilité à la fissuration à chaud sont ensuite développées pour prédire de manière simple les variations de sensibilité à la fissuration à chaud en fonction des paramètres du procédé de premier ordre, à savoir la puissance laser et la vitesse de balayage ainsi que des conditions de préchauffage. Les tendances prédites sont qualitativement en accord avec les observations expérimentales. Les résultats permettent de discuter de l'impact des conditions d'élaboration sur la réduction de la fissuration à chaud et également d'identifier les paramètres métallurgiques clés de ce mécanisme de fissuration.